



# Study of flow conditions in a radial turbine operating at high pressure, high temperature and high rotational speed

Joëlle Najib

## ► To cite this version:

Joëlle Najib. Study of flow conditions in a radial turbine operating at high pressure, high temperature and high rotational speed. Electric power. Université Paris sciences et lettres, 2022. English. NNT : 2022UPSLM066 . tel-04050323

HAL Id: tel-04050323

<https://pastel.hal.science/tel-04050323>

Submitted on 29 Mar 2023

**HAL** is a multi-disciplinary open access archive for the deposit and dissemination of scientific research documents, whether they are published or not. The documents may come from teaching and research institutions in France or abroad, or from public or private research centers.

L'archive ouverte pluridisciplinaire **HAL**, est destinée au dépôt et à la diffusion de documents scientifiques de niveau recherche, publiés ou non, émanant des établissements d'enseignement et de recherche français ou étrangers, des laboratoires publics ou privés.

**THÈSE DE DOCTORAT  
DE L'UNIVERSITÉ PSL**

Préparée à MINES ParisTech

**Etude des conditions d'écoulement dans une turbine radiale opérant à haute pression, haute température et haute vitesse.**

**Study of flow conditions in a radial turbine operating at high pressure, high temperature and high rotational speed.**

Soutenue par

**Joëlle NAJIB**

Le 14 décembre 2022

Ecole doctorale n° 621

**Ingénierie des systèmes,  
matériaux, mécanique,  
énergétique**

Spécialité

**Energétique et génie des  
procédés**

**Composition du jury :**

Monica, SIROUX  
Professeur, INSA Strasbourg

*Présidente*

Vincent, LEMORT  
Professeur, Université de Liège

*Rapporteur*

Petar, VARBANOV  
Dr Habil, Brno University of Technology

*Rapporteur*

Amélie, DANLOS  
Maître de conférences, CNAM

*Examinateuse*

Maroun, NEMER  
Chargé de recherches, MINES Paris

*Examinateur*

Chakib, BOUALLOU  
Professeur, MINES Paris

*Directeur de thèse*



## Acknowledgements

I would like to begin by thanking Dr. Maroun NEMER, the director of the Centre of Energy Efficiency (CES) and my co-director. My sincere gratitude and appreciation go to him for his professional guidance and valuable comments and suggestions.

I extend my sincere gratitude to my Ph.D. director Prof. Chakib BOUALLOU for his constructive remarks and help in this journey.

I am also grateful to the members of the jury Prof. Monica SIROUX, Prof. Vincent LEMORT, Prof. Petar VARBANOV, and Dr. Amélie DANLOS who agreed to invest their time in reading this work and providing positive feedback and accepting to participate in the thesis defense.

I would like to thank my colleagues at the CES for their support and encouragement and for the good times, especially Rita, Ghiwa, and Rabih. In addition, I would like to thank Samer and Egoi for our continuous scientific discussions to improve the quality of this work.

I would also like to thank my University friends that are now family to me: Rita and Ghadie, thank you for your support during these eight years.

This Ph.D. thesis could not be completed without the support of a special person in my life. Thank you, Rudy, my fiancé, for being there for me during all the hard times in this journey. Thank you for your continuous encouragement and faith in me.

Finally, I would like to thank my whole family in Lebanon NAJIB, AOUN, and BECHARA, especially my beloved parents Antoine and Thérèse, my dear brother Bernard and my other half Christelle. Your continuous support and prayers were the reason behind this work. I am sincerely grateful for having you by my side.

# Table of Content

<b>TABLE OF CONTENT .....</b>	<b>IV</b>
<b>LIST OF FIGURES.....</b>	<b>VIII</b>
<b>LIST OF TABLES.....</b>	<b>XII</b>
<b>NOMENCLATURE .....</b>	<b>XIII</b>
<b>GENERAL INTRODUCTION .....</b>	<b>1</b>
<b>INTRODUCTION GENERALE.....</b>	<b>3</b>
<b>CHAPTER 1 : LITERATURE REVIEW .....</b>	<b>5</b>
1.1. INTRODUCTION .....	5
1.2. REGULATIONS OF THE GREENHOUSE EMISSIONS .....	5
1.3. NEW POWERTRAINS FOR AUTOMOTIVE APPLICATIONS.....	7
1.4. GAS TURBINE AS A RANGE EXTENDER FOR ELECTRIC CARS .....	13
1.4.1. Powertrain Rating Setup.....	15
1.4.2. Gas Turbine Architectures.....	16
Brayton cycle.....	16
Recuperated Gas Turbine Cycle.....	17
Reheated and Intercooled Gas Turbine Cycle .....	17
1.4.3. Gas Turbine Mechanical Drive Categories.....	18
1.4.4. Specific Gas turbine Configurations for Series Hybrid Electric Vehicles.....	20
1.5. GAS TURBINE MAIN COMPONENTS CHARACTERISTICS.....	21
1.5.1. Compressors .....	22
1.5.2. Recuperator (HEX).....	22
1.5.3. Combustion Chamber .....	24
➤ Flameless Combustion Chamber .....	25
1.5.4. Turbine.....	27
1.5.5. Bearings.....	27
1.5.6. Generator.....	28
1.6. TECHNICAL CHARACTERISTICS OF LEADING MIRCROTURBINES MANUFACTURERS.....	28
1.7. METHODS TO INCREASE THE GT CYCLE EFFICIENCY .....	29
1.7.1. Turbine Materials / Increasing Turbine Inlet Temperature .....	31
1.7.2. Turbine Cooling Techniques / Increasing Turbine Inlet Temperature .....	33
1.7.2.1 Internal Cooling Techniques .....	33
➤ Internal Smooth Channel Cooling .....	33
➤ Rib Turbulated Cooling .....	34
➤ Impingement Cooling .....	34
➤ Pin Fin Cooling.....	35
➤ Dimple Cooling .....	36
➤ LatticeWork (Vortex Cooling) .....	36
1.7.2.2 External Cooling.....	36
➤ Film cooling.....	37
➤ Transpiration Cooling.....	37
1.7.2.3 Turbine Cooling Disadvantages .....	38
1.7.2.4 Overview of Cooled Radial Turbines.....	38

1.7.3. NO <sub>x</sub> Emissions.....	39
➤ NO <sub>x</sub> Emissions in Gas Turbines .....	39
➤ Techniques to Remove NO <sub>x</sub> in Gas Turbines.....	40
1.7.4. 3D Printing Manufacturing Techniques for GT as a Range Extender .....	41
➤ 3D Printing of Microturbines .....	43
1.8. CONCLUSIONS .....	44
<b>CHAPITRE 1 : ETAT DE L 'ART .....</b>	<b>46</b>
<b>CHAPTER 2 : THERMODYNAMIC AND TECHNOLOGICAL STUDY OF AN INTERCOOLED RECUPERATED REHEATED GAS TURBINE CYCLE WITH COOLING TURBINE BLADE CONFIGURATIONS .....</b>	<b>56</b>
2.1. INTRODUCTION .....	56
2.2. OPTIMAL GT CYCLE AND OPTIMAL OPERATING CONDITIONS .....	56
2.2.1. Methodology .....	56
2.2.2. Results.....	59
2.2.3. Discussions .....	64
2.2.4. Exergy Analysis .....	65
2.3. THERMODYNAMIC STUDY OF GAS TURBINE CYCLES WITH COOLING BLADES.....	67
2.3.1. Methodology .....	68
2.3.2. Results.....	74
➤ Specific Conditions for the CC2 Configuration.....	78
2.4. COMPARISON OF DIFFERENT GT CONFIGURATIONS .....	79
2.5. TECHNOLOGICAL STUDY OF GT-SYSTEM COMPONENTS DESIGN .....	81
2.5.1. Turbomachines .....	82
➤ 3D Printing Technology Limitations .....	83
➤ Cooling Channel Generation .....	83
➤ Turbine Sizing .....	85
2.5.2. Heat Exchangers.....	86
➤ HEX Sizing.....	88
➤ Results .....	91
2.5.3. Results.....	93
2.6. CONCLUSIONS .....	95
<b>CHAPITRE 2: ETUDE THERMODYNAMIQUE ET TECHNOLOGIQUE DES CYCLES DE TURBINES A GAZ AVEC REFROIDISSEMENT DES AUBES.....</b>	<b>97</b>
<b>CHAPTER 3 STUDY OF FLUID FLOW BEHAVIOR OF RADIAL TURBINE ROTOR OPERATING AT HIGH TEMPERATURE AND HIGH PRESSURE. IMPACT OF COOLING.</b>	<b>117</b>
3.1. INTRODUCTION .....	117
3.2. RADIAL TURBINE ARCHITECTURE .....	119
3.3. MOLLIER DIAGRAM OF A RADIAL TURBINE.....	120
3.4. TURBINE ANALYSIS .....	121
3.5. MOMENT OF MOMENTUM BALANCE.....	122
3.6. RADIAL-INFLOW TURBINE PERFORMANCE PARAMETER .....	123
3.6.1. Velocity Ratio.....	123
3.6.2. Specific Speed and Specific Diameter .....	123
3.6.3. Total-to-static Efficiency and Total-to-total Efficiency .....	124

3.6.4. <i>Degree of Reaction</i> .....	124
3.6.5. <i>Flow <math>\varphi</math> and Load <math>\psi</math> Coefficient</i> .....	125
3.7. PRELIMINARY DESIGN STRATEGY OF A RADIAL-INFLOW TURBINE .....	125
3.7.1. <i>Mathematical Equations for the Meanline Design Methodology</i> .....	127
3.7.2. <i>Rotor Design</i> .....	128
3.7.3. <i>Nozzle Blade Design</i> .....	131
3.7.4. <i>Design Feasibility</i> .....	132
3.7.5. <i>Loss Correlations</i> .....	133
3.7.5.1 Incidence Loss.....	133
3.7.5.2 Passage Loss.....	134
3.7.5.3 Tip Clearance Loss .....	135
3.7.5.4 Trailing Edge Loss .....	135
3.7.5.5 Windage Loss .....	136
3.7.5.6 Exit Energy Loss .....	136
3.7.6. <i>Validation of the Meanline Design Code</i> .....	137
3.8. PARAMETRIC STUDY FOR THE MEANLINE DESIGN CODE .....	138
3.9. COMPUTATIONAL FLUID DYNAMICS CFD- UNCOOLED TURBINE .....	140
3.9.1. <i>ANSYS Vista RTD</i> .....	142
3.9.2. <i>Comparison Between Vista RTD and VBA Code</i> .....	142
3.9.3. <i>3D Model Generations</i> .....	143
3.9.4. <i>Computational Fluid Dynamics</i> .....	143
3.9.5. <i>Turbulence Model</i> .....	143
3.9.6. <i>Mesh Generation</i> .....	145
3.9.7. <i>Physical Domain and Boundary Conditions</i> .....	145
3.9.8. <i>Validation of the Current Method</i> .....	146
3.9.9. <i>Modeling of the Uncooled HP Turbine for IRReGT Cycle</i> .....	148
3.9.10. <i>CFD Results</i> .....	151
3.10. DISCUSSIONS .....	153
3.11. 3D SIMULATION OF A COOLED TURBINE .....	154
➤ <i>Cooling Channel Generation</i> .....	155
3.12. NUMERICAL SIMULATION METHODOLOGY OF A COOLED TURBINE BLADE .....	156
3.12.1. <i>3D Generation of the Cooled Blade</i> .....	157
3.12.2. <i>Mesh Generation</i> .....	158
3.12.3. <i>Cooled Turbine Setup</i> .....	158
3.12.4. <i>Comparison Between Cooled and Uncooled Turbine Blade For The Same TIT- Case Study</i> .....	159
➤ Temperature and Pressure Variation .....	159
➤ Heat Transfer Coefficient .....	161
➤ Turbine Efficiency .....	162
➤ Discussions .....	163
3.13. IMPACT OF TURBINE EFFICIENCY ON THE CYCLE PERFORMANCE .....	163
3.14. CONCLUSION .....	165
<b>CHAPITRE 3: ETUDE DU COMPORTEMENT DE L'ECOULEMENT DES FLUIDES DANS UN ROTOR DE TURBINE RADIALE FONCTIONNANT A HAUTE TEMPERATURE ET HAUTE PRESSION. IMPACT DU REFROIDISSEMENT.....</b>	<b>167</b>
<b>GENERAL CONCLUSION AND PERSPECTIVES .....</b>	<b>183</b>
<b>CONCLUSION GENERALE ET PERSPECTIVES .....</b>	<b>185</b>

<b>APPENDICE A: EXPERIMENTAL SETUP .....</b>	<b>188</b>
<b>REFERENCES .....</b>	<b>191</b>

# List of Figures

Figure 1.1: Historical CO <sub>2</sub> emissions performance for passenger cars [4].....	5
Figure 1.2: Techniques to improve the powertrain efficiency.....	6
Figure 1.3: (a) Chrysler GT engine, (b) the first GT car invented by Chrysler [36]. .....	8
Figure 1.4: (a) Scuderi Split cycle engine [56], (b) GT engine concept [57] , (c) Stirling engine concept [58], (d) Steam vapor machine cycle, (e) Ericsson engine concept [59], (f) Thermoacoustic machine [1], (g) Energy process in fuel cell [60]. .....	11
Figure 1.5: GT as an auxiliary power unit for SHEV.....	13
Figure 1.6: Jaguar C-X75 powertrain [66]. .....	14
Figure 1.7: Intercooled Recuperated 80 kw Fulcrum turbine.....	15
Figure 1.8: Mechanical power required to drive the vehicle and different constant speed and on slope of 5% and 10% [1].....	15
Figure 1.9: GT Brayton cycle.....	16
Figure 1.10: PV and TS diagrams of the GT Brayton cycle.....	16
Figure 1.11: Recuperated GT cycle (RGT) (a) schematic presentation, (b) Mitsubishi MTEE 30 kW RGT.....	17
Figure 1.12: Intercooled GT cycle.....	18
Figure 1.13: Reheated GT cycle.....	18
Figure 1.14: single shaft rotor (a) schematic representation, (b) real photo [83]. .....	19
Figure 1.15: Twin-shaft GT cycle.....	19
Figure 1.16: Multi-spool arrangement GT cycle.....	19
Figure 1.17: GT configurations from the literature.....	20
Figure 1.18: IRReGT cycle, (a) schematic presentation, (b) IRReGT cycle under development by Stellantis.....	22
Figure 1.19: (a) Axial compressor, (b) Centrifugal compressor [89]. .....	22
Figure 1.20: The different types of HEX: (a) plate-fin, (b) primary surface, (c) tubular recuperators [92]. .....	23
Figure 1.21: Optimized plate and fin HEX in 3D printing [99]. .....	24
Figure 1.22: Materials depending on the recuperator operating temperature [92]. .....	24
Figure 1.23:Cross section of (a) tubular combustor, (b) tuboannular combustor, (c) annular combustor [103]. .....	25
Figure 1.24: The effect of fuel/air ratio and temperature on NOx emissions [90]. .....	25
Figure 1.25: Comparison between flame (left) and flameless ( right) combustion chamber [107].....	26
Figure 1.26: (a) Axial turbine, (b) radial turbine.....	27
Figure 1.27:Permanent Magnet Alternator from Mecc Alte [117].....	28
Figure 1.28: Cross-section of the Capstone turbine [118].....	29
Figure 1.29: Steps to increase the GT cycle efficiency.....	30
Figure 1.30: Smooth cooling channel.....	34
Figure 1.31: Cooled blade with rib turbulated configuration.....	34
Figure 1.32: (a) Turbine inlet guide vane's typical use of impingement cooling [145], (b) Jet impingement model.....	34
Figure 1.33: (a) Pin fin cooling model [146], (b) Left : staggered array; right: inline array.....	35
Figure 1.34: Dimple cooling [146].....	36
Figure 1.35: Latticework blade cooling method [159]. .....	36
Figure 1.36: Film cooling configuration [162].....	37
Figure 1.37: Schematic presentation of transpiration cooling.....	38

Figure 1.38: Firing temperature effects on NOx emissions for natural gas and fuel oil [178].....	40
Figure 1.39: (a) SCNR, (b) DLE, (c) Catalyst Combustor [88], (d) SCR [80].....	41
Figure 1.40: Schematic representation of a typical (a) FDM setup (b) 3DP setup (c) SLA setup (d) SLS setup [194].....	42
Figure 1.41: Build direction and internal supporting structures introduced within hollow cooling passage [133]. .....	44
Figure 2.1: Recuperated gas turbine cycle. ....	57
Figure 2.2: Methodology for the thermodynamic analysis.....	59
Figure 2.3: Variation of the compressor work, the net specific work, and the cycle efficiency with the number of compressor stages. ....	60
Figure 2.4: Variation of the turbine work, the net specific work, and the cycle efficiency with the number of turbine stages.....	61
Figure 2.5: Variation of different parameters with the maximum pressure. ....	61
Figure 2.6: Variation of compressor outlet exhaust temperature and the exhaust temperature.....	62
Figure 2.7: Variation of air mass flow rate with the maximum pressure. ....	62
Figure 2.8: Variation of different parameters with the TIT.....	63
Figure 2.9: Variation of the cycle efficiency and specific work with the isentropic efficiency of the turbine.....	63
Figure 2.10: IRReGT cycle configuration.....	64
Figure 2.11: (TS) diagram of the IRReGT cycle.....	65
Figure 2.12: Exergy destruction in the IRReGT cycle for a TIT = 1100 °C and a maximum pressure of 9 bar.....	67
Figure 2.13: (a) RGT with cooling turbine, (b) IRReGT cycle with a cooled HP turbine, (c) IRReGT with cooled HP and LP turbines.....	70
Figure 2.14: Schematic presentation of the HP cooled turbine as a heat exchanger. ....	71
Figure 2.15: (a) Expansion for the uncooled turbine, (b), (c) Expansion for a cooled turbine.....	74
Figure 2.16: The impact of the HP TIT on the cycle efficiency and the coolant mass fraction for $T_w=950^\circ\text{C}$ and $T_w=1100^\circ\text{C}$ . ....	75
Figure 2.17: The impact of increasing the coolant mass fraction on the cycle efficiency and power output. ....	76
Figure 2.18: Sensibility analysis of the turbine efficiency with increasing TIT for both cases. ....	76
Figure 2.19: The impact of coolant effectiveness on the coolant mass fraction and the cycle efficiency. ....	77
Figure 2.20: The impact of HEX pinch variation on the cycle efficiency and the thermal power.....	78
Figure 2.21: New configuration of the IRReGT cycle with a cooled HP turbine with no CC2.....	78
Figure 2.22: Impact of increasing HP turbine TIT on the mixing temperature.....	79
Figure 2.23: Efficiency and net specific work for different cooled GT cycle configurations.....	81
Figure 2.24: (a) Uncooled RGT cycle components, (b) Uncooled IRReGT components.....	82
Figure 2.25: cross-section of a typical radial turbine spool showing potential cooling path [132].....	84
Figure 2.26: Internally cooled turbine by HIETA Technologies [210]. ....	84
Figure 2.27: Internal cooling concepts with results of initial solid stress analysis ( red circles where the solid stress exceeds the yield point of the material) [132]. ....	85
Figure 2.28: The weight of the turbomachinery systems for different GT configurations.....	86
Figure 2.29: (a) wavy fins, (b) louver fins, (c) offset fins [238]. ....	87
Figure 2.30: Schematic view of the offset strip fin. ....	88
Figure 2.31: Design steps of the Counter-flow plate-fin heat exchanger.....	90
Figure 2.32: The impact of fin spacing on the HEX weight and the heat transfer coefficient. ....	91
Figure 2.33: Impact of increasing the HEX mass flow rate on its weight.....	91

Figure 2.34: Impact of pinch variation on the HEX weight.....	92
Figure 2.35: Recuperator weight estimation for four GT configurations.....	92
Figure 2.36: Intercooler weight estimation for four GT configurations.....	93
Figure 2.37: Comparison of the efficiency and weight of different GT configurations.....	94
Figure 2.38: Comparison of the net specific work and weight of different GT configurations.....	94
Figure 2.39: Comparison between the components' weight for the different studied cycles.....	95
Figure 3.1: Flowchart of the proposed methodology.....	118
Figure 3.2: Radial turbine main components [111].....	119
Figure 3.3: Meridional view of a turbine stage.....	119
Figure 3.4: Turbine indices [253].....	120
Figure 3.5: Enthalpy-Entropy diagram of the turbine stage [111].....	121
Figure 3.6: Velocity triangle of a radial turbine at the inlet (left) and the outlet (right) with zero swirls at the exit.....	122
Figure 3.7: Balje diagram [112].....	124
Figure 3.8: Performance of a radial turbine in the function of the Flow and the Load coefficient [256].....	125
Figure 3.9: Methodology of meanline design of the radial turbine. (a) 'PMean ' code, (b) 'Mean' code.....	127
Figure 3.10: Generalized stage performance chart [253].....	128
Figure 3.11: Flow angle at rotor inlet as a function of the number of rotor blades [254].....	130
Figure 3.12: Distribution of losses in a radial turbine [259].....	133
Figure 3.13: Tip clearances of a radial rotor [258].....	135
Figure 3.14: Windage losses due to the rotor backflow [250].....	136
Figure 3.15: Impact of rotor rotational speed on (a) its diameter, (b) its efficiency, and power output.....	138
Figure 3.16: Effect of the inlet pressure and temperature on power output and the rotor inlet diameter.....	139
Figure 3.17: Effect of maximum pressure on the rotor leading edge height.....	139
Figure 3.18: Effect of mass flow rate on the impeller efficiency and the power output, and the rotor diameter.....	140
Figure 3.19: Impact of velocity ratio on the rotor inlet diameter, efficiency, and power output.....	140
Figure 3.20: Methodology for 3D simulation.....	142
Figure 3.21: Velocity triangles at the inlet (left) and the outlet (right) of the turbine with red for the VBA code and black for vista RTD.....	142
Figure 3.22: Boundary layer over a flat plate.....	144
Figure 3.23 : $u^+$ in function of $y^+$ [268].....	145
Figure 3.24: Comparison of velocity triangles at the inlet (left) and the outlet (right) of the rotor between [269] (blue) and the validation code (red).....	147
Figure 3.25: Comparison of the temperature variation map, (a) Odabae et al. [267], (b) Validation Code.....	148
Figure 3.26: (a) Rotor 3D geometry, (b) Stator 3D geometry.....	149
Figure 3.27: Rotor mesh generation.....	150
Figure 3.28: Stator mesh generation.....	150
Figure 3.29: Computational fluid domain for stator and rotor.....	151
Figure 3.30: Stator and rotor in 3D.....	151
Figure 3.31: Temperature distribution in the turbine stage (a) 3D view, (b) Blade-to-blade view....	152
Figure 3.32: Pressure distribution in the turbine stage (a) 3D view, (b) Blade-to-blade view.....	152
Figure 3.33: Mach number distribution in the turbine stage.....	152

Figure 3.34: Velocity streamline at 50% span at $N = 120\ 000$ rpm, $P_{max} = 9$ bar.....	153
Figure 3.35: Design methodology for the cooled turbine.....	155
Figure 3.36: Zone with the highest temperature for an uncooled turbine operating at 9 bar and $TIT = 1450$ °C.....	155
Figure 3.37: Cooled turbine blade configuration from 3D Inventor. ....	157
Figure 3.38: Cooled turbine geometry (a) cross-sectional configuration, (b) complete turbine. ....	157
Figure 3.39: The three bodies of the cooled turbine blade in Design Modeler. ....	158
Figure 3.40: Mesh generation for (a) the blade and the coolant, and (b) the hot gas body. ....	158
Figure 3.41: Computational fluid domain for stator and rotor. ....	159
Figure 3.42: Distribution of temperature on the turbine blade for the same TIT and $P_{max}$ (a) cooled rotor, (b) uncooled rotor. ....	160
Figure 3.43: Distribution of pressure on the turbine blade for the same TIT and $P_{max}$ (a) cooled rotor, (b) uncooled rotor.....	161
Figure 3.44: Temperature variation of the coolant in the cooling channel.....	161
Figure 3.45: The efficiency of the designed turbine at different TIT.....	163
Figure 3.46: Comparison of different output parameters between the uncooled standard IRReGT cycle and the IRReGT cycle with a cooled turbine. ....	164
Figure 3.47: Exergy destruction of different components of the two cycles.....	165

# List of Tables

Table 1.1: Summary of different energy converters and their properties in the automotive application.	10
Table 1.2: Comparison of advantages and disadvantages of different energy converters.....	12
Table 1.3: State-of-the-art of different automotive manufacturers in SHEV configurations.....	14
Table 1.4: A summary overview of the literature for GT configurations as range extenders for electric vehicles.....	21
Table 1.5: Microturbines' technical properties for leading manufacturers.....	29
Table 1.6: Properties of different materials used for turbines.....	32
Table 1.7: The pros and cons of the different materials used for turbines.....	33
Table 1.8: Overview of studies on different pin fin cooling configurations .....	35
Table 2.1: Condition parameters for the IRReGT cycle with a HP cooled turbine.....	69
Table 2.2: Properties of the chosen realistic cycles.....	80
Table 2.3: Possible regions to remove the mass and introduce the cooling channel.....	85
Table 2.4: Geometric dimensions of the offset fins for the HEX.....	90
Table 3.1: Review of the turbine design methodology.....	118
Table 3.2: Recommendations for radial turbine design.....	132
Table 3.3: Input parameters.....	137
Table 3.4: Output design validation. ....	137
Table 3.5: Summary of the design procedure in two publications. ....	146
Table 3.6: Operating conditions. ....	146
Table 3.7: Preliminary design validation.....	146
Table 3.8: Rotor geometry design validation. ....	147
Table 3.9: Comparison of the total-to-static efficiency.....	147
Table 3.10: Comparison of the total-to-total efficiency. ....	148
Table 3.11: HP turbine properties. ....	148
Table 3.12: Preliminary design results from Vista RTD. ....	149
Table 3.13: Grid sensitivity study results. ....	150
Table 3.14: Comparison between the proposed methodology and CFD results.....	153
Table 3.15: Comparison between 9 bar and 3 bar. ....	154
Table 3.16: Boundary conditions. ....	159
Table 3.17: Parameters applied for the LMTD method, and the obtained U for both the analytical and the 3D simulation analysis. ....	162
Table 3.18: Turbine Efficiency for the different turbine configurations. ....	163
Table 3.19: Operating conditions. ....	164
Table 3.20: Paramètres appliqués pour la méthode LMTD, et les U obtenus pour l'analyse et la simulation 3D. ....	180

## Nomenclature

A	Heat transfer area	$\text{m}^2$
b	Turbine blade height	m
C	Absolute velocity	$\text{m/s}$
c	Turbine blade chord	m
$C_p$	Specific heat capacity at constant pressure	$\text{kJ}/(\text{kg}\cdot\text{k})$
d	diameter	mm
$D_s$	Specific diameter	-
e	Exergy	$\text{kJ/kg}$
$ed$	Exergy destruction	$\text{kJ/kg}$
$F_{sa}$	Correction factor	-
$h$	Specific enthalpy	$\text{kJ/kg}$
$LCV$	Lower calorific value	$\text{kJ/kg}$
$\dot{m}$	Mass flow rate	$\text{kg/s}$
$m_a$	Mass of air	$\text{kg/s}$
$m_f$	Mass of fuel	$\text{kg/s}$
$m_t$	Total mass	$\text{kg/s}$
N	Rotational speed	RPM
$n_s$	Specific speed	-
Nu	Nusselt number	-
P	Pressure	Pa
q	Heat transfer	$\text{kJ/kg}$
Q	Heat transfer	kJ
$\dot{Q}_5$	volume flow	$\text{m}^3/\text{s}$
r	radius	m
$R_{conv}$	Cooling factor	-
$R_f$	Fouling factor	-
Re	Reynolds number	-
$r_{s5}$	Radius at shroud	m
$r_{h5}$	Radius at hub	m
S	Perimeter	m
$St_{in}$	Stanton number	-
t	Blade pitch	m
T	Temperature	K
$t_b$	Blade thickness	m
TIT	Turbine Inlet Temperature	K

$U$	Blade speed	m/s
$V$	Velocity	m/s
$W$	Relative velocity	m/s
$W_{net}$	Work	kJ/kg
$\omega$	Rotational speed	rad/s
$\Delta Z_R$	Axial length	m
$\rho$	Density	Kg/m <sup>3</sup>
$\Delta h_{act}$	Actual enthalpy drop	kJ/kg
$\Delta h_{is}$	Isentropic enthalpy drop	kJ/kg
$\Delta h_0$	Total enthalpy drop	kJ/kg

## Abbreviations

AM	Additive Manufacturing
amb	ambient
APU	Auxiliary Power Unit
CC	Combustion Chamber
COP26	26 <sup>th</sup> Conference of Parties
DED	Direct Energy Deposition
DLE	Dry Low Emissions
DMD	Direct Metal Deposition
FDM	Fused Deposition Modeling
ECC	Environmental Concept Car
EU	European Union
EV	Electric Vehicle
EVs	Electric Vehicles
GHG	Greenhouse Gas Emissions
GT	Gas Turbine
GTs	Gas Turbines
HEX	Heat Exchanger
HP	High Pressure
ICCT	International Council on Clean Transportation
ICE	Internal Combustion Engine
IRReGT	Intercooled Recuperated Reheated Gas Turbine
LENS	Laser Engineering Net Shaping
LMD	Laser Metal Deposition
LOM	Laminated Object Manufacturing
LP	Low Pressure
max	maximal

MGT	Micro Gas Turbine
Nc	Number of compressor stages
$N_R$	Number of rotor blades
Nt	Number of turbine stages
RGT	Recuperated Gas Turbine
SCR	Selective Catalytic Reduction
SCNR	Selective NonCatalytic Reduction
SHEV	Series Hybrid Electric Vehicles
SLA	Stereolithography
SLM	Selective Laser Melting
SLS	Selective Laser Sinetering

### Chemical Compounds

$CH_4$	Methane
CO	Carbon Monoxide
$CO_2$	Carbon Dioxide
$H_2O$	Water
$N_2$	Nitrogen
NOx	Nitrogen oxides
$O_2$	Oxygen
UHC	Unburned Hydrocarbons

### Greek Letters

$\eta$	Efficiency of the GT cycle	-
$\eta_c$	Efficiency of the cooled turbine	
$\eta_u$	Efficiency of the uncooled turbine	
$\pi_c$	Compression ratio	
$\pi_t$	Expansion ratio	
$\lambda$	Excess of air ratio	
X	Extracted mass fraction ratio	
$\epsilon$	Effectiveness of the turbine as a heat exchanger	
$\psi$	Load Coefficient	
$\varphi$	Flow Coefficient	
$\alpha$	Absolute flow angle	
$\beta$	Relative flow angle	

### Subscript

c	coolant
C	Compressor

cc	Combustion chamber
i	inlet
o	outlet
g	Hot gas
cc1	First combustion chamber
cc2	Second combustion chamber
HP-C	High Pressure Compressor
HP-T	High Pressure Turbine
LP-T	Low Pressure Turbine
LP-C	Low Pressure Compressor
mix	Mixture between the coolant air and the hot gas
is	Isentropic state
t	Total state
T	Turbine
w	wall
1	Volute inlet
2	Stator inlet
3	Stator exit (inlet of the vaneless space)
4	rotor inlet
5	rotor outlet
'	cooled

## General introduction

The global community is increasingly concerned about climate change. Human activities are responsible for the release of greenhouse gases. There is no doubt that the road transportation sector contributes significantly to noxious emissions. As a result, efforts are focused on investigating new energy converters for automotive applications to replace internal combustion engines with a suitable powertrain. The new energy converter should provide similar performance to the internal combustion engine, as well, it should be efficient, compact, and lightweight to be simply integrated into the vehicle.

On the other hand, electric vehicles have gained a lot of attention since they do not directly release harmful emissions. The battery vehicles have, however, numerous drawbacks from multiple perspectives. The main disadvantages of these battery vehicles are their limited autonomy and long charging times. Increasing the autonomy of the electric car requires increasing the battery's size, resulting in a heavier system and higher cost.

Consequently, with the growth of series hybrid electric vehicles and among different powertrains, gas turbines are chosen as convenient energy converters for series hybrid electric vehicles for many reasons. The gas turbines can operate with a wide range of fuels and have a reduced number of moving parts resulting in reduced vibration and noise pollution. In addition, gas turbines have reduced NOx emissions compared to internal combustion engines. The considered booster consists of a gas turbine system coupled with a generator that charges the battery of the electric vehicle once depleted, as illustrated in Figure 0.1. As a result, the gas turbine cycle operates at its optimum efficiency since it is decoupled from vehicle speed.

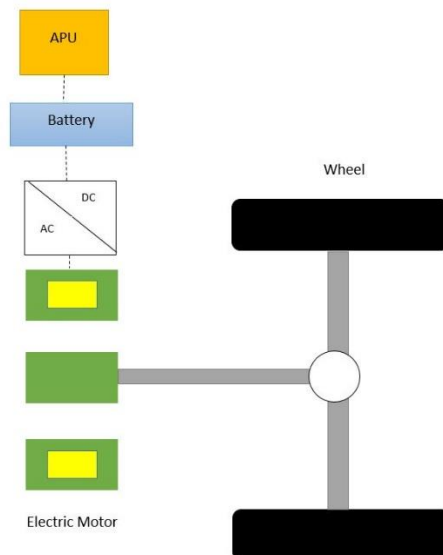


Figure 0.1. Range Extender in electric cars.

A previous study conducted by Bou Nader [1] in MINES ParisTech has identified the IRReGT gas turbine cycle consisting of a double stage compression with an intercooler, a double expansion with reheating, and with a regenerator as the most convenient cycle in terms of efficiency and net specific work.

The first scientific objective is to propose a new configuration of the gas turbine cycle that has higher efficiency and net specific work than the current literature configuration. This target can be reached in

three main steps including choosing the optimal architecture, increasing the operating pressure, and increasing the turbine inlet temperature.

For this purpose, Chapter 1 presents a detailed literature review of the different powertrains used to boost the autonomy of electric cars reaching the gas turbine. Then, Chapter 1 sheds light on the challenges that come along with choosing the best gas turbine configuration. An increase in turbine inlet temperature enhances the cycle efficiency and the net specific work of the turbine. As this temperature is limited by the material properties, cooling the turbine blade is a solution to overcome the material limitations and reach higher temperatures. Therefore, new manufacturing methods are introduced for small-scale cooled radial turbines, such as 3D printing, which is suitable for designing complex geometries. Furthermore, while increasing the turbine inlet temperature improves cycle performance, it also increases NOx emissions. Hence, NOx removal methods are also discussed in this chapter.

Chapter 2 includes a detailed thermodynamic analysis of the gas turbine system to choose the optimal operating conditions including the number of compressor and turbine stages, and the optimal operating pressure offering the highest efficiency and the highest net specific work. Thermodynamic analyses of different gas turbine configurations with cooled turbines are conducted to ensure a further increase in turbine inlet temperature. Using 1D analysis, it is possible to determine what mass of coolant is required to cool the turbine blade considered as a heat exchanger. Furthermore, the impact of cooling the turbine blade is not only tested on the overall cycle efficiency but also on the turbine (as a component) efficiency by imposing a new definition of the cooled turbine efficiency. Part two of Chapter 2 examines the various components of the gas turbine architecture from a technological standpoint. Weight, size, and complexity are important considerations since the range extender is integrated into the vehicle. The best gas turbine cycle configuration with blade cooling techniques is selected based on the previous statements.

Chapter 3 highlights the third scientific objective that targets designing the cooled compact radial turbine. First, the design methodology of a radial uncooled turbine is investigated from the 1D preliminary design to the 3D simulation. The design tool is validated by comparing the results with an existing commercialized turbine. Then, a design of a cooled turbine is realized based on both the existing designed turbine and the 3D printing technological limitations. The benefits of turbine cooling are evaluated by comparing the temperature distribution along the turbine blade for both the cooled and the uncooled turbine. Based on the CFD results, a thermodynamic analysis is conducted to reevaluate the cycle performance.

# Introduction générale

La communauté mondiale est de plus en plus préoccupée par le changement climatique. Les activités humaines sont responsables de l'émission de gaz à effet de serre. Il ne fait aucun doute que le secteur du transport routier contribue de manière significative aux émissions nocives. Par conséquent, des efforts sont déployés pour étudier de nouveaux convertisseurs d'énergie pour les applications automobiles afin de remplacer les moteurs à combustion interne par un système de traction adapté. Le nouveau convertisseur d'énergie doit offrir des performances similaires à celles du moteur à combustion interne. Il doit également être efficace, compact et léger pour être simplement intégré au véhicule.

D'autre part, les véhicules électriques ont suscité beaucoup d'intérêt car ils ne dégagent pas directement d'émissions nocives. Les véhicules à batterie présentent toutefois de nombreux inconvénients à plusieurs égards. En effet, leur autonomie est limitée et leurs temps de charge sont longs. Pour accroître l'autonomie de la voiture électrique, il faut augmenter la taille de la batterie, ce qui se traduit par un système plus lourd et un coût plus élevé.

Par conséquent, avec la croissance des véhicules électriques hybrides en série et parmi les différentes chaînes de traction, les turbines à gaz sont choisies comme convertisseurs d'énergie pratiques ces véhicules pour de nombreuses raisons. Celles-ci peuvent fonctionner avec une large gamme de carburants et ont un nombre réduit de pièces mobiles, ce qui réduit les vibrations et la pollution sonore. En outre, les turbines à gaz ont des émissions de NOx réduites par rapport aux moteurs à combustion interne. Le booster considéré consiste en un système de turbine à gaz couplé à un générateur qui recharge la batterie du véhicule électrique une fois celle-ci épuisée, comme l'illustre la Figure 0.1. Par conséquent, le cycle de la turbine à gaz fonctionne à son efficacité optimale puisqu'il est découplé de la vitesse du véhicule.

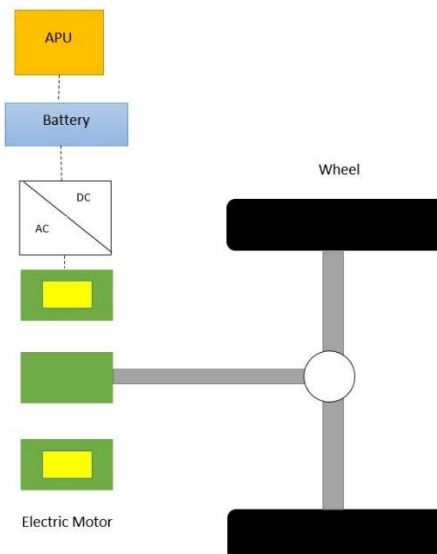


Figure 0.1. Prolongateur d'autonomie dans les véhicules électriques.

Une étude précédente menée par Bou Nader [1] à MINES ParisTech a identifié le cycle de turbine à gaz IRReGT consistant en une compression à double étage avec un refroidisseur intermédiaire, une double expansion avec réchauffage, et avec un régénérateur comme le cycle, comme étant le plus approprié en termes d'efficacité et de travail spécifique net.

Le premier objectif scientifique est de proposer une nouvelle configuration du cycle de la turbine à gaz qui présente un rendement et un travail spécifique net plus élevés que la configuration actuelle de la littérature. Cet objectif peut être atteint en trois étapes principales : choix de l'architecture optimale, augmentation de la pression de fonctionnement et augmentation de la température d'entrée de la turbine.

À ce titre, le chapitre 1 propose une étude bibliographique détaillée des différents groupes propulseurs utilisés pour accroître l'autonomie des voitures électriques jusqu'à la turbine à gaz. Ensuite, le chapitre 1 met en lumière les défis qui accompagnent le choix de la meilleure configuration de la turbine à gaz. Une augmentation de la température d'entrée de la turbine améliore le rendement du cycle et le travail spécifique net de la turbine. Puisque cette température est limitée par les propriétés des matériaux, le refroidissement des aubes de la turbine est une solution pour surmonter les limites des matériaux et atteindre des températures plus élevées. Ainsi, de nouvelles méthodes de fabrication sont introduites pour les turbines radiales refroidies à petite échelle, comme l'impression 3D, qui permet de concevoir des géométries complexes. En outre, si l'augmentation de la température d'entrée de la turbine améliore les performances du cycle, elle augmente également les émissions de NOx. Les méthodes d'élimination des NOx sont donc également abordées dans ce chapitre.

Le chapitre 2 comprend une analyse thermodynamique détaillée du système de turbine à gaz afin de choisir les conditions de fonctionnement optimales, notamment le nombre d'étages de compresseur et de turbine, et la pression de fonctionnement optimale offrant le meilleur rendement et le travail spécifique net le plus élevé. Ensuite, des analyses thermodynamiques de différentes configurations de turbines à gaz avec des turbines refroidies sont effectuées pour garantir une augmentation supplémentaire de la température d'entrée de la turbine. En utilisant l'analyse 1D, il est possible de déterminer la masse de fluide de refroidissement nécessaire pour refroidir la pale de la turbine considérée comme un échangeur de chaleur. En outre, l'impact du refroidissement de l'aube de la turbine n'est pas seulement testé sur l'efficacité globale du cycle mais aussi sur l'efficacité de la turbine (en tant que composant) en imposant une nouvelle définition de l'efficacité de la turbine refroidie. La deuxième partie du chapitre 2 examine les différents composants de l'architecture de la turbine à gaz d'un point de vue technologique. Comme le prolongateur d'autonomie est intégré au véhicule, le poids, la taille et la complexité revêtent une importance significative. Sur la base des considérations précédentes, la meilleure configuration du cycle de la turbine à gaz avec refroidissement des aubes est sélectionnée.

Le chapitre 3 met en évidence le troisième objectif scientifique qui vise à concevoir une turbine radiale compacte refroidie. Tout d'abord, la méthodologie de conception d'une turbine radiale non refroidie est étudiée depuis la conception préliminaire 1D jusqu'à la simulation 3D. L'outil de conception est validé en comparant les résultats avec une turbine commercialisée existante. Ensuite, la conception d'une turbine refroidie est réalisée sur la base de la turbine existante et des limites technologiques de l'impression 3D. L'avantage du refroidissement de la turbine est évalué en comparant la distribution de la température le long de la pale de la turbine pour la turbine refroidie et non refroidie.

# Chapter 1 : Literature review

## 1.1. Introduction

Due to global warming caused by CO<sub>2</sub> and NOx emissions from the transportation sector, significant research efforts have been invested to find a substitute for internal combustion engines. Beyond the investigated powertrains, gas turbines are selected as potential energy converters for series hybrid electric vehicles. Gas turbines are a promising solution because of their compactness, low emissions, high reliability, and multi-fuel capability. This chapter presents first a literature review of the different gas turbine configurations including several cycle architectures and components properties to improve cycle efficiency. The effect of a higher pressure ratio, as well as higher turbine inlet temperature, is assessed. Therefore, the development of new turbine materials and cooling techniques is investigated. Then, the impact of turbine inlet temperature on NOx emissions is conducted and NOx removing techniques are presented. Finally, the last part of this chapter discusses the different forms of additive manufacturing and their advantages in producing complex geometries as the cooled small-scale turbine.

## 1.2. Regulations of the Greenhouse Emissions

In July 2009, the leaders of the European Union (EU) and the G8 decided to reduce greenhouse gas emissions (GHG) by 80% below 1990 levels by 2050 [2]. Twenty-Three percent (23%) of the greenhouse gas emissions in the EU come from the transportation sector. According to the International Council On Clean Transportation (ICCT), Light-duty vehicles and trucks are responsible for 40 % of transportation emissions [3]. The auto industry has reacted in different countries to reduce the CO<sub>2</sub> emissions from passenger cars. Figure 1.1 illustrates the historical decrease in CO<sub>2</sub> emissions. For example, the EU emissions in 2015 were 120 g/km in 2015 and were reduced to 95 g/km in 2021.

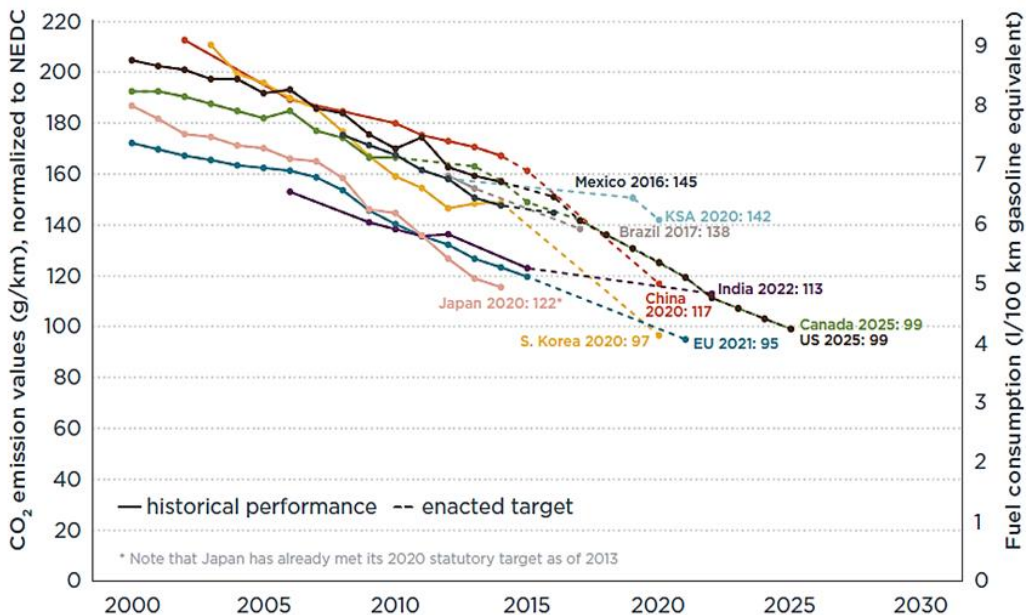
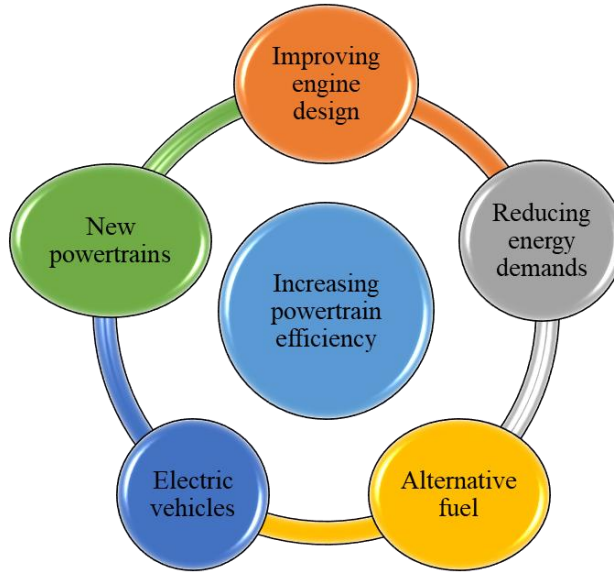


Figure 1.1: Historical CO<sub>2</sub> emissions performance for passenger cars [4].

On top of that, the 26<sup>th</sup> Conference of the Parties (COP26), in November 2021, emphasized the importance of fighting against climate change. The participants reaffirmed their commitment to keeping

the increase in global average temperature well below 2 °C and continuing to limit it to 1 °C by 2100 [5]. One of the decisions that have been made was to reduce the dependence on fossil fuels. Therefore, more than 30 countries and six major car manufacturers have ensured their intention to move to zero-emission vehicles by 2040 and to accelerate the decarbonization of road transport.

To reach these targets, a shift in the transport sector is mandatory. Several advancements are made to the current vehicles to reduce GHG emissions, such as improving the overall efficiency of the internal combustion engine (ICE), reducing energy demands, switching to cleaner alternative fuels, and introducing new powertrains, as depicted in Figure 1.2.



**Figure 1.2: Techniques to improve the powertrain efficiency.**

Several technologies have been introduced to improve the performance of ICE in recent years by varying the engine design. ICE with variable displacement and variable compression gained popularity due to their lower fuel consumption. Asthana et al. [6] discussed the techniques to vary the engine compression ratio and presented the historical development made by automotive manufacturers in this field such as Mercedes Benz, Ford, Nissan, and Peugeot. Doric and Klinar [7] investigated the variable displacement concept of the piston using fluid dynamics in a 1D formulation. Results show that this technique has a beneficial impact on fuel consumption. Another method to improve the performance of ICE is to add turbochargers. This method was initially introduced by Alfred Buechi, a swiss engineer. Based on the studies in this field, this technology had a positive impact on both the fuel consumption and the environmental emissions of ICE [8]. Several other developments were also considered, including friction loss reductions, lubrication system, and waste heat recovery.

There has been as well considerable interest in reducing vehicle energy demands over the past few years to reduce fuel consumption and emissions. Choosing the right material for an automobile is fundamental to ensuring its quality and effectiveness. The material should verify the following properties: lightweight, cost-effective, reliable, and manufacturable [9]. As well, the evaluation and the optimization of the vehicle's aerodynamics is another way to make the vehicle more energy efficient and environmentally friendly as suggested in [10]. Additionally, reducing the driving and the tire's rolling resistance is another parameter to take into consideration [11]. A final step to reducing vehicle energy consumption is to optimize the thermal energy requirements for passenger comfort [12].

The high dependency on fossil fuels as a primary source of energy is one of the biggest challenges. Clean and green fuels are one solution to reduce GHG emissions. Hydrogen, natural gas, propane, and

alcohols such as methanol, ethanol, and butanol are clean eco-friendly fuels. Some of these fuels can be used in ICE with little or no modifications, but others require significant engine modifications and/or adaptations [13]. These alternative fuels can help reduce toxic emissions. As a result, UOP LLC, a Honeywell company announced the construction of units in Hawaii to convert biomass into green transportation fuels. The project rhymes with the Hawaii Clean Initiative goal that aims to reach 70% of green energy by 203 [14]. Natural gas also gained attention to reach sustainable road transportation. Carslaw and Fricker [15] considered that natural gas is a realistic substitute for diesel and petrol. Moreover, many studies assessed different types of green fuels and their environmental impact. Bongartz et al. [16] investigated the technical and environmental impact of H<sub>2</sub> and the production of methane, methanol, and dimethyl ether (DME) for use in ICE vehicle applications. The four types of fuels lead to a reduction in GHG emissions compared to fossil fuels. However, all of them, require very low-cost H<sub>2</sub> to be competitive with fossil fuels. Another study [17] discussed the alternative fuel options to turn to clean transport in India. Among the investigated types of eco-friendly fuels, compressed natural gas and ethanol are preferred since the technologies for their usage are developed. Recently, researchers assessed the injection of hydrogen in ICE [18]. Despite many advantages of this technique, including its high volumetric efficiency, some disadvantages related to the increased formation of NOx should be addressed [19]. Heavy duty vehicles have also been the interest of studies to overcome their nocive emissions. A study by Verger et al. [20] has identified ethanol as the best alternative for fossil fuels in heavy-duty vehicles, taking into consideration the cost, the sustainability, and the emissions. Nevertheless, high levels of ethanol pose challenges like phase separation and ignition quality.

On the other hand, the authorities in different countries are encouraging automakers to develop Electric Vehicles (EVs) as a solution to climate change. Since electric vehicles do not emit NOx directly, they have a lower environmental and health impact than ICE. The International Energy Agency estimated that by 2030, the number of EVs will be 145 million [21]. In the same year, Mercedes-Benz aims to produce carbon-neutral passenger vehicles and make more than 50 % of its sales with hybrid or electric vehicles. Electrification will also extend to their vans, trucks, and buses [20]. EVs are composed of a motor and a lithium-ion battery pack to propel the vehicle [22]. These vehicles require lithium-ion batteries because of their high specific energy and power density, high nominal voltage, low self-discharge rate, and long cycle life [23]. Although EVs offer many advantages in terms of reduced pollution, simplicity, reliability, and accessibility, they have significant challenges [24]. The limited autonomy of EVs is one of the main reasons to limit their commercialization. For example, the maximum driving range of the Nissan Leaf is only 346 km [25]. Furthermore, the charging time of EVs is significantly high (4 to 8 hours), even when using supercharges (30 minutes) [26]. There is another challenge related to the charging stations; although the huge number of stations installed in the last few years, compared to gasoline these numbers are far less [27]. Furthermore, the battery is the most critical component in EVs. It is the most expensive and heavy component. Increasing EVs' autonomy means a larger and heavier battery. An electric car's battery, for example, can weigh around 200 kg considering a 20kWh lithium batteries [28].

Considering the presented statements, it is evident that new powertrain architectures will be necessary to overcome these challenges.

### **1.3. New Powertrains for Automotive Applications**

Literature reports many attempts to substitute the internal combustion engine with new energy converters. Bou Nader [1] investigated various energy converters to identify the best powertrain architecture in automotive applications. The aim is to choose a suitable configuration offering similar performance to conventional vehicles. With the development of series hybrid configurations, studies

were focused on the selection of range extender technologies. Heron and Rinder [29] evaluated the potential of different range extender technologies and presented a comparison between them. Tran et al. [30] developed a comprehensive review of different types of EV range-extending technologies, highlighting the different advantages and disadvantages. Based on all the previous studies, the following is a review of the main energy converters, their specifications, and their cons and pros in the automotive sector.

The Split cycle engine is an ICE where the intake and the compression occur in one cylinder, and the expansion and exhaust occur in a second cylinder. The first split cycle was realized by the Scudero Group in 2001 [31]. Detailed thermodynamic analysis of the split cycle is conducted in [32]. Numerous studies investigated the split cycle as a substitute to the ICE since it offers higher efficiency by 5 % and higher power by 15 to 20 % [33]. The researchers tackle different parts of the split cycle including an air hybrid concept [34], a turbocharged cycle, a cycle with an internal heat exchanger, and the combustion process. However, disadvantages related to its need for expensive materials and higher cost compared to ICE have limited its commercialization.

Gas Turbines (GTs) are thermodynamic machines that convert the thermal energy in the combustion chamber into mechanical power on the turbine shaft. The first turbine system was patented by John Barber in 1797 [35]. Gas turbines are used in different applications including industrial applications, aircraft, marine applications, and all power generation systems. Numerous studies have investigated different configurations for the GT cycle to improve its efficiency and output power. The configurations include a combined gas turbine cycle, gas turbine with recuperator, gas turbine with intercooling, gas turbine with reheat, gas turbine with isothermal expansion, and others. The main developments occur in increasing the operating temperatures and the efficiency of the components. The gas turbine was initially investigated as a prime mover for cars by Chrysler in 1950, as depicted in Figure 1.3. The cycle consists of a recuperated gas turbine cycle with a radial compressor and a radial turbine. Then, he revealed seven generations of gas turbine cars with different improvements on many components [36].

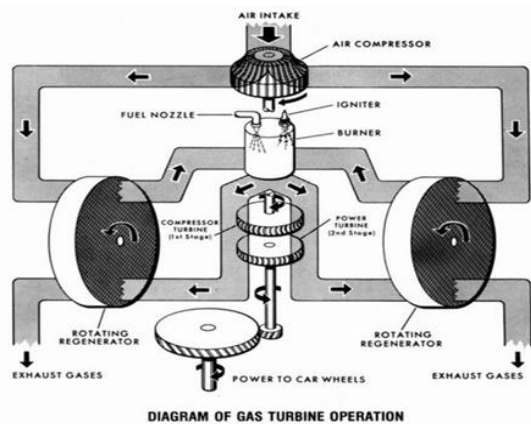


**Figure 1.3:** (a) Chrysler GT engine, (b) the first GT car invented by Chrysler [36].



(b)

As Chrysler produced 50 turbine cars, Volkswagen signed a contract with Williams Research Corporation and developed the microbus station wagon [37]. Additional prototypes for heavy vehicles were also produced such as the 1965 Chevrolet Turbo Titan III propelled by a GT-309 engine operating at 35 000 rev/min and the 1972 GMC Astro Gas Turbine [38]. There have been prototypes of other GT cars in racing vehicles such as the Rover-BRM that participated in Le Mans in 1963, Formula 1 in 1971, and the Lotus 56 [39]. However, their high fuel consumption and slow acceleration restrict their application in the marketplace. These problems result from operating the GT systems at high speed even

at idle conditions, and mechanically coupling the turbine to the vehicle-driving load. Recent studies have focused on using GTs as auxiliary power units as a solution to the limited range and high cost of electric cars (next section).

The Stirling engine is an external combustion engine patented and invented by Robert Stirling in 1816 [40]. It consists of a closed-cycle regenerative heat engine with a permanent working fluid in which heat is applied to the outside of the engine. This machine has gained a lot of attention throughout the years mainly due to its improved efficiency compared to ICE [41]. The large development of the Stirling engine has made it possible to be used in passenger cars, such as the 4-98 and the 4-215 Ford [42]. Although this type of engine is characterized by lower fuel consumption and better acceleration performance, drawbacks related to leakage problems and high costs should be overcome [43].

Vapor cycle machines are also external combustion engines, known as steam engines that operate according to the Rankine cycle. The first steam vehicle was designed, constructed, and operated by Nicolas Cugnot in 1769 in France. It takes until 1963 for the steam engines in automotive to appear in the US, for example, the Model G steam touring car and Ford Falcon Steam car [1]. The studies continued to replace the ICE with the steam engine. In 1969, GM introduced the Chevelle SE 124 in 1969, which had many advantages, including low noise pollution and high torque. However, the system was heavy and higher in cost than the ICE and presented technical challenges. The attempts continued when Honda integrated the first steam Rankine cycle in 2007 [44], followed by BMW in 2009 [45]. Although the benefits in terms of low emissions and silent operation, the size and weight of the condenser and the technical issues related to using water are mainly big limitations for their use in mass production.

Ericsson engines, invented in 1833, are external heat supply engines working according to a Joule thermodynamic cycle. It consists of reciprocating piston-cylinder machines. They differ from the Stirling engine by the presence of valves around the cylinders to isolate them from the heat exchanger [46]. These engines are particularly useful for low-power solar energy conversion, micro-cogeneration from fossil fuels or biomass, and waste heat recovery [47]. The first spark ignition ICE invented by Lenoir was an Ericsson engine but the technical issues related to the combustion chamber have limited the success of this type of engine [1]. To the authors' knowledge, there are no real applications of the Ericsson engine in the automotive sector and all the investigations in this field remain scientific and research studies.

Thermoacoustic machines consist of the conversion of thermal into mechanical energy and vice-versa using the thermoacoustic effect, which appears spontaneously under special conditions [48]. When a fluid particle moves back and forth along a wall, a thermoacoustic process occurs. Temperature oscillations always accompany pressure oscillations. Therefore, the combination of all these oscillations and their interaction with the rigid walls are the origin of various effects [49]. In automotive powertrain applications, thermoacoustic systems are mainly used in cold generation [50], electric power generation [51], and waste heat recovery [52]. However, the technical and technological aspects of these machines are critical and need further development and expertise.

Fuel cells are electrochemical energy converters that transform chemical energy into electrical energy. William Grove realized the first fuel cell in 1839. There are six groups of fuel cells depending on the electrolyte and the operating temperature [30]. The fuel cell is composed of an electrolyte and two electrodes, an anode and cathode. Hydrogen is introduced at the anode where it forms a proton and an electron. The former is retained in the electrolyte, whereas the latter passes through an external circuit, so this chemical energy is converted into electrical energy. In combination with oxygen, some heat and

water are produced. In commercial vehicles, such as buses and cars, fuel cells may be advantageous due to their ability to store energy physically, in the form of hydrogen [53]. Many automotive manufacturers used this technology in their concept cars such as PSA, Toyota [55]. However, some technical problems related to water freezing, hydrogen storage, security, complexity, and cost should be solved.

Table 1.1 summarizes the properties of different energy converters, illustrated in Figure 1.4, including Split cycle engine, Gas Turbine (GT) cycle, Stirling engine, Vapor cycle machine, Ericsson engine, and Fuel cell.

**Table 1.1: Summary of different energy converters and their properties in the automotive application.**

Energy Converter	Efficiency Range	Power to Weight Ratio (W/kg)	Power to Size Ratio (W/L)	Emissions	Powertrain Compatibility
ICE	35 to 38% (Gasoline) 38 to 42% (Diesel)	400-600 (atmospheric) 800-1200 (turbochargers)	300 – 750	Norm Euro 6 after-treatment emissions	All powertrain architectures
Split Cycle Engine	40 – 43% without regenerator	250 – 900	275 – 650	Reduced emissions compared to ICE	Conventional and electrified powertrain architectures
GT Cycle	20 – 30% simple GT 45 – 52 % Advanced	450 – 1400	225 – 900	Reduced emissions at source compared to ICE	Suited for series and range extender powertrain architectures
Stirling Engine	34% to 42%	225 – 350	225 – 350	Controlled at source through continuous combustion and EGR	Compatible with all powertrain architectures
Vapor Cycle Machine	18 to 30%	100 - 225	75-175	Controlled through continuous combustion and EGR system	Compatible with all powertrain architectures but more suitable for SHEV
Ericsson Engine	25-35% (realistic) 45% (simulations)	/ 150 – 250	150 – 300	Controlled at source through continuous combustion	Compatible with all powertrain architectures. More suitable for SHEV
Thermoacoustic Machines	7 % (WHR) 35% (CHP)	65 - 130	33-100	Controlled at source through continuous combustion	Compatible only with serial or range extender powertrains
Fuel Cells	45-50 %	125 - 1000	125-700	Zero emission	Compatible only with series hybrid electric vehicle powertrains

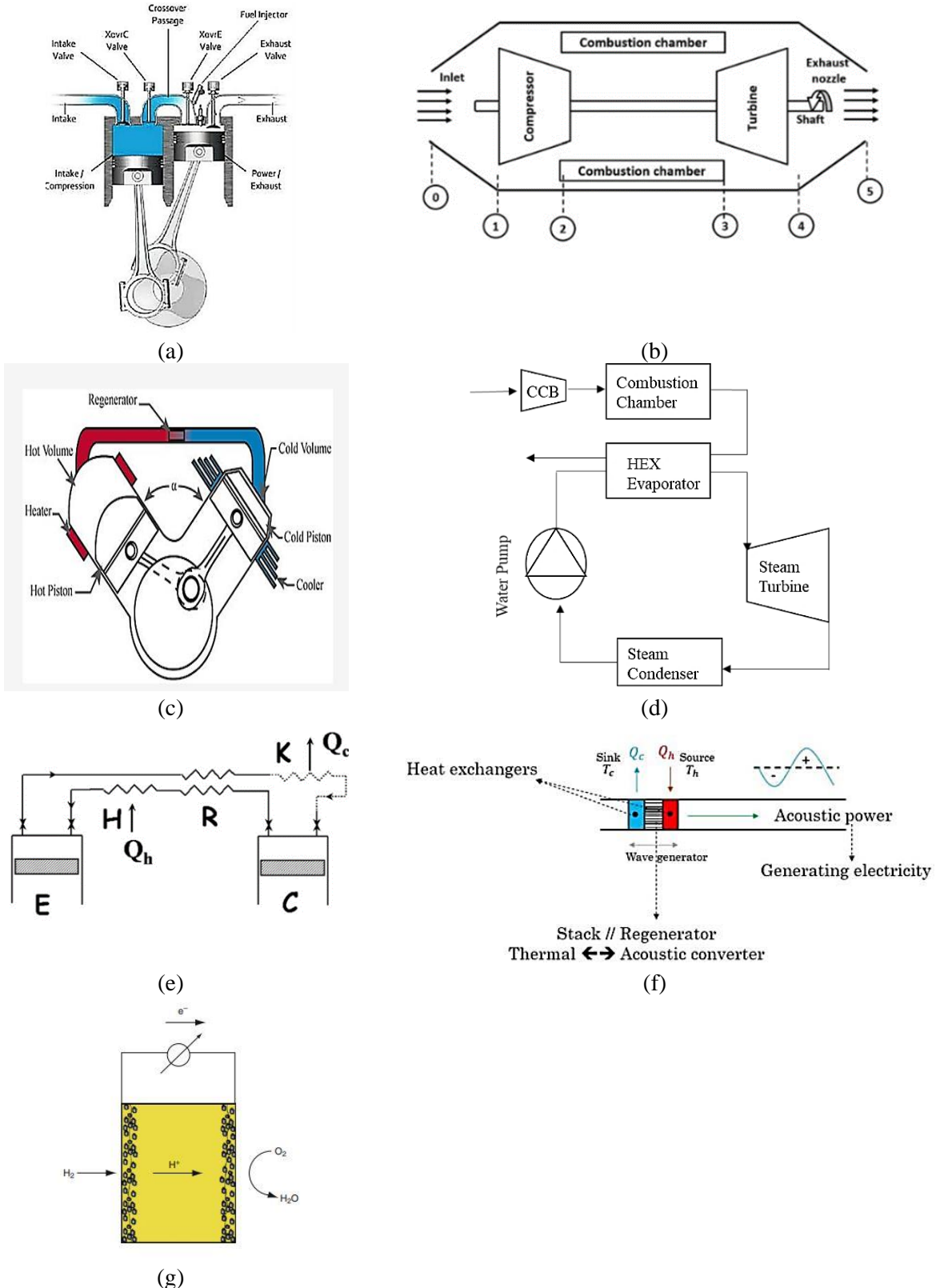


**Figure 1.4:** (a) Scuderi Split cycle engine [56], (b) GT engine concept [57] , (c) Stirling engine concept [58], (d) Steam vapor machine cycle, (e) Ericsson engine concept [59], (f) Thermoacoustic machine [1], (g) Energy process in fuel cell [60].

The best energy converter should verify several properties: low emissions, high efficiency, reduced vibrations and noise, and low maintenance. Table 1.1 shows that the gas turbine cycle and fuel cells present numerous benefits compared to other energy converters. Advanced GT cycles have high

efficiency (45 - 52 %), offer the highest power-to-weight ratio (450 - 1400 W/kg), have lower emissions than internal combustion engines, and are suited for series and range extender powertrain architectures. On the other hand, fuel cells also have high efficiency (45 – 50 %), a high power-to-weight ratio (125-1000 W/kg), and zero emissions.

The advantages and disadvantages of each energy converter are presented in Table 1.2. Among these presented powertrains, gas turbines are selected based on quantitative (efficiency range, weight to power density, and size to power density) and qualitative (compatibility with the powertrain, multifuel capability, cogeneration capability, needs for specific materials) technological criteria mainly with the increase of attraction of Series Hybrid Electric Vehicles (SHEV).

**Table 1.2: Comparison of advantages and disadvantages of different energy converters.**

Energy Converter	Advantages	Disadvantages
ICE	Low-cost, high-power density, fast startup.	Low efficiency, high emissions, high noise, and vibrations.
Split Cycle Engine	Low emissions, high efficiency.	High cost, still under research, needs expensive material.
GT Cycle	Compatible with a variety of fuels, low emissions, few moving parts, low noise and vibrations, low maintenance, and high efficiency at optimal load.	Low efficiency, high cost, slow start-up.
Stirling Engine	Low emissions, good efficiency, low vibration and noise, multifuel capability.	High cost and leakage problems.
Vapor Cycle Machine	Low emissions operate at various fuels, low noise.	Low efficiency, water freezing challenges, metallurgic limitation.
Ericsson Engine	Good efficiency, low cost, multifuel capability.	Complexity because of valves, metallurgic limitation, and low technological maturity.
Thermoacoustic Machines	Reduced number of moving parts, multi-fuel capability, no lubrication need, and simple system.	Internal losses, needs expertise, low power to weight ratio, and power to size ratio.
Fuel Cells	Zero emissions, high efficiency, long driving range, high power density, and few moving parts.	High cost, needs specific infrastructure, driving range limited by the hydrogen storage, safety.

GT systems offer many advantages when used in SHEV compared to other powertrains. First, GTs have a reduced number of moving parts leading to reduced vibrations and low maintenance costs. As well, GT systems emit less noise than ICE, estimated at around 5dB less [61]. In addition, GT benefits include their multi-fuel capability (natural gas, biogas, kerosene, diesel, propane...) and their low emissions of carbon monoxide (CO) and NOx compared to ICE [36]. One of the main advantages of using them in SHEV is the ability to operate at their optimal load seeking high efficiency because the GT system is decoupled from the vehicle load [62].

## 1.4. Gas Turbine as a Range Extender for Electric Cars

Recent studies have focused on using GTs as auxiliary power units as a solution to the limited range and high cost of electric cars. The GTs are combined with a generator, so the mechanical work of the turbine is converted to electric power [63]. Figure 1.5 illustrates the proposed configuration. The Auxiliary Power Unit (APU) consists of a GT cycle that gives a mechanical rotation at the shaft at the outlet of the turbine. Through the alternator, this mechanical rotation is converted into electric power, which is responsible for charging the battery of the electric car once depleted. This configuration is a solution for both the environmental emissions of ICE and the limited autonomy range of electric cars. Its main advantage is that the GT cycle operates independently from the vehicle speed. Hence, the optimal operating point of the GT is easily controllable to obtain the GT's best efficiency.

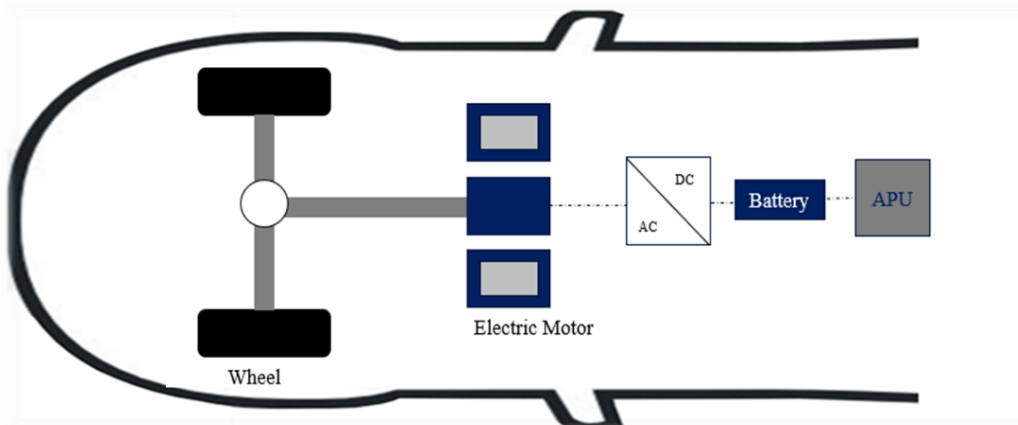


Figure 1.5: GT as an auxiliary power unit for SHEV.

According to the 2012 Amendments to Zero Emission Vehicle Regulations [64], the range extender should verify some criteria including an APU range less or equal to the main battery range, and working only once the battery is depleted.

Many attempts in literature have investigated GTs in SHEV. Sim et al. [65] assessed the feasibility of a micro-power pack using automotive alternators powered by a GT to recharge the batteries of EVs. The GT cycle consists of a Brayton cycle with a power turbine. A series of experiments were conducted to measure the performance of the electric booster. Results show that GT is a promising solution to boost the autonomy of EVs. GT has also been shown to reduce toxic emissions and fuel consumption in SHEV. A new hybrid configuration incorporating a Micro-Gas Turbine (MGT), a battery pack, and a traction electric motor is described in [63]. A simulation of the vehicle's performance using MATLAB software is conducted, and the results are compared with those of equivalent vehicles with diesel or gasoline engines or conventional diesel vehicles. As a result, the MGT offers benefits compared to other configurations in terms of less CO and NOx emissions. Ji et al. [62] conducted a numerical and experimental study to test the feasibility of micro gas turbines in electric cars. The system presented fewer emissions and a higher power-to-weight ratio compared to conventional vehicles; as the ICE generated 32 g of NOx and 79.8 kg of CO<sub>2</sub> per kg of fuel while the MGT only released 2.53 g of NOx and 7.12 kg of CO<sub>2</sub> per kg of fuel. Christodoulou et al. [61] proposed a hybrid configuration including a microturbine, a battery, and a traction motor. The results proved that this configuration can lead to a reduction in fuel consumption.

As well, some automobile manufacturers developed series hybrid electric vehicles using GTs as autonomy extenders. Their applications are observed in passenger cars, as well as in heavy-duty

vehicles. Table 1.3 presents a state-of-the-art of SHEV that utilizes GTs as auxiliary power units to boost their autonomy. General Motors proposed a vehicle propelled by a 40 kW gas turbine. In the same year, Volvo revealed the Environmental Concept car (ECC) achieving a speed of 180 km/h. Then, ETV Motors devoted a Toyota Prius car, equipped with a microturbine as a range extender. As well, Capstone turbine announced the production of a supercar, the CTM-180 at the LA Auto show. The range of this supercar can reach up to 500 miles on a single tank of fuel. In addition, Jaguar presented a supercar the C-X75 driven by a twin-shaft turbine from Bladon Jets, whose range is up to 110 Km with a speed of 330 km/h (Figure 1.6). Techrules also was one of the automotive manufacturers, which revealed a 30kW turbine as a booster for electric cars in 2016. The vehicle autonomy reached 1850 km with an average consumption of 4.8L/100 km.

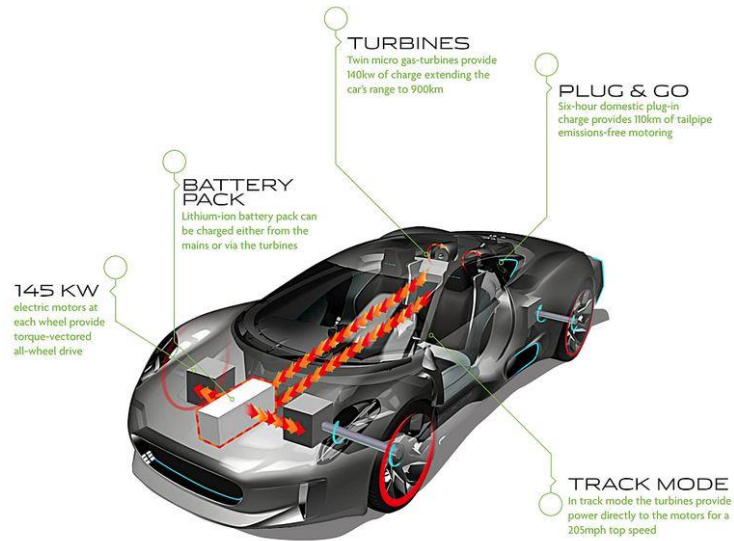


**Figure 1.6: Jaguar C-X75 powertrain [66].**

The GT system gained attention also in heavy-duty vehicles. Wrightspeed presented the Fulcrum turbine (Figure 1.7) that consists of an intercooled recuperated 80 kW GT operating at 100 000 rpm, and whose weight is 1/10 of a piston engine. Walmart introduced the Walmart Advanced Vehicle Experience (WAVE), a range-extending series hybrid tractor. The main properties of each developed GT cycle in automotive were explained by a study at Chalmers University [39] and a study in MINES ParisTech [1].

**Table 1.3: State-of-the-art of different automotive manufacturers in SHEV configurations.**

Automotive manufacturers	SHEV properties	References
General Motors	40 kW turbine in EV-1 series	[67]
Volvo	Environmental Concept Car (ECC)	[68]
ETV Motors	Toyota Prius equipped with a microturbine	[69]
Capstone	CTM-380 at the LA Auto show	[70]
Jaguar	Jaguar C-X75 driven by a twin-shaft turbine from Bladon Jets	[71]
Techrules	30 kW turbine rotating at 96 000 rpm as a booster to the EV	[72]
Wrightspeed	Fulcrum GT, an intercooled recuperated GT cycle rotating at 100 000 rpm	[73]
Walmart	WAVE range-extending series hybrid	[74]

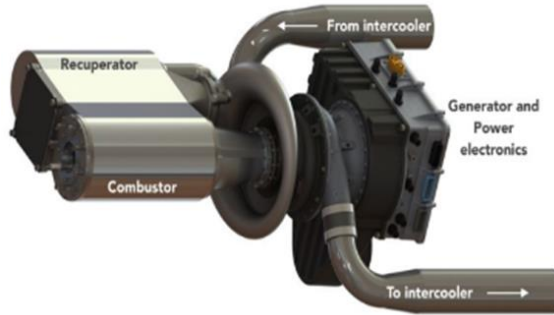


**Figure 1.7: Intercooled Recuperated 80 kw Fulcrum turbine.**

#### 1.4.1. Powertrain Rating Setup

The new powertrain is designed to ensure the same rating and the same performance as an ICE. Many studies have investigated the required tractive power.

Tan et al. [75] found that a minimum range extender power of 10 kW is necessary to maintain the state of charge of SHEV in Asian cities according to the Malaysian Urban Drive Cycle. Mackay [76] suggested that a GT system of 24 kW is suitable for passenger cars and small buses. This power takes into consideration the vehicle weight estimated to be 1300 kg and a vehicle velocity of 100 km/h on a 6% slope. Energy recovery during deceleration is also included. Zhao et al. [77] found that a power requirement of 27.5 kW is sufficient for a vehicle weight of 14500 kg driven at 120 km/h, taking into consideration the wind resistance and friction. Other studies [79] suggested a mechanical power of 30 kW for the range extender. According to Figure 1.8, the necessary power for a GT cycle as an auxiliary power unit for SHEV is around 20 kW- 25 kW. The study takes into consideration different parameters such as the vehicle weight (1210 kg), the battery mass (259 kg) and capacity (10 kWh), the vehicle speed (90,130,160 km/h), and road slopes (10%, 5%). Therefore, based on the surveyed studies, the power considered in this thesis is 20 kW.

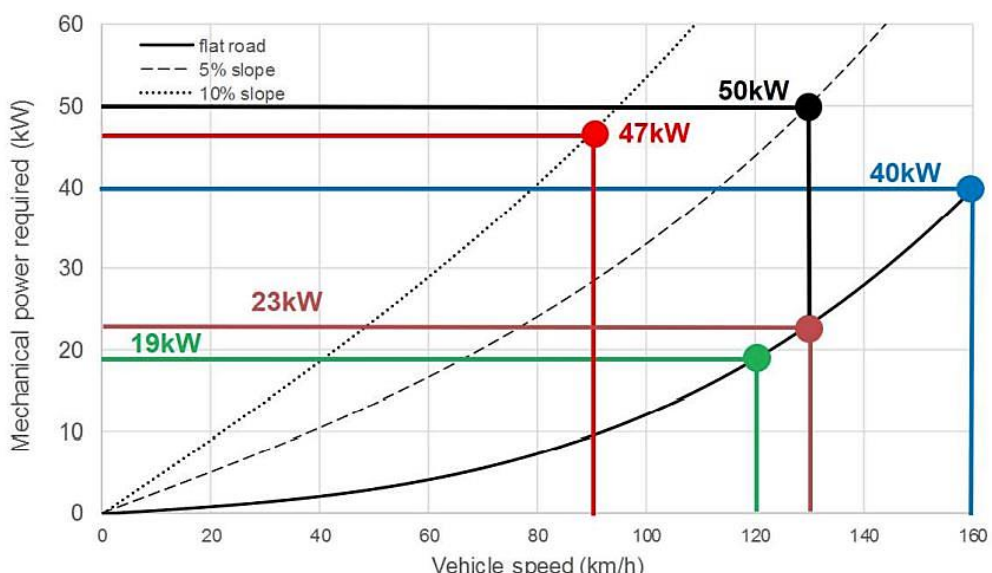


**Figure 1.8: Mechanical power required to drive the vehicle at different constant speed and on slope of 5% and 10% [1].**

### 1.4.2. Gas Turbine Architectures

GTs are thermodynamic machines capable of converting the thermal energy of the working fluid into useful mechanical energy on the turbine shaft. This mechanical energy can be used directly or converted into electrical power by adding an electric generator. A simple gas turbine cycle operates according to the Brayton cycle. Many components are added to the Brayton cycle to increase the cycle efficiency and the net specific work.

#### Brayton cycle

The Brayton cycle is composed of a compressor, a combustion chamber, and a turbine as depicted in Figure 1.9. The compressor compresses the air that enters the combustion chamber, where it gains energy. Leaving the combustion chamber with high temperature and pressure, the fluid is expanded into the turbine. The output mechanical power is generally used to drive an electric generator and produces electricity.

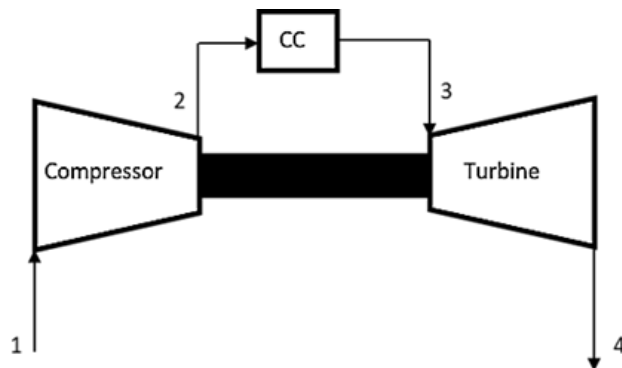


Figure 1.9: GT Brayton cycle.

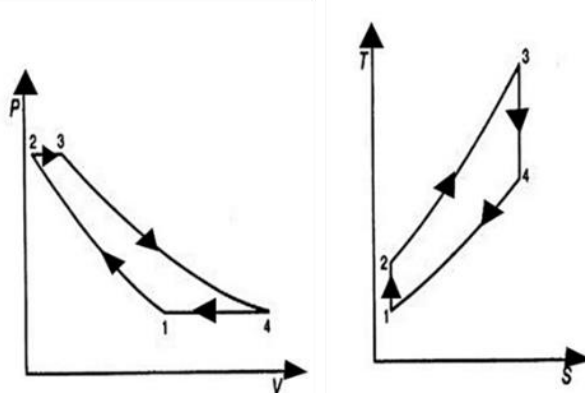


Figure 1.10: PV and TS diagrams of the GT Brayton cycle.

The ideal Brayton cycle consists of four processes as shown in Figure 1.10:

- Isentropic compression (1-2)
- Isobaric combustion (2-3)
- Isentropic expansion (3-4)
- Isobaric cooling (4 -1)

The efficiency of a Brayton GT cycle is around 20 – 30 %. According to a study [1], a mass flow rate of 500 kg/h is needed to achieve a power output of 20 kW. On the other hand, the gas temperature at the

outlet of the turbine remains higher than the ambient temperature. Consequently, the hot turbine exhaust gas can be utilized to heat the air before entering the combustion chamber using a recuperator.

### Recuperated Gas Turbine Cycle

To increase the efficiency of the system, the heat from the exhaust gas is recovered using an air-to-air recuperator. The recuperator preheats the air at the outlet of the compressor using the hot exhaust gas to reduce the fuel consumption in the combustion chamber. Adding a recuperator can lead to an increase in the cycle efficiency from 17 % to 30 % [80]. The efficiency of this cycle is estimated between 35 – 44 %. Figure 1.11 shows at the left a recuperative gas turbine cycle (RGT), and at the right the Mitsubishi MTEE, a 30 kW RGT.

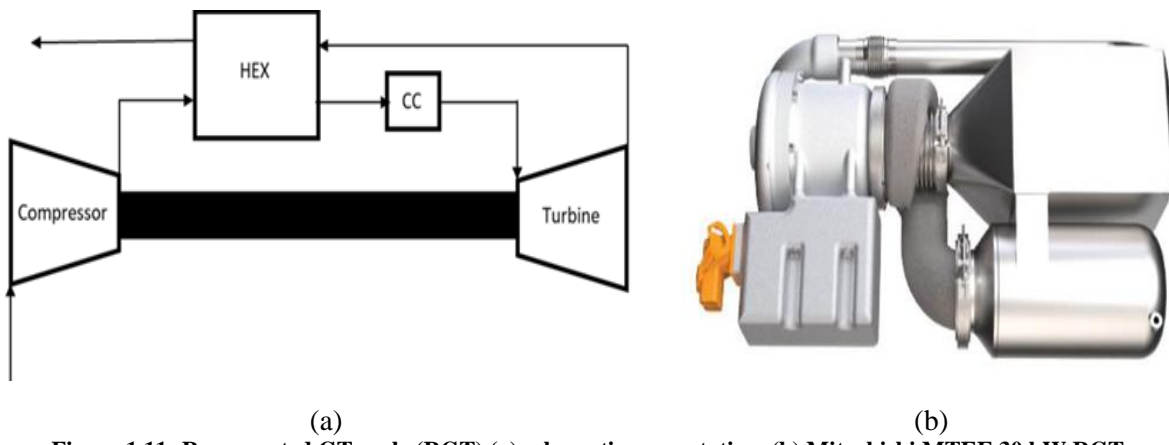


**Figure 1.11: Recuperated GT cycle (RGT) (a) schematic presentation, (b) Mitsubishi MTEE 30 kW RGT.**

The recuperator consists of a counterflow heat exchanger through which the turbine outlet gas and the cold air pass in opposite directions. For an ideal case (infinite heat transfer area), the exit temperature of the cold stream at the inlet of the combustion chamber is the turbine exhaust temperature. Therefore, the recuperator effectiveness (and pinch) are two important parameters that affect its performance. Moran and Shapiro [81] demonstrate that increasing the recuperator effectiveness from 60 to 80 %, increases the cycle efficiency by five efficiency points. Although reducing the recuperator pinch is beneficial in terms of higher efficiency, it increases its mass and weight.

### Reheated and Intercooled Gas Turbine Cycle

Increasing the GT net work can be achieved either by decreasing the compressor work or by increasing the turbine work. Adding an intercooler between the compressor stages reduces the compressed air volume, thus the work of the compressor for a given pressure, leading to a lower energy consumption. By this configuration, the compression gets closer to the isothermal transformation, which matches the minimum work. Figure 1.12 illustrates the corresponding intercooled GT cycle. The efficiency is estimated between 35 – 44 %. Considering a power output of 20 kW, around 450 kg/h of air is required [1].

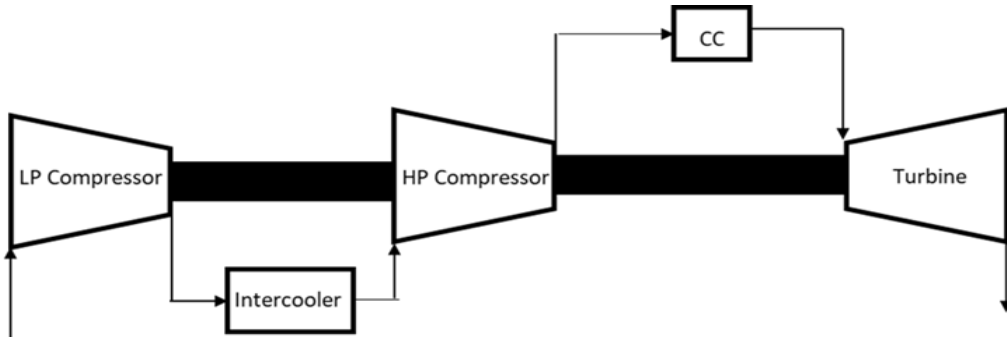


Figure 1.12: Intercooled GT cycle.

Reheating consists of dividing the turbine into several stages and adding combustion chambers between them, as depicted in Figure 1.13. Thus, the gas leaving the first turbine enters the second combustion chamber where additional fuel is burnt to raise the temperature again. By entering the second turbine, more energy is extracted. This configuration leads to an increase in the cycle net specific work and the turbine outlet temperature.

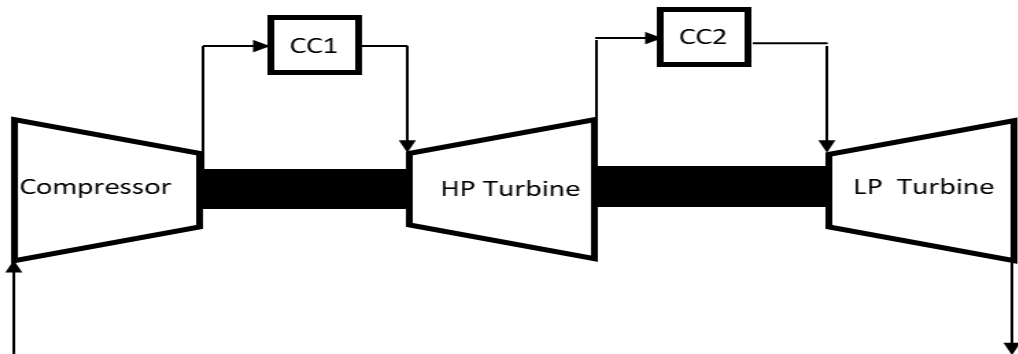
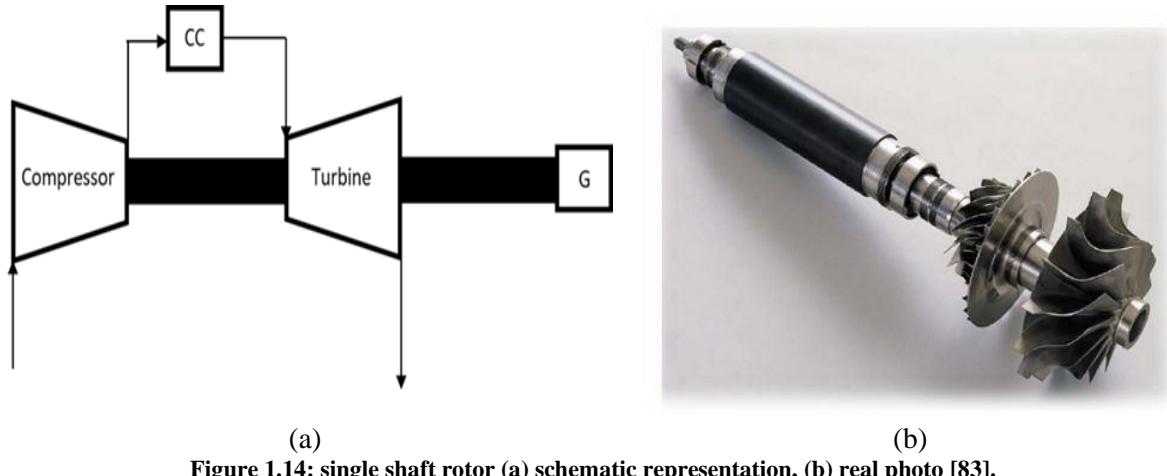


Figure 1.13: Reheated GT cycle.

The benefits of reheating between turbine stages and intercooling between compressor stages are significant. There is an increase in work output, and regeneration is enhanced. Consequently, by combining reheating and intercooling with regeneration, the gas turbine performance can be improved. The efficiency of such configuration is estimated between 39 – 47 %, and around 300 kg/h of air is required to obtain a power output of 20 kW [1].

#### 1.4.3. Gas Turbine Mechanical Drive Categories

The mechanical drive is divided into three main categories. The first category is illustrated in Figure 1.14. It consists of the compressor and the turbine mounted on the same shaft and the alternator either on the turbine side (Figure 1.14a) or on the compressor side (Figure 1.14b). In this case, the output shaft has the same speed as the turbine/compressor shaft and is used to drive electric generators coupled or not with a gearbox. This configuration is convenient when the gas turbine is needed to operate at a constant speed [82].



**Figure 1.14:** single shaft rotor (a) schematic representation, (b) real photo [83].

In the case of a twin-shaft turbine, a gas turbine drives only the compressor and another turbine named “the free turbine” is connected to the driven system. Figure 1.15 represents the twin-shaft turbine architecture. The two turbines are not coupled mechanically but aerodynamically. Thus, the compressor is driven at a steady speed and is not affected by the load [84]. The main benefit of this configuration for the single shaft gas turbine is the flexibility and the ability to run at variable speeds.

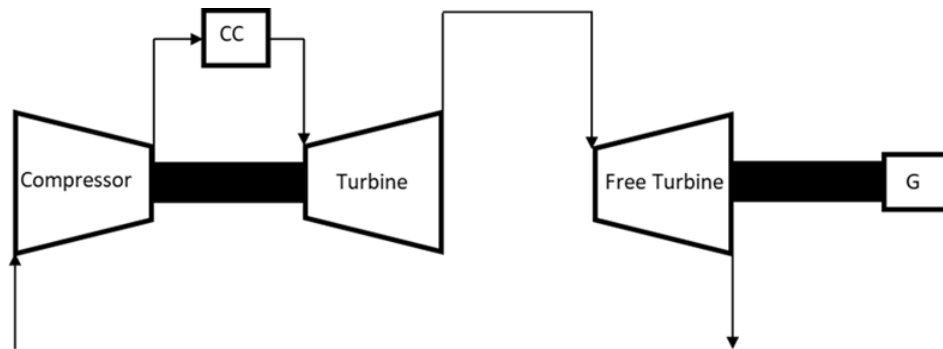


**Figure 1.15:** Twin-shaft GT cycle.

Another configuration is the multi-spool arrangement illustrated in Figure 1.16, a mechanical separation of the compressor stages. Each compressor is driven by its turbine at different rotating speeds [85]. In other words, the HP compressor is driven by the High-Pressure (HP) turbine, and the LP compressor is driven by the LP turbine. This arrangement is generally used in high-power systems.

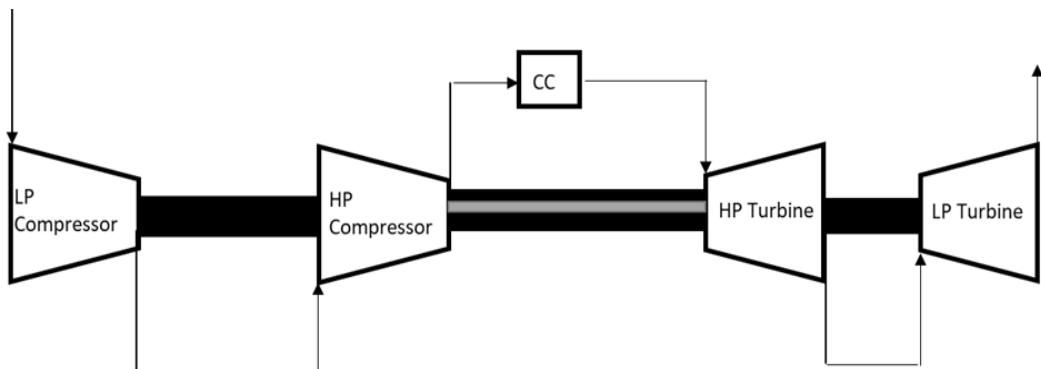


**Figure 1.16:** Multi-spool arrangement GT cycle.

In summary, the mechanical drive configuration is determined by the application. Single-shaft rotors are used when the gas turbine runs at a constant speed. Variable speeds would be better served by the second configuration. Lastly, multi-spool arrangements are chosen for high-power systems.

#### 1.4.4. Specific Gas turbine Configurations for Series Hybrid Electric Vehicles

After explaining the main architectures of a GT cycle, in the coming section, an overview of the most relevant studies in the literature investigating different configurations of the GT cycle as a booster for electric vehicles is presented. Based on the surveyed studies, a large sample of the most relevant designs was chosen to identify the selected architecture, the operating conditions as well as the efficiency, as shown in Table 1.4 and illustrated in Figure 1.17.

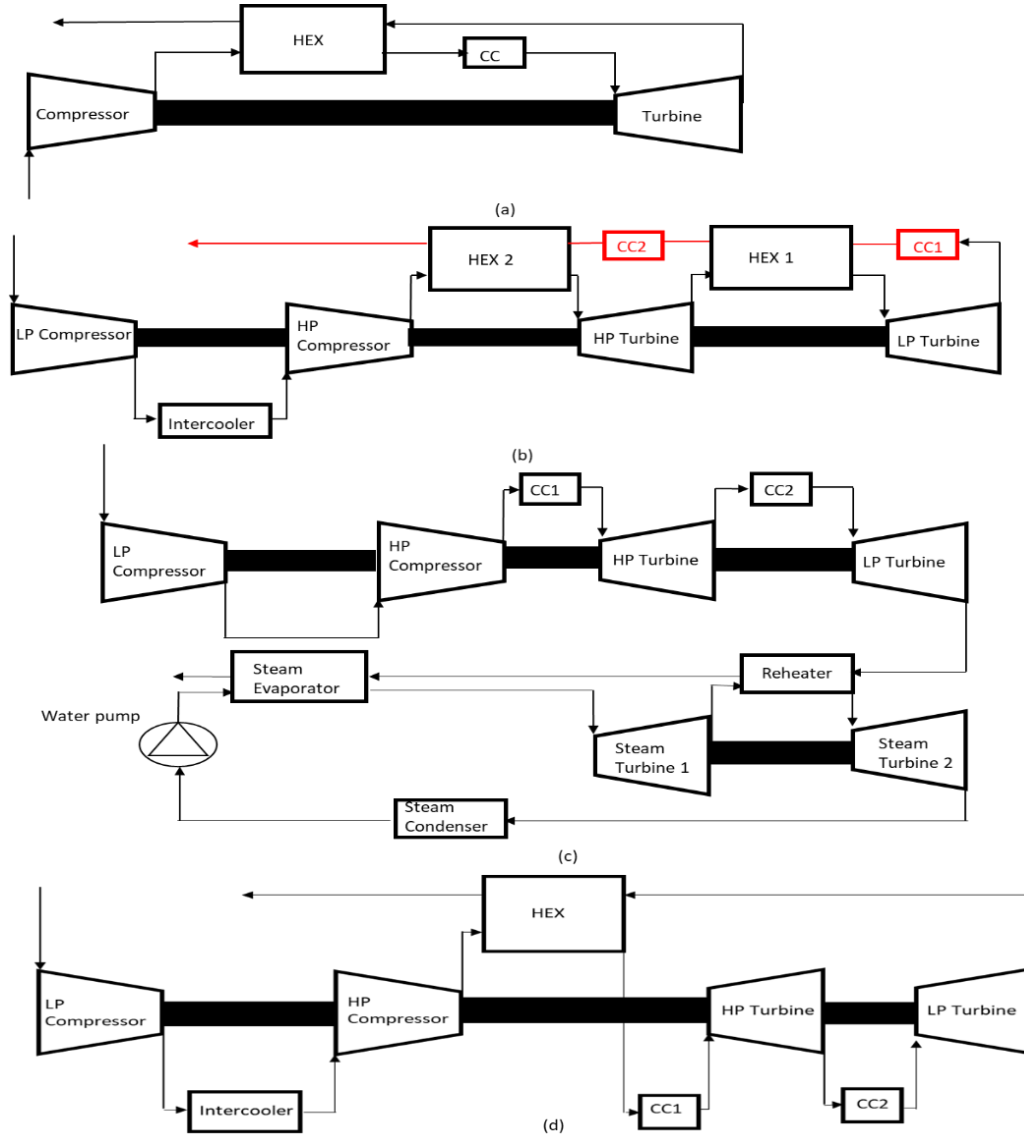


Figure 1.17: GT configurations from the literature.

Some studies investigated the recuperated GT cycle as range extenders in electric cars. It consists of a Brayton cycle with a recuperator to recover the heat at the outlet of the turbine. Mackay [76] developed a GT cycle to drive hybrid vehicles, suitable for passenger cars and small buses. The operating pressure ratio is 3 and the turbine inlet temperature (TIT) is 816°C. The efficiency of the current GT cycle is 30%. Ji et al. [62] developed a numerical and an experimental study of the recuperated GT cycle. The results show that the cycle efficiency is 35% for recuperator effectiveness of 0.7, a pressure ratio of 3.2, and a TIT of 1152 K.

Other researchers tackled different GT configurations. Bou Nader et al. [86] conducted an exergo-technological analysis to determine the most convenient cycle for electric cars. The identified GT cycles are prioritized based on their efficiency and net specific work. The study shows that a downstream-intercooled reheat external combustion GT cycle is the optimal realistic cycle with the highest efficiency (40.7%) for regenerator effectiveness of 0.85, a maximum pressure ratio of 4, and a TIT of 1250 °C. Whereas, Barakat et al. [87] investigated the feasibility of combined GT cycle configurations as substitutes for ICE. The cycle configuration consists of a Brayton cycle coupled to a Steam Rankine cycle. The study is based on thermodynamic exergy, energy, and integration assessment. The reheat GT coupled to a turbine reheat Steam Rankine cycle is selected having a system efficiency of 47.2% at a TIT of 1250°C. Besides, Bou Nader [1] selected the Intercooled Recuperated Reheated (IRReGT) cycle as the most suitable in terms of efficiency and power density. The cycle consists of two compression stages with an intercooler, a recuperator, and two expansion stages with reheating using two combustion chambers. The cycle efficiency is 39 % for TIT = 950 °C, 45.7% for TIT= 1100°C, and 47% for TIT = 1250 °C. The maximum compression ratio is 4 and the maximum expansion ratio is 3.5.

**Table 1.4: A summary overview of the literature for GT configurations as range extenders for electric vehicles.**

GT configurations	Efficiency (%)	Conditions	Author	Figure
Recuperated GT cycle	30	Pressure ratio 3, TIT = 816 °C	Mackay [76]	Figure 1.17a
Recuperated GT cycle	35	Pressure ratio 3.2, TIT = 1152 K	Ji et al. [62]	Figure 1.17a
Downstream-intercooled reheat external combustion GT cycle	40.7	Pressure ratio of 4, TIT = 1250 °C	Bou Nader et al. [86]	Figure 1.17b
Reheat GT coupled to a turbine Reheat Steam Rankine cycle	47.2	Compression ratio 3.5, Expansion ratio 4, TIT = 1250°C	Barakat et al.[87]	Figure 1.17c
IRReGT cycle	47	Compression ratio 4, Expansion ratio 3.5, TIT =1250 °C	Bou Nader [1]	Figure 1.17d

Among the investigated configurations, the RGT configurations have the lowest efficiencies (30 – 35%). The efficiency is higher in the case of downstream-intercooled reheat external combustion GT cycle (40.7 %). The efficiency is the highest for the Reheat GT coupled to a turbine Reheat Steam Rankine cycle and the IRReGT cycle (47.2 % - 47%).

## 1.5. Gas Turbine Main Components Characteristics

This section presents the characteristics of the different components of the IRReGT cycle since this configuration includes all the possible components. The IRReGT cycle consists of two compression stages with intercooling, a recuperator, and two expansion stages with reheating, as illustrated in Figure 1.18a. Figure 1.18b presents the IRReGT cycle that is under development in Stellantis. Two important

advantages result from reheating turbine stages and intercooling compressor stages: increasing net work output and increasing regeneration potential. Therefore, when reheating and intercooling are combined with regeneration, significant improvements in GT performance can be achieved. The choice of the suitable component is based on the state of the art of the different technologies and constraints.

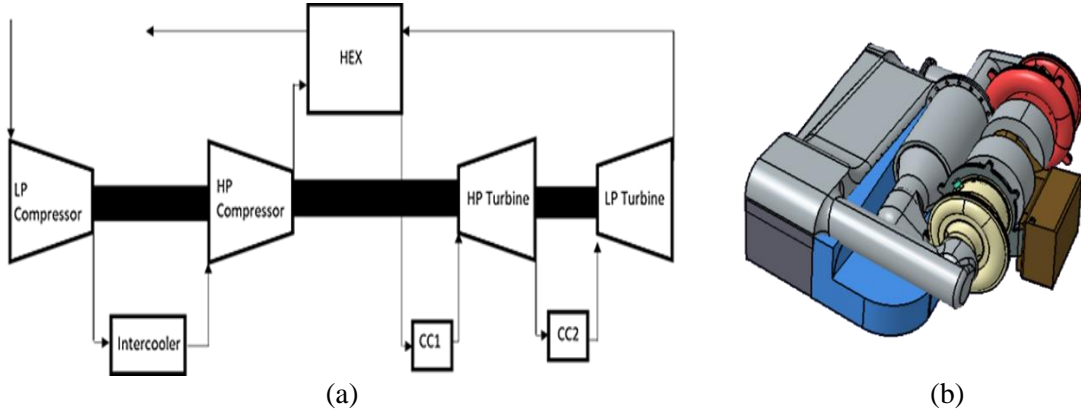


Figure 1.18: IRReGT cycle, (a) schematic presentation, (b) IRReGT cycle under development by Stellantis.

### 1.5.1. Compressors

Gas turbines rely on compressors to produce highly compressed air that enters into a combustion chamber, where it is combined with fuel and ignited. There are two types of compressors: axial compressors (Figure 1.19a) and centrifugal compressors (Figure 1.19b) [88].

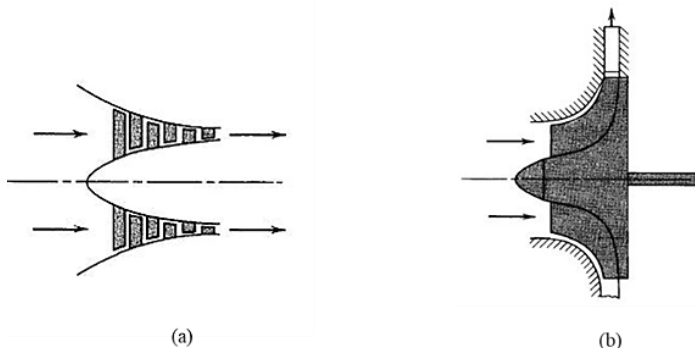


Figure 1.19: (a) Axial compressor, (b) Centrifugal compressor [89].

Axial compressors are commonly used for high flow and pressure ratios of 1.4 to 1.5 [90]. Higher pressure ratios can be achieved by using multistage compressors [89]. These are designed to drive heavy industrial turbines. The centrifugal compressors, on the other hand, are used for low flow conditions and higher pressure ratios between 1.5 and 5 [90]. They are suitable for small, compact turbochargers.

### 1.5.2. Recuperator (HEX)

The recuperator is a compact heat exchanger designed to recover the heat of the exhaust gas by preheating the air before entering the combustion chamber. Adding a recuperator leads to a reduction in fuel consumption and an increase in the efficiency of the gas turbine. The recuperator's effectiveness has a significant impact on the GT efficiency. A study showed that for HEX effectiveness of 0.7, the cycle efficiency of a GT can reach 35 % for TIT = 1152 K [62]. For this reason, studies are focusing nowadays on improving the effectiveness of recuperators and their heat transfer rates, as well as their

pressure losses. GTs that are integrated into vehicles are greatly influenced by these parameters, where HEX weight limitations and installation limitations are of great importance [91].

A convenient recuperator for the microturbine should have these properties: high heat transfer effectiveness ( $> 90\%$ ), low relative pressure loss ( $< 3\%$ ), compactness, and low cost [92].

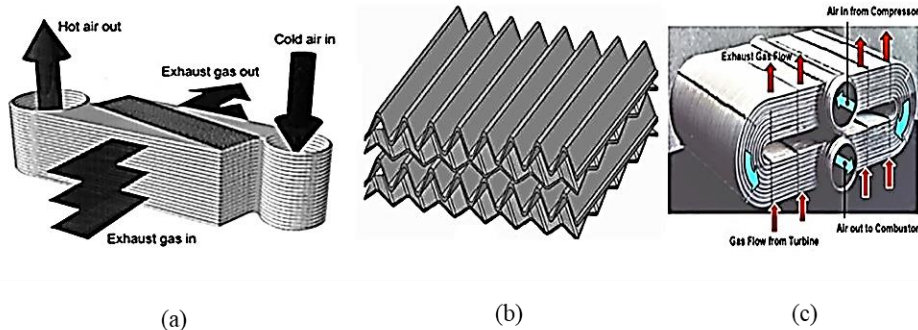


**Figure 1.20: The different types of HEX: (a) plate-fin, (b) primary surface, (c) tubular recuperators [92].**

HEXs are divided into three categories according to their heat transfer geometry: plate-fin [93], primary-surface (plate heat exchanger, with bolted, welded, or brazed plates [94]), and tubular (tubes within an outer shell [95]) recuperators as presented in Figure 1.20. Literature has revealed that the primary-surface recuperators are more suitable than the plate-fin and tubular heat exchangers due to their good compactness, high effectiveness (~90%), and low-pressure drop (<5%) [92], while plate-fin recuperators are efficient but expensive, and tubular recuperators are bulky and large. Wang et al. [96] affirmed that recuperators with cross-wavy primary surface channels are suitable for microturbines based on the experimental analysis conducted that shows an acceptable compromise between heat transfer coefficient and pressure drop. The same authors [97] implemented a genetic algorithm procedure to optimize a cross-wavy primary surface and cross-corrugated primary surface heat exchanger used for microturbines. The algorithm considers many parameters including weight, compactness, and pressure drops. Results show a decrease of the material weight by 12 % and 17- 36 % respectively for the cross-wave and the cross-corrugated heat exchanger.

Plate-fin heat exchangers also gained large attention. Robey et al. [98] proposed a plate pin-fin heat exchanger for supercritical CO<sub>2</sub> cycles using 3D printing. As well, Wakim [99] redesigned a compact plate-fin heat exchanger to be manufactured by metal 3D printing, illustrated in Figure 1.21. Local parametrical and topological optimization was used to enhance the corresponding thermal-hydraulic performance using offset and wavy fins. The volume and the weight of the HEX were both reduced by 50 % (13.5 kg) compared to commercial plate fin HEX with an effectiveness of 85 % and an outlet temperature of 900 °C.

The recuperator material is another important parameter that should be taken into consideration, since operating at high temperatures can lead to corrosion, erosion, and creep resistance of the material used. Recent studies are investigating new materials including Nickel alloys such as Inconel [100], and ceramics [101] due to their mechanical properties, and high resistance to corrosion at high temperatures. Figure 1.22 shows how the recuperator operating temperature affects the used material.

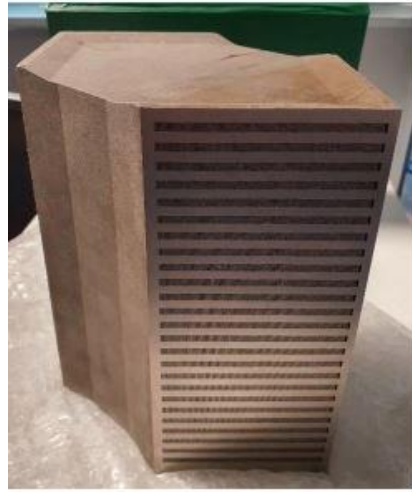


**Figure 1.21: Optimized plate and fin HEX in 3D printing [99].**

Significant progress has been achieved in developing ceramic materials for aircraft applications [102], they can also be used in recuperators for microturbines. Carman et al. [101] proposed a new concept design that consists of a ceramic micro-channel heat exchanger to be used in microturbines of temperatures up to 1300 °C. The cycle efficiency of 39.4 % is reached for a square cross-sectional design and an efficiency of 42.2 % for a triangular cross-sectional design.

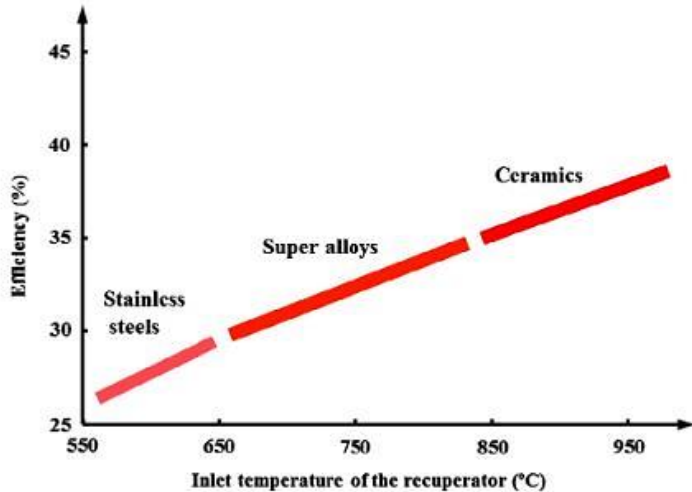


**Figure 1.22: Materials depending on the recuperator operating temperature [92].**

### 1.5.3. Combustion Chamber

The combustion chamber of a gas turbine is where the energy that drives the whole system is added. Its main purpose is to increase the temperature of the high-pressure gas. There are three designs for combustion chambers in a gas turbine: tubular (can), tuboannular (can-annular), and annular [88] as depicted in Figure 1.23.

Tubular combustors, also known as "can combustors" are applicable in large industrial turbines. Their benefits include their simple design, their low maintenance, and long life [88]. However, these combustors are large, and heavy and produce high-pressure losses [103]. An annular combustor differs from a can combustor in that the flame tubes are enclosed within a single cylindrical casing. This configuration results in a more compact and lighter design. The last configuration is the annular

combustion chamber, which is commonly used for aircraft applications, where high temperatures and low emissions are important [90]. Compared to the tuboannular combustor, it has lower pressure loss and is more compact [103].

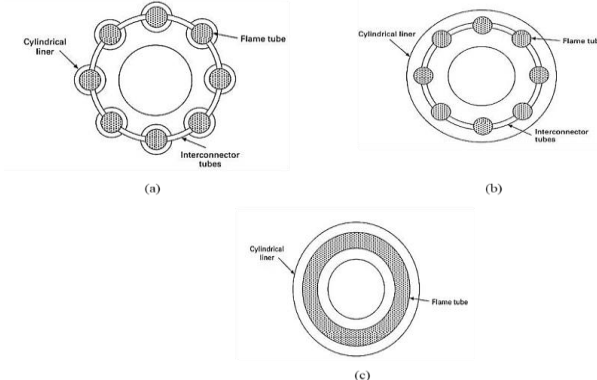


**Figure 1.23:** Cross section of (a) tubular combustor, (b) tuboannular combustor, (c) annular combustor [103].

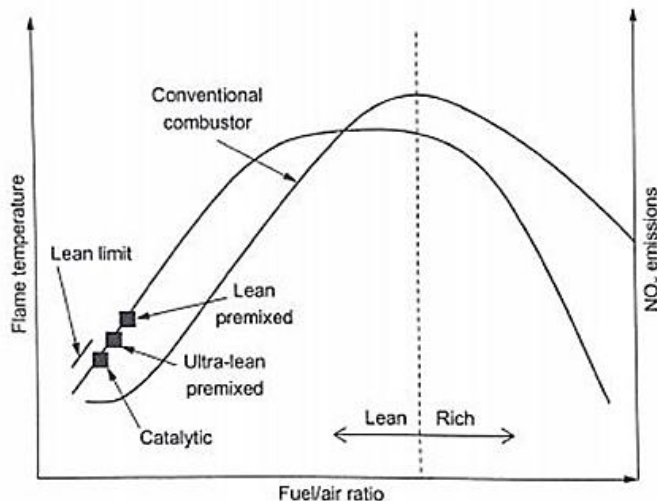


**Figure 1.24:** The effect of fuel/air ratio and temperature on NOx emissions [90].

The main combustion chamber parameters are the pressure drop (ideally equal to zero), the combustion chamber efficiency (depends on mixture ratio, combustion length, vaporization), the outlet temperature (related to the turbine materials constraints), and the flame stability. NOx, CO<sub>2</sub>, and H<sub>2</sub>O are released during combustion. Therefore, new regulations are submitted to reduce NOx emissions. The amount of these emissions depends on the temperature, time, and concentration of the combustion chamber. Figure 1.24 shows the relation between NOx emissions, flame temperature, and equivalence ratio. In stoichiometric conditions, the flame temperature is maximum, resulting in high emissions of NOx. Operating in lean combustion reduces NOx emissions but is coupled with combustion instability. On the other hand, operating in rich conditions reduces NOx emissions but produces CO and unburned hydrocarbons (UHC). As a consequence, the lean area is considered and many techniques to reduce NOx emissions are proposed in Section 0.

#### ➤ Flameless Combustion Chamber

Higher flame temperature is essential to improve the performance of the combustion and increase the power output of the turbine. The presence of oxygen and nitrogen for a sufficient resident time at high flame temperature leads to NOx production. The flameless combustion chamber describes the process where no flame front is available. The exhaust gas is recirculated and mixed with the air and then

preheated before the combustion phenomenon. Thus, no peak temperatures are present, and NOx emissions are reduced. The flameless combustion advantages compared to traditional combustor chambers includes low noise due to low-pressure oscillation, low energy consumption related to high efficiency, and low NOx emissions [104]. Figure 1.25 presents both a flame combustion chamber on the left and a flameless combustion chamber on the right. The figure shows that no peak temperature is observed in the flameless case, in contrast to the flame case.

Many studies investigated the operating mechanism of flameless combustion and conditional aspects. Caviogoli et al. [105] developed a laboratory burner to reproduce the same phenomenon that occurs in a real-size flameless combustion chamber. Another study evaluated the most relevant parameter that affects the combustion process [106], including the inlet temperature, the oxygen to fuel ratio, the residence time, and the dilution rate. It was shown that if the temperature exceeds 1400 K, the combustion is stable for all oxygen to fuel ratios, while for temperatures below 1000 K the mixture should be twice rich as the stoichiometric ratio. In addition, the expected temperature is affected by the residence time and the dilution level. To reach high temperatures, the residence time, as well as the dilution level, should be decreased.

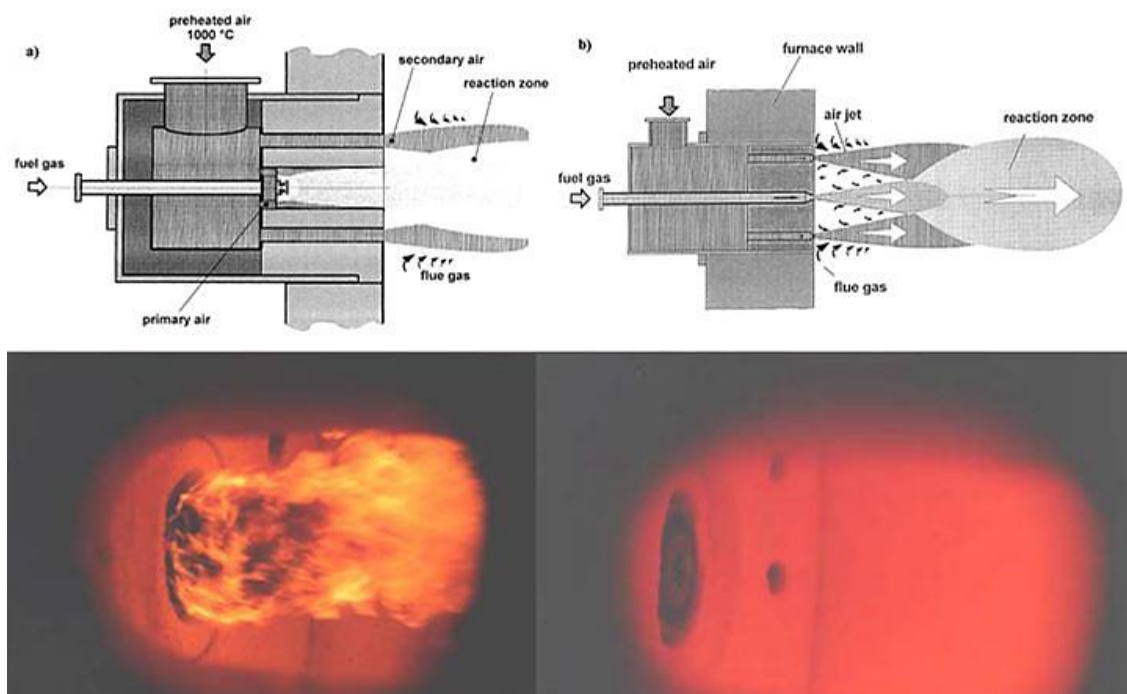


**Figure 1.25: Comparison between flame (left) and flameless (right) combustion chamber [107].**

The use of flameless combustion chambers in gas turbines was also investigated to reduce the emitted NOx [104]. Flamme [108] examined the feasibility of the flameless combustion chamber in gas turbine applications. The obtained results were promising. Then, Wang et al. [109] conducted a technical, environmental, and economic study for a recuperative flameless combustion chamber at a gas turbine power station. Results show that this technology can lead to a reduction in NOx emissions, and a reduction in the cost compared to selective catalytic reduction. Mackay [76] developed a 24 kW RGT cycle to drive hybrid electric vehicles. The combustion chamber used is a flameless catalytic with a high air/fuel ratio of 134:1. The emissions are less than a standard combustion chamber. Bazoooyar and Darabkhani [110] developed a numerical analysis of a hydrogen flameless combustor for a microturbine. The microturbine combustor was designed and optimized using CFD simulations. Results demonstrate

significant benefits of this technique in lowering NOx emissions and improving the cycle overall efficiency.

#### 1.5.4. Turbine

As for the compressor, there are two categories of turbines: axial and radial turbines. The main difference between radial and axial turbines is the direction of the fluid. In axial turbines, the working fluid is parallel to the shaft, while, in radial turbines, the working fluid is radial to the shaft. Figure 1.26 illustrates the two types of turbines. Even though axial turbines have higher efficiency than radial turbines, they have a higher cost and lower expansion ratios. For the same pressure ratio, several axial turbine stages are needed [90].

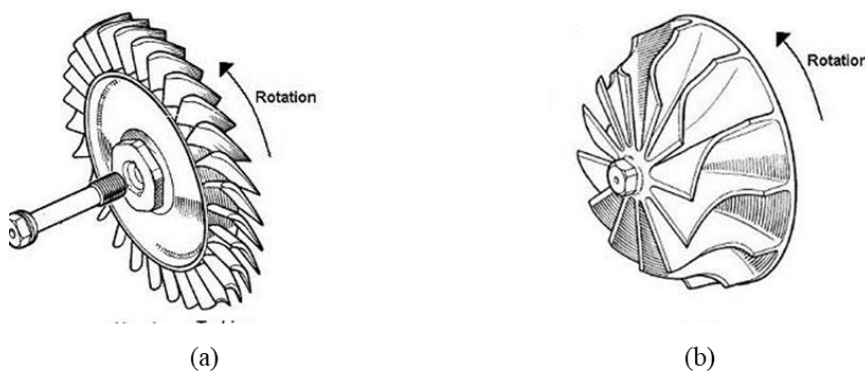


**Figure 1.26: (a) Axial turbine, (b) radial turbine.**

Axial turbines are used for high flow rates and low-pressure ratios because for low flow rates the blade of axial turbines becomes very small which prevents maintaining a small tip clearance and leads to an increase in efficiency drop [111]. In conclusion, axial turbines are used in power plants and industrial applications, whereas radial turbines are used in turbocharges and range extenders due to their compactness and low cost.

Turbines are also divided into impulse and reaction turbines. In impulse turbines, the enthalpy drop occurs only in the nozzles, while, in reaction turbines, the enthalpy drop occurs in both the nozzles and the impellers [112]. The turbine is the most critical component in the GT cycle. The efficiency of the GT cycle is related to TIT, higher TIT leads to higher turbine efficiency. However, TIT is limited by the material melting temperatures and constraints. As a result, the development of new materials like Nickel alloys and ceramics and cooling blade technologies are proposed to reach higher temperatures [113].

#### 1.5.5. Bearings

In microturbines, oil-lubricated or air-lubricated bearings are commonly used [114]. The former is a reliable technology, but needs numerous components such as an oil pump, an oil filter, and an oil cooling system, resulting in higher costs and more maintenance. The main categories of oil bearings are high-speed metal balls or rollers, floating sleeves, and ceramic surfaces. The last form is the most beneficial in terms of operating temperature, life, and lubricant flow. The operation is simpler in microturbines with air bearings, and with low maintenance requirements due to the non-existence of the oil system [113]. In addition, when using air bearings, the cost, size, and weight are reduced because of the elimination of oil lubricating parts [76]. This technology is widely applied in airplane auxiliary power units.

Many studies have investigated the air bearings to be used in microturbines. Mackay [76] confirmed in his paper that by using air bearings, the range extender will be lighter and cheaper. Shan et al. [115] discussed the design, fabrication, and testing of a silicon-based microturbine concept. The study focuses on the design of the journal and thrust air bearing. Experimental tests show stable operations. A study conducted by Muruganandam et al. [116] proposed a design analysis of air bearings for high-speed microturbines using MATLAB. Results show that the designed air bearings are efficient and stable for turbine speeds from 5010 to 100 000 rpm.

### 1.5.6. Generator

Microturbines produce power either by directly driving a high-speed generator from a single turbocompressor shaft or by using a separate power turbine. In a single-shaft high-speed generator configuration, a permanent magnet alternator (usually samarium cobalt) is used. This power generator converts AC to DC and then rectifies it to 60 Hz [114]. For a single shaft, the generator serves as a starting motor to start the turning of the turbocompressor until reaching a sufficient rotational speed that allows the compressor to take the air. For multi-shaft configurations, a separate starting system is needed. The improvements in magnetic materials have contributed to more efficient, resistant, and lighter generators [113]. Figure 1.27 represents a permanent magnet alternator designed by MeccAlte.



**Figure 1.27:Permanent Magnet Alternator from Mecc Alte [117].**

Although their high efficiency and small size, the major weakness of permanent magnetic electric motors is the presence of rare-earth materials, resulting in bad environmental footprints and high cost. Therefore, in 1883, Nikola Tesla invented the Induction motor in which the magnetic field is created from electrical current to generate torque, without using a magnet. This result in a low-cost production motor and high reliability. Apart from this, permanent magnet motors are highly efficient at low speeds, whereas Induction motors are efficient at high speeds. Due to this, several electric vehicle models now feature "dual motors" that use both induction motors and permanent magnet motors, including the Tesla Model 3.

## 1.6. Technical Characteristics of Leading Microturbines Manufacturers

The microturbine, as discussed in the sections above, is composed of different components. The following Table 1.5 summarizes the technical components of leading microturbine manufacturers. It incorporates the power of the microturbine, the type of compressor, the type of turbine, and the type of bearings. In addition, it incorporates the microturbine cycle efficiency and configuration. Only microturbines having power up to 45 kW are considered. Figure 1.28 represents a cross-section of the Capstone turbine with its different components. The last column of the table corresponds to the IRReGT cycle proposed by Bou Nader [1] which is under development in Stellantis.

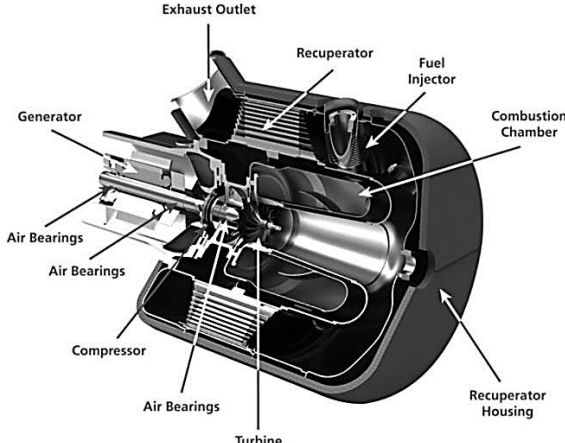


**Figure 1.28:** Cross-section of the Capstone turbine [118].

**Table 1.5: Microturbines' technical properties for leading manufacturers.**

Manufacturers	Elliott Energy	Et Group	Capstone Turbine	Delta Motor	Brayton Energy	Bladon Jets	Stellantis
Power (kW)	45	45	30	17	12	12	25
Pressure ratio	4	-	3.2	-	-	-	3
RPM (rev/min)	116 000	60 000	96 000	120 000	-	140 000	120 000
GT cycle	-	RGT	RGT	RGT	RGT	-	IRReGT
Efficiency (%)	30	28	28	-	-	-	46.9
Compressor	Single stage centrifugal	-	Single stage centrifugal	-	-	-	Double stage
Turbine	Radial	-	Radial	-	Radial	-	Radial
Shaft	Single	-	Single	Single	-	Single	single
Bearings	Oil	-	Air	-	Air	Air	-
References	[119]	[120]	[121]	[122]	[123]	[124]	[1]

As seen in Table 1.5, among the investigated microturbine manufacturers, the maximal pressure ratio is 4 (Elliott Energy), and the maximal rotational speed is 140 000 rpm (Bladon Jets). Additionally, two main gas turbine cycles are used: the recuperated gas turbine cycle (RGT) and the intercooled recuperated reheated gas turbine cycle (IRReGT). On the other hand, all the turbine manufacturers have used a single-stage centrifugal compressor and a single-stage radial turbine mounted on the same shaft. As for the bearings, air bearings are employed by most manufacturers for microturbine configurations.

## 1.7. Methods to Increase the GT Cycle Efficiency

The performance of a GT cycle is evaluated using its power output and its efficiency. The gas turbine efficiency improvements have resulted from a combination of thermodynamic and technological efforts [125], presented in Figure 1.29:

- Choosing the optimal gas turbine cycle configuration
- Increasing the maximum pressure
- Increasing the turbine inlet temperature

Many researchers assessed different configurations for the gas turbine cycle to enhance the cycle performance. Reheating, recuperating and intercooling were investigated. As shown and explained previously, adding a recuperator leads to a reduction in fuel consumption [126]. As well, cooling the compressed air at the compressor stages reduces the amount of compressive work, and gives an opportunity to further increase the overall pressure ratio [125]. Reheating between the turbine stages increases the turbine output work [127]. All these effects result in higher total efficiency. Based on the surveyed studies presented in detail in Section 0, the IRReGT cycle is the optimal GT cycle architecture. It combines a recuperator, with intercooling between the compressor stages and reheating between the turbine stages.

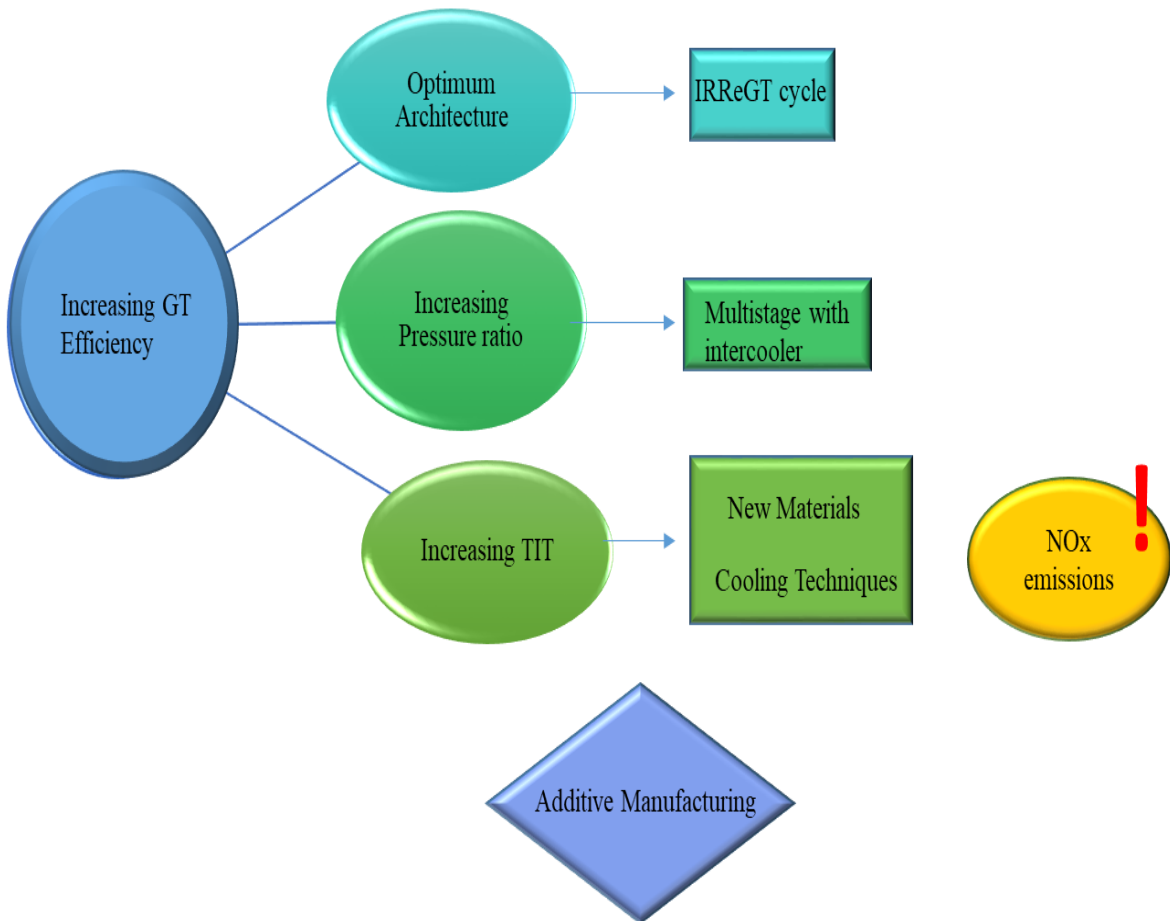


**Figure 1.29: Steps to increase the GT cycle efficiency.**

Regarding the study conducted by Ji et al. [62], the performance of the GT cycle is closely related to the recuperator effectiveness, pressure ratio, and TIT. For instance, the efficiency of the GT cycle is significantly affected by the recuperator's effectiveness. The higher the recuperator effectiveness, the higher the efficiency. Nada [128] confirmed that the cycle efficiency increases with the compressor pressure ratio and the turbine inlet temperature. At a given temperature, higher pressure ratios result in higher efficiency. In addition, increasing the pressure ratio is beneficial in increasing the power density and reducing the mass flow rate. The system will therefore be smaller and more compact, reducing noise pollution. One method to increase the pressure ratio is achieved by adding an intercooler between the compressor stages [125]. However, if the pressure ratio is increased beyond a certain value, the overall efficiency will decrease. In this case, the gas turbine's net useful power decreases as a result of the increased power required to operate the compressor [88].

Another interesting technique to enhance the cycle efficiency is increasing TIT [88]. For instance, an increase in efficiency of 12 % is obtained from the GT configuration when TIT increases from 950 °C up to 1100 °C. The efficiency increases by around 20% when TIT increases from 950 °C to 1250 °C for the same system configuration [1]. Increasing TIT has other advantages, particularly in recuperated GT cycles, as it leads to a favorable temperature difference between the hot and cold streams in the HEX. This results in improved HEX effectiveness and further improvements in gas turbine thermodynamic efficiency. However, TIT is limited by the turbine material melting temperatures, as well as material fatigue and stress. As long as the temperature does not exceed 1100 °C, it is not necessary to use special materials, and the turbine can be made using familiar, low-cost alloys [87]. Therefore, TIT limit can be extended in two ways: either by developing materials that can withstand higher temperatures or by cooling the turbine blades [91]. These two techniques necessitate new technologies of manufacturing to develop compact complex cooled turbines such as Additive Manufacturing [129]. As a result of the increase in TIT, NOx emissions are another challenge that should also be addressed, so methods of reducing NOx emissions need to be discussed as well.

To conclude, the efficiency of the GT cycle is an important parameter to evaluate its performance. Choosing the optimal GT architecture, increasing the pressure ratio and the TIT are used to enhance the efficiency of the GT cycle. There are, however, some challenges in implementing these procedures. In terms of the pressure ratio, the efficiency will decrease as the compressor work increases beyond its optimal value. In the case of TIT, cooling techniques are necessary to efficiently utilize known and low-cost materials. However, these techniques require the use of a new method to produce sophisticated small complex geometries, namely 3D printing. Finally, as a result of TIT, pollutants such as NOx are released at higher levels. Therefore, methods for reducing these pollutants are used.

In the following sections, a detailed overview of solutions to overcome the limitations of material temperatures is conducted. Part one discusses new materials, while part two details different cooling technologies that can be used to keep using low-cost materials at high temperatures. Then, the methods for reducing NOx emissions are discussed. Finally, the last part assesses the Additive Manufacturing techniques by introducing their cons and pros.

### **1.7.1. Turbine Materials / Increasing Turbine Inlet Temperature**

Gas turbine cycle efficiency is related to the turbine blade material and turbine inlet temperature (TIT). Therefore, turbine blade materials should have higher melting temperatures, good oxidation/corrosion resistance, and a high-temperature strength [130]. Furthermore, turbines are subjected to high rotational speed, leading to huge centrifugal forces on their blades. These forces manifest themselves through creep rupture and fatigue failure. As well, turbine blades are exposed to high vibrations and resonance that can cause damage [80]. Therefore, the development of new materials for turbines is of interest.

Traditionally, turbine blades have been made from iron alloys. However, as inlet temperatures increased, alternative metals and nickel-based alloys were developed [80], following which Inconel emerged [131]. Inconel 718 is a niobium-modified precipitation hardening nickel-iron alloy. This alloy presents high strength, creep resistance, and good fatigue life at high temperatures up to 700 °C. Inconel 718 has a great weldability property compared to other nickel-based super-alloy. Due to its excellent resistance to high temperatures, it can be used in different applications such as gas turbines, aircraft, and turbocharger rotors [130]. Some studies using Inconel for turbine design are presented in the following. Using Selective Laser Melting Technology, Zhang et al. [132] developed a two-part publication describing the design, simulation, and testing of an internally cooled radial turbine. The experimental

results were consistent with the simulation results. HiEta turbomachinery has used Inconel 718/625 in its cooled radial turbine. High temperatures of 1200 °C are reached [100].

Ceramics are also attractive candidates. In addition to operating at high temperatures, they are corrosion and oxidation-resistant. Furthermore, they are much lighter than other metals and have a lower thermal coefficient (~1/3 of metals). However, they are brittle at high temperatures [131]. Silicon Nitride Ceramics has been used by different turbine manufacturers to improve the acceleration of the turbochargers by reducing their inertia such as the turbocharges by Mitsubishi [134], the one developed by Nissan [135], and also Garrett [136] constructed turbocharges from Silicon Nitride Ceramics.

Several studies investigated the feasibility of ceramic turbines. AGATA, the European EUREKA project conducted a project to design a gas turbine for a hybrid electric vehicle including three ceramic components: a catalytic combustor, a radial turbine, and a heat exchanger [137]. Results show that it was possible to meet the design requirements using ceramic materials. Another project is the CGT Japanese project dedicated to producing a 300 kW ceramic RGT engine achieving 42% cycle efficiency for TIT =1350°C. The obtained results are in good agreement with the design goals [138]. In addition, other researchers investigated the feasibility of ST5+ ceramic microturbine engines [139]. Moreover, Matsunuma et al. [140] developed a GT by replacing the metallic rotor, nozzle, and casing with ceramic components. Therefore, ceramic materials showed good results at high temperatures, but some degradation is obtained on the metallic ceramic component interface. As well, McDonald and Rodgers [113] proposed a methodology to design, manufacture, and test a 7.5 kW ceramic microturbine coupling a ceramic radial turbine, a ceramic combustor, and a ceramic recuperator.

Based on these findings, the properties of different materials used for GT applications are assessed in Table 1.6. As seen, ceramic has the lightest weight and the lowest thermal expansion factor, while Iron has the highest fusion temperature, and Inconel 718 presents relevant properties.

**Table 1.6: Properties of different materials used for turbines.**

Material	Density (kg/m <sup>3</sup> )	Linear thermal expansion factor (10 <sup>-6</sup> 1/k)	Fusion temperature (°C)
Iron	7870	11.7	1538
Ceramic	3600-3800	3-5	1000-1500
Inconel 718	8193	11.5	1336
Stainless Steel	7700	16.9	1400-1450

On the other hand, Table 1.7 states the advantages and disadvantages of the different materials used for turbines based on [141].

All the presented materials have limitations when operating at high temperatures. Iron alloys were replaced by Nickel alloys. Ceramic materials are brittle at high temperatures and costly. Therefore, although Inconel 718 can't handle temperatures above 700 °C, they are anti-corrosive material, with high strength, and affordable price. Consequently, to benefit from both operating at high temperatures and using low-cost materials (like Inconel 718), cooling techniques are used.

**Table 1.7: The pros and cons of the different materials used for turbines.**

Material	Advantages	Limitations
Iron alloys		High temperature → replaced by nickel alloys
Ceramic (SiC and SiN <sub>4</sub> )	<ul style="list-style-type: none"> <li>-Higher melting points than metal</li> <li>-Resistant to corrosion and oxidation</li> <li>-Lighter than metal</li> <li>-Expansion factor 1/3 metal</li> <li>-Anti-corrosive (hot corrosion)</li> </ul>	Brittle at high temperature
Inconel 718	<ul style="list-style-type: none"> <li>-High strength</li> <li>-Creep resistance</li> <li>-Good fatigue life</li> <li>-Affordable cost</li> </ul>	The maximum acceptable temperature is 700 ° C

### 1.7.2. Turbine Cooling Techniques / Increasing Turbine Inlet Temperature

The simplest way to cool the turbine blades is achieved by taking air from the compressor or the last stage of the turbine and introducing it from the turbine blade root to the turbine holes [80]. Two types of cooling techniques exist: internal cooling and external cooling. The first consists of compressed air flowing inside the channel of the turbine blade. The heat transfer occurs between the turbine blade and the coolant air. The latter consists of injecting cooling air through holes on the surface of the turbine blade. The coolant air forms a layer between the turbine surface and the hot gas. Although cooling the turbine blade by introducing cooling air leads to a decrease in the turbine efficiency, it improves the overall cycle performance due to higher turbine inlet temperatures. The latter generally overcome the loss by the coolant flow and improves the cycle efficiency.

#### 1.7.2.1 Internal Cooling Techniques

This section presents different techniques of internal cooling and their specifications including smooth channel cooling, rib turbulated cooling, impingement cooling, pin fin d=cooling, dimple cooling, and vortex cooling.

##### ➤ Internal Smooth Channel Cooling

Smooth cooling channels (Figure 1.30) are the simplest, and the cheapest in terms of geometry and realization. Cooling channels are arranged either in a radial direction with the coolant flow exiting at the top of the blade, or in a flow-directional manner with the coolant leaving at the trailing edge of the blade. They are generally used in small-scale turbines.



Figure 1.30: Smooth cooling channel.

### ➤ Rib Turbulated Cooling

The introduction of turbulators or ribs in the smooth cooling channel generates a considerable increase in the level of turbulence, leading to higher pressure drops, but allows a considerable increase in the heat exchange coefficient. Therefore, a lower mass of coolant is needed to ensure the cooling of the turbine blade [142]. However, this technique is more complex and more expensive than the smooth cooling channel configuration.

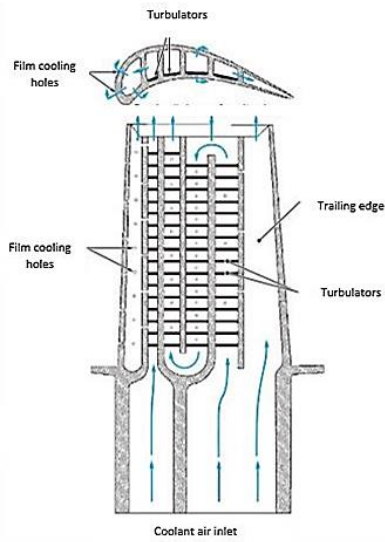


Figure 1.31: Cooled blade with rib turbulated configuration.

The rib turbulators, illustrated in Figure 1.31 are generally used in multipass systems and arranged on two opposite walls of the cooling passage [9]. The channel aspect ratio, the rib configurations, and the Reynolds number of the coolant flow affect the heat transfer coefficient in the cooling passage [143].

### ➤ Impingement Cooling

The impingement cooling technique is generally applied on the leading edge where the heat load is the greatest and the mid-chord of the turbine blade [144] as illustrated in Figure 1.32a.

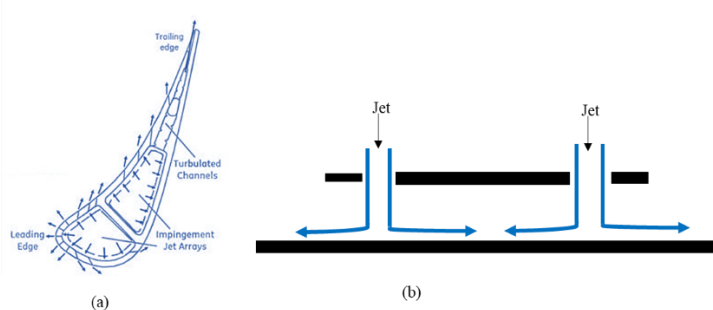


Figure 1.32: (a) Turbine inlet vane's typical use of impingement cooling [145], (b) Jet impingement model.

In jet impingement cooling, one or more jets of high-speed air encounter the wall to be cooled. The concept is simple; it consists of a plenum feeding a series of holes or nozzles, designed and optimally distributed, separated from the surface to be cooled [142], as seen in Figure 1.32b.

This solution is the most effective and allows reaching a high local heat transfer coefficient. The latter depends on the jet-hole size and distribution, the cooling channel cross-section, and the surface shape [146]. This cooling method is usually used for stator vanes [147].

### ➤ Pin Fin Cooling

The pin fin cooling method is generally applied at the trailing edge of the turbine blade [148]. It consists of introducing small cylinders called fins in a narrow channel, as seen in Figure 1.33a. The orientation of the fins is orthogonal to the flow to increase the turbulence, achieving a higher heat exchange coefficient.

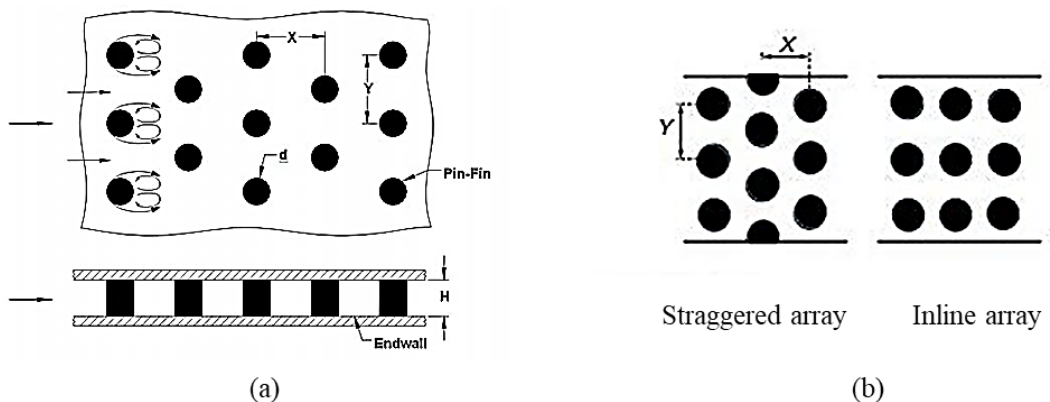


**Figure 1.33: (a) Pin fin cooling model [146], (b) Left : staggered array; right: inline array.**

In addition, the heat transfer coefficient is improved by using a series of pins either in an inline or staggered array as presented in Figure 1.33b [149]. In practice, the pins' diameter to height ratio ranges between 0.5 and 4 [142]. Numerous factors have a considerable impact on the heat transfer coefficient distribution including the spacing of the pins, the pin's size, and shape [150].

**Table 1.8: Overview of studies on different pin fin cooling configurations.**

Author	Parameter	Results
Chyu et al. [151]	Pin fin shape	Pin fin with a sharp edge has a higher Nusselt number
Jeng et Tzeng [152]	Inlines vs staggered array	Staggered array leads to a higher Nusselt number
Kirsch et al.[153]	Oblong vs cylindrical shape	Oblong fins have lowest Nusselt number
Axtmann et al. [154]	Fins spacing	Higher heat transfer for small spacing
Lyall et al. [155]		

Table 1.8 represents an overview of some studies that investigated geometrical parameters and the obtained results. It can be concluded that the heat transfer is more significant as the pin fin edge is sharper, and as the fin spacing is smaller. Additionally, a staggered array is more beneficial than an inline arrangement in terms of higher heat transfer, and higher Nusselt number.

### ➤ Dimple Cooling

Dimple cooling is another configuration to enhance the turbulence and the heat transfer coefficient of a smooth channel [156]. This configuration generates flow separation and reattachment with pairs of vortices [146]. The heat transfer in the dimpled channel is 2 to 2.5 times higher than in a smooth channel, with pressure losses of 2 to 4 times compared to the smooth channel [9]. Figure 1.34 represents a cooling passage with dimples.

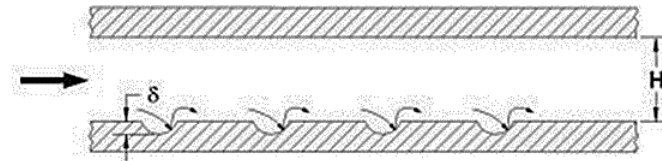


Figure 1.34: Dimple cooling [146].

Numerous parameters affect the heat transfer distribution including the number of dimples, the dimples' size, depth, distribution, and shape [157]. Vorayos et al. [158] developed a detailed study of heat transfer behavior on a flat plate with spherical dimpled surfaces.

### ➤ LatticeWork (Vortex Cooling)

Latticework cooling also known as vortex cooling is initially conducted from the Soviet design engineering system 25 years ago. As illustrated in Figure 1.35 the lower and upper halves of the cooling passage of a channel are formed with different sub-channels oriented at some angle  $\beta$ .

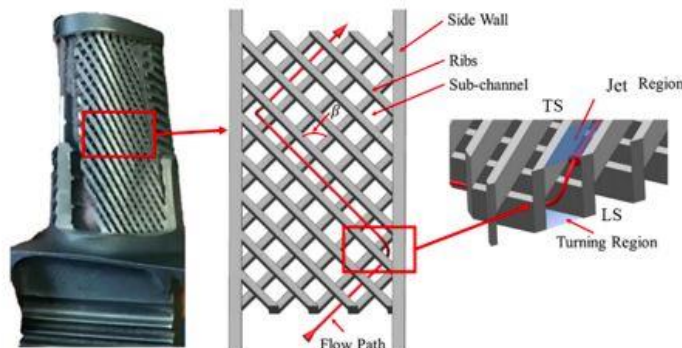


Figure 1.35: Latticework blade cooling method [159].

The flow enters the root of the turbine blade, passes through the sub-channels, and stays there until it reaches the wall. The flow then turns by an angle of  $2\beta$  and enters the crossing channel. It switches from a pressure side sub-channel to a suction side sub-channel or vice versa. The coolant flow exits the channel either by film cooling or by trailing edge holes [160].

The advantages of this technology are summarized by:

- Robust architecture
- Heat transfer enhancement compared to turbulated serpentines
- Similar pressure losses to turbulated serpentines
- Higher blade strength

#### 1.7.2.2 External Cooling

The second type of cooling technique is external cooling, consisting of injecting the coolant into the turbine blade surface using holes. On the surface blade of the turbine blade, coolant air forms a layer of protection. This section presents two main external cooling techniques including film cooling and transpiration cooling.

### ➤ **Film cooling**

Film cooling consists of the introduction of the coolant from the inside of the blade to the outside surface exposed to high temperatures through one or several holes [161]. Therefore, a thin layer is formed on the external wall of the surface, inducing a decrease in the wall temperature.

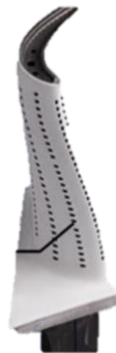


**Figure 1.36: Film cooling configuration [162].**

This cooling configuration is applied at different turbine locations such as the leading edge, the blade tip, the suction, and the pressure side [163].

Several flow properties and geometric parameters affect the efficiency of this cooling mechanism. These include fluid properties (density, mass velocities), the number of holes in the cooling chamber, pitch-to-diameter ratio, and hole orientation [164]. Liu et al. [165] conducted an experimental study to investigate the heat transfer on a turbine blade cooled with film cooling.

### ➤ **Transpiration Cooling**

Transpiration cooling is another form of external cooling that creates a thin film on the blades' surface. Unlike film cooling, this method involves injecting coolant onto a porous layer rather than through holes, as seen in Figure 1.37 [166]. The coolant film protects the turbine's external wall from the hot gas and reduces the heat flux conducted to the wall.

Transpiration cooling describes a path of complex geometry composed of numerous holes that correspond to the pores of the porous material. The coolant in the proposed configuration is assumed to constantly be in thermal equilibrium with the wall and, in particular, that the outlet temperature is equal to the external temperature of the wall. Moreover, because all pores are equally spaced across the external surface, the outlet jets combine and form a continuous layer [142]. Coolant air is conveyed with hot gas and constantly replaced by new coolant. This type of cooling is effective at high temperatures as it uniformly covers the entire blade with cool air [167].

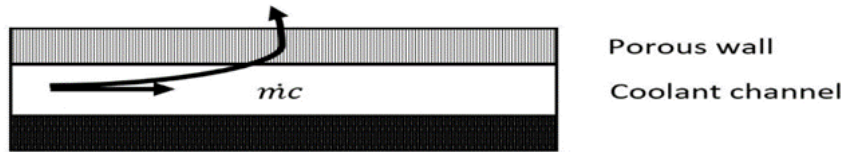


**Figure 1.37: Schematic presentation of transpiration cooling.**

### 1.7.2.3 Turbine Cooling Disadvantages

The main advantage of blade cooling is the possibility to increase the turbine inlet temperature with no limitations for the materials melting temperatures. However, some disadvantages of this technique are presented in [147] and summarized as follows:

- Reduction in turbine work due to bypassing a fraction of the coolant
- When mixing between the coolant flow and the mainstream flow occurs, the turbine work is lost due to the mixture's lower temperature
- The flow in the combustion chamber may be disturbed due to the mass extraction from the compressor
- Cooled blades cost higher than uncooled blades

### 1.7.2.4 Overview of Cooled Radial Turbines

Studies on radial turbine blade cooling are not limited to the thermodynamic performance of the cooled turbine but also the technological manufacturing aspect. Based on the surveyed studies, a large sample of the most relevant cooled radial turbine configurations is presented.

Roelke [168] provides a detailed review of NASA-sponsored research on cooled radial rotor technology and its applications between the 1970s and 1990s. As well, Lane [169] summarizes a series of US Army programs examining the design of radial turbines with internal cooling passages. The first designed air-cooled turbine was conducted by Pratt & Whitney Aircraft for Army application [170]. The radial turbine was designed for a stator-inlet of 1260 °C, in which both the rotor and stator were cast. However, the experimental results did not match the required design goals. Another cooled rotor was investigated in 1976 using Hot-Isostatic Pressure-bonding [171]. The rotor blades were cast as an integral piece. The cooling concept was obtained using a two-dimensional finite element model taking into consideration the generated stress and the heat transfer. The cooling technique consists of a fully convective design, and the coolant fraction is 3% of the mainstream. In addition, Garrett Airesearch [172] developed a laminated cooled radial turbine for Army purposes, operating at 2300 °F. This manufacturing process allows complex cooling configurations. The amount of cooling fraction needed is 5.85 %. The conducted tests were with positive results in terms of aerodynamic and mechanical aspects. This technique, however, did not impress many designers.

Other researchers suggested various methodologies to investigate the temperature and the heat transfer coefficient variation in internal cooling passages. Hamed et al. [173] developed a three-dimensional temperature distribution methodology for a cooled rotor of a radial inflow turbine using the finite element method. The prediction of the turbine's external temperature is based on empirical correlations for the heat transfer coefficients. This method showed good compatibility with other analytical methods and experimental measurements. Kumar and DeAnna [174] conducted a thermal and stress analysis for

cooled radial turbines. The modeling method consists of coupling a solid and a fluid solver. The procedure will be tested at the NASA Lewis Research Center. Furthermore, a new formulation of turbulent compressible flows was developed in [175] for problems with steady-state solutions. The developed model describes the flow within a coolant passage in a radial turbine blade. Several improvements were made in the numerical methodology to improve the convergence, accuracy, and robustness of the code. Additionally, an experimental study was conducted by [176] to measure the heat transfer within the internal cooling channel of a radial rotor blade. The tested model is a 1.15 times scale, manufactured with Lucite and tested using thermocouples and liquid crystals to indicate temperatures. A comparison between the heat transfer between the stationary and the rotating rotor is investigated. Results showed that the heat transfer characteristics within the coolant passage were affected by rotation; a reduction of 20% of the heat transfer occurs for the wheel without rotation.

Recently, Zhang et al. developed a two-part publication to design, simulate and test an internally cooled radial turbine. The first part [132] focuses on the optimization of the coolant channel geometry taking into consideration the mechanical stress constraints. The second part [133] focalizes on the advantage of using Selective Laser Melting Technology for manufacturing a cooled radial rotor. In addition, the cooled and uncooled wheels were tested experimentally using Thermal History Paint to measure the blade surface temperature. The authors concluded first that the CFD simulations allow a good prediction for the temperature distributions on the turbine blade.

Among all the presented cooling techniques, convection cooling is chosen for many reasons. Although other cooling techniques offer higher heat transfer, convection cooling in a smooth channel is a simple configuration, suitable for small-scale turbines, and does not present manufacturing complexity.

### 1.7.3. NOx Emissions

The term NOx describes the sum of NO and NO<sub>2</sub> contents but also can include different species such as (N<sub>2</sub>O, N<sub>2</sub>O<sub>4</sub>, and N<sub>2</sub>O<sub>5</sub>). The formation of NOx during combustion depends on the temperature range (type of flame), the stoichiometric ratio, and the nitrous species present in the combustion zone. NOx formation during combustion has two major sources: air nitrogen (thermal NOx and prompt NOx) and fuel nitrogen.

Thermal NOx describes the reaction between the nitrogen N<sub>2</sub> and the oxygen O<sub>2</sub> in the combustion air to produce NOx. This type of NOx emission depends mainly on the maximum temperature, the residence time, the turbulence, and the excess oxygen. The thermal NOx mechanism is best described by the ZELDOVICH mechanism of NO formation. However, Prompt NOx is created when radical hydrocarbons produced during the combustion of fuel rapidly react with the nitrogen in the combustion air to form transition compounds which are then oxidized to NOx when the oxygen in the combustion air reacts with them. This mechanism is related to low-temperature combustion processes. Last, Fuel nitrogen is the process where nitrogen in the fuel oxidizes with the oxygen in the combustion air to form NOx [177].

#### ➤ NOx Emissions in Gas Turbines

As seen in the section before, GTs are combustion systems composed mainly of a compressor, a combustion chamber, and a turbine. Thermal NOx formation accounts for the majority of NOx emissions in gas turbines [178].

Increasing the firing temperature in a GT machine has benefits in terms of maximizing the turbine efficiency, and therefore the maximum electrical output. However, operating under such conditions

increases the thermal NOx formation and affects the turbine material. In addition, NOx emissions and firing temperature depend on the type of fuel in the combustor, as seen in Figure 1.38. Fuel oil has a higher flame temperature and leads to higher NOx emissions than natural gas. For instance, for the same firing temperature of 1800 °F (982 °C), the concentration of NOx for fuel oil is approximately triple times the NOx emitted from natural gas.

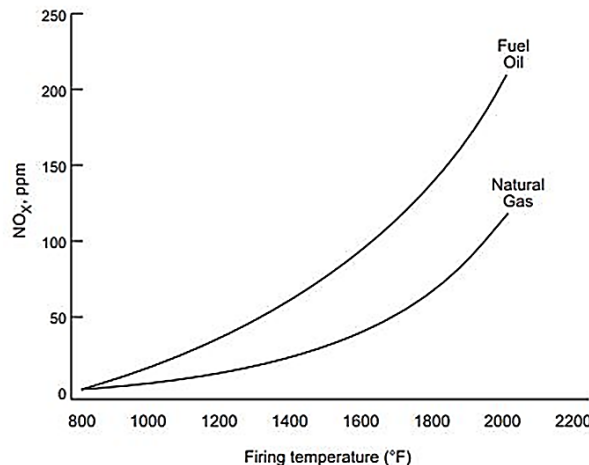


**Figure 1.38: Firing temperature effects on NOx emissions for natural gas and fuel oil [178].**

### ➤ Techniques to Remove NOx in Gas Turbines

There are five basic techniques for controlling NOx emissions from GTs: steam or water injection, Dry Low Emissions (DLE), catalytic combustion, Selective Catalytic Reduction (SCR), Selective NonCatalytic Reduction (SCNR), and SCONOX.

The first technique is steam or water injection, also named wet control, this technique consists of injecting water or steam into the combustion chamber to reduce the peak temperature. It can be used with other pre or post-combustion control techniques. The steam injection technique is more complicated and is not as effective as water injection [179]. The lowest concentration of NOx achieved with injection is 25 ppm for natural gas and 42 ppm for oil [180]. Although water injection has many benefits, it increases the production of CO and UHC [103]. Another NOx reduction technique is the Dry Low Emissions (DLE) in Figure 1.39b. It consists of reducing NOx emissions in the combustion chamber without adding water or steam. This technique includes lean combustion and staged combustion [178]. In a lean pre-mix combustor, the air and fuel are mixed well before entering the combustion chamber, limiting the overall temperature. On the other hand, staged combustion consists of reducing the residence time by adding several zones [178]. Catalytic combustion, Figure 1.39c, is also a NOx-eliminating technique that involves mixing air and fuel before passing them through a catalyst. During this reaction, the heat of combustion is released. Unlike conventional combustion chambers, catalyst combustion does not require a high equivalence ratio. Hence, NOx emissions are reduced [103].

In addition to the previous methods, three major post-combustion techniques are discussed. The SCR illustrated in Figure 1.39d, was first installed in Japan and was first implemented in the United States in the mid -the 1980s. This process consists of injecting ammonia into the gas turbine exhaust air that reacts with the NOx particles in the presence of a catalyst to give nitrogen and water [181]. This technique is

suitable for lower exhaust temperature systems. On the other hand, the SNCR process depicted in Figure 1.39a is very similar to SCR but operates without using a catalyst [182] and with higher temperatures (900-1100°C) [183]. Furthermore, the SCR removes a larger volume of NOx (90%) [184] compared to SNCR (30-60%) [185]. However, several concerns are associated with both processes regarding the storage, transport, and slipping of ammonia [186]. Lastly, the SCONox technique removes both CO and NOx from the exhaust air of the gas turbine. No ammonium is injected, but on the contrary, the catalyst is platinum and the removal reagent is potassium carbonate. The CO is oxidized to CO<sub>2</sub>, which then is exhausted from the stack. NO is oxidized to NO<sub>2</sub>, then reacts with the potassium carbonate to form potassium nitrites and nitrates on the surface of the catalyst [180]. The main disadvantages of this technique are the high cost compared to SCR, and the pressure drop that affects the GT efficiency. This process is used for system temperatures in the range of 230 °C and 370°C [186].

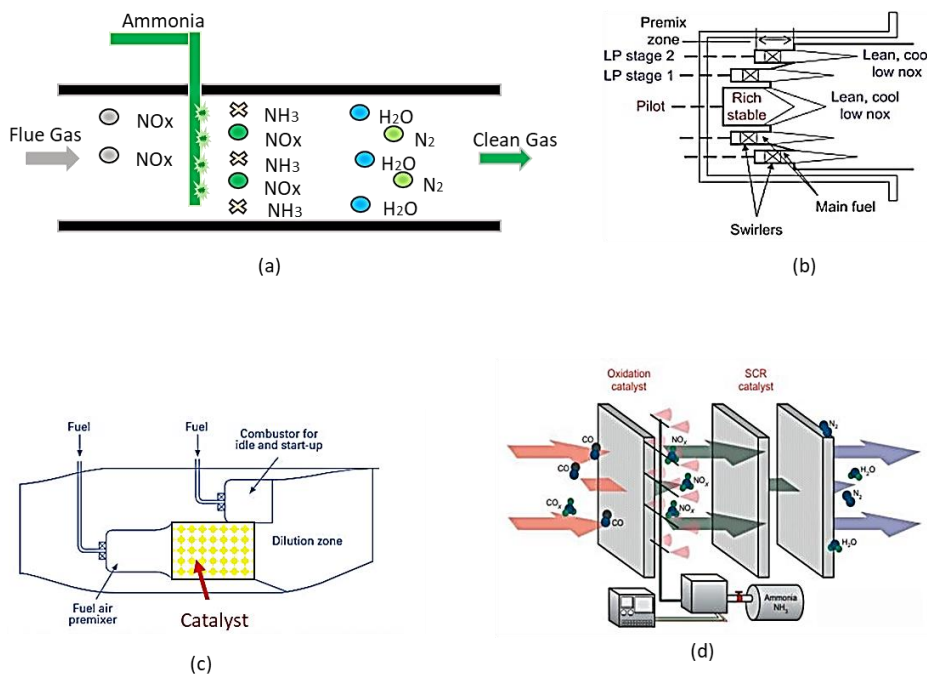


**Figure 1.39: (a) SCNR, (b) DLE, (c) Catalyst Combustor [88], (d) SCR [80].**

#### 1.7.4. 3D Printing Manufacturing Techniques for GT as a Range Extender

The development of new materials and the introduction of complicated techniques such as blade cooling urge the development of new methods to produce them. After the forging and the casting, 3D printing has replaced all conventional technologies [187].

3D printing is an additive manufacturing (AM) technique that consists of making an object from a three-dimensional (3D) model using a layer-over-layer manufacturing approach. Charles Hull was the first to develop a commercial rapid prototyping technology in 1986 [188]. In recent years, this technology is gaining rapid attention and development due to its numerous advantages. 3D manufacturing benefits include the possibility to manufacture complex geometries with high precision, customized material, and time-saving [189]. The lead time is estimated to be lower up to 90%, and the costs lower by 70%. Another benefit of 3D printing is that a wide variety of materials can be used, including metals, plastics, ceramics, and concrete.

AM has been widely used in different applications including biomedical, construction, automotive, and aerospace. In the medical field, 3D printing has been widely used for the production of medical model implants, crowns, bridges, and CT-imaged tissue replicas [190]. As well, 3D printing is beneficial for the construction industry in terms of increased customization, reduced construction time, and construction cost. As an example, in China cheap houses were built by WinSun in less than a day [191]. In addition, some automotive companies like Porshe, are using 3D printing to generate spare parts for their vehicles. An attempt was conducted by one Hong-kong-based car company, XEV, to develop a fully 3D printed vehicle [192]. Researchers in the aerospace industry are also attracted to 3D printing since it produces lightweight objects. SpaceX has tested a 3D printed engine, the SuperDraco, to power the Dragon spacecraft [193].

AM consists of five main methods, including Fused Deposition Modeling (FDM), Powder Bed Fusion, Stereolithography (SLA), Direct Energy Deposition (DED), and Laminated Object Manufacturing (LOM). These systems differ mainly in terms of the material used and the applications. Ngo et al. [189] proposed a detailed review of the different methods of AM, their applications, and their challenges. In addition, Wang et al. [194] conducted an overview of 3D printing techniques of polymer composite materials and the properties and performance of 3D printed composite parts as well as their potential applications in the fields of biomedical, electronics, and aerospace engineering. In addition, Frazier [195] investigates material science and business consideration to achieve the gains in performance related to the 3D printing process. Moreover, Hajare and Gajbhiye [196] discussed the difficulties and drawbacks of AM and the efforts made to ensure its evolution. Based on the prior studies, a summary is given of the main aspects of 3D techniques, including their benefits and drawbacks.

FDM is the most common process. The technique was commercially introduced by Stratasys Inc., USA, in the 1990s, and utilizes polymer filaments [197]. Heating is applied at the nozzle to ensure that the filaments melt into a semi-liquid state. Then, there are extruded layer by layer on the platform to obtain the desired part as shown in Figure 1.40a. This technique is a simple, low cost and high-speed method [194]. Although there are some advantages to using this method, there are also some limitations due to the low mechanical properties and poor surface quality of the objects printed [198].

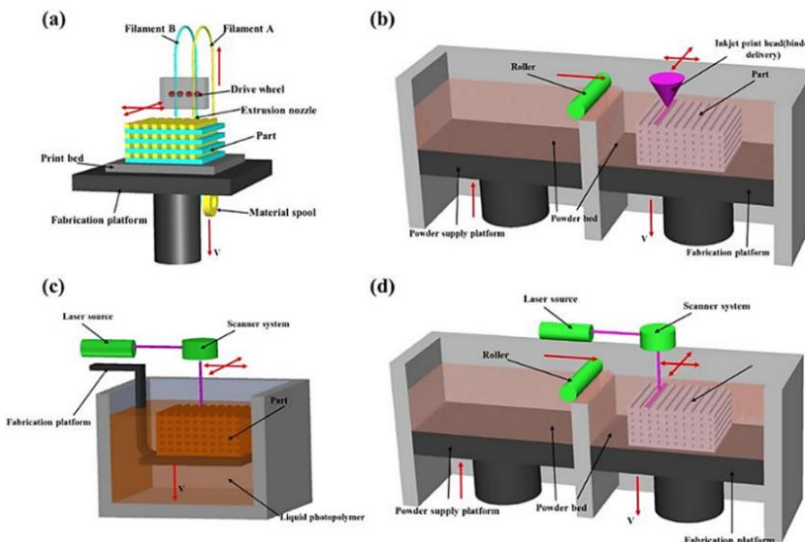


**Figure 1.40: Schematic representation of a typical (a) FDM setup (b) 3DP setup (c) SLA setup (d) SLS setup [194].**

Another method is powder bed fusion which consists of spreading powders on a platform. The powders in each layer are fused using either a laser (selective laser melting (SLM), selective laser sintering (SLS)) or a binder, as shown in Figure 1.40d. The former is only suitable for powders with low melting/sintering

temperatures [189]. The latter is Powder-liquid 3D (3DP) printing technology, illustrated in Figure 1.40b, which was developed at the Massachusetts Institute of Technology (MIT) in 1993 as a rapid-prototyping technology [199]. The main benefits of this technique are the large choice of material selection and its high quality. On the other hand, this technique is high cost and high porosity. SLA is the earliest method developed. It uses a UV laser in a controlled direction to react with a resin platform, leading to its polymerization, as shown in Figure 1.40c. This same method is repeated on every layer of uncured resin [188]. The key advantage of this technique is its high resolution and high quality. However, some disadvantages related to the high cost and toxicity of uncured resin are concerning. Another technique is DED, which goes by a variety of names, including Laser Engineering Net Shaping (LENS), Direct Metal Deposition (DMD), and Laser Metal Deposition (LMD). Metal powder is thrown through a nozzle mounted on a multiple-axis arm onto a surface heated with a laser or electron beam where it solidifies to form a new layer [200]. DED reduces time and cost and provides excellent mechanical properties. On the other hand, some limitations are present in printing complex geometries with fine details. The last method is LMO which consists of cutting and lamination or rolls of sheets by a layer-by-layer approach using a mechanical cutter or a laser. The benefits of LMO are the vast materials and the excellent manufacturing of large structures. Some concerns appear when manufacturing complex geometries [201].

### ➤ 3D Printing of Microturbines

Numerous studies have been conducted in the literature to develop microturbines using AM to take advantage of reduced manufacturing time and the possibility of developing complex small geometries. A review of major additive technologies and their microturbine applications is proposed.

Several efforts focused on developing microturbines for the organic Rankine cycle. Arifin et al. [202] investigated the feasibility of a radial rotor for a small-scale organic Rankine cycle. SLM is the chosen method with Aluminium Silicon Powder. The printed rotor is obtained within 5 hours. In addition, Rahbar et al. [203] proposed an effective and comprehensive methodology for developing a small-scale radial inflow turbine made entirely from the resin using the SLA technique. Hernández-Carrillo et al. [204], likewise, used the FDM technique to generate a radial turbine with a 1kW scale and a 49mm impeller diameter. Its goal is to evaluate the performance and structural reliability of thermoplastic impellers for use in low-temperature microturbines. Moreover, a customized microturbine generator kit of output power between 1 and 200 kW is proposed [205]. To reduce costs and speed up the design process, 3D printing was used to validate the nozzles and the rotors of the customized turbine.

3D printing is also used to generate air-cooled microturbines. Zhang, et al. [132] recently published a two-part study on designing, simulating, and testing an internally cooled radial microturbine. SLM was used to manufacture the designed wheel from nickel alloy Inconel 625. The turbine was built in a vertical direction, as shown in Figure 1.41. The shaft was generated directly, eliminating the need for welding. As part of the build process, an array of supports was added to ensure the internal geometry including the cooling channels was successfully constructed.

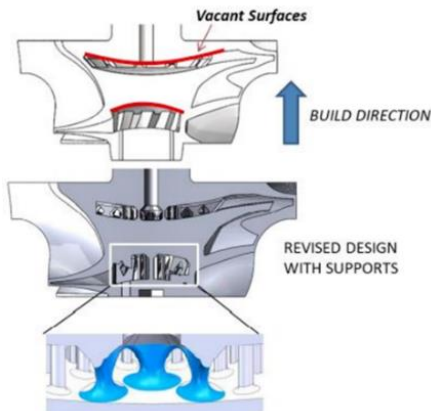


**Figure 1.41: Build direction and internal supporting structures introduced within hollow cooling passage [133].**

## 1.8. Conclusions

With the growing interest in fighting against global warming and carbon dioxide emissions, especially in the transport sector, researchers are looking to replace internal combustion engines with new powertrains. Gas Turbines are investigated as auxiliary power units to extend the autonomy of series hybrid electric vehicles. The gas turbines are connected to an alternator, and the mechanical energy is converted to electric energy to charge the battery of the electric car once depleted. The literature review can be summarized as follows :

- Gas turbines are potential energy converters to boost the autonomy of electric cars. They present many advantages compared to internal combustion engines as the reduced number of moving parts, low vibrations, and reduced emissions.
- Among different GT configurations, the IRReGT cycle is considered the best architecture in terms of higher efficiency and net specific work.
- The performance of a GT cycle is evaluated by its overall efficiency. The latter increases by choosing the optimal architecture, increasing the pressure ratio and increasing the TIT.
- A higher pressure ratio can be achieved by combining compressor stages with intercooling between them. The pressure ratio, however, has an optimal value above which efficiency will decrease.
- The development of new materials like Inconel and ceramics, as well as blade cooling techniques, are two main solutions proposed to overcome the material temperature limitations.
- The cooling technique is a convenient method to reach higher turbine inlet temperatures while using low-cost materials. Convection cooling is chosen over other cooling configurations for cooling turbine blades because of its simplicity.
- Although increasing TIT improves cycle efficiency, it also increases the NOx emissions. Hence, NOx pre and post-removing techniques are discussed.
- With the development of new materials and the complexity of turbine configurations, new manufacturing techniques are required. The design of a cooled compact radial turbine is therefore made possible using advanced manufacturing technologies, such as 3D printing.

Based on the literature, this thesis aims to conduct a detailed methodology to design a cooled radial turbine operating at high pressure, and high temperature to boost the autonomy of electric cars.

Therefore, this thesis carries out four studies divided into the two following chapters. As the design parameters of the radial turbine are affected by the GT cycle, Chapter 2 presents a thermodynamic

analysis and a technological study of different gas turbine configurations to determine the optimal operating conditions of the GT cycle, based on which the operating conditions of the radial turbine are determined. Then, Chapter 3 develops a detailed design tool of a cooled radial turbine from 1D preliminary analysis to 3D simulation, to manufacturing and testing.

In the next chapter, a detailed thermodynamic analysis determines the optimal operating conditions for the gas turbine cycle to maximize the net specific work and efficiency. A detailed thermodynamic analysis of the GT cycle with cooling techniques is also conducted. An assessment of the cooling blades' effects on both the turbine and the overall cycle efficiency is presented. Moreover, as the GT cycle is integrated into the vehicle, the range extender should be lightweight, compact, and with no technological complexity. The proposed system must be analyzed technologically to account for its weight and complexity.

# Chapitre 1 : Etat de l'Art

## 1.1. Introduction

En raison du réchauffement climatique causé par les émissions de CO<sub>2</sub> et de NOx du secteur des transports, d'importants efforts de recherche ont été investis pour trouver un substitut aux moteurs à combustion interne. Les turbines à gaz sont sélectionnées comme convertisseurs d'énergie potentiels pour les véhicules électriques hybrides en série. Les turbines à gaz constituent une solution prometteuse en raison de leur compacité, de leurs faibles émissions, de leur grande fiabilité et de leur capacité à fonctionner avec plusieurs carburants. Ce chapitre présente d'abord un état de l'art sur les différentes configurations de turbines à gaz, y compris plusieurs architectures de cycle et les propriétés des différents composants pour améliorer l'efficacité du cycle. L'effet d'un rapport de pression plus élevé, ainsi que d'une température d'entrée de turbine plus élevée, est évalué. Par conséquent, le développement de nouveaux matériaux de turbine et de techniques de refroidissement est étudié. Ensuite, l'impact de la température d'entrée de la turbine sur les émissions de NOx est analysé et les techniques d'élimination des NOx sont présentées. Enfin, la dernière partie du chapitre aborde les différentes technologies d'impression 3D et leurs avantages dans la production de géométries complexes.

## 1.2. Régularisation des Emissions de Gaz à Effet de Serre

En juillet 2009, les dirigeants de l'Union européenne (UE) et du G8 ont décidé de réduire les émissions de gaz à effet de serre de 80 % par rapport aux niveaux de 1990 d'ici 2050 [2]. Vingt-trois pour cent (23 %) des émissions de gaz à effet de serre dans l'UE proviennent du secteur des transports. Selon le conseil international pour un transport propre (ICCT), les véhicules légers et les camions sont responsables de 40 % des émissions du secteur des transports [3]. L'industrie automobile a réagi dans différents pays pour réduire les émissions de CO<sub>2</sub> des voitures particulières. La Figure 1.1 illustre la diminution des émissions de CO<sub>2</sub> dans le passé. Par exemple, les émissions de l'UE étaient de 120 g/km en 2015 et ont été réduites à 95 g/km en 2021.

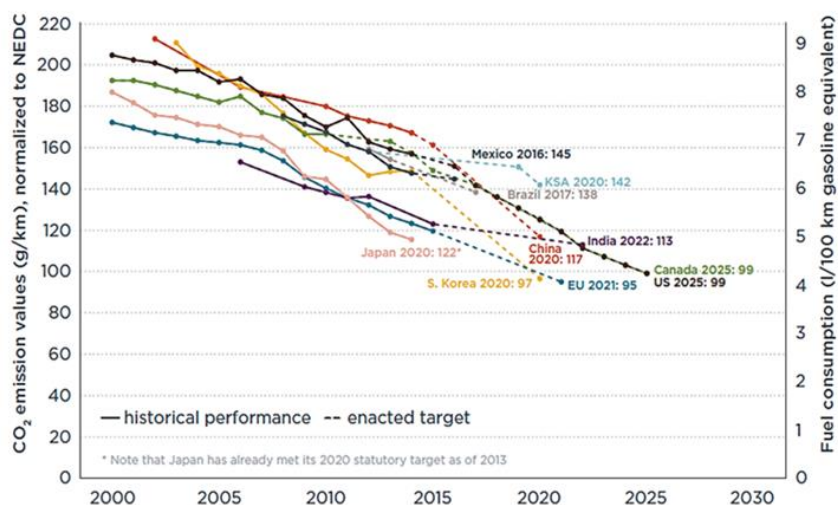


Figure 1.1. Performances historiques des émissions de CO<sub>2</sub> pour les voitures particulières [4].

En outre, la 26e conférence des parties (COP26), qui s'est tenue en novembre 2021, a souligné l'importance de la lutte contre le changement climatique. Les participants ont réaffirmé leur engagement à maintenir l'augmentation de la température moyenne mondiale bien en dessous de 2°C et à continuer

de la limiter à 1°C d'ici 2100 [5]. L'une des décisions prises a été de réduire la dépendance aux combustibles fossiles. Ainsi, plus de 30 pays et six grands constructeurs automobiles ont assuré leur intention de passer à des véhicules à émission zéro d'ici 2040 et d'accélérer la décarbonisation du transport routier. En conséquence, les autorités de différents pays encouragent les constructeurs automobiles à développer des véhicules électriques pour éviter les émissions de gaz à effet de serre. Bien que les véhicules électriques offrent de nombreux avantages en termes de réduction de la pollution, de simplicité, de fiabilité et d'accessibilité, ils présentent des défis importants [24]. Leur autonomie réduite est l'une des principales raisons qui limitent leur commercialisation. Par exemple, l'autonomie maximale de la Nissan Leaf n'est que de 346 km [25]. En outre, le temps de charge des batteries est considérablement élevé (4 à 8 heures), même en utilisant des chargeurs rapides (30 minutes) [26]. Enfin, la batterie est le composant le plus critique des véhicules électriques. C'est le composant le plus cher et le plus lourd. L'augmentation de l'autonomie des véhicules électriques implique une batterie plus grande et plus lourde. Par exemple, on estime que la batterie d'une voiture électrique pèse environ 200 kg, selon sa capacité [28]. Pour surmonter ces inconvénients, de nouvelles architectures de groupes motopropulseurs sont proposées.

### 1.3. Nouvelles Chaînes de Traction

De nombreux travaux ont porté sur le remplacement du moteur à combustion interne par de nouveaux convertisseurs d'énergie. Bou Nader [1] a étudié différents convertisseurs d'énergie pour identifier la meilleure architecture dans les applications automobiles. L'objectif est de choisir une configuration adaptée offrant des performances similaires à celles des véhicules conventionnels. Avec le développement des configurations hybrides en série, les études se sont concentrées sur la sélection des technologies de prolongation d'autonomie. Heron et Rinder [29] ont évalué le potentiel de différentes technologies de prolongation d'autonomie et ont présenté une comparaison entre elles. Tran et al. [30] ont élaboré un bilan complet des différents types de technologies de prolongation de l'autonomie des EV, en soulignant les différents avantages et inconvénients. Parmi les différentes chaînes de traction, les turbines à gaz (GT) ont été choisies sur la base de critères technologiques qualitatifs et quantitatifs, surtout dans les véhicules électriques hybrides en série (SHEV).

Les systèmes de turbines à gaz (GT) offrent de nombreux avantages lorsqu'ils sont utilisés dans les SHEV par rapport aux autres groupes motopropulseurs. Premièrement, les GTs ont un nombre réduit de pièces mobiles, ce qui réduit les vibrations et les coûts de maintenance. De plus, les systèmes GTs émettent moins de bruit que les moteurs à combustion interne, estimés à environ 5dB de moins [61]. En outre, les avantages des GTs incluent leur capacité multicarburant (gaz naturel, biogaz, kéroène, diesel, propane...) et leurs faibles émissions de CO et de NOx par rapport aux moteurs à combustion interne [36]. L'un des principaux avantages de leur utilisation dans les SHEV est la possibilité de fonctionner à leur charge optimale en recherchant une efficacité élevée, car le système GT est découpé de la charge du véhicule [62].

### 1.4. Turbine à Gaz dans les Véhicules Electriques Hybrides en Série

Des études récentes se sont concentrées sur l'utilisation des GTs comme unités de puissance auxiliaires et donc comme solution à l'autonomie limitée et au coût élevé des voitures électriques. Les GTs sont combinées avec un générateur, de sorte que le travail mécanique de la turbine est converti en énergie électrique [63]. La Figure 1.2 illustre la configuration proposée. Cette configuration est une solution à la fois aux émissions environnementales des moteurs à combustion interne et à l'autonomie limitée des voitures électriques. Son principal avantage est que le cycle GT fonctionne indépendamment de la

vitesse du véhicule. Ainsi, le point de fonctionnement optimal de la GT est facilement contrôlable pour obtenir la meilleure efficacité du cycle GT.

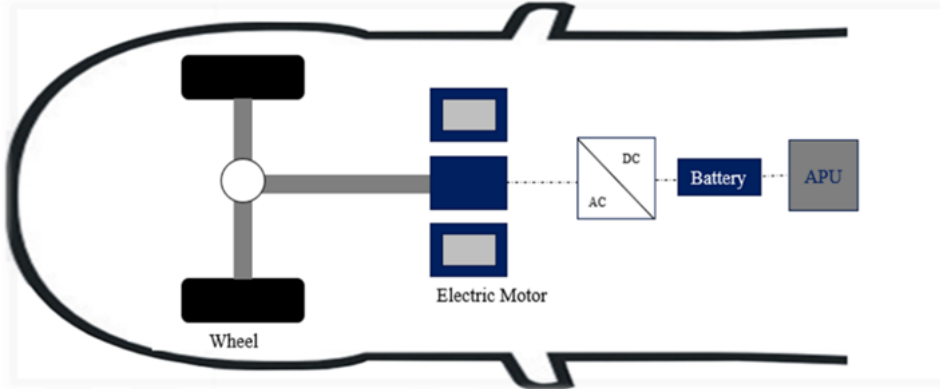


**Figure 1.2: Turbine à gaz comme unité de puissance auxiliaire dans les véhicules électriques hybrides en série.**

Le nouveau système de propulsion est conçu pour garantir la même puissance et les mêmes performances qu'un moteur à combustion interne. De nombreuses études ont évalué la puissance requise du cycle de turbine à gaz [75].

Sur la base des études recensées, la puissance considérée dans cette thèse est de 20 kW. Cette puissance prend en compte le poids du véhicule estimé à 1210 kg, la masse de la batterie (259 kg) et la vitesse du véhicule (90,30,160 km/h) sur différentes pentes (10 %, 5 %) [1].

## 1.5. Configurations des Cycles de Turbine à Gaz

Les turbine à gaz sont des machines thermodynamiques capables de convertir l'énergie thermique du fluide de travail en énergie mécanique utile sur l'axe de la turbine. Cette énergie mécanique peut être utilisée directement ou convertie en énergie électrique en ajoutant un générateur électrique. Un cycle simple de turbine à gaz fonctionne selon le cycle de Brayton.

### 1.5.1. Configurations Prometteuses

Le cycle de Brayton est composé d'un compresseur, d'une chambre de combustion et d'une turbine, comme le montre la Figure 1.3.

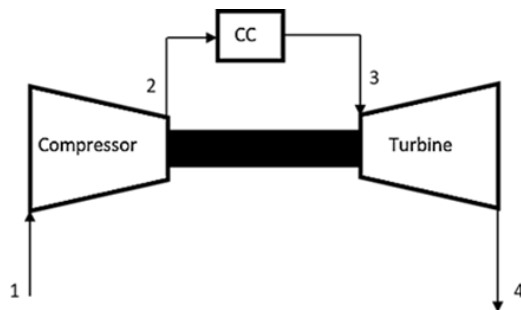


**Figure 1.3: GT Brayton cycle.**

Pour augmenter l'efficacité du système, la chaleur des gaz d'échappement est récupérée à l'aide d'un récupérateur air-air. Ce dernier préchauffe l'air à la sortie du compresseur en utilisant les gaz

d'échappement chauds pour réduire la consommation de carburant dans la chambre de combustion. L'ajout d'un récupérateur peut conduire à une augmentation de l'efficacité du cycle de 17 % à 30 % [80].

L'augmentation du travail net du cycle GT peut être obtenue soit en diminuant le travail du compresseur, soit en augmentant le travail de la turbine. L'ajout d'un refroidisseur intermédiaire entre les étages du compresseur réduit le volume d'air comprimé, et donc le travail du compresseur ce qui permet de réduire la consommation d'énergie. Le réchauffage consiste à diviser la turbine en plusieurs étages et à ajouter des chambres de combustion entre eux. Cette configuration conduit à une augmentation du travail spécifique net du cycle et de la température de sortie de la turbine. Cette dernière améliore le potentiel de régénération [81].

### **1.5.2. Types d'Entrainement Mécanique**

L'entraînement mécanique se divise en trois grandes catégories. La première catégorie comprend le compresseur et la turbine montés sur le même arbre et l'alternateur soit du côté du compresseur, soit du côté de la turbine. Cette configuration est pratique lorsque la turbine à gaz doit fonctionner à une vitesse constante [82]. Dans le cas d'une turbine à double arbre, une turbine à gaz n'entraîne que le compresseur et une autre turbine est connectée au système entraîné. Le principal avantage de cette configuration est la flexibilité et la possibilité de fonctionner à des vitesses variables. Une autre configuration est une séparation mécanique des étages de compresseurs. Chaque compresseur est entraîné par sa turbine à des vitesses de rotation différentes [85]. Cette configuration est généralement exploitée dans les systèmes de grande puissance.

### **1.5.3. Configuration Convenable de GT**

Après avoir expliqué les principales architectures d'un cycle GT, la section suivante présente une synthèse des études les plus pertinentes de la littérature sur les différentes configurations du cycle GT pour prolonger l'autonomie des véhicules électriques. Sur la base des études recensées, un large échantillon des configurations les plus intéressantes a été choisi pour identifier l'architecture sélectionnée, les conditions de fonctionnement ainsi que le rendement. Certaines études ont investigué le cycle GT avec récupérateur. D'autres recherches ont abordé différentes configurations de GT, notamment les cycles de GT avec une combustion externe [86], le cycle combiné (cycle GT avec cycle de Rankine) [87] et le cycle IRReGT. Ce dernier se compose de deux étages de compression avec refroidissement intermédiaire et deux étages de détente avec réchauffement intermédiaire et un récupérateur. Parmi les configurations examinées, le cycle IRReGT combine à la fois la configuration la plus simple et le rendement le plus élevé. Par conséquent, il est considéré comme le cycle de base dans la suite de l'étude.

## **1.6. Propriétés des Principaux Composants des Turbines à Gaz**

Cette partie est consacrée aux caractéristiques des différentes composantes du cycle IRReGT, illustré dans la Figure 1.4. La sélection du composant convenable est basée sur l'état de l'art des différentes technologies et contraintes.

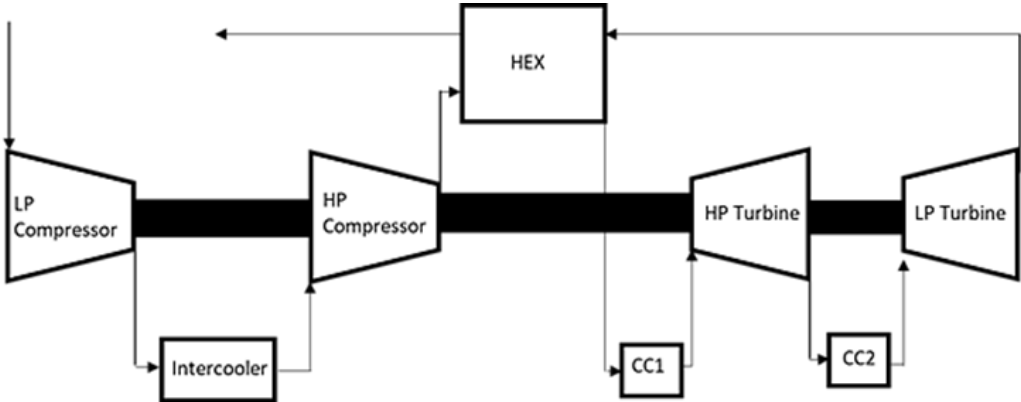


Figure 1.4: IRReGT cycle.

### 1.6.1. Compresseurs

Les turbines à gaz s'appuient sur des compresseurs pour comprimer l'air avant son entrée dans la chambre de combustion, où il est mélangé au combustible. Il existe deux types de compresseurs : les compresseurs axiaux et les compresseurs centrifuges [88]. Les compresseurs axiaux sont généralement utilisés pour des débits élevés et des rapports de pression de 1.4 à 1.5 [90]. Des rapports de pression plus élevés peuvent être obtenus en utilisant des compresseurs multi-étages [89]. Ceux-ci sont conçus pour entraîner des turbines industrielles lourdes. Les compresseurs centrifuges, quant à eux, sont utilisés pour des conditions de faible débit et des rapports de pression plus élevés entre 1.5 et 5 [90]. Ils sont adaptés aux petits turbocompresseurs compacts surtout dans les véhicules.

### 1.6.2. Récupérateur

Le récupérateur est un échangeur de chaleur compact conçu pour récupérer la chaleur des gaz d'échappement en préchauffant l'air avant son entrée dans la chambre de combustion. Les HEX sont divisés en trois catégories en fonction de leur géométrie de transfert de chaleur. Le matériau du récupérateur est un autre paramètre important à prendre en considération, car le fonctionnement à haute température peut entraîner la corrosion et l'érosion du matériau utilisé. Un récupérateur approprié pour la microturbine devrait avoir les propriétés suivantes : efficacité élevée du transfert de chaleur (> 90%), faible perte de pression relative (< 3%), compacité et faible coût [92].

Des études récentes portent sur de nouveaux matériaux, notamment les alliages de nickel tels que l'Inconel 625 et 718 [132], et les céramiques [113], en raison de leurs propriétés mécaniques et de leur résistance élevée à la corrosion à haute température. Cependant, la complexité de leur fabrication et leur coût élevé limitent leur utilisation et nécessitent davantage de développement.

### 1.6.3. Chambre de Combustion

La chambre de combustion d'une turbine à gaz est l'endroit où l'énergie qui fait fonctionner l'ensemble du système est ajoutée. Les principaux paramètres de la chambre de combustion sont la perte de charge (idéalement égale à zéro), le rendement de la chambre de combustion (qui dépend du rapport de mélange, de la durée de combustion, de la vaporisation), la température de sortie (liée aux contraintes des matériaux de la turbine) et la stabilité de la flamme. Des émissions de NOx, du CO<sub>2</sub> et du H<sub>2</sub>O sont libérées lors de la combustion. C'est pourquoi de nouvelles réglementations sont présentées pour réduire les émissions de NOx. La quantité de ces émissions dépend de la température, de la durée et de la concentration dans la chambre de combustion.

La chambre de combustion sans flamme décrit le processus dans lequel il n'y a pas de front de flamme. Les gaz d'échappement sont recirculés et mélangés à l'air, puis préchauffés avant le phénomène de

combustion. Ainsi, il n'y a pas de pics de température et les émissions de NOx sont réduites. Les avantages de la combustion sans flamme par rapport aux chambres de combustion traditionnelles sont notamment un faible niveau de bruit dû à l'oscillation à basse pression, une faible consommation d'énergie liée à un rendement élevé et de faibles émissions de NOx [104].

#### 1.6.4. Turbine

Comme pour le compresseur, il existe deux catégories de turbines : les turbines axiales et les turbines radiales. La principale différence entre les turbines radiales et axiales est la direction du fluide. Les turbines axiales sont utilisées pour des débits élevés et des rapports de pression faibles [111]. Les turbines axiales sont utilisées dans les centrales électriques et les applications industrielles, tandis que les turbines radiales sont utilisées dans les turbocompresseurs et les prolongateurs d'autonomie en raison de leur compacité et de leur faible coût. Le rendement du cycle GT est lié à la température d'entrée de la turbine (TIT), une TIT plus élevée entraîne un meilleur rendement de la turbine. Cependant, la TIT est limitée par les températures de fusion des matériaux de fabrication. Par conséquent, le développement de nouveaux matériaux et de nouvelles technologies de refroidissement des aubes sont proposés pour atteindre des températures plus élevées [113].

### 1.7. Méthodes Pour Augmenter le Rendement des GTs

La performance d'un cycle GT est évaluée en fonction de sa puissance et de son rendement thermique. Les améliorations du rendement des turbines à gaz sont le résultat d'une combinaison d'efforts thermodynamiques et technologiques [125] :

- Choix de la configuration optimale du cycle de la turbine à gaz
- Augmentation de la pression maximale
- Augmentation de la température d'entrée de la turbine

De nombreux chercheurs ont évalué différentes configurations pour le cycle de la turbine à gaz afin d'améliorer les performances du cycle. Le réchauffage [128], la récupération [206] et le refroidissement intermédiaire ont été étudiés [207]. L'ajout d'un récupérateur entraîne une réduction de la consommation de carburant [126]. De même, le refroidissement de l'air comprimé aux étages du compresseur réduit la quantité de travail de compression et permet d'augmenter le taux de compression [125]. Le réchauffage entre les étages de la turbine augmente le travail de sortie de la turbine [127]. Tous ces effets se traduisent par un rendement total plus élevé. D'après les études présentées en détail dans la Section 0, le cycle IRReGT est l'architecture optimale du cycle GT. Il combine un récupérateur, avec un refroidissement intermédiaire entre les étages du compresseur et un réchauffage entre les étages de la turbine.

D'après l'étude menée par Ji et al. [62], la performance du cycle GT est étroitement liée à l'efficacité du récupérateur, au rapport de pression et au TIT. Par exemple, l'efficacité thermique du cycle GT est significativement affectée par l'efficacité du récupérateur. Plus l'efficacité du récupérateur est élevée, plus l'efficacité thermique est élevée. Nada [128] a confirmé que le rendement du cycle augmente avec le rapport de pression du compresseur et la température d'entrée de la turbine. À une température donnée, des rapports de pression plus élevés entraînent un meilleur rendement. En outre, l'augmentation du rapport de pression permet d'augmenter la densité de puissance et de réduire le débit massique. Le système sera donc plus petit et plus compact, ce qui réduira la pollution sonore. Une méthode pour augmenter le rapport de pression est obtenue en ajoutant un refroidisseur intermédiaire entre les étages du compresseur [125]. Cependant si le rapport de pression est augmenté au-delà d'une certaine valeur, le rendement global diminue. Dans ce cas, la puissance utile nette de la turbine à gaz diminue en raison de l'augmentation de la puissance nécessaire au fonctionnement du compresseur. Une autre technique

intéressante pour améliorer l'efficacité du cycle est l'augmentation du TIT [88]. Par exemple, une augmentation de l'efficacité de 12 % est obtenue à partir de la configuration GT lorsque le TIT augmente de 950 °C à 1100 °C. L'efficacité augmente d'environ 20 % lorsque la température à l'entrée de la turbine passe de 950 °C à 1250 °C pour la même configuration de système [1]. Cependant, la TIT est limitée par les températures de fusion des matériaux de la turbine, ainsi que par la fatigue et les contraintes des matériaux. Tant que la température ne dépasse pas 1100 °C, il n'est pas nécessaire d'utiliser des matériaux spéciaux et la turbine peut être fabriquée à l'aide d'alliages courants et peu coûteux [87]. Par conséquent, la limite de la TIT peut être repoussée de deux façons : soit en développant des matériaux qui peuvent résister à des températures plus élevées, soit en refroidissant les aubes de la turbine [91]. Ces deux techniques nécessitent de nouvelles technologies pour développer des turbines refroidies complexes et compactes, comme l'impression 3D [129]. En raison de l'augmentation de la TIT, les émissions de NOx constituent un autre défi qui doit également être abordé, de sorte que les méthodes de réduction des émissions de NOx doivent également être discutées.

### 1.7.1. Matériaux de Turbine

L'efficacité du cycle GT est liée au matériau et au TIT des aubes de turbine. Par conséquent, les matériaux des aubes de turbine doivent avoir des températures de fusion plus élevées, une bonne résistance à l'oxydation/corrosion et une résistance à haute température [130]. En outre, les turbines sont soumises à une vitesse de rotation élevée, ce qui entraîne d'énormes forces centrifuges sur leurs pâles. Ces forces se manifestent par une rupture par fluage et une défaillance par fatigue. En outre, les aubes de turbine sont exposées à de fortes vibrations et à des résonances qui peuvent causer leurs détériorations [80]. Le développement de nouveaux matériaux pour les turbines est donc intéressant comme le Ceramic et l'Inconel 718 [141].

### 1.7.2. Méthodes de Refroidissement des Aubes de Turbine

Le mode le plus simple de refroidissement des aubes de turbine consiste à prélever de l'air du compresseur ou du dernier étage de la turbine et à l'introduire depuis le pied de l'aube jusqu'aux orifices de la turbine [80]. Il existe deux techniques de refroidissement : le refroidissement interne et le refroidissement externe. La première consiste à faire circuler de l'air comprimé à l'intérieur du canal de l'aube de la turbine. Le transfert de chaleur se produit entre l'aube de la turbine et l'air de refroidissement. La seconde consiste à injecter l'air de refroidissement par des trous sur la surface de l'aube de la turbine. L'air de refroidissement forme une couche entre la surface de la turbine et le gaz chaud. Bien que le refroidissement de l'aube de la turbine par l'introduction d'air de refroidissement entraîne une diminution du rendement de la turbine, il améliore les performances globales du cycle en raison des températures d'entrée plus élevées. Ces dernières permettent généralement de surmonter la perte par le flux de refroidissement et d'améliorer le rendement du cycle.

### 1.7.3. Inconvénients du Refroidissement des Aubes

Le principal avantage du refroidissement des aubes est la possibilité d'augmenter la température d'entrée de la turbine sans aucune limitation des températures de fusion des matériaux. Cependant, certains inconvénients de cette technique sont présentés dans [147] et résumés comme suit :

- Réduction du travail de la turbine en raison d'une fraction du fluide de refroidissement.
- Lorsque le mélange entre le flux de refroidissement et le flux principal se produit, le travail de la turbine est perdu en raison de la température plus basse du mélange.
- L'écoulement dans la chambre de combustion peut être perturbé en raison de l'extraction du fluide de refroidissement du compresseur.

- Les aubes refroidies coûtent plus cher que les aubes non refroidies.

#### 1.7.4. Emissions de NOx

La formation de NOx pendant la combustion dépend de la tranche de température (type de flamme), du rapport stœchiométrique et des espèces présentes dans la zone de combustion. La formation de NOx pendant la combustion a deux sources principales : l'azote de l'air (NOx thermique et NOx prompt) et l'azote du combustible.

Il existe cinq techniques de base pour contrôler les émissions de NOx des GT : l'injection de vapeur ou d'eau, le procédé Dry Low Emissions (DLE), la combustion catalytique, la réduction catalytique sélective (SCR), la réduction non catalytique sélective (SCNR) et le SCONOx, présentés dans la Figure 1.5.

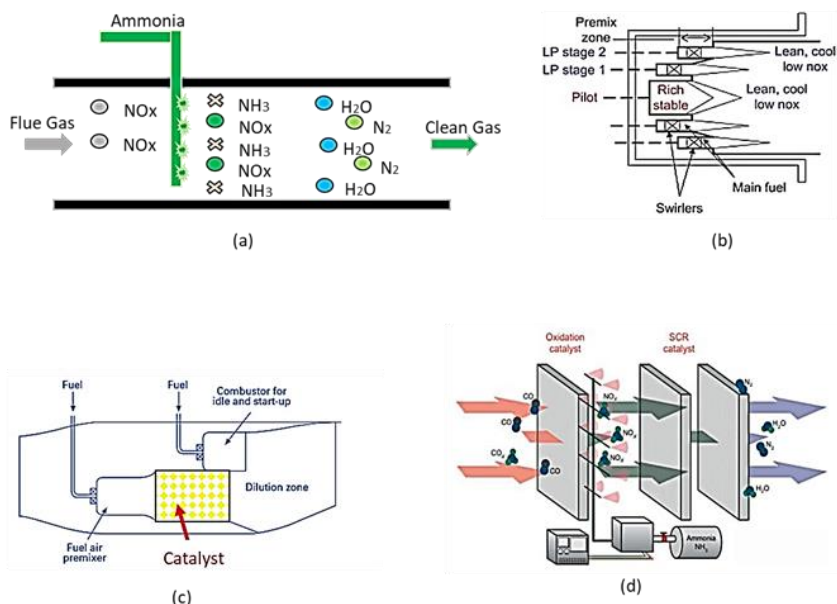


Figure 1.5: (a) SCNR, (b) DLE, (c) Catalyst Combustor [17], (d) SCR [80].

#### 1.7.5. Impression 3D

Le développement de nouveaux matériaux et l'introduction de techniques compliquées comme le refroidissement des aubes des turbines obligent à développer de nouvelles méthodes pour les produire. L'impression 3D est une technique de fabrication additive (AM) qui consiste à fabriquer un objet à partir d'un modèle tridimensionnel en utilisant une approche de fabrication couche par couche. Cette technologie est largement utilisée dans différentes applications, notamment dans les domaines biomédical, de construction, de l'automobile et de l'aérospatiale. La fabrication additive comprend cinq méthodes principales, y compris le modèle de dépôt par fusion (FDM), la fusion sur lit de poudre, la stéréolithographie (SLA), le dépôt par énergie directe (DED) et la fabrication d'objets stratifiés (LOM), présentés dans la Figure 1.6. Ces systèmes se distinguent principalement par le matériau utilisé et les applications.

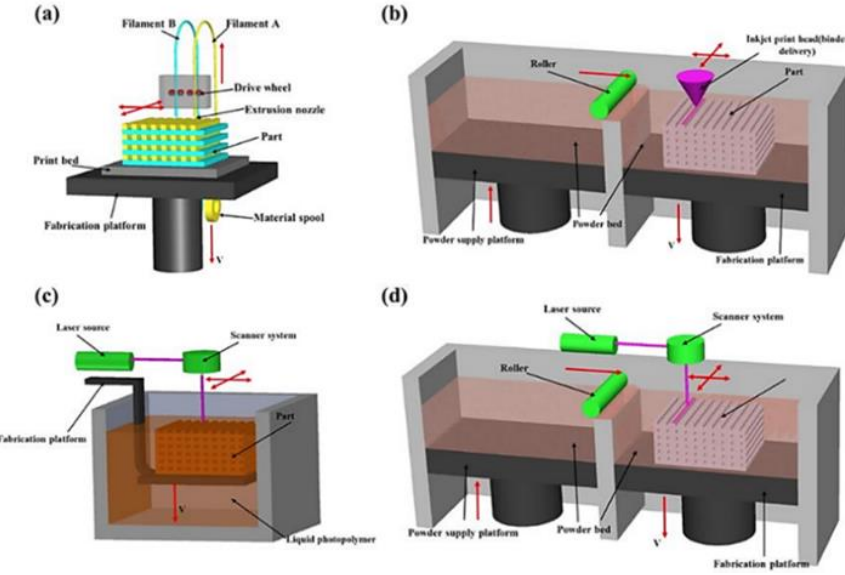


Figure 1.6: Schematic representation of a typical (a) FDM setup (b) 3DP setup (c) SLA setup (d) SLS setup [194].

## 1.8. Conclusions

Avec l'intérêt croissant pour la lutte contre le réchauffement climatique et les émissions de dioxyde de carbone, notamment dans le secteur de transports, les chercheurs cherchent à remplacer les moteurs à combustion interne par de nouvelles chaînes de traction. Les turbines à gaz sont étudiées comme unités de puissance auxiliaire pour prolonger l'autonomie des véhicules électriques hybrides en série. Les turbines à gaz sont connectées à un alternateur, et l'énergie mécanique est convertie en énergie électrique pour charger la batterie de la voiture électrique une fois épuisée. La littérature existante peut être résumée comme suit :

- Les turbines à gaz sont des convertisseurs d'énergie potentiels pour augmenter l'autonomie des voitures électriques. Elles présentent de nombreux avantages par rapport aux moteurs à combustion interne, comme le nombre réduit de pièces mobiles, les faibles vibrations et les émissions réduites.
- Parmi les différentes configurations de GT, le cycle IRReGT est considéré comme l'architecture de base pour le reste de l'étude en termes de rendement plus élevé et de travail spécifique net.
- La performance d'un cycle GT est évaluée par son efficacité globale. Ce dernier augmente en choisissant l'architecture optimale, en augmentant le rapport de pression, et en augmentant la TIT.
- Un rapport de pression plus élevé peut être obtenu en combinant des étages de compresseur avec un refroidissement intermédiaire entre eux. Le rapport de pression a toutefois une valeur optimale au-delà de laquelle le rendement diminue.
- Il existe une limite à la TIT imposée par les propriétés des matériaux. Le développement de nouveaux matériaux comme l'Inconel et les céramiques, ainsi que les techniques de refroidissement des pales, sont deux solutions principales proposées pour surmonter les limites de température des matériaux. Le refroidissement par convection est préféré aux autres configurations de refroidissement des aubes de turbine en raison de sa simplicité.
- Bien que l'augmentation de la TIT améliore l'efficacité du cycle, elle augmente également les émissions de NOx. Par conséquent, les techniques de pré- et post-élimination des NOx sont discutées.

- Avec le développement de nouveaux matériaux et la complexité des configurations de turbine, de nouvelles techniques de fabrication sont nécessaires. La conception d'une turbine radiale compacte refroidie est donc rendue possible par l'utilisation de technologies de fabrication avancées, telles que l'impression 3D.

En se basant sur la littérature, cette thèse a pour objectif de mener une méthodologie détaillée pour concevoir une turbine radiale refroidie pour le cycle IRReGT fonctionnant à haute pression, et à haute température pour booster l'autonomie des voitures électriques.

Dans le chapitre suivant, une analyse thermodynamique détaillée détermine les conditions de fonctionnement optimales pour le cycle actuel afin de maximiser le travail spécifique net et le rendement. Une analyse thermodynamique détaillée du cycle GT avec des techniques de refroidissement est également réalisée. Une évaluation des effets des aubes de refroidissement sur la turbine et l'efficacité globale du cycle est exposée. De plus, comme le cycle GT est intégré au véhicule, le prolongateur d'autonomie doit être léger, compact et sans complexité technologique. Le système proposé doit faire l'objet d'une analyse technologique pour tenir compte de son poids et de sa complexité technologique.

# **Chapter 2 : Thermodynamic and Technological Study of an Intercooled Recuperated Reheated Gas Turbine Cycle with Cooling Turbine Blade Configurations**

## **2.1. Introduction**

GT systems are potential energy converters for future vehicle powertrains. Compared to other energy converters, these systems offer inherent benefits to vehicles, such as high efficiency, multifuel capability, cogeneration capability, low vibration and noise, and a reduction in the number of components, and weight.

GTs are mainly popular in series hybrid electric vehicles (SHEV), where a fully electric drive is provided with an adequate battery capacity sizing leading to reduced direct emissions. In these powertrains, the electric motor provides the mechanical driving power, while the GT decoupled from the vehicle load, can operate at maximum efficiency.

Based on these findings, this chapter presents a methodology for the identification of the optimal GT cycle for SHEV powertrains in terms of higher efficiency and suitable technical aspects. Thus, the study starts with a parametric assessment to choose the optimal configuration of the GT cycle and the corresponding optimal operating conditions in terms of efficiency and specific output work. Then, the exergetic study identified the combustion chamber as the primary source of exergy destruction. As a result, increasing TIT is being investigated to benefit from increased GT efficiency. As TIT is limited by material constraints, turbine blade cooling is explored. Therefore, the second part of this chapter consists of thermodynamic analysis of the range extenders with cooled turbine blade configurations.

Finally, as the range extender is integrated into the vehicle, the GT system should be highly efficient, compact, lightweight, and technically realizable. As a result, a technological study is realized to estimate the system weight and complexity for different GT configurations.

## **2.2. Optimal GT Cycle and Optimal Operating Conditions**

This section presents the methodology applied to identify the most suitable gas turbine cycle in terms of efficiency and net specific work. The study includes an analysis to determine the optimal operating conditions at different stages of the cycle. The thermodynamic analysis is developed using Visual Basic for Applications (VBA) and NIST REFPROP (National Institute of Standards and Technology (NIST), Colorado, USA).

Various technological constraints for automotive components are based on state-of-the-art data of available and newly developed technologies. These technical constraints include the maximum TIT, the maximum compression ratio per stage, and the maximum component efficiency. The design constraints of cars include, however, the number of compression and expansion stages, and the number of heat exchangers, all of which simplify the system integration complexity. The initially considered cycle is the recuperated GT cycle.

### **2.2.1. Methodology**

The considered cycle is the recuperated gas turbine cycle represented in Figure 2.1. The first law of thermodynamics is applied to calculate the compressor and the turbine work, neglecting the heat transfer with the surroundings and the variation of kinetic and potential energy at the inlet and outlet of each

component. The air is considered as the working fluid. The isentropic efficiency of the compressor, and the turbine, and the recuperator effectiveness are considered constant and equal to 0.8, 0.85, 0.8, respectively, based on Chrysler gas turbine vehicles [36] and Bou Nader [1]. The thermodynamic analysis takes into consideration the air/fuel ratio in the combustion chamber. The reaction is lean mixture combustion between air and the fuel, the latter is methane. When the compressor stages are increased, an intercooler is added to cool the compressed air before it enters the next compressor stage. The intercooler is subjected to ambient conditions, and due to pinch, the temperature at its outlet is assumed 35 °C.

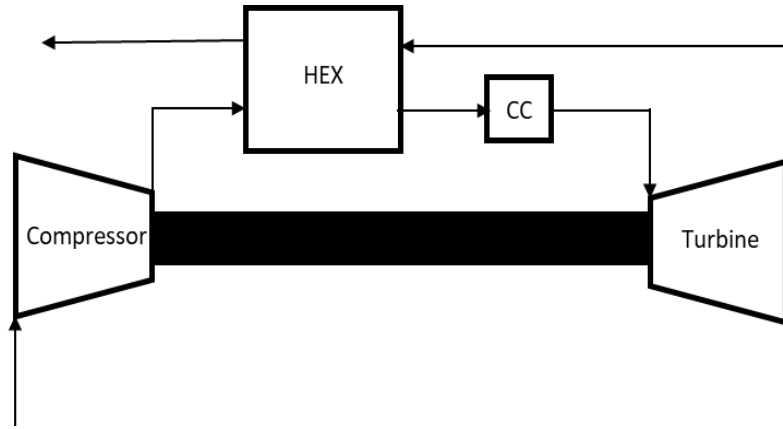
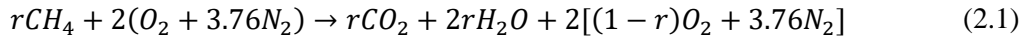


**Figure 2.1: Recuperated gas turbine cycle.**

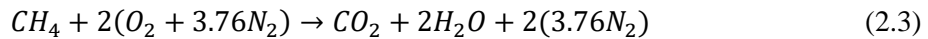
The combustion of the methane is presented in Equation (2.1):



$r$  is the ratio between the real fraction of fuel mass flow ( $m_f$ ) to air mass flow ( $m_a$ ) to the stoichiometric fraction calculated as shown in Equation (2.2):

$$r = \frac{\left(\frac{m_f}{m_a}\right)_{real}}{\left(\frac{m_f}{m_a}\right)_{st}} \quad (2.2)$$

$\left(\frac{m_f}{m_a}\right)_{st}$  is calculated from the stoichiometric equation of the methane combustion presented below :



$$\left(\frac{m_f}{m_a}\right)_{st} = \left(\frac{m_f}{m_{O2}}\right) * \left(\frac{m_{O2}}{m_a}\right) = \left(\frac{16}{64}\right) * 0.23 = 0.0575 \quad (2.4)$$

The excess of air coefficient ( $\lambda$ ) is the reverse of  $r$ , expressed by  $\lambda = \frac{1}{r}$ .

After the first combustion chamber, the remaining mass of the different components at the exit of the combustion chamber is calculated using Equations (2.5) - (2.9), by switching from molar equations to mass equations by introducing molar masses:

$$Y_{CH_4} = 0 \quad (2.5)$$

$$Y_{O_2} = \frac{2 * (1 - r) * 32}{m_t} \quad (2.6)$$

$$Y_{N_2} = \frac{7.52 * 28}{m_t} \quad (2.7)$$

$$Y_{CO_2} = \frac{44 * r}{m_t} \quad (2.8)$$

$$Y_{H_2O} = \frac{2 * 18 * r}{m_t} \quad (2.9)$$

The total mass flow ( $m_t$ ) is obtained using Equation (2.10) :

$$m_t = 16r + 2(32 + 2.76 * 28) = 16r + 274.56 \quad (2.10)$$

In order to check if the combustion can occur in a new combustion chamber, the remaining oxygen mass should be verified and should not be zero. Then, the products of the previous combustion equation are taken as reactants and Lavoisier's law of conservation of mass is applied. The same methodology is used to determine the components at the exit of each additional combustion chamber.

The compressor work is obtained by Equation (2.11) :

$$W_C = h_{C-outlet} - h_{C-inlet} \quad (2.11)$$

$W_C$  : Compressor specific work (kJ/kg)

$h_{C-outlet}$  : Specific enthalpy at compressor outlet (kJ/kg)

$h_{C-inlet}$  : Specific enthalpy at compressor inlet (kJ/kg)

The expression used for the turbine is presented in Equation (2.12):

$$W_T = h_{T-inlet} - h_{T-outlet} \quad (2.12)$$

$W_T$  : Turbine specific work (kJ/kg)

$h_{T-inlet}$  : Specific enthalpy at turbine inlet (kJ/kg)

$h_{T-outlet}$  : Specific enthalpy at turbine outlet (kJ/kg)

The heat generated by the combustion chamber is determined by Equation (2.13):

$$q_{cc} = h_{cc-outlet} - h_{cc-inlet} = LCV * \left(\frac{m_f}{m_a}\right)_{real} \quad (2.13)$$

$q_{cc}$  : Specific heat added in the combustion chamber (kJ/kg)

$h_{cc-outlet}$  : Specific enthalpy at the combustion chamber outlet (kJ/kg)

$h_{cc-inlet}$  : Specific enthalpy at the combustion chamber inlet (kJ/kg)

$LCV$  : Lower calorific value (kJ/kg)

$m_f$ : Fuel mass flow (kg/s)

$m_a$ : Air mass flow (kg/s)

The total net specific work is the difference between the turbine work and the compressor work as shown in Equation (2.14):

$$W_{net} = W_T - W_C \quad (2.14)$$

The efficiency of the cycle is calculated by:

$$\eta = \frac{W_{net}}{q_{cc}} \quad (2.15)$$

The methodology conducted in the thermodynamic analysis is illustrated in the chart in Figure 2.2. The inputs parameter are: the ambient pressure ( $P_{amb} = 1.013$  bar), the ambient temperature ( $T_{amb} = 25$  °C), the maximum pressure ( $P_{max}$ ), the number of compressor stages ( $N_c$ ), the compressor pressure ratio ( $\pi_c$ ), considered the same for all the stages, the number of turbine stages ( $N_t$ ), the expansion ratio ( $\pi_t$ ), considered the same for all the stages and the excess of air coefficient ( $\lambda$ ).

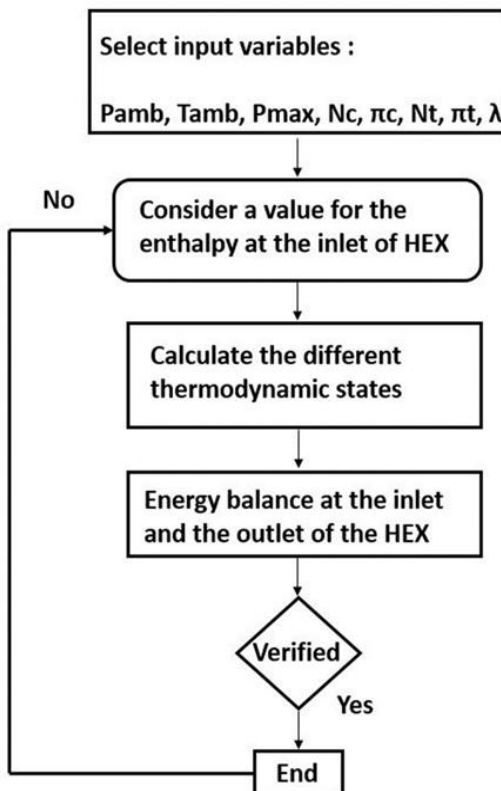


Figure 2.2: Methodology for the thermodynamic analysis.

The analysis is done by varying the different parameters in the GT cycle and comparing the results to choose the optimal configuration in terms of higher efficiency and higher net specific work. The different tested parameters are the number of compressor stages, the number of turbine stages, the maximum pressure, the turbine inlet temperature, and the turbine isentropic efficiency.

### 2.2.2. Results

The analysis is conducted by varying the number of compressor stages (intercooler + compressor) for the same maximum pressure to determine the convenient configuration. Although increasing the number of compressor stages leads to a more complex system, it reduces the compressor's required work by approaching the isothermal transformation.

Results in Figure 2.3 show that for the same maximum pressure, the work needed by the compressor decreases with the increase in the number of stages. The addition of two compressor stages reduces the

compressor work by 50 kJ/kg and increases the cycle efficiency by 4 points when compared to a single stage. Adding three compressor stages reduces the compressor work by 14 kJ/kg and increases the cycle efficiency by 2 points when compared to a double stage. Additional compressor stages will not lead to further advantages on the cycle performance. As a result, the reduction of compressor work enhances the cycle performance by increasing the net specific work and the efficiency of the gas turbine cycle. Although adding three stages is beneficial for the cycle performance, its complexity is more relevant. Consequently, as a result of complex issues, the dual system was chosen in this study.

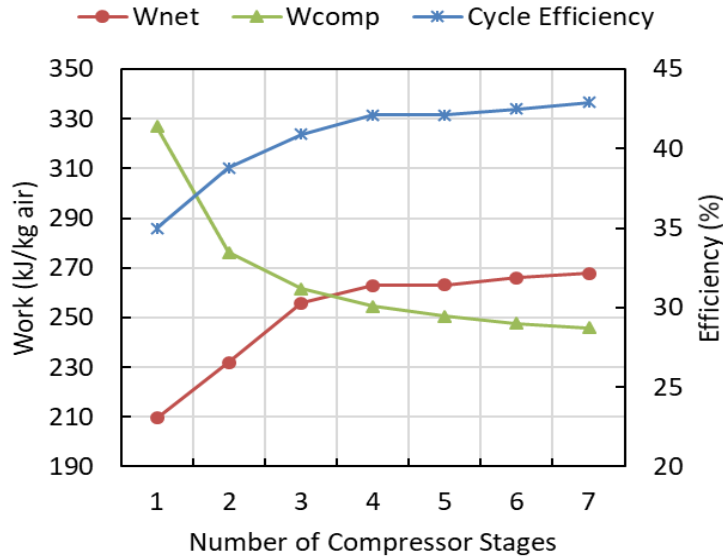


**Figure 2.3: Variation of the compressor work, the net specific work, and the cycle efficiency with the number of compressor stages.**

According to Figure 2.4, increasing the number of turbine stages improves the turbine work, as well as the net specific work. The work and the efficiency of a dual-stage turbine are respectively higher by 65 kJ/kg and 4 efficiency points when compared to a single-stage turbine. One additional turbine stage with reheating results in an increase of less than 30 kJ/kg in turbine work and 2 efficiency points increase in the cycle efficiency. Further increasing the number of turbine stages will not lead to further advantages of the cycle performance. Adding three stages will indeed increase the cycle efficiency and net specific work slightly, but the effect of system complexity is much more significant. As a result, two expansion stages are chosen.

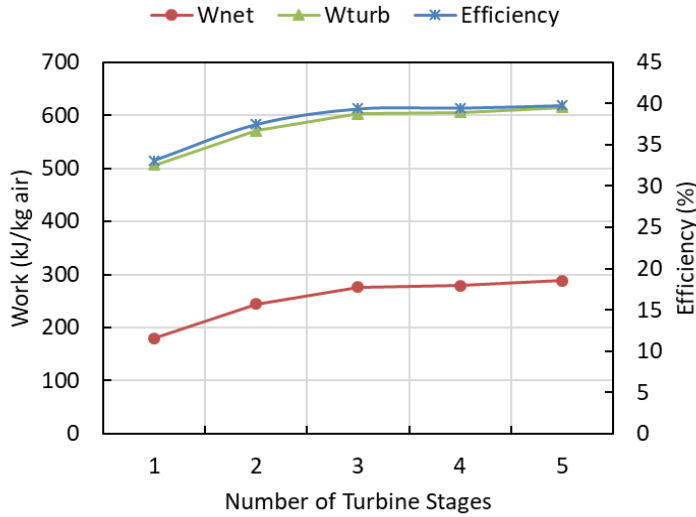


**Figure 2.4:** Variation of the turbine work, the net specific work, and the cycle efficiency with the number of turbine stages.

Considering a recuperated gas turbine cycle with two compression stages and two turbine stages, a variation of the maximum pressure of the system is conducted to choose the optimal pressure. The TIT is fixed. Figure 2.5 illustrates the impact of increasing the pressure on the cycle efficiency.

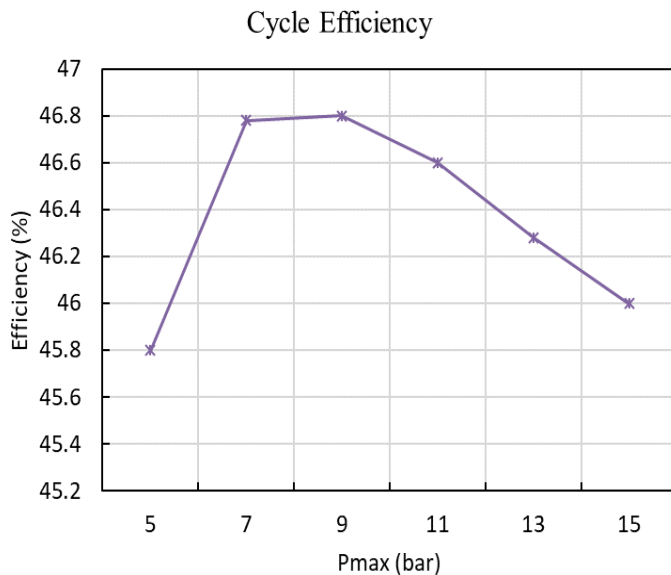


**Figure 2.5:** Variation of different parameters with the maximum pressure.

The efficiency curve represents a Pareto front. It can be seen that the efficiency of the gas turbine cycle increases at lower compression ratios, then when the maximum pressure reaches 9 bar a decrease in the efficiency is obtained. The reason for this can be seen by analyzing the results of Figure 2.6. The temperature at the exit of the compressor (inlet of the HEX) increases as the pressure increases. Therefore, since the TIT is fixed, the ability to recuperate energy is reduced, increasing the exhaust temperature.

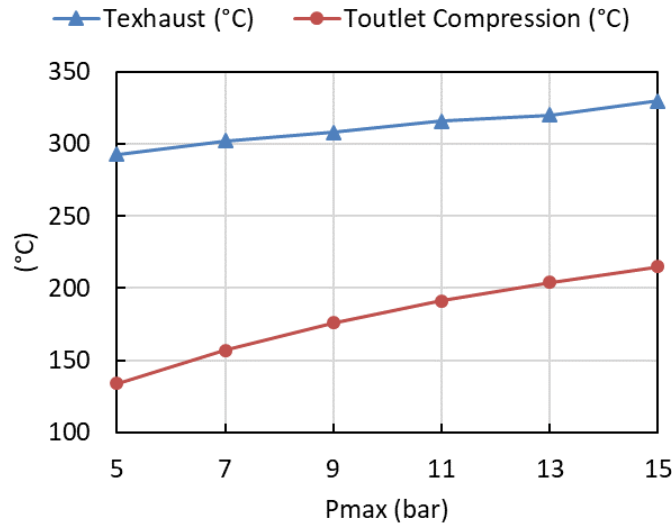


**Figure 2.6: Variation of compressor outlet exhaust temperature and the exhaust temperature.**

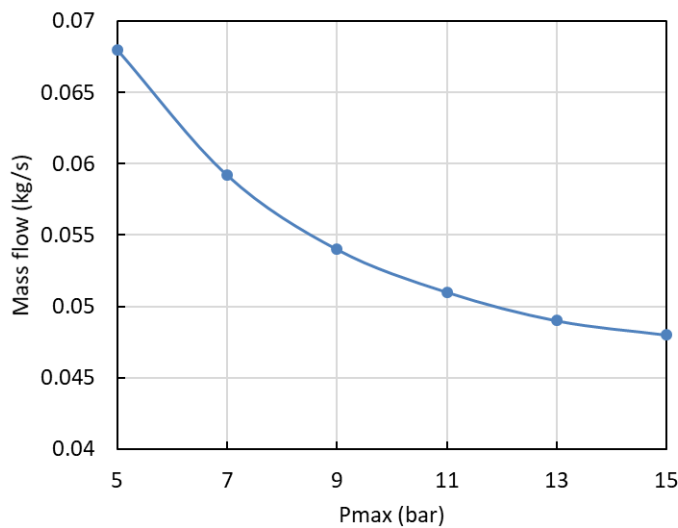


**Figure 2.7: Variation of air mass flow rate with the maximum pressure.**

Increasing the maximum pressure leads to higher turbine work and higher net specific work. As a result, for a fixed power, less air is required in the cycle. Figure 2.7 shows that by increasing the maximum pressure from 5 bar to 9 bar the mass flow rate is decreased from 0.068 kg/s to 0.054 kg/s.

The benefits of increasing the turbine inlet temperature are depicted in Figure 2.8. The turbine specific work, as well as the cycle efficiency, are higher. For instance, increasing the turbine inlet temperature by 400 °C increases the efficiency of the overall cycle by around 5.5 points. However, the material melting points limit the temperature at the inlet of the turbine. As long as the temperature does not exceed 1100 °C, it is not necessary to use special materials, and the turbine can be made using familiar, low cost alloys. While for temperatures exceeding 1250 °C, high cost materials are required [87].

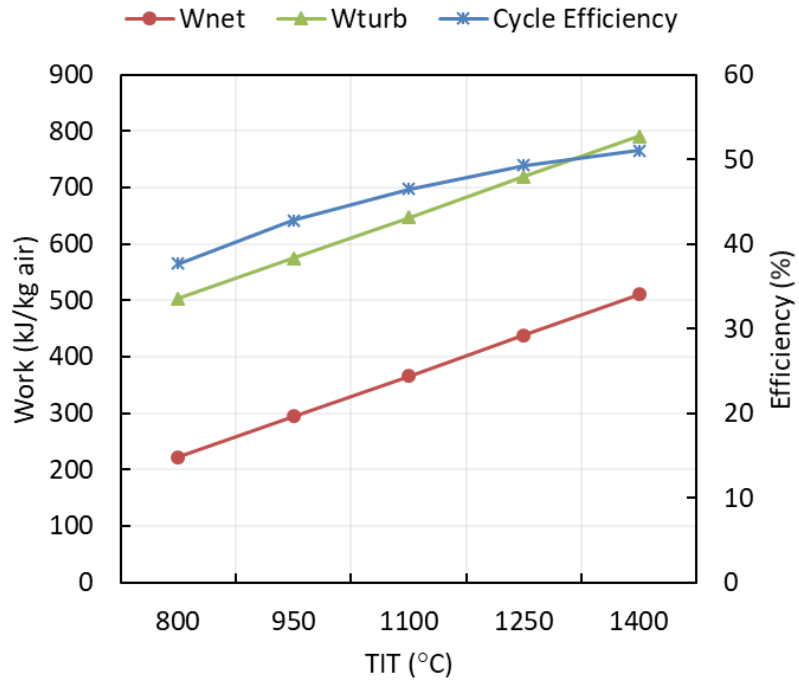


**Figure 2.8: Variation of different parameters with the TIT.**

The isentropic efficiency of the turbine is the ratio of the actual work of the turbine to the maximum work that can be accomplished by the turbine in the case of isentropic power. Higher turbine isentropic efficiency means lower thermal losses. As illustrated in Figure 2.9 increasing the turbine isentropic efficiency leads to a linear increase in both the cycle efficiency and the output work. The increase in turbine isentropic efficiency by 5 points increases the overall GT cycle efficiency by 3 points.

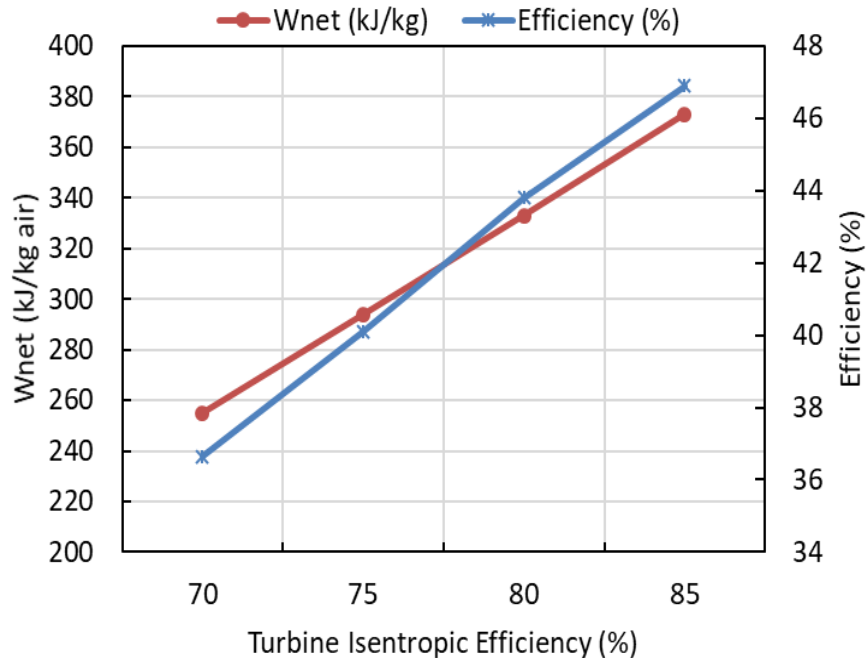


**Figure 2.9: Variation of the cycle efficiency and specific work with the isentropic efficiency of the turbine.**

### 2.2.3. Discussions

Based on the thermodynamic analysis before, several statements can be concluded from the previous section.

- Using multistage compressions and multistage expansions leads to an increase in the cycle efficiency. It will therefore result in a more complex, more expensive, and heavier GT cycle. Due to this, a dual-stage compression with intercooler and a dual-stage expansion with reheating are selected. In this way, the GT cycle will be with high efficiency and compact enough to be integrated into the EV.
- A Pareto front is obtained when the maximum pressure of the GT cycle is varied. The cycle efficiency increases for pressures under 9 bar, then decreases for pressures above 9 bar. Because of this, 9 bar is chosen as the GT cycle maximum pressure.
- The increase of the GT cycle temperature has numerous benefits on the cycle efficiency but due to turbine materials constraints and cost, it is limited.

According to these findings, the optimal IRReGT cycle illustrated in Figure 2.10 consists of a two-stage compression, an intercooler, a two-stage expansion, a reheater, and a recuperator. The (TS) diagram of the current cycle is depicted in Figure 2.11. The cycle maximum pressure is 9 bar. These results are in line with those from [1].

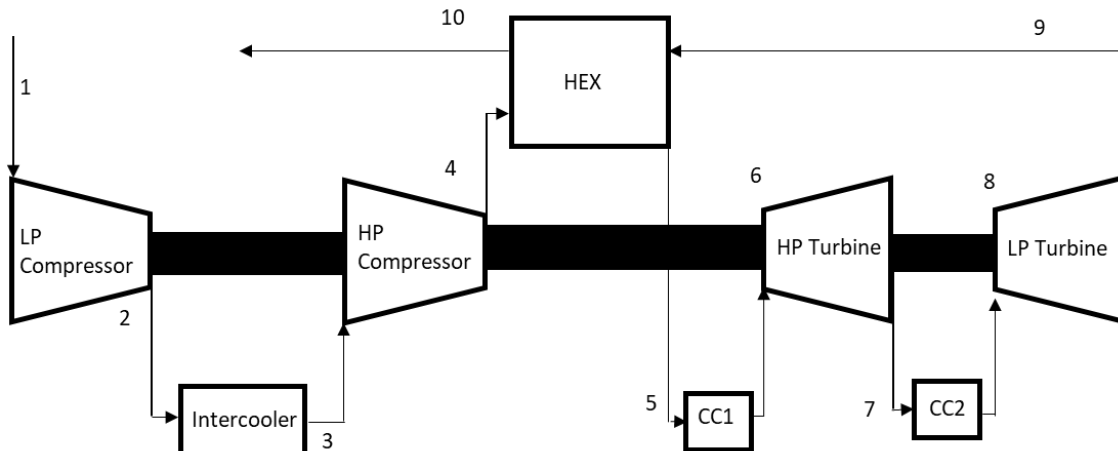


Figure 2.10: IRReGT cycle configuration.

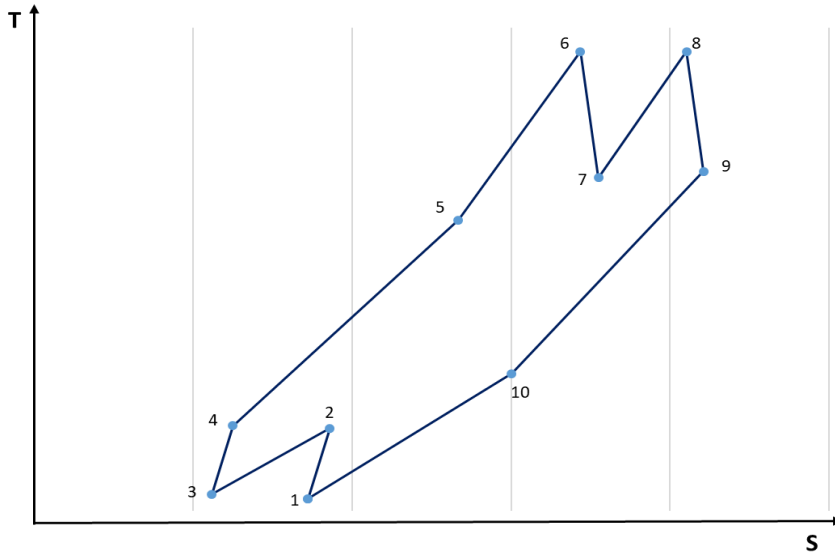


Figure 2.11: (TS) diagram of the IRReGT cycle.

#### 2.2.4. Exergy Analysis

The term 'Exergy' refers to the maximum amount of work that can be produced from a system as it reversibly settles to equilibrium with its environment; it is a measure of energy quality. It is based on the second law of thermodynamics. Therefore, an Exergy analysis is conducted in this section to evaluate the losses in the current cycle (IRReGT cycle) and to calculate the exergy efficiency, which measures how far the efficiency of the IRReGT is from its theoretical maximum. The formulation of exergy is extracted from [81]. The exergy calculation is achieved using REFPROP.

The exergy destruction in the compressor and the turbine are calculated using Equations (2.17) and (2.18), assuming no heat exchange with the surroundings.

$$e = h - T_0 * s \quad (2.16)$$

$$ed_C = W_C - (e_{C_{outlet}} - e_{C_{inlet}}) \quad (2.17)$$

$$ed_T = (e_{T_{outlet}} - e_{T_{inlet}}) - W_T \quad (2.18)$$

$e$  : Exergy (kJ/kg)

$h$ : Specific enthalpy (kJ/kg)

$T_0$ : Reference Temperature (K)

$s$ : Specific entropy (kJ/ kg.K)

$ed_C$  : Exergy destruction in the compressor (kJ/kg)

$e_{C_{outlet}}$ : Specific exergy at compressor outlet (kJ/kg)

$e_{C_{inlet}}$ : Specific exergy at compressor inlet (kJ/kg)

$ed_T$  : Exergy destruction in the turbine (kJ/kg)

$e_{T_{outlet}}$ : Specific exergy at turbine outlet (kJ/kg)

$e_{T_{inlet}}$ : Specific exergy at turbine inlet (kJ/kg)

The exergy destruction in the heat exchanger is determined using Equation (2.19).

$$ed_{HEX} = [(e_{Hot_{inlet}} - e_{Hot_{outlet}}) + (e_{Cold_{inlet}} - e_{Cold_{outlet}})] \quad (2.19)$$

- $ed_{HEX}$ : Exergy destruction in the heat exchanger (kJ/kg)
- $e_{Hot,inlet}$ : Specific exergy at the inlet of the hot fluid of the HEX (kJ/kg)
- $e_{Hot,outlet}$ : Specific exergy at the outlet of the hot fluid of the HEX (kJ/kg)
- $e_{Cold,inlet}$ : Specific exergy at the inlet of the cold fluid of the HEX (kJ/kg)
- $e_{Cold,outlet}$ : Specific exergy at the outlet of the cold fluid of the HEX (kJ/kg)

The exergy destruction in the combustion chamber is obtained using Equation (2.20) based on [87], considering the average temperature in the combustion chamber is estimated from Equation (2.21).

$$ed_{CC} = \frac{T_0}{\hat{T}} \Delta Q_{CC} \quad (2.20)$$

$$\hat{T} = \frac{\Delta Q_{CC}}{\Delta S_{CC}} = \frac{h_{CC,outlet} - h_{CC,inlet}}{S_{CC,outlet} - S_{CC,inlet}} \quad (2.21)$$

- $ed_{CC}$  : Exergy destruction in the combustion chamber (kJ/kg)
- $\hat{T}$ : Average temperature in the combustion chamber (K)
- $\Delta Q_{CC}$ : Enthalpy difference in the combustion chamber (kJ/kg)
- $\Delta S_{CC}$  : Entropy difference in the combustion chamber (kJ/kg.K)
- $T_0$ : Reference temperature (K)

Therefore, the exergetic efficiency of the overall GT cycle is calculated using Equation (2.22).

$$\eta_{ex} = \frac{W_{net}}{WCarnot_{net}} \quad (2.22)$$

- $\eta_{ex}$  : Exergetic efficiency
- $W_{net}$ : Net specific output work (kJ/kg)
- $WCarnot_{net}$ : Net specific output work considering a Carnot cycle (kJ/kg)

From Figure 2.12, it can be seen that the main exergy destruction is produced in the combustion chamber (28 % in the first combustion chamber, 19 % in the second combustion chamber) for the current cycle for TIT = 1100°C. The exergy destruction of the compressor and the turbine are less significant and can be reduced by increasing the efficiencies of these components.

These significant losses in the combustion mean that a lot of energy present in the fuel is being wasted, as it could produce useful work. Therefore, several studies [208] have suggested increasing the average temperature to reduce exergy destruction [209]. Achieving this requires reducing the difference between the inlet air temperature and the flame temperature and increasing the TIT, which is limited due to material constraints. Therefore, in the next section, a further increase in the TIT of the GT cycle is assessed by introducing the cooling techniques to overcome the material constraints.



**Figure 2.12: Exergy destruction in the IRReGT cycle for a TIT = 1100 °C and a maximum pressure of 9 bar.**

### 2.3. Thermodynamic Study of Gas Turbine Cycles with Cooling Blades

Since increasing the turbine inlet temperature leads to a higher cycle efficiency, cooling techniques are mandatory to avoid problems related to thermal stress, oxidation, creep, and component operating life. Different cooling technologies exist including water, steam, and most commonly air. In general, micro-scale turbine blades are subjected to internal convection cooling. It consists of a smooth channel passing a fraction of compressed air from the compressor exit and inserted into the root of the turbine. The coolant is heated as it cools the blade. The coolant is usually discharged at the trailing edge and mixed with the main flow. Convection cooling technology has been developed so that today the coolant can be directed inside the blade where it is most needed, such as at the leading [147]. The benefit of this cooling configuration is its simplicity and lower price compared to other methods. Cooling method selection depends on temperature levels at each stage of the cycle, as well as range extender system feasibility. Hence, to simplify the system-integration complexity in vehicles; convection cooling is chosen. Thermal and turbomachinery experts HiETA Technologies [210] have demonstrated the feasibility of an internally cooled microturbine.

Various studies investigated the methodology of one-dimensional thermodynamic analysis for a cooled turbine blade mainly in predicting the coolant mass flow needed to keep the turbine temperature below its limit, as well as the temperature at the coolant outlet. As an example, Louis et al. [211] examined various types of cooling including internal convection and impingement by air, film cooling by air, internal convection and impingement by steam, and closed-loop cooling by water. Therefore, in the case of air convection cooling, cooled turbine blades are modeled as heat exchangers operating at constant metal temperatures. Results show that an optimum inlet temperature exists for each blade temperature. In addition, a new cooling model for aero-thermal application was proposed by [212]. The model identifies the coolant requirements and the temperatures of both the pressure and the suction surface of the blade. Furthermore, Jordal et al. [213] compared two models for predicting convective cooling in turbine blades. The first model is based on empirical correlations and needs little input with the ability to calculate the mass of coolant and its outlet temperature. However, the second model needs more geometrical inputs for the blade shape and as an output predict also the pressure drop in the cooling

channel. Results show that both models give the same results for the coolant outlet temperature and the mass flow. Therefore, the authors suggested combining these two models.

Other researchers analyzed the GT system by modeling each component of the cycle separately and then evaluating the overall performance. Sanjay et al. [214] compared the impact of different cooling techniques on the performance of a combined cycle power plant. A parametric study has been carried out based on modeling the elements of the current cycle. It has been found that upon the tested configurations, closed-loop steam cooling offers the highest cycle efficiency and the highest specific work. Another study [215] evaluated the efficiency and the specific work of a simple air-cooled gas turbine used for Marine applications by modeling the different gas turbine components. The turbine blades were subjected to internal convection cooling where the air was taken from the compressor discharge. The obtained results verify the relation between the cycle efficiency and the compression ratio and TIT.

However, only a few studies have attempted to define the 'efficiency' of cooled turbines. Therefore, there is no consensus on how to evaluate this 'efficiency', which has complicated practical applications. As a general rule, turbine efficiency is calculated as the ratio of the actual work of the turbine to its isentropic or ideal work. Two primary definitions exist in the literature, unmixed and mixed efficiency for film or transpiration cooling. In the first case, the coolant and the mainstream expand separately and isentropically assuming an adiabatic and fully reversible expansion process. Hartsel [216] proposed this formulation, but critics contend that its value may reach values higher than 1 when taking the real properties of the hot gas and coolant into consideration. The mixed efficiency, however, describes the phenomenon when the coolant and the hot gas mix before expanding. The mixing and the expansion process depend on the mixing conditions referred to as Mainstream-Pressure (MP), Fully Reversible (FR), and Weighted-Pressure (WP) [237]. All these definitions were discussed in the literature [218] and have presented some concerns to predict the real performance of the cooled turbine. In addition, a study by Uysal [219] compared work outputs of three different turbines with similar inlet and exit pressures but different expansion processes. An isentropic expansion occurs in the first turbine, whereas an actual expansion without cooling occurs in the second turbine, while a cooling expansion occurs in the third turbine. It can be seen that the highest turbine work is achieved for the first turbine, which operates without an increase in entropy. Further, it can be seen that the actual work produced by the cooled turbine is lower than the work generated for the uncooled turbine.

Based on these findings, this section assesses new GT cycle configurations based on the IRReGT cycle but with introducing the convection cooling blade techniques. Numerous GT architectures with cooling turbine blades are investigated and compared in terms of higher efficiency and higher net specific work. This section aims to evaluate the impact of cooling the turbine blades on the cycle performance. The coolant mass needed and its outlet temperature is calculated using empirical correlations from the previous cited literature. Additionally, this section introduces a new definition of the 'cooled turbine efficiency', with the purpose to test the impact of cooling on the performance of the turbine itself. The proposed definition is optimistic; it underestimates the decrease in turbine efficiency since the parameters related to the turbine design are not considered (turbine blade surface, blade chord...).

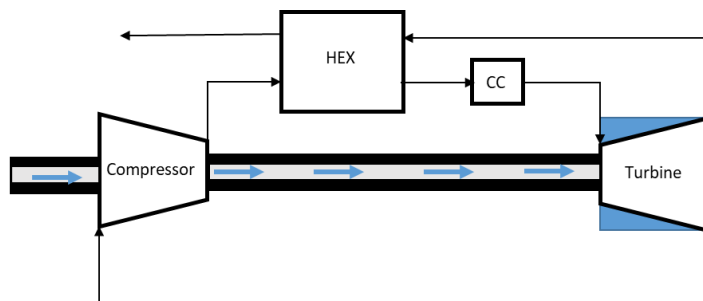
### **2.3.1. Methodology**

Three GT systems with cooling blade configurations are assessed in this section and illustrated in Figure 2.13. The first configuration (Figure 2.13a) consists of a RGT cycle with a cooled turbine. The coolant air is extracted before the compressor inlet and inserted through the hollow shaft of the cooled turbine. The coolant air and the mainstream mix at the exit of the turbine. The second configuration (Figure

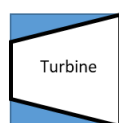
2.13b) consists of only cooling the first turbine, the HP turbine of the IRReGT cycle through internal convection cooling. A fraction of the compressed air is extracted to cool the HP turbine blade. The coolant air passes through a hollow shaft to the turbine blade, where it flows in the coolant channel reaching the trailing edge. Then, it exits at the exit of the HP turbine and mixes with the mainstream flow. The remaining mass of air is cooled to 35 °C. Then, the air is compressed in the second compressor. The fluid is preheated in a heat exchanger before entering the first combustion chamber and then is expanded through the first turbine stage. Then, the mixing flow is preheated into the second combustion chamber before being expanded through the LP turbine. Because the HP turbine is cooled, a higher TIT can be achieved, compared with an uncooled LP turbine. Therefore, the temperature at the inlet of the LP turbine is limited to material properties. In the cooled HP turbine, there is no expansion for the coolant. The expansion occurs only for the remainder mainstream. Depending on the chosen TIT at the HP turbine and its outlet temperature a second combustion chamber is added. At the exit of the HP turbine, the coolant and the hot gas mix, and both expand producing work. The compression ratio of the LP compressor is higher than the HP compressor to guarantee the introduction of the coolant flow in the HP turbine. The last proposed configuration (Figure 2.13c) consists of cooling both the LP and the HP turbines. The HP turbine is cooled from a fraction of air from the exit of the LP compressor, while the LP turbine is cooled from air extracted before the LP compressor stage. The isentropic efficiencies of the uncooled turbine, and the compressors are respectively 0.85, 0.8, while the regenerator effectiveness 0.8 based on Chrysler Corporation [36] for all the configurations. The operating conditions are presented in Table 2.1 and are based on the previous sensibility analysis and components' technological constraints. It should be noted that the losses of the coolant and the hot gas resulting from the difference in velocities are not taken into consideration.

**Table 2.1: Condition parameters for the IRReGT cycle with a HP cooled turbine.**

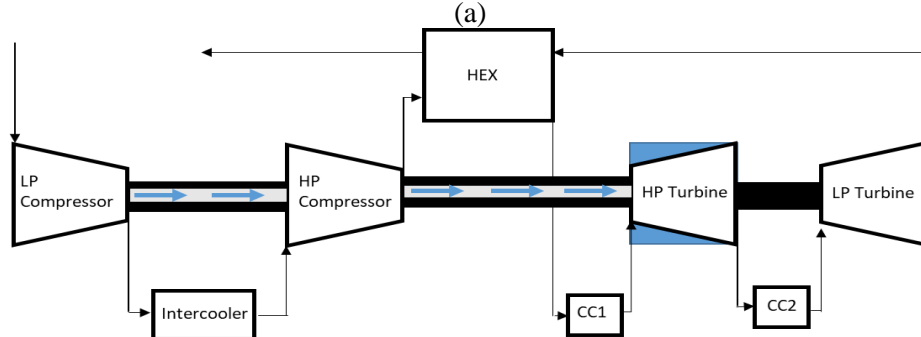
Parameters	Operating Conditions
LP compressor inlet temperature	25 °C
LP compressor inlet pressure	1.013 bar
Pressure ratio LP compressor	3.2
Intercooler outlet temperature	35 °C
Pressure ratio HP compressor	3
Expansion ratio HP turbine	3.2
Expansion ratio LP turbine	3
TIT LP turbine	1100 °C
Isentropic efficiency compressor	0.8
Isentropic efficiency uncooled turbine	0.85
Regenerator effectiveness	0.8



Cooled Turbine



(a)

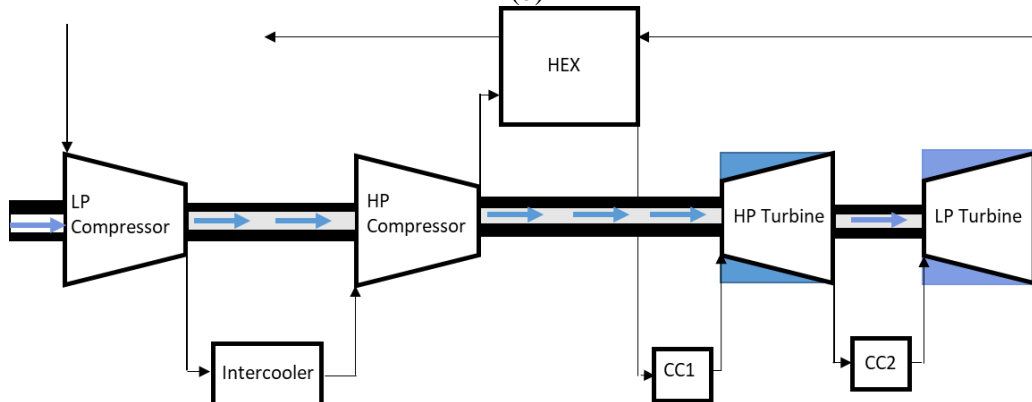


Cooled Turbine



Coolant flow

(b)



Blue arrow → Coolant flow HP turbine  
 Blue arrow → Coolant flow LP turbine

(c)

**Figure 2.13: (a) RGT with cooling turbine, (b) IRReGT cycle with a cooled HP turbine, (c) IRReGT with cooled HP and LP turbines.**

The considered thermodynamic analysis is the same as the approach proposed in the cited studies. The thermodynamic study focuses on determining the mass of coolant needed to cool the turbine blade based on empirical correlations and assumptions from the literature. The turbine is considered a heat exchanger with a constant wall temperature.

The first step of the thermodynamic analysis is the calculation of the coolant mass flow rate. The coolant air circulates through passages reaching the trailing edge, where it exits and mixes with the mainstream before entering the second combustion chamber. The internally cooled turbine is treated as a heat exchanger (Figure 2.14) operating at a constant metal temperature ( $T_w$ ). The coolant outlet temperature ( $T_{c,o}$ ) is expressed in function of the heat exchanger's effectiveness ( $\varepsilon$ ).

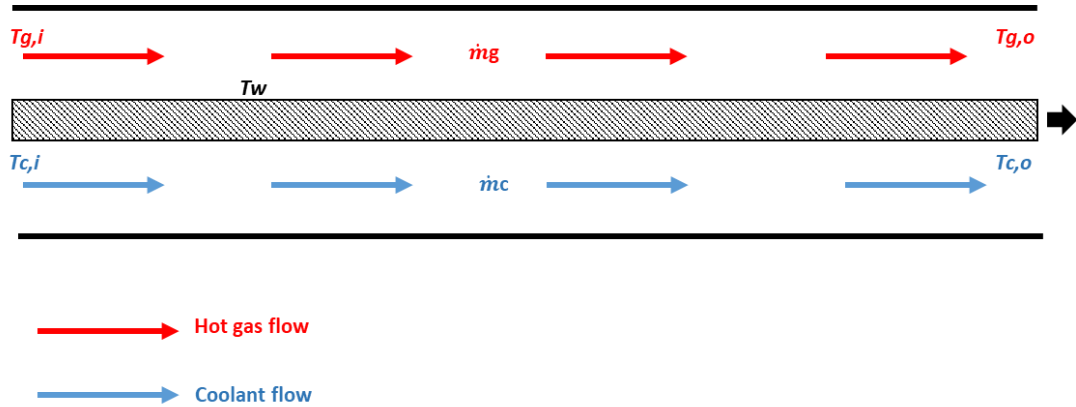


**Figure 2.14: Schematic presentation of the HP cooled turbine as a heat exchanger.**

The fraction of compressed air for turbine blade cooling is determined by:

$$X = \frac{\dot{m}_c}{\dot{m}_c + \dot{m}_g} \quad (2.23)$$

$X$ : coolant air mass fraction ratio

$\dot{m}_c$ : coolant air mass (kg/s)

$\dot{m}_g$ : hot gas mass (kg/s)

The blade heat effectiveness is expressed by:

$$\varepsilon = \frac{T_{c,o} - T_{c,i}}{T_w - T_{c,i}} \quad (2.24)$$

$\varepsilon$ : blade heat effectiveness

$T_{c,i}$ : inlet coolant temperature (K)

$T_{c,o}$ : outlet coolant temperature (K)

$T_w$ : wall temperature or material temperature (K)

The cooling air effectiveness depends on different parameters: the cooling air temperature, the heat transfer coefficient, the heat transfer area, and the temperature difference. Jordal [147] determines the cooling efficiency for different cooling methods: 0.45 - 0.65 for convection cooling, 0.8 for impingement cooling, and between 0.9 - 1 for film cooling.

The cooling factor ( $R_{conv}$ ):

$$R_{conv} = \frac{(T_{g,i} - T_w)Cp_g}{\varepsilon(T_w - T_{c,i})Cp_c} \quad (2.25)$$

$$R_{conv} = \frac{(T_{g,i} - T_w)}{(T_w - T_{c,i})} * \frac{(T_w - T_{c,i})}{(T_{c,o} - T_{c,i})} * \frac{Cp_g}{Cp_c} \quad (2.26)$$

$$R_{conv} = \frac{(T_{g,i} - T_w)}{(T_{c,o} - T_{c,i})} * \frac{Cp_g}{Cp_c} \quad (2.27)$$

At the exit of the cooled turbine, the coolant air and the hot gas are assumed to have the same pressure, thus, they mix at the exit of the cooled turbine before entering the second combustion chamber. The enthalpy of the mixed flow is obtained using the energy balance.

$$\dot{m}_g h_g + \dot{m}_c h_c = (\dot{m}_g + \dot{m}_c) h_{mix} \quad (2.28)$$

$h_g$ : Specific enthalpy of the hot gas at the outlet of the cooled turbine (kJ/kg)

$h_c$ : Specific enthalpy of the coolant at the outlet of the cooled turbine (kJ/kg)

$h_{mix}$ : Specific enthalpy after mixing the coolant and the hot gas at the outlet of the cooled turbine (kJ/kg)

The heat flux between the hot gas and the coolant air is calculated by:

$$Q = \dot{m}_c * Cp_c * (T_{c,o} - T_{c,i}) = \dot{m}_g * Cp_g * (T_{g,i} - T_{g,o}) = \overline{h_g} * A_{s,g} * (T_{g,i} - T_w) \quad (2.29)$$

$$q = X * Cp_c * \varepsilon * (T_w - T_{c,i}) \quad (2.30)$$

$Q$ : Heat flow that occurs between the coolant and the turbine blade (kJ)

$q$ : Heat flow that occurs between the coolant and the turbine blade (kJ/kg) of gas + coolant

$Cp_c$ ;  $Cp_g$ : Specific heat capacity at constant pressure (J/(kg. K))

$\overline{h_g}$ : Average convective heat transfer coefficient (kW/m<sup>2</sup>°K)

$A_{s,g}$ : Exposed area of heat transfer (m<sup>2</sup>)

The exposed area of heat transfer is calculated based on pitch line conditions using Equation (2.31).

$$A_{s,g} = (A_{s,g})_{pl} * F_{sa} = \gamma * F_{sa} * A_g = \gamma * F_{sa} * \frac{\dot{m}_g}{\rho_g} * C_g \quad (2.31)$$

Where  $F_{sa}$  is a correction factor to account for the actual blade surface,  $C$  is the velocity, and  $\gamma$  is a ratio between the exposed area of heat transfer and the area of hot gas.

$$\gamma = \frac{(A_{s,g})_{pl}}{A_g} = \frac{2bc}{btcos\alpha} = \frac{2c}{tcos\alpha} = \frac{S_g}{t * cos\alpha} \quad (2.32)$$

Where  $b$  is the blade height,  $c$  is the blade chord,  $S_g$  is the blade perimeter,  $t$  is the blade pitch, and  $\alpha$  is the inlet flow angle.

The ratio of the mass of coolant to the mass of the hot gas flow is determined by the correlation below that relates the Stanton number ( $\overline{St}_{in}$ ) with the geometrical parameters of the turbine blade.

$$\frac{\dot{m}_c}{\dot{m}_g} = \gamma * F_{sa} * \left[ \frac{Cp_g}{Cp_c} \right] * \overline{St}_{in} * \left[ \frac{(T_{g,i} - T_w)}{\varepsilon(T_w - T_{c,i})} \right] \quad (2.33)$$

$$\frac{\dot{m}_c}{\dot{m}_g} = R_{conv} * \overline{St}_{in} * \frac{S_g}{t * \cos\alpha} * F_{sa} \quad (2.34)$$

Stanton numbers based on the cascade inlet area, according to [220] are typically equal to 0.005. To estimate the ratio of coolant mass fraction to hot gas mass, Louis et al. [211] suggested an approximation of the correlation presented previously:

$$\frac{\dot{m}_c}{\dot{m}_g} = 0.0158 * R_{conv} \quad (2.35)$$

The second step of the thermodynamic analysis consists of determining the cooled turbine efficiency, thus, a new definition of the ‘cooled turbine efficiency’ is proposed. Uncooled turbine isentropic efficiency is defined as the ratio of actual work to ideal work, as shown in Equation (2.36). A turbine's ideal work corresponds to the maximum work it can attain while generating no entropy.

$$\eta_{uncooled} = \frac{h_{T,i} - h_{T,o}}{h_{T,i} - h_{T,ois}} \quad (2.36)$$

$h_{T,i}$ : Specific enthalpy at the inlet of the turbine (kJ/kg)

$h_{T,o}$ : Specific enthalpy at the outlet of the turbine (kJ/kg)

$h_{T,ois}$ : Specific isentropic enthalpy at the outlet of the turbine (kJ/kg)

The difference between the uncooled turbine and the cooled turbine is that in the cooled turbine, in addition to the expansion of the hot gas, there is a heat loss due to heat transfer with the coolant flow. The heat is extracted from the turbine along the blade. Thus, two possible cases can be used to estimate the change in turbine efficiency. In the first case, the hot air is first expanded and then heat is extracted (Figure 2.15b), while in the second case, heat is extracted from the hot air and then expanded in the turbine (Figure 2.15c). The real turbine efficiency is approximately the average of both.

Therefore, the efficiency of the cooled turbine for the first case can be calculated by:

$$\eta_{cooled} = \frac{h_{T,i} - h_{T,o'}}{h_{T,i} - h_{T,ois}} = \frac{h_{T,i} - h_{T,o} - q}{h_{T,i} - h_{T,ois}} \quad (2.37)$$

While for the second case, the efficiency is calculated using Equation (2.38) :

$$\eta_{cooled} = \frac{h_{T,i'} - h_{T,o'}}{h_{T,i} - h_{T,ois}} = \frac{h_{T,i'} - h_{T,o'}}{h_{T,i} - h_{T,ois'} + q} \quad (2.38)$$

From the previous two definitions, it can be concluded that the efficiency of the cooled turbine is lower than the uncooled turbine. It decreases with the increase in heat loss.

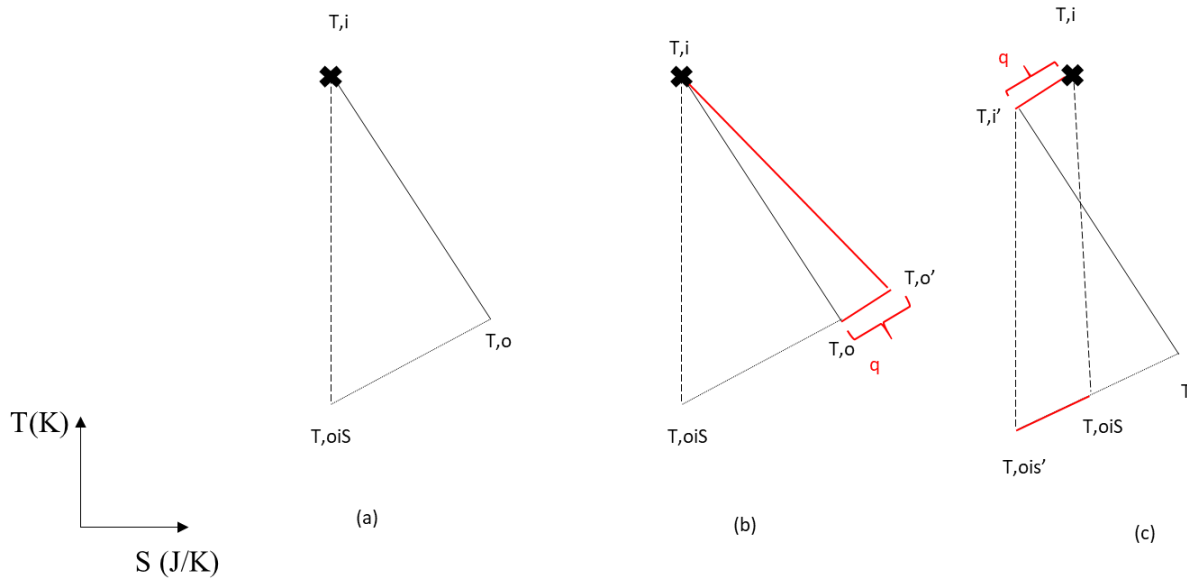


**Figure 2.15: (a) Expansion for the uncooled turbine, (b), (c) Expansion for a cooled turbine.**

The output net specific work for the second configuration is calculated applying Equation (2.39).

$$W_{net} = [(1 - X) * W_{HP-T} + W_{LP-T}] - [W_{LP-C} + (1 - X) * W_{HP-C}] \quad (2.39)$$

$W_{HP-T}$ : HP turbine specific work (kJ/kg)

$W_{LP-T}$ : LP turbine specific work (kJ/kg)

$W_{LP-C}$ : LP compressor specific work (kJ/kg)

$W_{HP-C}$ : HP compressor specific work (kJ/kg)

The efficiency of the IRReGT with a cooled HP turbine is calculated using Equation (2.40).

$$\eta = \frac{W_{net}}{(1 - X) * q_{cc1} + q_{cc2}} \quad (2.40)$$

$q_{cc1}$ : Specific heat added in the first combustion chamber (kJ/kg)

$q_{cc2}$ : Specific heat added in the second combustion chamber (kJ/kg)

### 2.3.2. Results

This study assesses the influence of cooling the turbine blades on the cycle performance. The cycle efficiency depends on the main turbine variables: the turbine blade temperature, the turbine inlet temperature, the turbine efficiency, and the coolant effectiveness. The following results are subjected to the IRReGT with only a cooled HP turbine.

The cycle consists of two compressor stages operating at the same pressure ratio, for a maximum pressure of 9 bar and an isentropic efficiency of 0.8. There is also two turbine stages with reheating operating at the same expansion ratio. Since the HP turbine is cooled, its temperature is not limited by the material constraints. However, since the LP turbine is uncooled, thus its temperature is limited by the material properties. Therefore, the presence of a second combustion chamber depends on the temperature at the outlet of the HP turbine. If the temperature of the mixing stream is lower than the material operating temperature, a second combustion chamber is added. The same conclusions can be

drawn for the other configurations when testing the effect of these parameters on the cycle performance, since they are simulated but not presented in the manuscript.

Considering two different turbine materials handling temperatures of 950 °C and 1100 °C, thermodynamic analysis is carried out by varying TIT on the HP turbine as seen in Figure 2.16. As the HP TIT increases, although a higher mass coolant fraction is required to cool the turbine blades, the cycle efficiency increases too. As the material melting temperature rises, the required coolant mass fraction decreases, and the cycle efficiency increases. For instance, when the TIT reaches 1400 °C, the coolant mass fraction is 0.012 and the GT cycle reaches 50.5 % for  $T_w = 1100$  °C, while the efficiency is 47.9 % and the coolant fraction is 0.014 for  $T_w = 950$  °C.

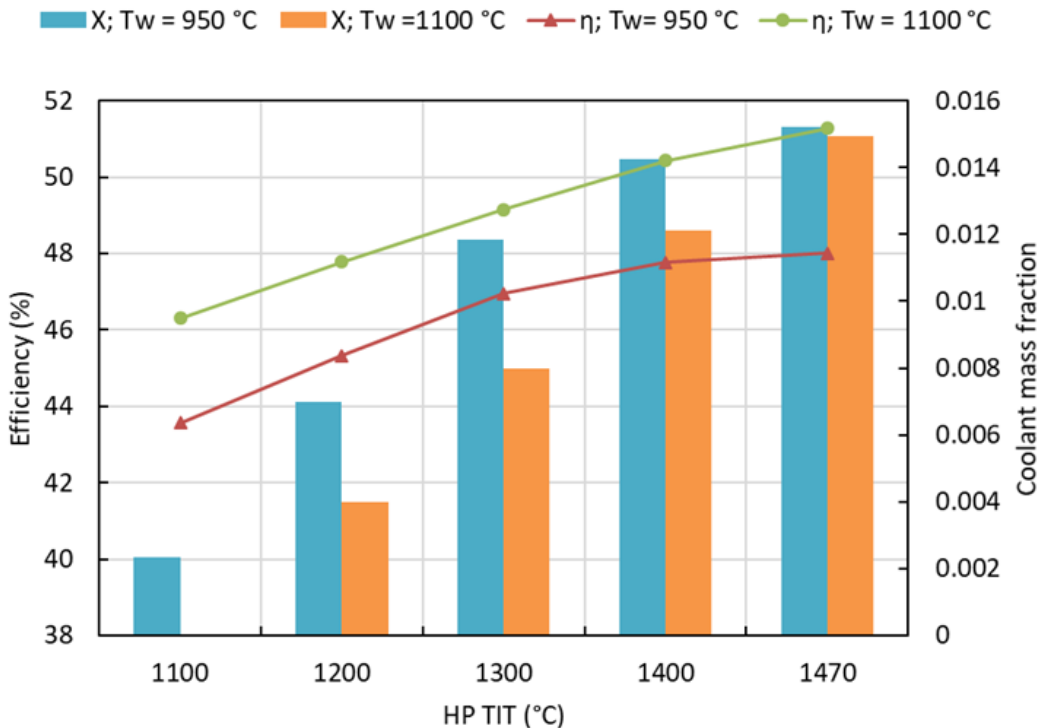


**Figure 2.16: The impact of the HP TIT on the cycle efficiency and the coolant mass fraction for  $T_w = 950$  °C and  $T_w = 1100$  °C.**

It should be noted that each TIT is associated with a fraction of air required to cool the blades. At a given temperature, if this fraction of air increases, the cycle efficiency decreases. Thus, the calculated coolant mass fraction is the optimal air mass that guarantees at the same time the cooling of the turbine blades and the optimal efficiency of the cycle. For instance, as seen in Figure 2.17, the required mass fraction for TIT = 1450 °C is 0.014, increasing this mass fraction leads to a decrease in the net specific work and a decrease in the overall cycle efficiency.

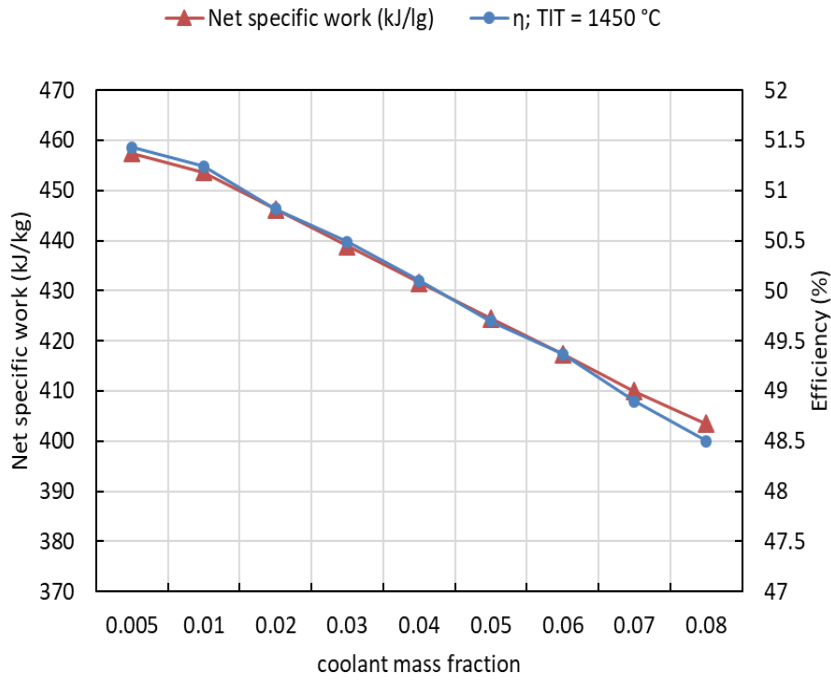


Figure 2.17: The impact of increasing the coolant mass fraction on the cycle efficiency and power output.

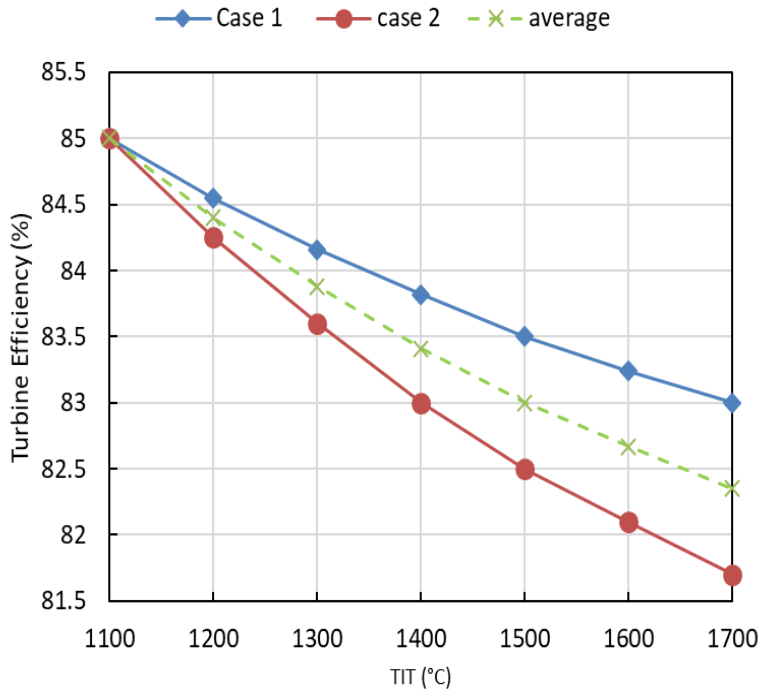
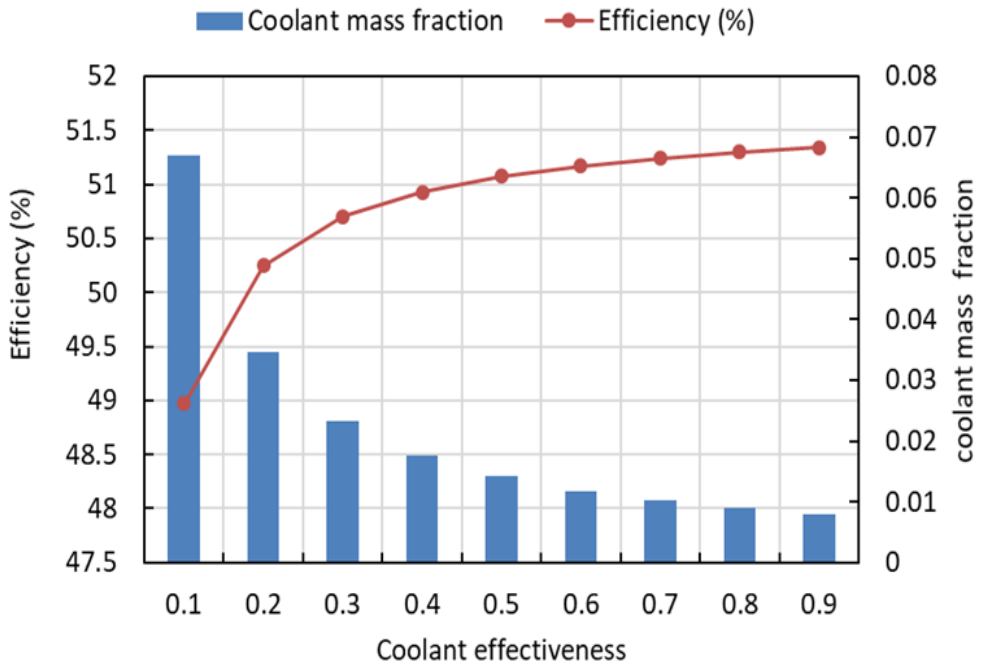


Figure 2.18: Sensibility analysis of the turbine efficiency with increasing TIT for both cases.

The heat is removed from the turbine along the blade, but to account for the loss in efficiency two estimations are considered: either the heat is extracted before the expansion process, or after the expansion process. Both correlations are used to calculate the cooling turbine efficiency for different TIT as depicted in Figure 2.18. It can be seen that the efficiency calculated by expanding the turbine than extracting heat is higher than the case when the air is cooled and then expanded. This is evident since the efficiency of a cooled turbine is mainly determined by the ratio between heat flux and

temperature. In other words, the efficiency of the cooled turbine depends on at which temperature the heat is extracted. The average efficiency is considered a compromise for the two cases. For instance, the worst-case scenario estimates that increasing the turbine inlet temperature by 400 °C, reduces the turbine efficiency by 2.5 points, while the best-case scenario estimates a decrease in efficiency by 1.5 points.

It can be concluded from the obtained results that, although cooling the turbine blade by introducing cooling air leads to a decrease in the turbine efficiency, it improves the overall cycle performance due to higher turbine inlet temperatures. The latter generally overcome the loss by the coolant flow and improves the cycle efficiency. For instance, it is true that increasing TIT by 400 °C decreases the turbine efficiency around 2.5 points, but it will increase the GT cycle overall efficiency by 4.5 points.



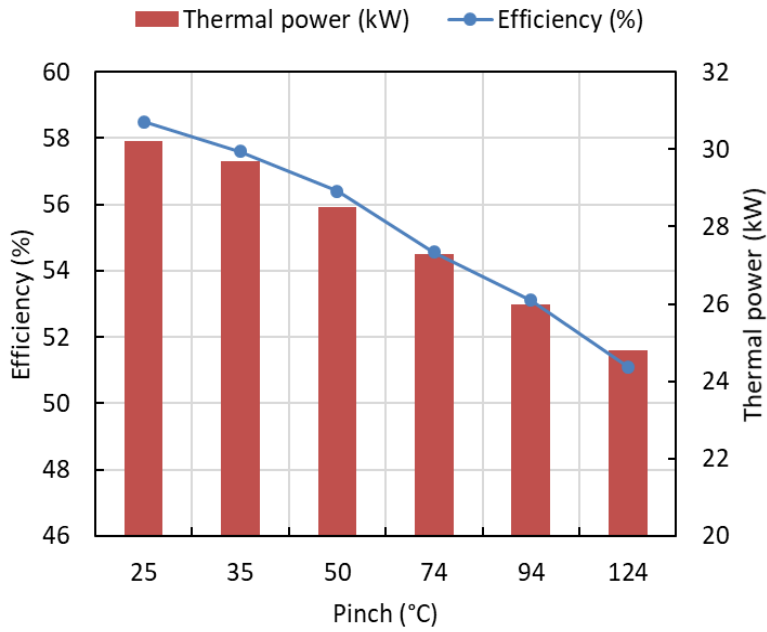
**Figure 2.19: The impact of coolant effectiveness on the coolant mass fraction and the cycle efficiency.**

Figure 2.19 shows the effect of the coolant effectiveness on both the coolant mass and the cycle efficiency. The coolant effectiveness depends on the internal heat transfer area and the heat transfer coefficient of the blade. The variation of the coolant effectiveness from 0.1 to 0.9 decreases the coolant mass fraction from 0.0669 to 0.0079 and increases the cycle efficiency by 2.37 points.

Since a higher heat transfer coefficient is expected with increasing coolant effectiveness, a lower coolant mass fraction is required. Another advantage of higher coolant effectiveness is that the temperature of the coolant at the exit of the HP turbine is higher leading to a higher mixture temperature before entering the CC2. Thus, less energy consumption is needed in the CC2.

GT system efficiency also depends on other components such as the HEX. A study of the impact of the pinch variation on the cycle efficiency is presented in Figure 2.20. The cycle efficiency is adversely affected by increasing the pinch of the recuperator. Increasing the pinch from 25 °C to 124 °C reduces the thermal power by 5 kW and the cycle efficiency by 7 points.

The impact of these parameters on the cycle performance and their behavior is the same for all the suggested configurations.



**Figure 2.20: The impact of HEX pinch variation on the cycle efficiency and the thermal power.**

#### ➤ Specific Conditions for the CC2 Configuration

This section assesses the impact of a further increase of the HP turbine's TIT on the mixing temperature ( $T_{mixing}$ ).  $T_{mixing}$  describes the resultant temperature after mixing the coolant air and the hot gas at the outlet of the cooled turbine. It can be seen from Figure 2.22 that increasing TIT leads to an increase in the  $T_{mixing}$ . For instance, for TIT higher than 1470 °C,  $T_{mixing}$  reaches 1100 °C. As a result, in an IRReGT cycle including only a cooled HP turbine and an LP turbine that cannot handle temperatures above 1100 °C, the HP turbine's TIT is limited to 1470 °C, and the second combustion chamber can be removed. The GT cycle efficiency for this configuration reaches 51.2 % for TIT = 1470 °C.

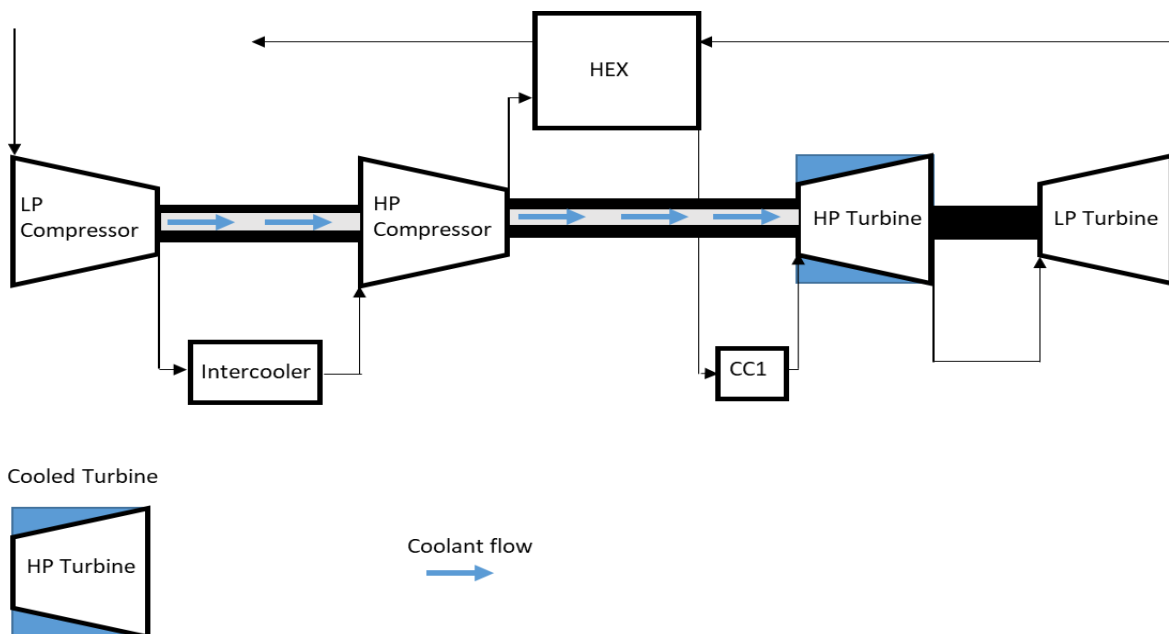


**Figure 2.21: New configuration of the IRReGT cycle with a cooled HP turbine with no CC2.**

Based on the previous statement, a new configuration of the GT cycle can be proposed when the TIT at the inlet of the HP turbine reaches 1470 °C. It consists of two compression stages with an intercooler, a recuperator, a combustion chamber, and two expansion stages with a cooled HP turbine and an uncooled LP turbine as illustrated in Figure 2.21. When the HP turbine's TIT exceeds 1470 °C, the cooling blade technique for the LP turbine is required since  $T_{mixing}$  exceeds 1100 °C. The same logic can be applied to the other GT configurations.

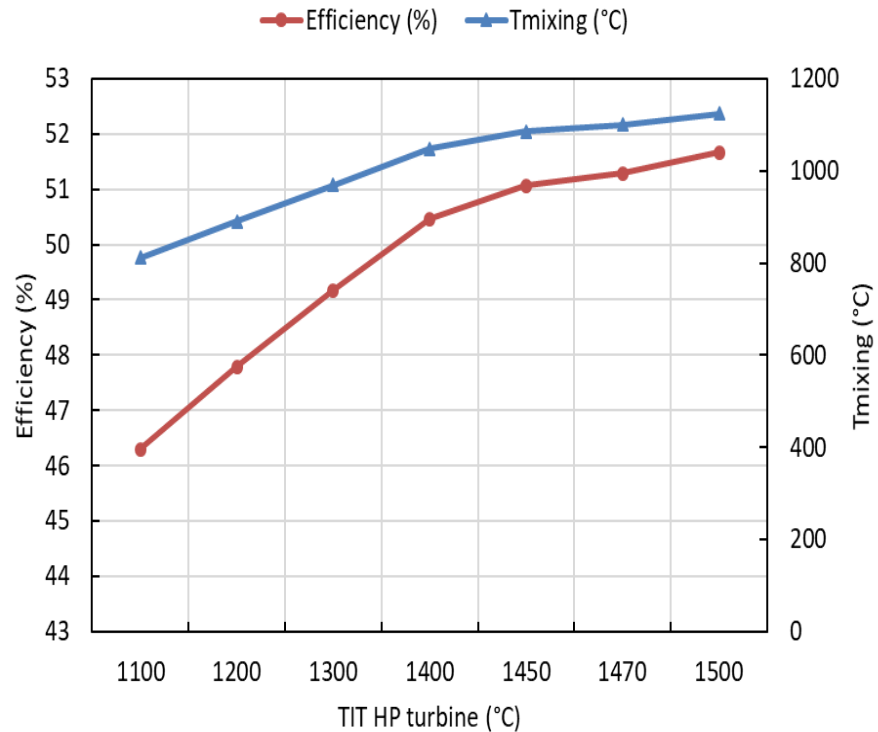


Figure 2.22: Impact of increasing HP turbine TIT on the mixing temperature.

## 2.4. Comparison of different GT Configurations

Four realistic GT configurations are compared in this section, where their operating conditions are summarized in Table 2.2. Taking into consideration that the maximum allowable pressure for a single stage centrifugal compressor is 3 bar, the operating pressure for the RGT cycle is 3 bar, while the other configurations operate at 9 bar. Due to technological constraints, TIT of each architecture depends on the turbine and the recuperator material. The same turbine material is used in all the architectures. The maximum temperature for the recuperator should not exceed 900 °C as the ASME pressure vessel recommendation when using stainless steel [221]. However, the hot air temperature at the inlet of the recuperator can be a little bit higher since the hot air is not subjected to high pressure and since the presence of a pinch. Therefore, the proposed configurations and their operating conditions are based on these constraints. Based on these statements, the first configuration is the baseline cycle, the IRReGT cycle. The second configuration involves RGT cooled turbine blades operating at TIT = 1250 °C. IRReGT with cooled HP turbine operating at TIT = 1450 °C in the third configuration. The last configuration consists of the IRReGT cycle with a cooled HP turbine and a cooled LP turbine operating at TIT = 1700 °C.

The results of the thermodynamic analysis are illustrated in Figure 2.23. Among the investigated GT cycles, several conclusions can be drawn. First, comparing the baseline IRReGT cycle and the IRReGT

cycle with a cooled HP turbine, it can be seen that the cooling technique is beneficial in increasing the cycle efficiency (4.1 points) and the net specific work (80 kJ/kg) due to the advantage of reaching higher TIT that exceeds the material limiting temperature. As well, while the use of cooling decreases turbine efficiency, increasing the TIT boosts the overall cycle efficiency. This explains the increased efficiency of the IRReGT cycle with cooling. As the LP turbine is not cooled, the TIT for the HP turbine is limited to 1450 °C.

**Table 2.2: Properties of the chosen realistic cycles.**

Configurations	Operating Conditions	Reason
IRReGT cycle	P = 9 bar TIT = 1100 °C	Baseline cycle.
Cooled RGT cycle	P = 3 bar TIT = 1100 °C	The maximum pressure ratio for a centrifugal compressor is 3.
IRReGT cycle with a cooled HP turbine	P = 9 bar TIT HP turbine = 1450 °C TIT LP turbine = 1100 °C	As only the HP turbine is cooled, any further elevation of the HP TIT results in the TIT LP turbine exceeding 1100 °C, which is not possible because of the limitations of the turbine materials. -The maximum temperature of the recuperator should not exceed 900 °C due to material limitations. However, the hot air temperature at the inlet of the recuperator can be a little bit higher since the hot air is not subjected to high pressure, and due to pinch.
IRReGT cycle with cooled HP and LP turbines	P= 9 bar TIT HP turbine = 1700 °C	-Adding a second combustion chamber does not make sense due to the limitation of the recuperator temperature.

In addition, intercooling and reheating between the compressor and turbine stages, respectively, provide three important benefits: higher pressure ratio, higher work output, and increased regeneration potential. This results in a significant improvement in cycle performance and is what makes the IRReGT cycle with a cooled HP turbine more efficient than the cooled RGT cycle (41.34%).

Finally, comparing the IRReGT cycle with only a cooled HP turbine and the IRReGT cycle with two cooled turbines, it can be seen that the latter has better performance, in terms of higher efficiency (51.8 %), and net specific work (539 kJ/kg). This result is due to the further increase of TIT of the HP turbine with no limitations since the LP turbine is also cooled. However, the improvement in the cycle efficiency is negligible compared to the cycle's technological complexity.

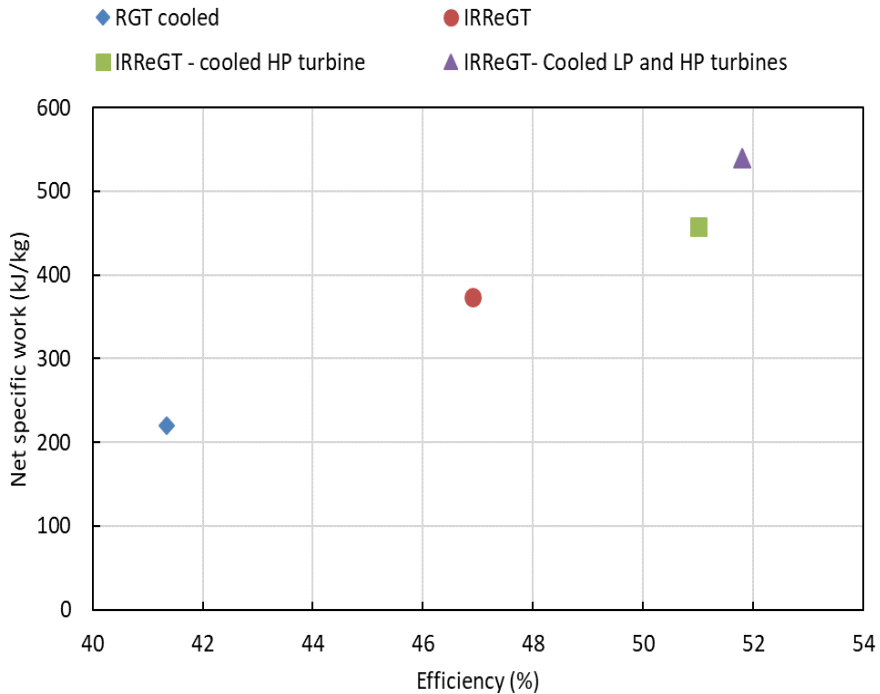


**Figure 2.23: Efficiency and net specific work for different cooled GT cycle configurations.**

Among the investigated configurations, it can be seen that the IRReGT cycle with a cooled HP turbine and the IRReGT with two cooled turbines present the best performance. The former has an efficiency of 51%, while the latter has an efficiency of 51.8 %. For the latter, the net specific work is 539 kJ/kg, while 457 kJ/kg for the former. According to the data, efficiency and output work are not significantly different between these two configurations.

## 2.5. Technological Study of GT-System Components Design

A technological assessment is carried out for the GT architecture to account for the weight of the system as well as the technical constraints of each component. Therefore, the GT system was divided into different subsystems which are:

- The turbomachines composed of the centrifugal compressor and the radial cooled turbine and the radial uncooled turbine with their accessories
- The intercooler and the recuperator that forms the heat exchangers
- The combustion chambers
- The electric motor/generator
- The bearings

The components of both the RGT cycle and the IRReGT are presented respectively in Figure 2.24a and Figure 2.24b.

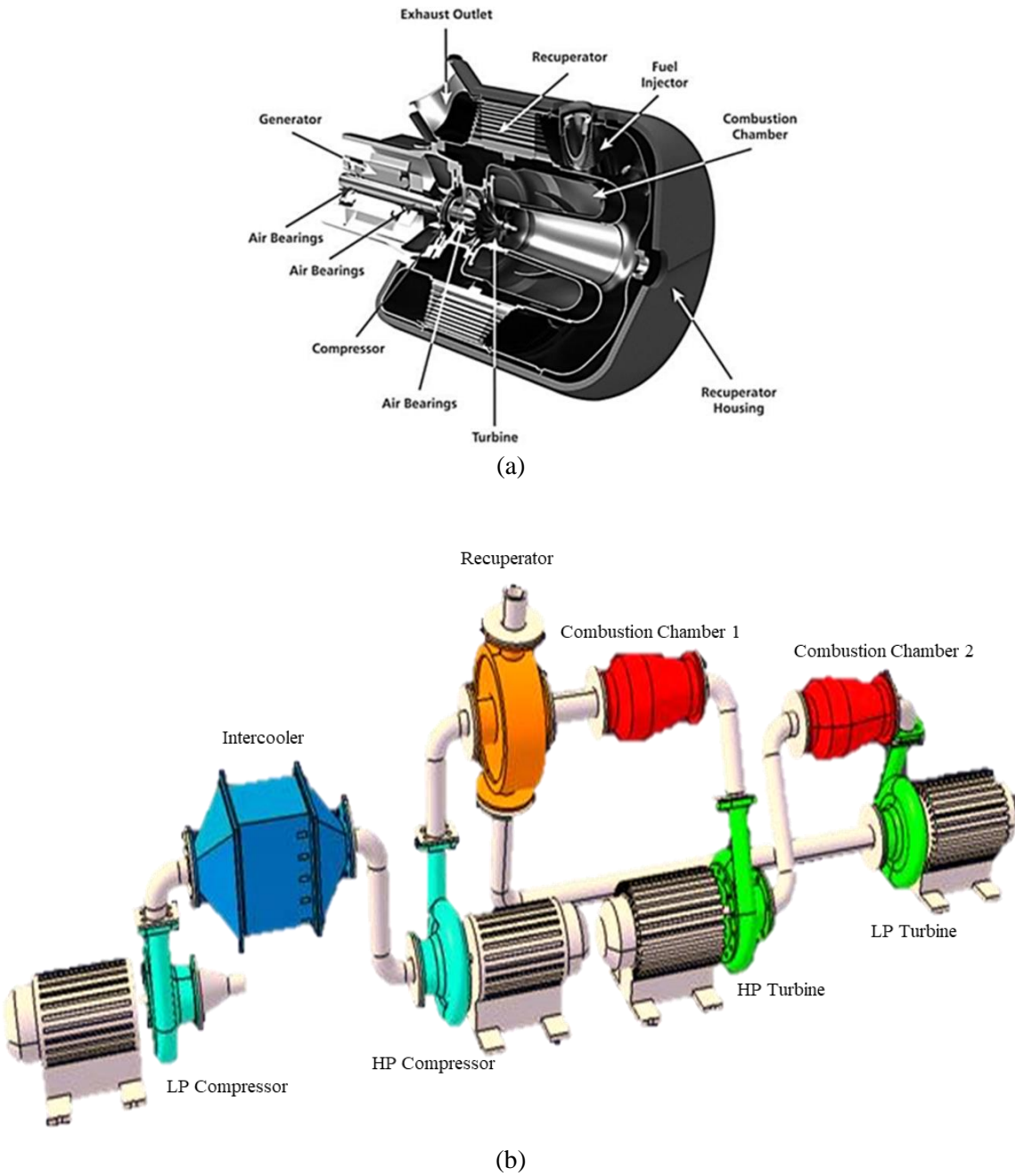


**Figure 2.24: (a) Uncooled RGT cycle components, (b) Uncooled IRReGT components.**

### 2.5.1. Turbomachines

A centrifugal compressor and a radial turbine are generally used in microturbines. As seen from the previous sections, increasing the turbine inlet temperature is beneficial for enhancing the cycle performance in terms of cycle efficiency and net specific work. As the TIT is limited by the turbine material constraints, the blade cooling technique is used. Casting radial turbine wheels is a traditional, low-cost process that has been used for many years. While the cooling technique is common in axial turbomachinery, it has not been widely utilized in radial turbines due to the smaller wheel diameters and the blade's limited space. Adding cooling features to radial turbines to increase TIT is now possible with additive manufacturing techniques, which allow the fabrication of complex internal geometries without additional manufacturing steps. Therefore, this section first discusses the technological constraints of

the cooled turbine in terms of manufacturing complexity and cooling channel generation, then estimates the weight of the compressor and the turbine.

### ➤ 3D Printing Technology Limitations

3D printing uses computer-aided design (CAD) to create three-dimensional objects. The technology, also known as additive manufacturing, can generate various objects of different sizes, shapes, colors, and severity using a layering approach. This manufacturing technique has gained large popularity in different sectors, especially in aerospace. The biggest advantage of 3D printing is the ability to generate complex geometries within hours, which is faster than traditional processes. A further advantage of additive manufacturing is its ability to produce lightweight parts, which are particularly useful in automotive and aerospace applications. In addition, the use of 3D printing gives the ability to print on demand and avoid overstocking. As well, this technique provides a key to waste reduction. Additive manufacturing does, however, have many limitations regarding print quality and materials. Most printed geometry should undergo post-processing to create a smooth surface finish. Furthermore, the materials selected for 3D printing are limited to plastics and metals.

In creating printing parts, several design recommendations can help improve part quality, surface finish, and dimensional accuracy. The minimum wall thickness is an important parameter to tackle when using 3D printing since a very thin wall thickness can generate a deformation of the component body. The minimum wall thickness depends on the printer type, the material, and the orientation. A design guideline for parts made from TiAl6V4 recommended a minimum wall thickness of 0.3 mm and 0.4 mm depending on the orientation angle [222]. On the other hand, Materialise, a 3D printed industry for Stainless Steel parts recommended a minimum wall thickness of 0.5 mm [223]. 3D printing was widely used to manufacture novel heat exchangers. A microchannel heat exchanger from stainless steel was fabricated using the SLM technique with a wall thickness of 0.1 mm [224]. In addition, a recent study investigated the manufacturing of a high-temperature printed heat exchanger using Stainless steel 316L considering a wall thickness of 0.16 mm [99]. The HEX manufacturing was successful offering a remarkable weight saving compared to conventional techniques. Another important design parameter when considering geometries with the grave is the hole diameter. For materials made from TiAl6V4, a minimal bore diameter of 2 mm is required [222]. On the other hand, Hydra research recommended a hole size higher than 2 mm [225]. Based on Hubs [226], a leading manufacturing company, holes between 0.5 mm and 6 mm can be reliably printed without support for metal bodies. As well, zhang et al. [132] recommended a diameter of 0.5 mm for a coolant channel introduced in an Inconel 625 radial turbine manufactured with the SLM technique. The designed turbine was tested experimentally and validated. Although 3D printing techniques allow the creation of small geometries, the latter can affect the flow's physical properties, primarily its velocity, when considering reduced diameters. Very reduced channel results in increasing the flow velocity, leading to higher losses into the channel and maybe the flow transition to turbulent behavior.

As a consequence, the challenge in this thesis is to produce a compact, complex, small-size printed turbine with cooling channels. It is important to consider three main factors: the size of the turbine to be integrated into the vehicle, and the accommodation of the cooling channels without increasing internal losses.

### ➤ Cooling Channel Generation

Within the axial turbine design community, heat transfer techniques and active cooling designs are well-established, and some of these approaches can be successfully applied to radial turbomachinery. As a

result of radial turbomachinery's aerodynamic properties, some modifications need to be made. Commonly, in axial turbines, the coolant is extracted from the compressor and introduced through the shaft to the turbine side. The same concept is applied in this study. Figure 2.25 illustrates the turbomachinery concept suggested by HiETA, it consists of a compressor and a turbine mounted on the same shaft. The extracted coolant air from the compressor flows through the hollow shaft and enters the turbine.

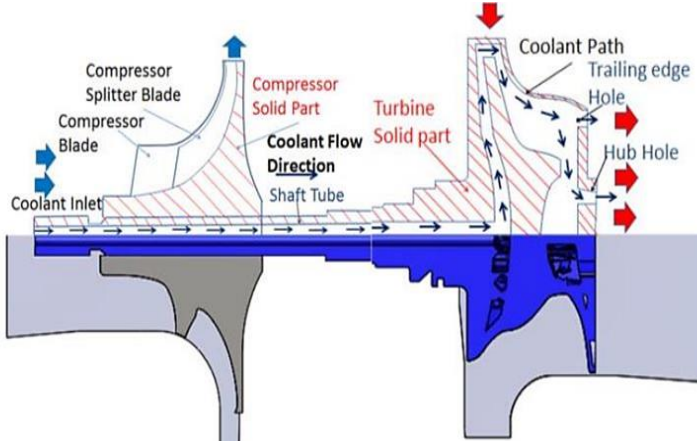


**Figure 2.25:** cross-section of a typical radial turbine spool showing potential cooling path [132].

The first contact between the hot fluid and the turbine blade occurs at the blade's leading edge, the most hotting spot of the turbine. As a result, the coolant flow should be directed towards the leading edge of the blade for maximum benefit. When the fluid passes through a turbine blade, it expands, resulting in a reduction in temperature. As a consequence, the cooling of the turbine blade is mandatory only in the first part of the turbine blade.

Although the large advantages of film cooling and other cooling techniques listed in Section 1.7.2, this study will consider only the rotor internal convection cooling as suggested by HiETA [132] due to the simplicity and feasibility of this cooling method in radial turbomachines. The cooled radial turbine of HiETA is presented in Figure 2.26. It consists of an internally cooled radial turbine capable of operating at 1200 °C. The introduction of cooling channels helped in reducing the temperature at the leading edge by 100 °C.



**Figure 2.26:** Internally cooled turbine by HIETA Technologies [210].

Cooling the turbine blade and generating coolant channels involves challenges to achieving both efficient cooling for the turbine blade and respecting the material stress. Zhang et al. [132] conducted a topology optimization analysis to determine areas that can be safely removed from the radial turbine without compromising solid stress distribution. The study is based on comparing different cooling

channels using numerical simulation and considering a fixed temperature through the turbine wheel. Figure 2.27 illustrates the three coolant concepts and the stress analysis in each region where the areas marked with red represent where the solid stress is higher than the yield point of the material.

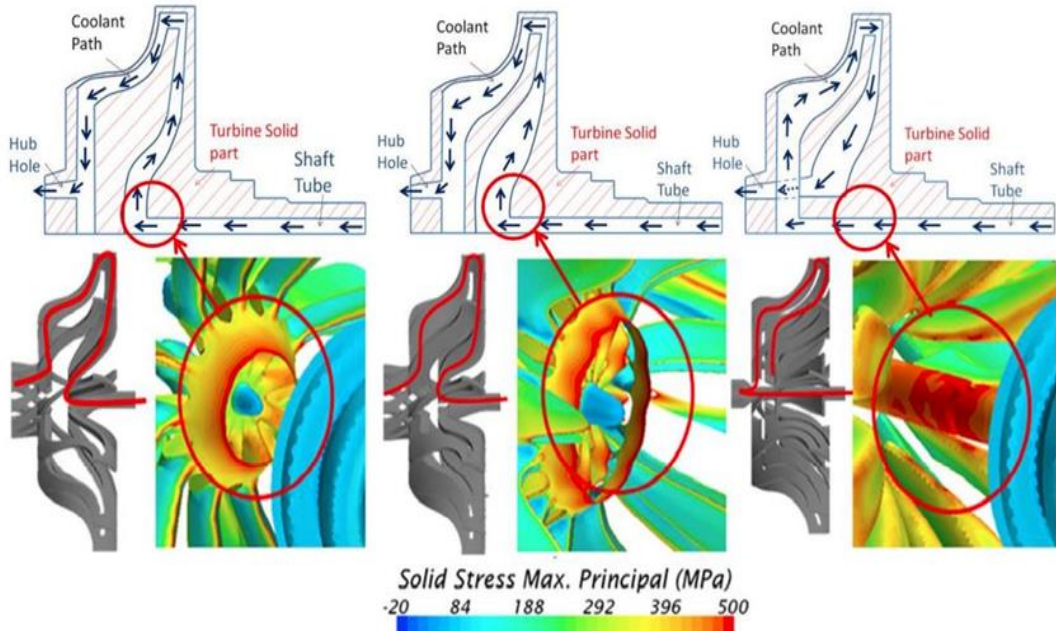


**Figure 2.27:** Internal cooling concepts with results of initial solid stress analysis ( red circles where the solid stress exceeds the yield point of the material) [132].

The obtained results are presented in Table 2.3. It can be seen that no mass should be removed from the connection between the hub and the blades. However, the area at the trailing edge had the lowest solid stress, so it was there that the majority of the mass was removed. Lastly, the main body of the blade can be hollowed out to provide a cooling channel by removing all the internal mass.

**Table 2.3: Possible regions to remove the mass and introduce the cooling channel.**

Location	Results
Between the shaft and the turbine wheel backface	A region with high stress
Between the hub and the blade	A high-stress region, the mass should not be removed
Trailing edge area	The majority of mass can be removed
The main body of the blade	Mass can be removed for channel generation
Connecting the coolant channel and the hollow shaft	Challenging region but necessary for the connection

### ➤ Turbine Sizing

The considered GT configurations include a centrifugal compressor and a radial turbine that are similar to automotive turbochargers.

Thus, Reine and Bou Nader [227] established a mathematical relationship between the mass flow rate and the power-to-weight ratio in a turbocharger based on turbochargers from Garrett, Borgwarner, and MTI. This relation presented in Equation (2.41), is valid for turbochargers operating at 90 000 RPM and

with mass flow rates ranging from 100 to 800 kg/h. The calculated weight accounts for the weight of the compressor housing, the compressor wheel, the turbine housing, the turbine wheel, the shaft, and the oil-bearing system. It was also demonstrated that in a turbocharger system the compressor side accounts for 30 % of the total weight, while the turbine side accounts for 70 % of the turbocharger weight.

$$\dot{m}_{Turbo} = -273 * \left( \frac{P}{Weight} \right)^2 + 645 * \left( \frac{P}{Weight} \right) + 122 \quad (2.41)$$

$\dot{m}_{Turbo}$ : Mass flow rate across the turbomachines (kg/h).

P: Power across the turbomachines (kW).

Weight: Turbocharger weight (kg).

For the configurations with a double stage, it is considered that the HP turbine drives the HP compressor and forms a turbocharger, while the LP turbine drives the LP compressor and forms another turbocharger. When cooling techniques are assessed, the turbine weight is estimated to be reduced by 22 % due to the mass reduction of the turbine wheel since mass is removed to introduce the cooling channel [132].

The weight of the turbomachinery systems of different gas turbine configurations is presented in Figure 2.28. It can be seen that when cooling is applied the system weight decreases, hence, the baseline IRReGT is the heavier range extender. Between the cooled configurations, the IRReGT cycle with two cooled turbines is the lighter system (7.16 kg).

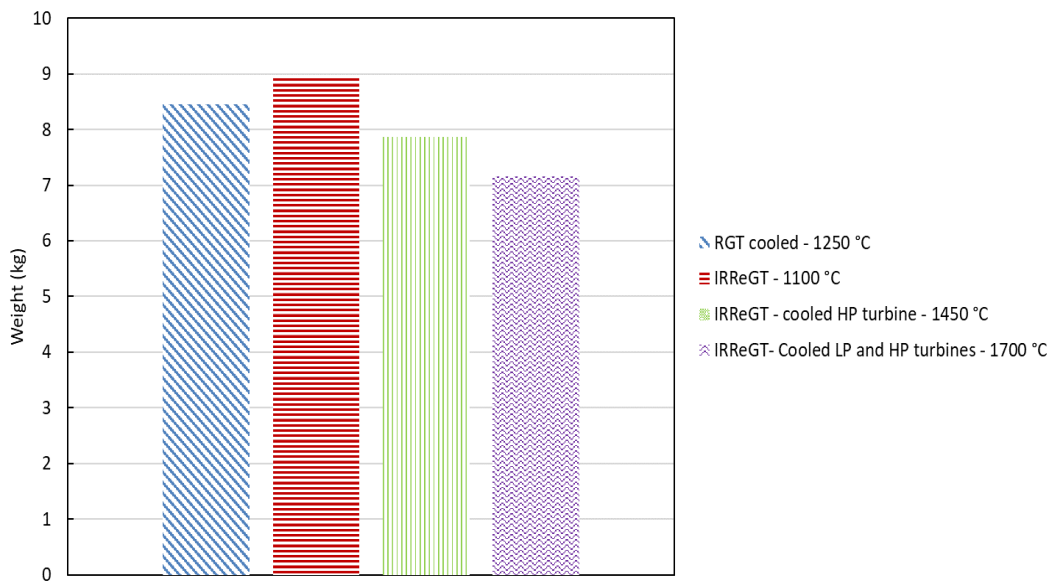


Figure 2.28: The weight of the turbomachinery systems for different GT configurations.

### 2.5.2. Heat Exchangers

Compact, highly efficient HEX is required to enhance the performance of the auxiliary power unit in automobile applications. Thus, two types of HEX are used: an intercooler and a recuperator. The former is used to reduce the compressor work, while the latter is used to recover the waste from the exhaust gas and preheat the air before entering the combustion chamber.

Many studies were interested in suggesting highly efficient recuperators for higher efficiency microturbines. McDonald [228] presented the different types of heat exchangers used in microturbines

and developed a cost-effective counterflow primary surface recuperator for high-temperature applications. Kays and London [229] carried out a comprehensive study on heat and fluid-flow performance characteristics for existing types of compact heat exchangers with experimental data.

Numerous studies have been carried out to develop correlations to represent the thermal-hydraulic performance of different HEX types mainly by representing the Nusselt number [230] or formulating the fanning friction factor ( $f$ ) and the Colburn  $j$ -factor [231]. Many works have focused on wavy plate-fin heat exchangers (Figure 2.29a). Ismail and Velraj [232] developed heat transfer correlations in the form of  $j$  and  $f$  in the laminar and turbulent regions using computational fluid dynamics (Fluent software) as a simulation tool. Junqi et al. [233] reported thermal-hydraulic correlations from experimental data of eleven wavy fin arrangements for a specific Reynolds number range. The correlations predicted 95 % of the experimental data. Qasem and Zubair [234] proposed generalized air-side  $f$ - and  $j$ - factor correlations. Twenty-one air-side geometries are simulated by an experimentally validated CFD model using ANSYS Fluent program. The results show that the suggested correlations are more accurate and generalized than the ones presented in the literature. On the other hand, Chang and Wang [235] proposed a generalized heat transfer correlation for louver fin geometry (Figure 2.29b) based on 91 samples of louver fins heat exchangers. As well, offset strip fins (Figure 2.29c) gained the attention of researchers since they are compact and highly efficient heat exchangers. Kedam et al. [236] developed a general model for heat transfer factors taking into consideration combined geometric variables for rectangular offset strip fin, and wavy fin heat exchangers for a wide range of Reynolds numbers. Another study [237] derived the dimensionless performance factors to obtain an effective design of offset strip fin heat exchanger.

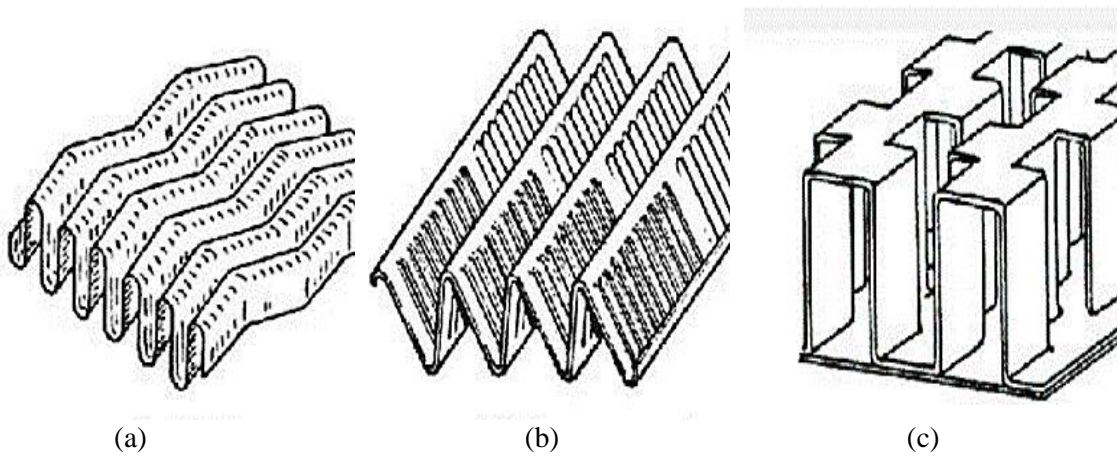


Figure 2.29: (a) wavy fins, (b) louver fins, (c) offset fins [238].

In addition, to improve the efficiency of the HEX without compromising the weight and cost, many optimization studies were conducted. Traverso and Massardo [239] studied the technical and economical aspects of plate-fin and primary surface recuperators since these proved that they are the most promising for microturbine applications. The optimization takes into consideration various parameters including the compactness, the pressure drops, and the cost. Wen et al. [240] proposed a multi-objective optimization with a genetic algorithm method for the optimization of a plate-fin heat exchanger. Sanaye and Hajabdollahi [241] presented a thermal modeling and economical optimization of a plate-fin heat exchanger. A genetic algorithm was applied to obtain the maximum effectiveness and the minimal total annual cost. A thesis conducted in MINES Paristech by Wakim [99] proposed a local parametrical and topological enhancement of conventional HEXs including wavy fins and offset fins. Results show that reducing the fin spacing, regardless of the fin type, minimizes the HEX weight for the same global heat

duty and pressure drop. Therefore, a highly efficient plate-fin HEX was 3D printed taking a fin spacing  $s = 0.8$  mm without any fluid blockage.

Based on the previous findings, this section presents at first the design methodology used for both the intercooler and the recuperator, then the estimation of each HEX weight to evaluate the total weight of the GT cycle configuration.

### ➤ HEX Sizing

The first step in designing a heat exchanger consists of determining the fluid properties (density, viscosity, specific heat  $C_p$ ) on each side of the heat exchanger using the fluid temperatures and inlet pressure. The design methodology and the used correlations are the same adopted by [99]. The HEX consists of a counterflow plate-fin. The offset strip fins are considered in this study for both the recuperator and the intercooler considering a pressure drop of 100 mbar. The main geometrical parameters are the fin height ( $h$ ), the fin length ( $x$ ), the fin thickness ( $t$ ), and the fin spacing ( $s$ ) presented in Figure 2.30.

The correlations for the friction factor ( $f$ ) for the intercooler and the recuperator is depicted in Equation (2.42), while the correlations for the Colburn factor ( $j$ ) for the recuperator and the intercooler is presented respectively in Equations (2.47) and (2.48) for a Reynolds number range between 500 and 1500.

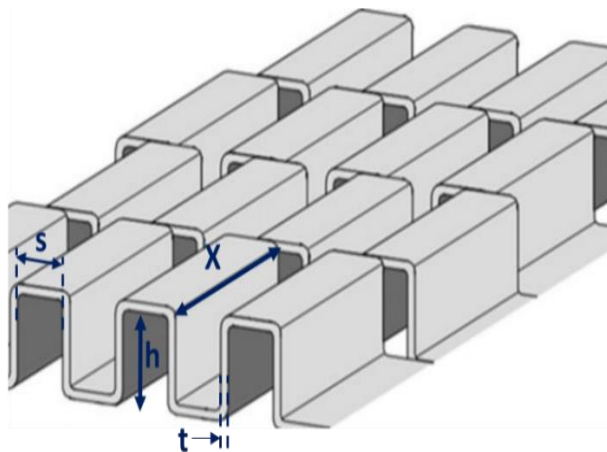


**Figure 2.30: Schematic view of the offset strip fin.**

The fluid is considered in a fully developed region where  $\frac{L}{D_h} > 100$ , with  $L$ , is the fluid flow length, and  $D_h = \frac{4A}{P}$  is the hydraulic diameter with  $A$  being the area ( $m^2$ ) and  $P$  (m) being the perimeter.

$$f = 9.6243 Re^{-0.7422} \alpha^{-0.1856} \delta^{0.3053} \gamma^{-0.2659} * [1 + (7.669 \times 10^{-8} Re^{4.429} \alpha^{0.92} \delta^{3.767} \gamma^{0.236})]^{0.1} \quad (2.42)$$

$$120 < Re < 10^4 \quad (2.43)$$

$$0.134 < \alpha = \frac{s}{h} < 0.9997 \quad (2.44)$$

$$0.012 < \delta = \frac{t}{x} < 0.048 \quad (2.45)$$

$$0.041 < \gamma = \frac{t}{s} < 0.121 \quad (2.46)$$

$$j = 0.6522 Re^{-0.5403} \alpha^{-0.1541} \delta^{0.1499} \gamma^{-0.0678} * [1 + (5.269 * 10^{-5} Re^{1.34} \alpha^{0.504} \delta^{0.456} \gamma^{-1.055})]^{0.1} \quad (2.47)$$

$$j = \exp (1.3) \alpha^{0.004} \delta^{0.251} \gamma^{0.031} Re^{0.0507 \ln Re - 1.07} Pr^{0.051} \quad (2.48)$$

The number of transfer units (NTU) can be estimated from the problem specifications knowing the heat exchanger effectiveness  $\varepsilon$  from the inlet and outlet temperatures, and the specific heat ratio  $C^*$  determined by the properties of the fluid at the mean temperatures as follows :

$$NTU = \frac{UA}{C_{min}} \quad (2.49)$$

$$c^* = \frac{C_{min}}{C_{max}} = \frac{(\dot{m}Cp)_{min}}{(\dot{m}Cp)_{max}} \quad (2.50)$$

$$\varepsilon = \frac{1 - \exp [-NTU(1 - c^*)]}{1 - c^* \exp [-NTU(1 - c^*)]} \quad (2.51)$$

$$UA = \frac{1}{[\frac{1}{h_c \eta_{s,c} A_c} + \frac{1}{h_h \eta_{s,h} A_h} + \frac{a}{A_w k_w} + \frac{R_{f,c}}{A_c} + \frac{R_{f,h}}{A_h}]} \quad (2.52)$$

The overall thermal coefficient ‘UA’ is calculated by neglecting in the first iteration the wall resistance and the longitudinal thermal conductance of Equation (2.52).

The surface and the fin's efficiency are calculated respectively using Equations (2.53) and (2.54).

$$\eta_s = 1 - \frac{A_{fin}}{A} (1 - \eta_{fin}) \quad (2.53)$$

$$\eta_{fin} = \frac{tgh(M * L)}{M * L} \quad (2.54)$$

$$M = \sqrt{\frac{2h}{k_{fin} t}} \quad (2.55)$$

$$L = 0.5h - t \quad (2.56)$$

$\varepsilon$ : Recuperative effectiveness (%).

$R_f$  : The fouling factor.

$\eta_s$  : The overall surface efficiency (%).

$\eta_{fin}$ : Single fin efficiency (%).

L: the fluid flow length (m).

As for the pressure drop ( $\Delta P$ ), it was calculated by considering the total pressure drops in the HEX, including the entrance effect, the momentum effect, the core friction, and the exit effect according to the following equation [242]:

$$\frac{\Delta P}{P_i} = \frac{G^2}{2g_c\rho_i} [(1 - \sigma^2 + k_c) + 2\left(\frac{\rho_i}{\rho_0} - 1\right) + f \frac{L}{r_h} \frac{\rho_i}{\rho_0} - (1 - \sigma^2 - k_e) \frac{\rho_i}{\rho_0}] \quad (2.57)$$

$\sigma$ : Ratio of minimum free flow area to the frontal area.

$k_c$  : The entrance pressure loss coefficient.

$k_e$ : The exit pressure drop coefficient.

i,0: suffix refers to the inlet and outlet.

$\rho$ : Fluid density.

The weight of the HEXs is calculated from the obtained volume and the chosen material. The intercooler is a plate-fin heat exchanger with offset strip fins made from aluminum. The regenerator consists of steel offset strip fins heat exchanger. The flowchart of the design methodology of both the regenerator and the intercooler is depicted in Figure 2.31. The main geometrical parameters of the fins are presented in Table 2.4.

Table 2.4: Geometric dimensions of the offset fins for the HEX.

s variable	h	x	t
	4	3.18	0.2

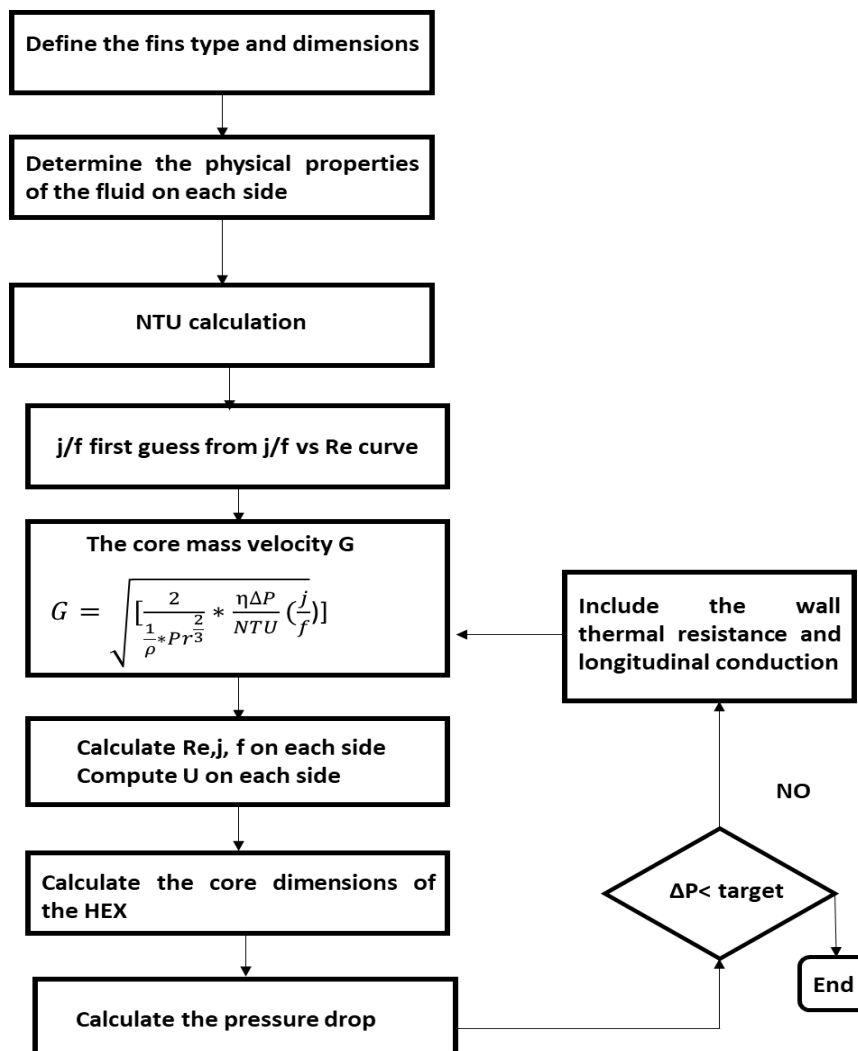
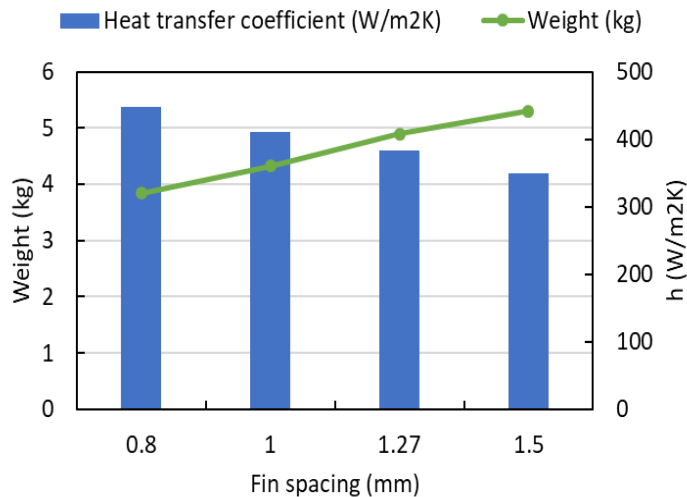


Figure 2.31: Design steps of the Counter-flow plate-fin heat exchanger.

## ➤ Results

The HEX weight is affected by the geometrical aspects including the design parameters, as well as the operating conditions including the mass flow rate and the inlet and output temperatures. As seen in Figure 2.32, a linear relationship exists between the fin spacing and the HEX weight. As the fin spacing increases the weight of the HEX increases, while the heat transfer coefficient decreases. The HEX weight increases since a higher number of fins and a larger area are required for a fixed heat power. As a result of the reduced flow velocity entering the fins, the heat transfer coefficient decreases. Therefore, a compromise should be realized to obtain both highly efficient and light HEX.



**Figure 2.32:** The impact of fin spacing on the HEX weight and the heat transfer coefficient.

The power of the GT range extender is related to the mass flow rate that enters the system. Increasing the power output of the GT system increases the mass flow rate needed. It is shown from Figure 2.33 that there is a linear relationship between the mass flow rate and the HEX weight. Therefore, for higher system power, heavier and bulkier heat exchangers are required. For example, for a doubled output power as if for a doubled mass flow, the weight of the HEX is also doubled.

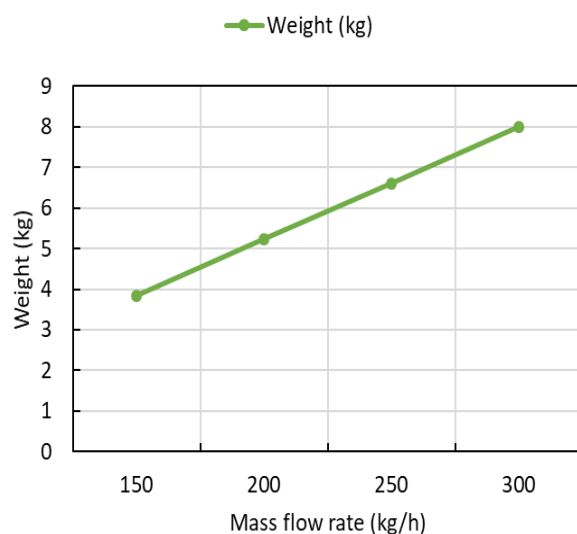


**Figure 2.33:** Impact of increasing the HEX mass flow rate on its weight.

The pinch sensibility analysis is conducted in Figure 2.34. Increasing the pinch leads to a reduction of the temperature of the cold air at the exit of the recuperator. This results in a decrease in the thermal power of the HEX as well as a reduction of the HEX's effectiveness.

Although reducing the pinch results in a higher temperature at the exit of the recuperator on the cold side and a higher HEX efficiency, it increases the HEX weight. For instance, reducing the HEX pinch from 124 °C to 25 °C multiplies the HEX weight by 3. In addition, it should be noted that the gradient of weight variation and thermal power when the pinch is below 50 °C varies drastically.

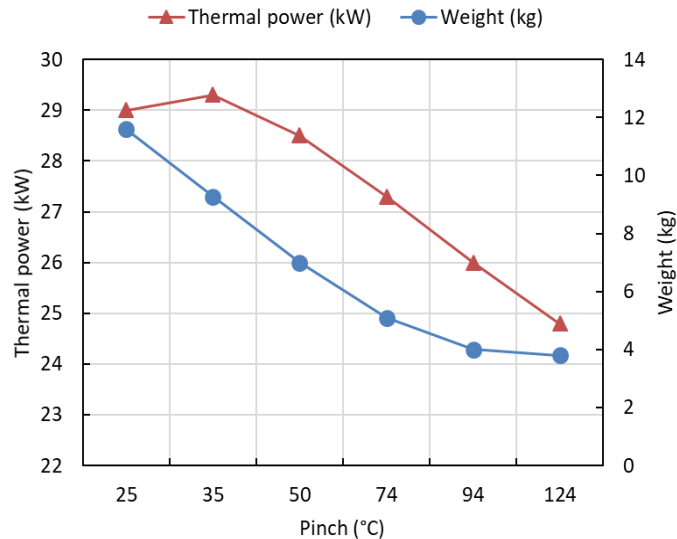


**Figure 2.34: Impact of pinch variation on the HEX weight.**

The estimated weight of the regenerator of the different GT architectures is presented in Figure 2.35. In all four configurations, the same design parameters for HEX are considered, including fin spacing, height, length, and pressure drop. Furthermore, the power output of the range extender is estimated at 20 kW. It can be seen that the heavier regenerator is for the RGT cycle mainly since the mass flow rate needed to achieve the fixed power output is higher (almost double the other configurations). Similarly, for the other configurations, the lighter regenerator corresponds to the cycle operating at higher temperatures, hence, lower mass flow rates. On the other hand, it can be seen that there is no considerable change in the heat transfer coefficient since the main geometrical parameters are the same.

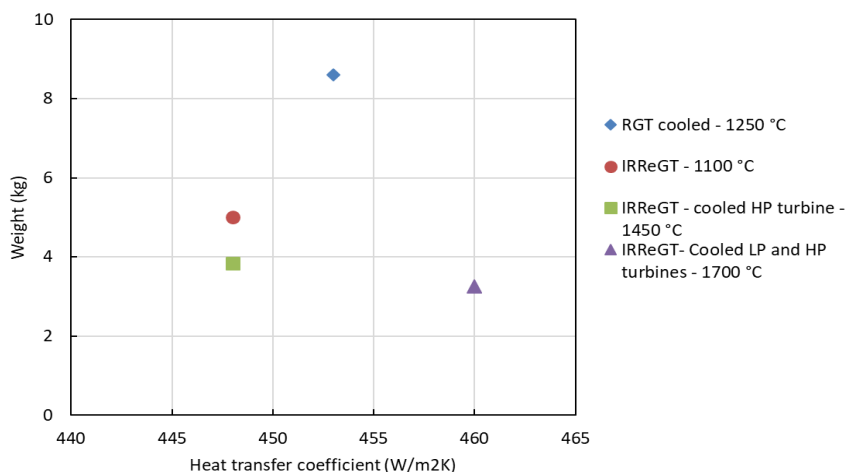


**Figure 2.35: Recuperator weight estimation for four GT configurations.**

In the intercooler, less thermal energy is exchanged than in the regenerator. As well, as aluminum material is used for the intercooler with approximately one-third the density of steel used for the regenerator, there is a greater weight difference between the intercooler and the regenerator, as shown in Figure 2.35 and Figure 2.36.

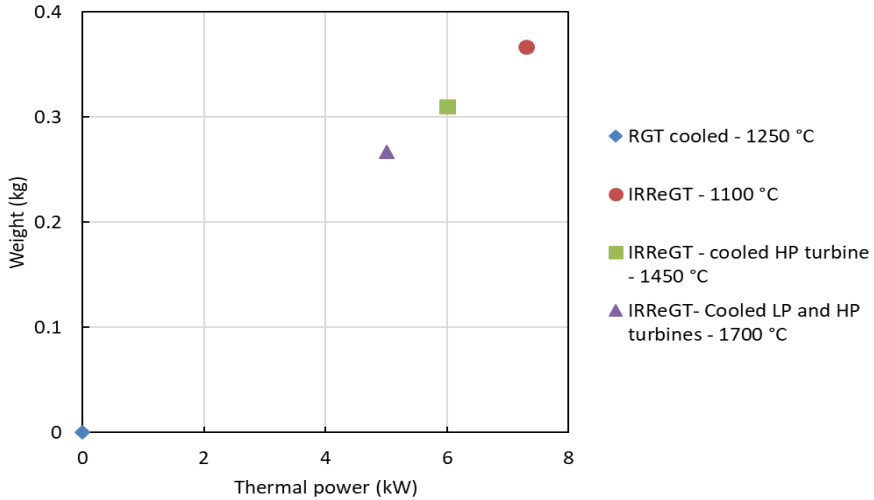


**Figure 2.36: Intercooler weight estimation for four GT configurations.**

### 2.5.3. Results

A weight assessment involves summing the weights of the various components.

This includes all the components:

- The turbomachinery system weight (compressors, turbines, shafts, and bearings) are calculated in Section 2.5.1.
- The heat exchangers weight (intercoolers and recuperators) are calculated in Section 2.5.2.
- The combustion chamber weight is estimated based on an existing combustion chamber [258] depending on its power output and mass flow rate [87].
- The electric generator is estimated to have a power-to-weight ratio of 3 kW/kg [243].
- The accessories, the valves, and the electric inverter are estimated as a package of 10 kg considered for all the configurations.
- A safety factor of 10 % is added to all the configurations.

It should be noted that for the cooled RGT cycle and the IRReGT cycle with two cooled turbines, the air is extracted before entering the compressor, hence an external system is needed to force the air to enter the shaft.

The comparison of the weight, efficiency, and net specific work of the considered cycles is presented in Figure 2.37, and Figure 2.38.

- Compared to other configurations, the cooled RGT cycle is the worst, it has the lowest net specific work, resulting in a high mass flow rate leading to heavy and bulky components.
- Through the introduction of cooling techniques, GT configurations have increased both net specific work and efficiency due to the reduction in mass flow rate, resulting in weight savings. For instance, comparing the baseline cycle and the IRReGT with a cooled HP turbine, it can be

seen that the cycle efficiency increases by 4 points, with no significant change in the system weight.

- There is no significant difference between the IRReGT cycle with a cooled HP turbine and the IRReGT cycle with two cooled turbines in terms of weight and efficiency.

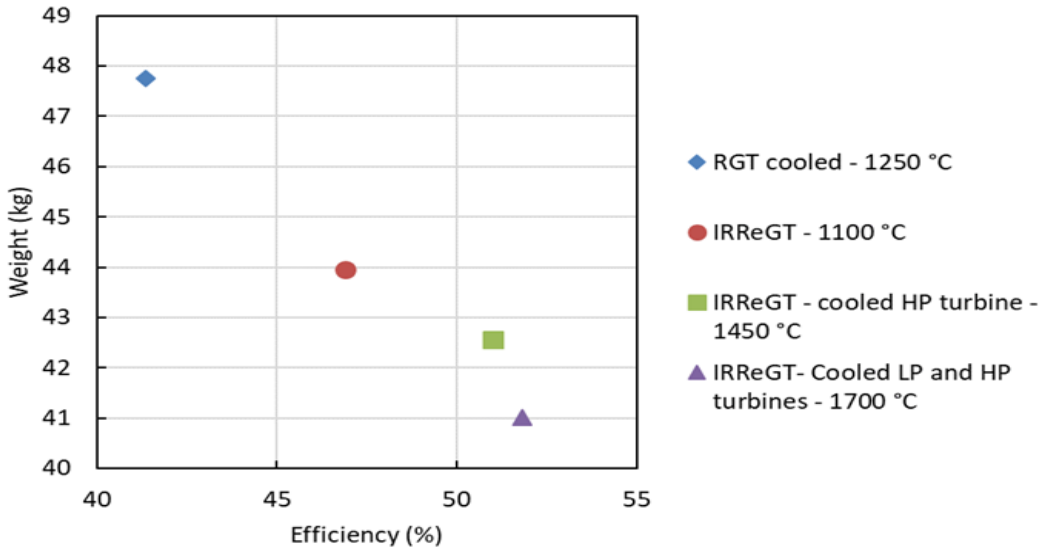


**Figure 2.37: Comparison of the efficiency and weight of different GT configurations.**

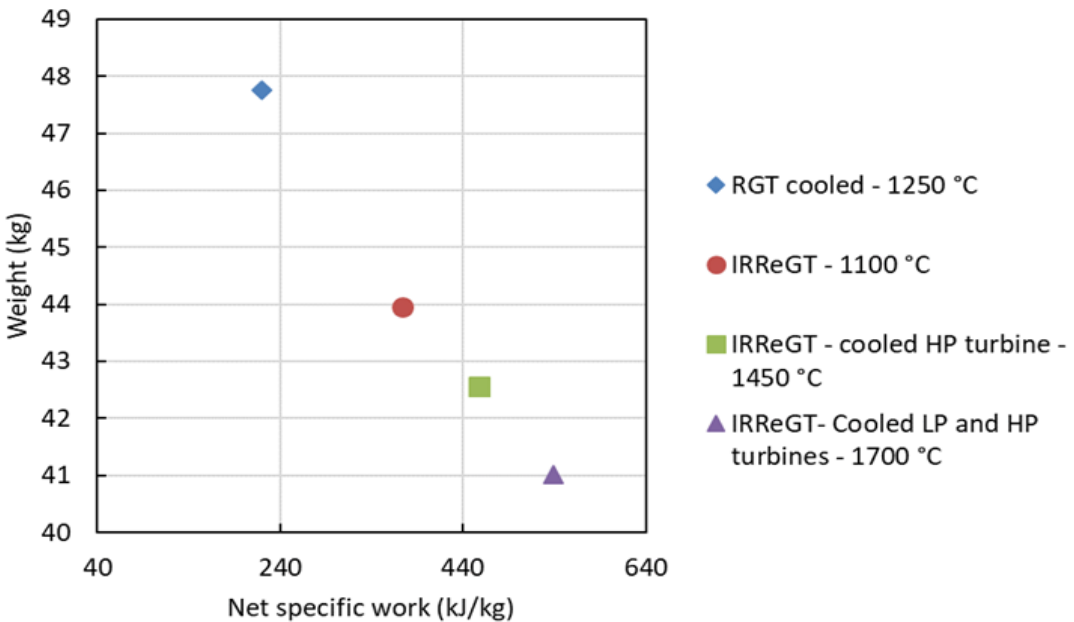


**Figure 2.38: Comparison of the net specific work and weight of different GT configurations.**

Figure 2.39 illustrates the part of each component from the system's overall weight for the different investigated configurations. It can be concluded that the worst configuration is the cooled RGT configuration which accounts for the heavier recuperator weight. Compared to other GT configurations, the IRReGT cycle with two cooled turbines is lighter (41 kg). However, the IRReGT cycle with a cooled HP turbine, despite being heavier (42.5 kg), has a simpler design since it only includes one cooled turbine.

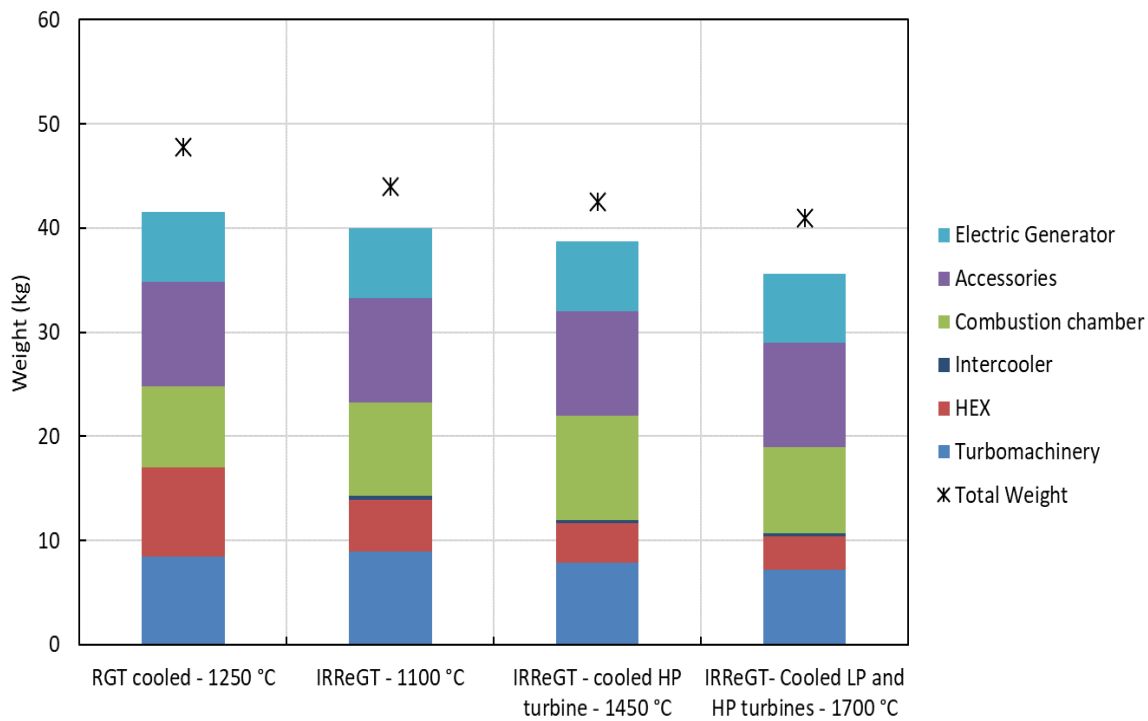


**Figure 2.39: Comparison between the components' weight for the different studied cycles.**

Based on these findings, the IRReGT cycle with a cooled HP turbine is the most convenient. First, it presents a higher efficiency (51 %) than the RGT, the standard IRReGT cycle, and a relatively very close efficiency to the IRReGT cycle with two cooled turbines. Likewise, the weight (42.5 kg) and the net-specific work (457.6 kJ/kg) follow the same pattern. In addition, the chosen cycle is less complicated than the IRReGT cycle with two cooled turbines since only one turbine is cooled, and since no external system to provide air before the compressor inlet to the shaft is present.

## 2.6. Conclusions

Gas turbines are potential energy converters for series hybrid electric vehicles. They are auxiliary power units capable of charging the batteries of electric cars once depleted. Many steps are proposed for improving gas turbine efficiency, such as selecting the best cycle architecture, increasing the pressure, and increasing the turbine inlet temperature.

Therefore, this chapter presents a methodology to choose the optimal GT cycle and its optimal conditions to be used as a range extender for SHEV. The first part of this chapter consists of conducting a parametric study for the recuperated GT cycle. The thermodynamic analysis has identified the IRReGT cycle with two compression stages with an intercooler, two expansion stages with reheating, and a recuperator operating at a maximum pressure of 9 bar as the most efficient cycle.

A detailed exergetic analysis determined that the combustion chamber accounted for the majority of energy loss. Increasing the turbine inlet temperature is a solution for both the exergy destruction in the combustion chamber and improving the cycle efficiency. As a consequence, novel GT configurations were suggested; they consist of GT cycles with cooled turbine blades based on the IRReGT uncooled cycle. Convection cooling was applied to reach higher turbine inlet temperature that overcomes the turbine material limitations. The thermodynamic analysis outlined the impact of cooling the turbine

blade on the cycle efficiency compared to the standard IRReGT cycle. According to the results for the different proposed cycles with blade cooling, the cycle efficiency was affected by the turbine blade temperature, the turbine inlet temperature, the turbine efficiency, and the coolant effectiveness. In addition, while cooling the turbine blade appeared to decrease the turbine's efficiency, the overall cycle efficiency increased due to higher turbine inlet temperatures, which generally overcome the loss of the coolant flow and improve the cycle efficiency.

The auxiliary power unit should be highly efficient, compact, and simple in design since it will be integrated into the vehicle. Therefore, the third part of this chapter sheds the light on the technological aspect of the GT cycles. Four realistic cycles were compared taking into consideration the material constraints of the turbine and the recuperator. The 3D printing technique was used for the turbine as it allows producing complex geometries in a compact package. The limitations of 3D printing, however, should be considered, such as the minimum wall thickness (0.16 mm) and the minimum diameter (0.5 mm). Additionally, the weight of different components of GT cycles was evaluated. Among the tested configurations, the IRReGT cycle with a cooled HP turbine and the IRReGT cycle with two cooled turbines presented the highest efficiency and the lowest weight. The first cycle, the IRReGT cycle with a cooled HP turbine was chosen since it is less complex and has a very close weight and efficiency than the other cycle. The thermodynamic analysis showed that temperatures of 1450 °C can be reached with an increase of the cycle efficiency of 4.1 points (51 %) compared to the basic IRReGT cycle (46.9 %) for melting material temperatures of 1100 °C. The efficiency of the cooled turbine appeared to decrease by around 2.5 points compared to the uncooled turbine. The weight of the booster was estimated to 42.5 kg.

Since the HP cooled turbine is the most critical component in the current cycle, the next chapter presents a detailed design approach for the cooled turbine. The HP cooled turbine consists of a radial turbine operating at 9 bar, with an expansion ratio of 3. The inlet temperature of the turbine is 1450 °C. This turbine reaches such high temperatures by introducing coolant air in a smooth cooling channel into the turbine blade, which passes through the hottest area, including the leading edge. The fraction of required coolant air is 1.41 %. Using additive manufacturing, this complex geometry is developed while respecting the limitations of 3D printing, such as the minimum wall thickness (0.16 mm) and maximum hole diameter (0.5 mm). The design procedure reported in Chapter 3 consists of a 1D simulation to predict the overall geometry of the turbine, followed by a 3D simulation in ANSYS CFX.

# **Chapitre 2: Etude Thermodynamique et Technologique des Cycles de Turbines à Gaz avec Refroidissement des Aubes**

## **2.1. Introduction**

Les cycles de turbine à gaz sont des convertisseurs d'énergie potentiels pour les futurs groupes motopropulseurs des véhicules. Par rapport à d'autres convertisseurs d'énergie, ces systèmes offrent des avantages inhérents aux véhicules, tels qu'un rendement élevé, une capacité multicarburant, une capacité de cogénération, un faible niveau de vibration et de bruit, et une réduction du nombre de composants et du poids.

Les turbines à gaz sont surtout populaires dans les véhicules électriques hybrides en série, où un entraînement entièrement électrique est fourni avec un dimensionnement adéquat de la capacité de la batterie, ce qui permet de réduire les émissions directes. Dans ces systèmes, les GT sont découplées de la charge du véhicule permettant leur fonctionnement à un rendement maximal.

Sur la base de ces résultats, ce chapitre présente une méthodologie pour l'identification du cycle GT optimal pour les groupes motopropulseurs SHEV en termes d'efficacité supérieure et d'aspects techniques appropriés. Ainsi, l'étude commence par une évaluation paramétrique pour choisir la configuration optimale du cycle GT et les conditions de fonctionnement optimales correspondantes en termes d'efficacité et de travail de sortie spécifique. Ensuite, l'étude exergétique a permis d'identifier la chambre de combustion comme la principale source de destruction d'exergie. En conséquence, l'augmentation du TIT est étudiée pour bénéficier à la fois d'une efficacité accrue du cycle GT et d'une destruction d'exergie réduite. Comme la TIT est limitée par les contraintes des matériaux, le refroidissement des aubes de turbine est exploré. Par conséquent, la deuxième partie de ce chapitre consiste en une analyse thermodynamique des prolongateurs d'autonomie avec des configurations d'aubes de turbine refroidies.

Enfin, comme le prolongateur d'autonomie, la turbine à gaz, est intégrée au véhicule, le cycle de turbine à gaz doit être hautement efficace, compact, léger et techniquement réalisable. En conséquence, une étude technologique est réalisée pour estimer le poids et la complexité du système pour différentes configurations de GT.

## **2.2. Configuration Optimale du Cycle de GT**

Cette section présente la méthodologie appliquée pour identifier le cycle de turbine à gaz le plus approprié en termes d'efficacité et de travail spécifique net. L'étude comprend une analyse visant à déterminer les conditions de fonctionnement optimales à différentes étapes du cycle. L'analyse thermodynamique est développée en utilisant Visual Basic for Applications (VBA) et NIST REFPROP (National Institute of Standards and Technology (NIST), Colorado, USA). Le cycle initialement considéré est le cycle GT avec récupération.

Diverses contraintes technologiques pour les composants automobiles sont basées sur les données de l'état de l'art des technologies disponibles et nouvellement développées. Ces contraintes techniques comprennent la TIT maximale, le taux de compression maximal par étage et l'efficacité maximale des composants. Les contraintes de conception des voitures comprennent cependant le nombre d'étages de compression et de détente, ainsi que le nombre d'échangeurs de chaleur, ce qui simplifie la complexité de l'intégration du système.

## 2.2.1. Méthodologie

Le cycle considéré est le cycle de turbine à gaz avec récupération représenté à la Figure 2.1. La première loi de la thermodynamique est appliquée pour calculer le travail du compresseur et de la turbine, en négligeant le transfert de chaleur avec l'environnement et la variation de l'énergie cinétique et potentielle à l'entrée et à la sortie de chaque composant. L'air est considéré comme le fluide de travail. Les rendements isentropiques du compresseur, de la turbine et du récupérateur sont considérés comme constants et égaux à 0.8, 0.85 et 0.8, respectivement, sur la base des véhicules à turbine à gaz Chrysler [36] et du système IRReGT de Bou Nader [1]. L'analyse thermodynamique prend en compte le rapport air/carburant dans la chambre de combustion. La réaction est une combustion en mélange pauvre entre l'air et le carburant, ce dernier étant du méthane. Lorsque les étages de compresseur sont augmentés, un refroidisseur intermédiaire est ajouté pour refroidir l'air comprimé avant qu'il n'entre dans l'étage de compresseur suivant. Le refroidisseur intermédiaire est soumis aux conditions ambiantes et, en raison du pincement, la température à sa sortie est supposée être de 35 °C.

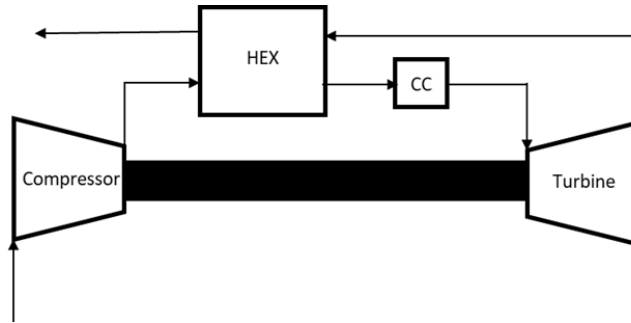


Figure 2.1 : Cycle de turbine à gaz avec récupération.

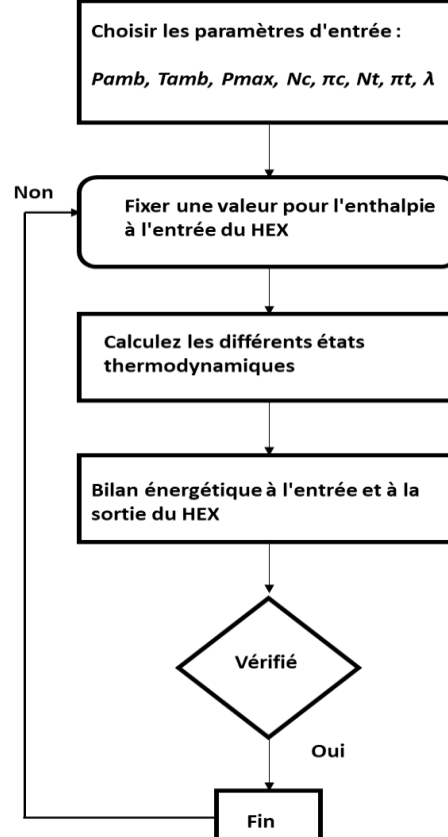


Figure 2.2 : Méthodologie de l'analyse thermodynamique.

La méthodologie utilisée pour l'analyse thermodynamique est illustrée dans le graphique de la Figure 2.2. Les paramètres d'entrée sont : la pression ambiante ( $P_{amb}$ ) est de 1.013 bar, la température ambiante ( $T_{amb} = 25^{\circ}\text{C}$ ), la pression maximale ( $P_{max}$ ), le nombre d'étages du compresseur ( $N_c$ ), le taux de compression ( $\pi_c$ ), le nombre d'étages de la turbine ( $N_t$ ), le taux d'expansion ( $\pi_t$ ) et le coefficient d'excès d'air ( $\lambda$ ).

L'analyse est exécutée en faisant varier les différents paramètres du cycle de turbine à gaz et en comparant les résultats pour choisir la configuration optimale en termes d'efficacité supérieure et de travail spécifique net supérieur. Les différents paramètres testés sont le nombre d'étages du compresseur, le nombre d'étages de la turbine, la pression maximale, la température d'entrée de la turbine et le rendement isentropique de la turbine.

## 2.2.2. Résultats

L'analyse est réalisée en faisant varier le nombre d'étages de compresseur (refroidisseur intermédiaire + compresseur) pour la même pression maximale afin de déterminer la configuration la plus appropriée. Bien que l'augmentation du nombre d'étages de compresseur conduise à un système plus complexe, elle réduit le travail nécessaire du compresseur en se rapprochant de la transformation isotherme.

Les résultats de la Figure 2.3 montrent que pour la même pression maximale, le travail nécessaire du compresseur diminue avec l'augmentation du nombre d'étages. L'ajout de deux étages de compressions réduit son travail de 50 kJ/kg et augmente l'efficacité du cycle de 4 points par rapport à un étage unique. L'ajout de trois étages de compressions réduit le travail du compresseur de 14 kJ/kg et augmente l'efficacité du cycle de 2 points par rapport à un double étage. Par conséquent, la réduction du travail du compresseur améliore les performances du cycle en augmentant le travail spécifique net et le rendement thermique du cycle de la turbine à gaz.

En raison de ces problèmes complexes, le cycle biétagé a été choisi dans cette étude, d'autant plus que l'ajout d'autres étages de compresseur n'a pas permis d'améliorer significativement le cycle de la turbine à gaz.

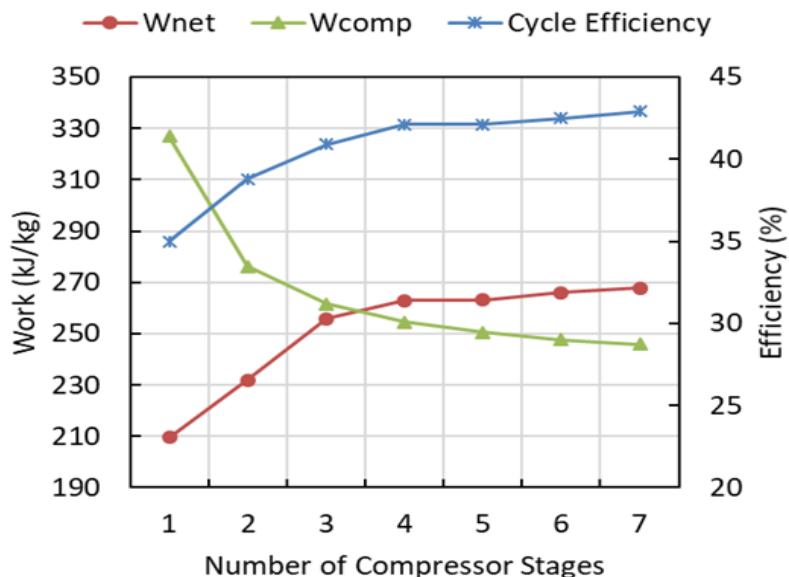


**Figure 2.3:** Variation du travail du compresseur, du travail spécifique net et du rendement du cycle en fonction du nombre d'étages du compresseur.

D'après la Figure 2.4, l'augmentation du nombre d'étages de la turbine améliore le travail de la turbine, ainsi que le travail spécifique net. Le travail et le rendement d'une turbine à deux étages sont respectivement supérieurs de 65 kJ/kg et de 4 points par rapport à une turbine à un étage. Les étages de turbine supplémentaires avec réchauffement intermédiaire entraînent une augmentation de moins de 30 kJ/kg du travail de la turbine et une augmentation de 2 points du rendement thermique du cycle. Les étages de turbine triples n'ont pas abouti à des avantages supplémentaires par rapport aux doubles étages. Par conséquent, deux étages de détente sont choisis.

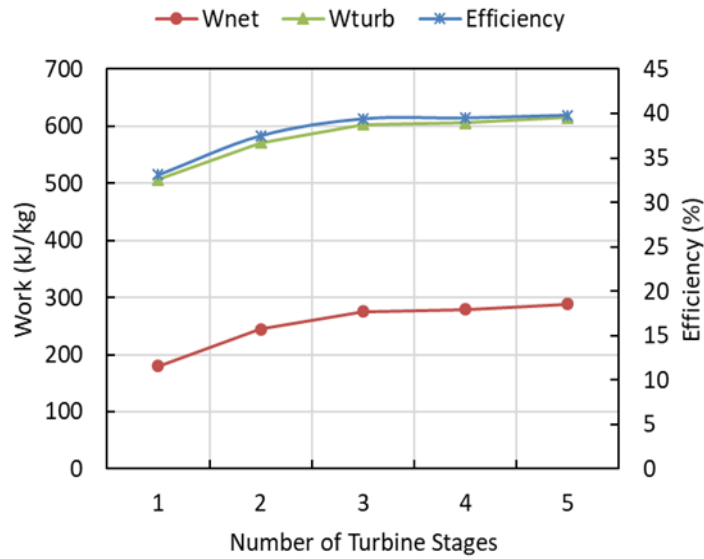


**Figure 2.4:** Variation du travail de la turbine, du travail spécifique net et du rendement du cycle en fonction du nombre d'étages de la turbine.

En considérant un cycle de turbine à gaz avec récupération, avec deux étages de compression et deux étages de turbine, une variation de la pression maximale du système est effectuée pour choisir la pression optimale en termes d'efficacité thermique et de travail spécifique plus élevés. La TIT est fixée à 1100°C. La Figure 2.5 illustre l'impact de l'augmentation de la pression sur les différents composants du cycle.

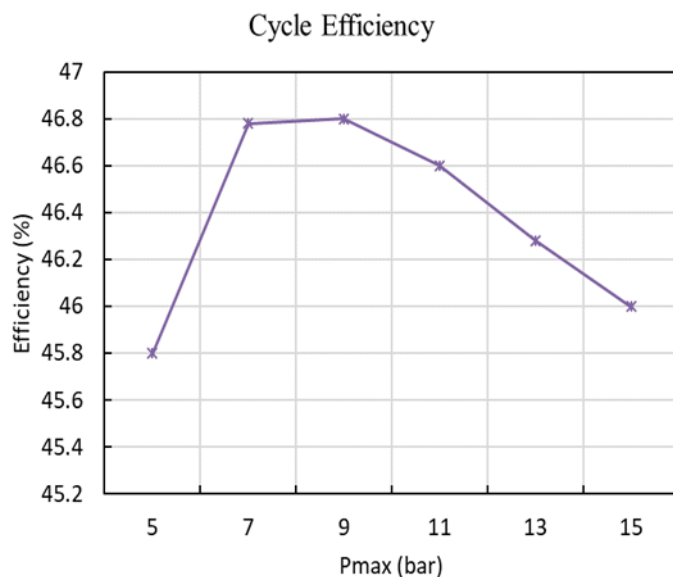


**Figure 2.5:** Variation des différents paramètres en fonction de la pression maximale.

La courbe du rendement thermique représente un front de Pareto. On constate que le rendement thermique du cycle de la turbine à gaz augmente à des taux de compression plus faibles, puis lorsque la pression maximale atteint 9 bars, on obtient une diminution du rendement. La raison en est l'augmentation de la puissance nécessaire pour faire fonctionner le compresseur, ce qui réduit la puissance utile nette que la turbine à gaz peut générer.

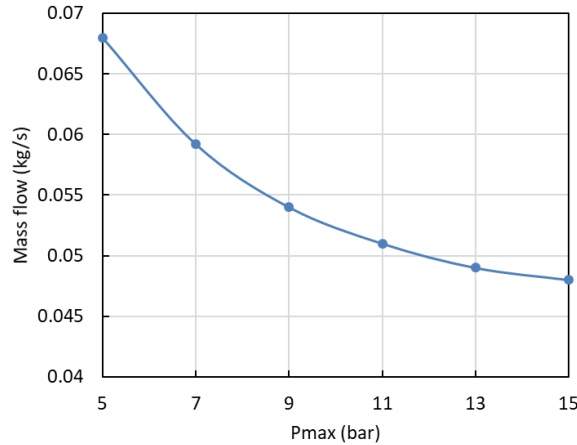


Figure 2.6: Variation du débit massique d'air en fonction de la pression maximale.

L'augmentation de la pression maximale entraîne une augmentation du travail de la turbine et du travail spécifique net. Par conséquent, pour une puissance fixe, moins d'air est nécessaire dans le cycle. La Figure 2.6 montre qu'en augmentant la pression maximale de 4 bar à 9 bar, le débit massique passe de 0.068 kg/s à 0.054 kg/s.

Les avantages de l'augmentation de la température d'entrée de la turbine sont illustrés à la Figure 2.7. Le travail spécifique de la turbine, ainsi que l'efficacité du cycle, sont plus élevés. Cependant, les points de fusion des matériaux limitent la température à l'entrée de la turbine. Tant que la température ne dépasse pas 1100 °C, il n'est pas nécessaire d'utiliser des matériaux spéciaux et la turbine peut être fabriquée avec des alliages courants et peu coûteux [87].

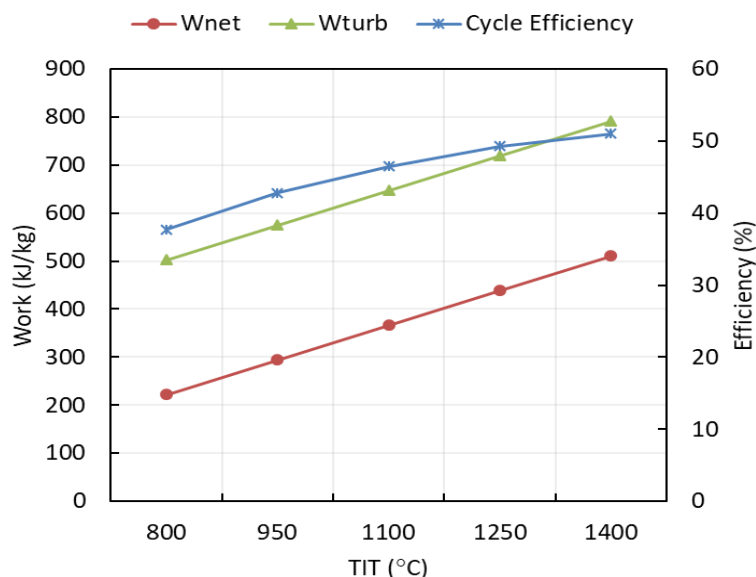


Figure 2.7: Variation de différents paramètres avec le TIT.

Le rendement isentropique de la turbine est le rapport entre le travail réel de la turbine et le travail maximal que peut accomplir la turbine dans le cas d'une puissance isentropique. Un rendement isentropique plus élevé de la turbine signifie des pertes thermiques plus faibles. Comme l'illustre la Figure 2.8, l'augmentation du rendement isentropique de la turbine entraîne une augmentation linéaire du rendement du cycle et du travail net.

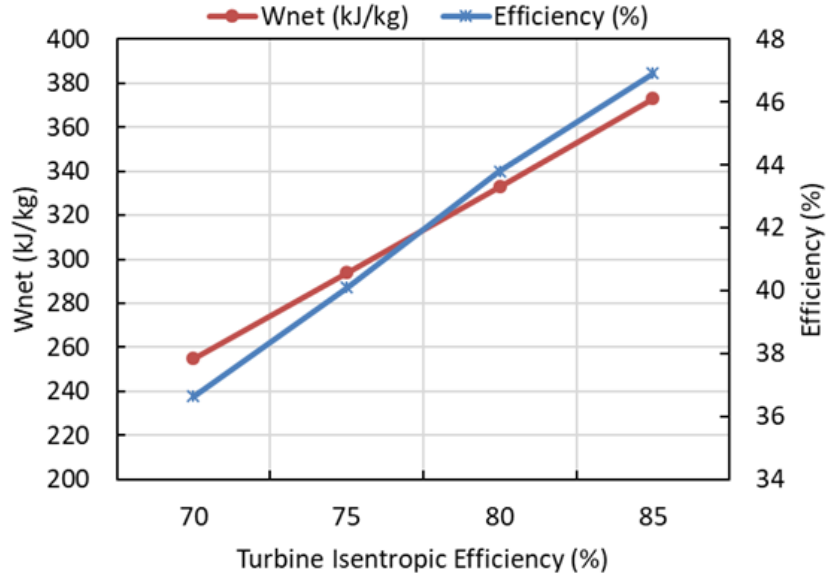


Figure 2.8: Variation du rendement du cycle et du travail spécifique avec le rendement isentropique de la turbine.

### 2.2.3. Discussions

Sur la base de l'analyse thermodynamique précédente, plusieurs conclusions peuvent être tirées.

- Les compressions et les expansions à plusieurs étages conduisent à une augmentation de l'efficacité du cycle. Il en résulte donc un cycle GT plus complexe, plus coûteux et plus lourd. Pour cette raison, une compression bi-étageée avec refroidisseur intermédiaire et une expansion bi-étageée avec réchauffage sont choisies. De cette façon, le cycle GT aura un rendement élevé et sera suffisamment compact pour être intégré dans le véhicule électrique.
- Un front de Pareto est obtenu lorsque la pression maximale du cycle GT varie. L'efficacité du cycle augmente pour les pressions inférieures à 9 bars, puis diminue pour les pressions supérieures à 9 bars. Pour cette raison, 9 bar est choisi comme la pression maximale du cycle GT.
- L'augmentation de la température du cycle GT est bénéfique pour le rendement du cycle, mais elle est limitée par les contraintes liées aux matériaux et au coût des turbines. L'avantage de l'application de la technique de refroidissement des aubes est la possibilité d'augmenter la TIT sans aucune limitation liée aux matériaux de fabrication. Cela permet d'augmenter l'efficacité globale du cycle.

D'après ces résultats, le cycle IRReGT optimal illustré à la Figure 2.9 se compose d'une compression bi-étages, d'un refroidisseur intermédiaire, d'une expansion bi-étages avec réchauffement intermédiaire et d'un récupérateur. La pression maximale du cycle est de 9 bar. Ces résultats sont en accord avec ceux de [1].

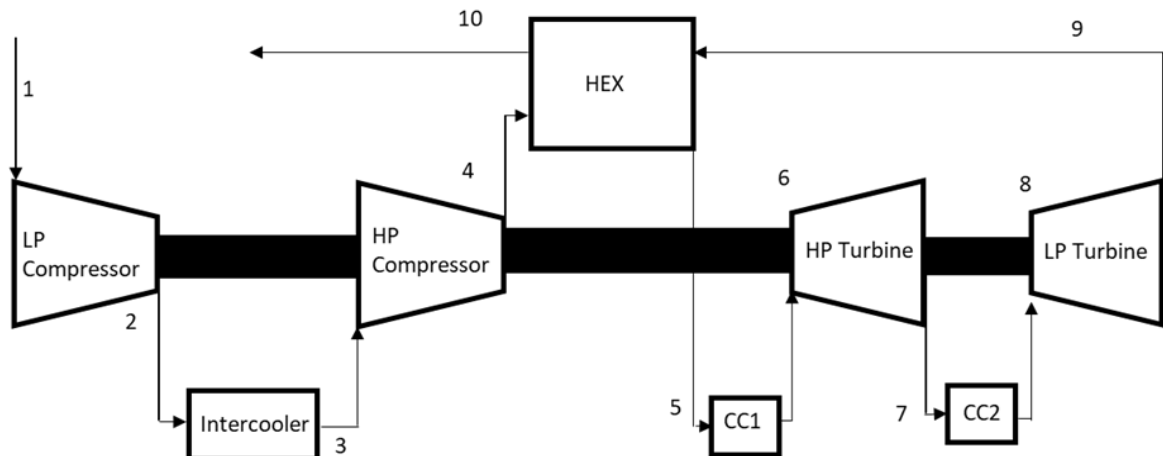


Figure 2.9: Configuration du cycle IRReGT cycle.

#### 2.2.4. Analyse exergétique

Le terme "exergie" désigne la quantité maximale de travail pouvant être produite par un système lorsqu'il s'équilibre de manière réversible avec son environnement ; c'est une mesure de la qualité de l'énergie. Il est basé sur la deuxième loi de la thermodynamique. Par conséquent, une analyse d'exergie est menée dans cette section pour évaluer les pertes dans le cycle actuel (cycle IRReGT) et pour calculer l'efficacité exergétique, qui mesure la différence entre l'efficacité de l'IRReGT et son maximum théorique. La formulation de l'exergie est extraite de [244].

La Figure 2.11 montre que la principale destruction d'exergie se produit dans la chambre de combustion (28 % dans la première chambre de combustion, 19 % dans la seconde chambre de combustion) pour le cycle actuel pour  $TIT = 1100^\circ\text{C}$ . La destruction d'énergie du compresseur et de la turbine est moins importante et peut être réduite en augmentant les rendements de ces composants.

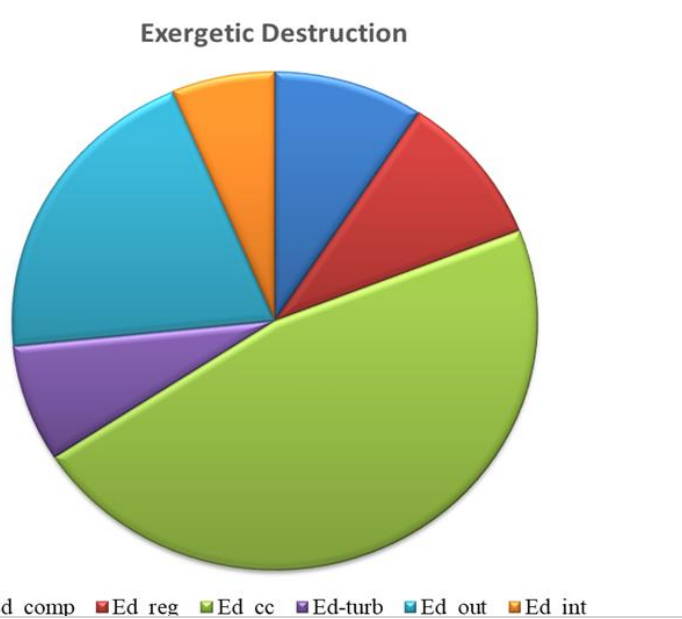


Figure 2.11: Destruction exergétique dans le cycle IRReGT pour un  $TIT = 1100^\circ\text{C}$  et une pression maximale de 9 bar.

En ce qui concerne les chambres de combustion, plusieurs études [208] recommandent d'augmenter la température moyenne pour réduire la destruction exergétique. Ceci peut être réalisé en réduisant la différence entre la température de l'air d'entrée et la température de la flamme et en augmentant la TIT,

qui est limitée par les contraintes métallurgiques. Ces pertes importantes signifient qu'une grande partie de l'énergie présente dans le combustible est gaspillée, alors qu'elle pourrait produire un travail utile.

Par conséquent, dans la section suivante, une nouvelle augmentation de la TIT du cycle GT est évaluée en introduisant les techniques de refroidissement pour surmonter les contraintes liées aux matériaux de fabrication.

### **2.3. Etude Thermodynamique des Cycles GT avec Refroidissement des Aubes**

Étant donné que l'augmentation de la TIT entraîne un meilleur rendement du cycle, les techniques de refroidissement sont obligatoires pour éviter les problèmes liés aux contraintes thermiques, à l'oxydation et à la durée de vie des composants. Il existe différentes technologies de refroidissement, notamment l'eau, la vapeur et, le plus souvent, l'air. En général, les aubes de turbine à micro-échelle sont soumises à un refroidissement par convection interne. Il s'agit d'un canal lisse dans lequel passe une fraction d'air comprimé provenant de la sortie du compresseur et inséré dans le pied de la turbine. Le fluide de refroidissement est chauffé lorsqu'il refroidit l'aube. Le fluide de refroidissement est généralement déchargé au niveau du bord de fuite et mélangé au flux principal. La technologie du refroidissement par convection a été développée de telle sorte qu'aujourd'hui le fluide de refroidissement peut être dirigé à l'intérieur de l'aube là où il est le plus nécessaire, comme aux bords d'attaque [147]. L'avantage de cette configuration de refroidissement est sa simplicité et son prix inférieur à celui des autres méthodes. Le choix de la méthode de refroidissement dépend également du niveau de température à chaque étape du cycle et de la faisabilité du prolongateur d'autonomie. Par conséquent, pour simplifier la complexité de l'intégration du système dans les véhicules, le refroidissement par convection est choisi. HiETA Technologies [210], experts en thermique et turbomachines, ont développé une microturbine à refroidissement interne utilisant la méthode de refroidissement par convection.

Diverses études ont examiné la méthodologie de l'analyse thermodynamique unidimensionnelle pour une aube de turbine refroidie, principalement pour prédire le débit massique du fluide de refroidissement nécessaire pour maintenir la température de la turbine en dessous de sa limite, ainsi que la température à la sortie du fluide de refroidissement.

D'autres scientifiques ont analysé le système GT en modélisant chaque composant du cycle séparément, puis en évaluant les performances globales [215]. Cependant, seules quelques études ont tenté de définir le "rendement" des turbines refroidies. Par conséquent, il n'y a pas de véritable accord sur la façon d'évaluer cette "efficacité", ce qui complique les approches théoriques.

Sur la base de ces résultats, cette section a pour objectif d'évaluer de nouvelles configurations du cycle GT basées sur le cycle IRReGT mais avec l'introduction des techniques de refroidissement par convection. Cette section vise à déterminer l'impact du refroidissement des aubes de turbine sur les performances du cycle. La masse de fluide de refroidissement nécessaire et sa température de sortie sont calculées en utilisant des corrélations empiriques de la littérature [211]. En outre, cette section introduit une nouvelle définition du "rendement de la turbine refroidie", dans le but de tester l'impact du refroidissement sur les performances de la turbine elle-même. La définition proposée est optimiste ; elle sous-estime la diminution du rendement de la turbine en raison de la négligence des paramètres liés à la géométrie de la turbine et les phénomènes 3D.

### 2.3.1. Méthodologie

Trois configurations de systèmes GT avec des aubes de refroidissement sont évaluées dans cette section et illustrées à la Figure 2.12. La première configuration (Figure 2.12a) consiste en un cycle RGT avec une turbine refroidie. L'air de refroidissement est extrait avant l'entrée du compresseur et inséré dans l'arbre creux de la turbine refroidie. L'air de refroidissement et le courant principal se mélangent à la sortie de la turbine. La deuxième configuration (Figure 2.12b) consiste à ne refroidir que la première turbine, la turbine HP du cycle IRReGT par refroidissement par convection interne. Une fraction de l'air comprimé est extraite pour refroidir l'aube de la turbine HP. L'air de refroidissement passe par un arbre creux jusqu'à l'aube de la turbine, où il circule dans le canal de refroidissement jusqu'au bord de fuite. Il sort ensuite à la sortie de la turbine HP et se mélange au flux principal. La masse d'air restante est refroidie à 35 °C. Ensuite, l'air est comprimé dans le deuxième compresseur. Le fluide est préchauffé dans un échangeur de chaleur avant d'entrer dans la première chambre de combustion, puis il est détendu dans le premier étage de la turbine. Ensuite, le flux de mélange est préchauffé dans la deuxième chambre de combustion avant d'être détendu par la turbine BP. Comme la turbine HP est refroidie, il est possible d'obtenir une TIT plus élevée, par rapport à une turbine LP non refroidie. Par conséquent, la température à l'entrée de la turbine BP est limitée par les propriétés des matériaux. Dans la turbine HP refroidie, il n'y a pas de détente du fluide de refroidissement. La détente se produit uniquement pour le reste du courant principal. En fonction de la TIT choisie à la turbine HP et de sa température de sortie, une deuxième chambre de combustion est ajoutée. À la sortie de la turbine HP, le réfrigérant et les gaz chauds se mélangent et se dilatent tous deux en produisant du travail. Le taux de compression du compresseur LP est supérieur à celui du compresseur HP pour garantir l'introduction du flux de réfrigérant dans la turbine HP. La dernière configuration proposée (Figure 2.12c) consiste à refroidir à la fois les turbines LP et HP. La turbine HP est refroidie à partir d'une fraction d'air provenant de la sortie du compresseur LP, tandis que la turbine LP est refroidie à partir de l'air extrait avant l'étage du compresseur LP. Les rendements isentropiques de la turbine non refroidie, des compresseurs et du régénérateur sont respectivement de 0.85, 0.8 et 0.8 selon Chrysler Corporation [36] pour toutes les configurations. Il est à noter que les pertes par mélange du fluide de refroidissement et du gaz chaud ne sont pas prises en compte.

L'analyse thermodynamique considérée est un raffinement de l'approche proposée par les études précédentes. L'étude thermodynamique se concentre sur la détermination de la masse du fluide de refroidissement nécessaire pour refroidir l'aube de la turbine en se basant sur des corrélations empiriques et des hypothèses issues de la littérature. La turbine est considérée comme un échangeur de chaleur avec une température de paroi constante.

La première étape de l'analyse thermodynamique est le calcul du débit massique du fluide de refroidissement. L'air de refroidissement circule dans des canaux jusqu'au bord de fuite, où il sort et se mélange au flux principal avant d'entrer dans la deuxième chambre de combustion. La turbine à refroidissement interne est traitée comme un échangeur de chaleur (Figure 2.13) fonctionnant à une température constante de paroi ( $T_w$ ). La température de sortie du fluide de refroidissement ( $T_{c,o}$ ) est exprimée en fonction de l'efficacité de l'échangeur de chaleur ( $\epsilon$ ).

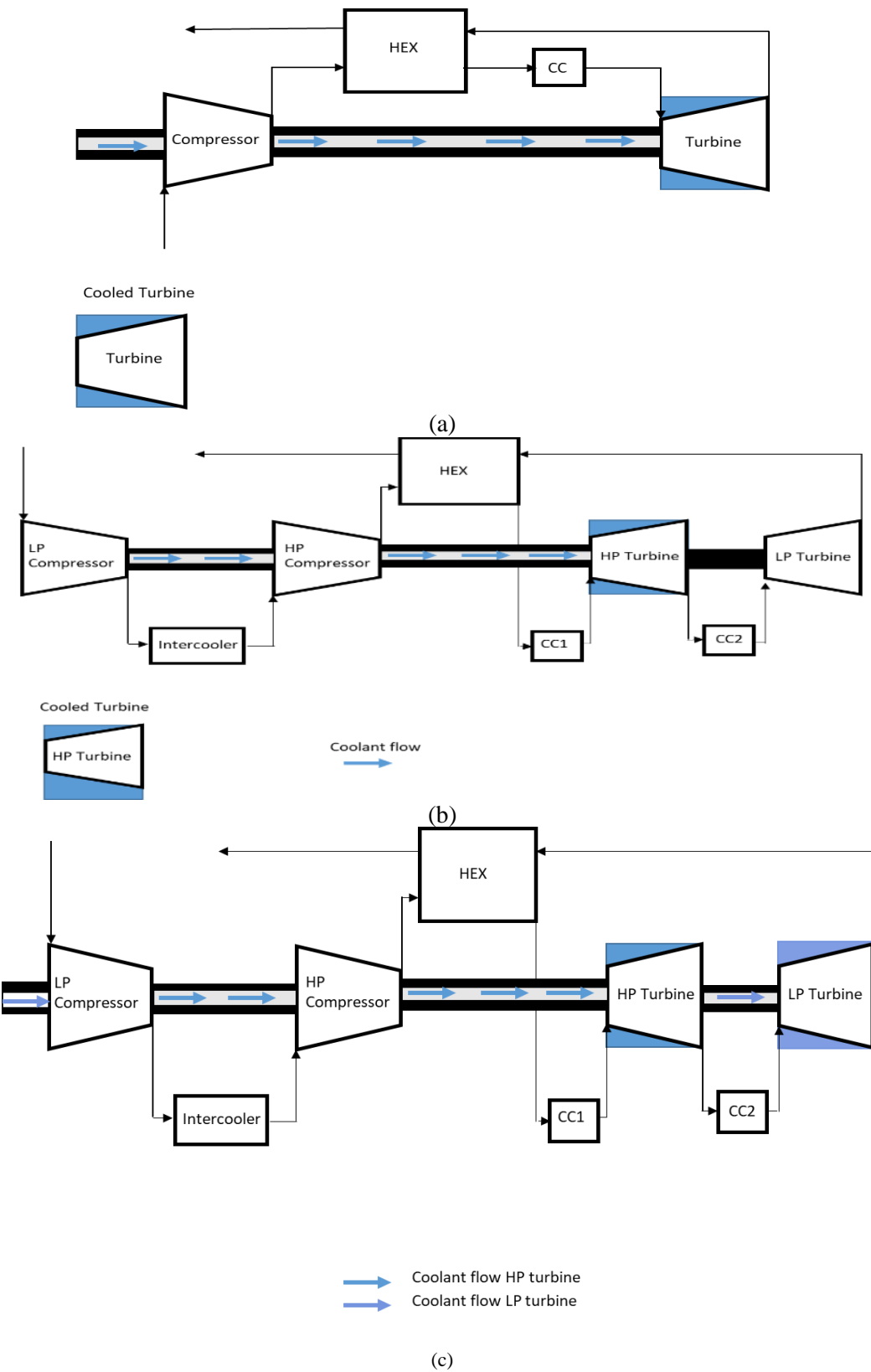


Figure 2.12 : (a) RGT avec aubes refroidies, (b) IRReGT cycle avec turbine HP refroidie, (c) IRReGT avec turbines HP et LP refroidies.

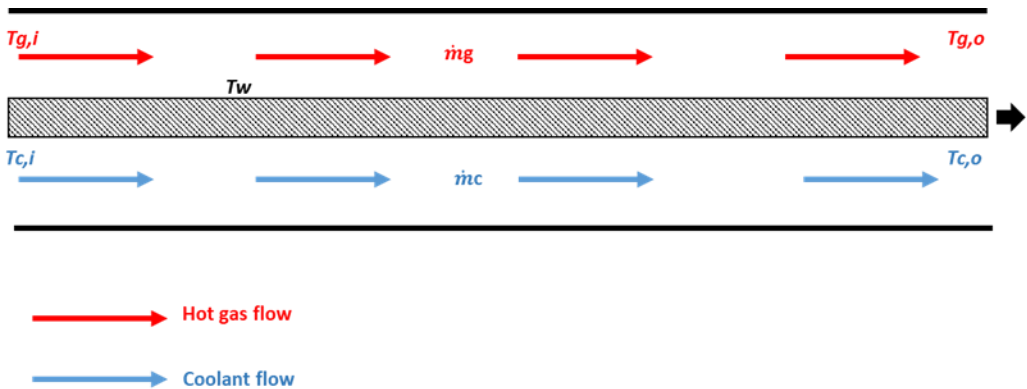


Figure 2.13: Présentation schématique de la turbine HP refroidie comme échangeur de chaleur.

La fraction d'air de refroidissement (X) est calculée par :

$$X = \frac{\dot{m}_c}{\dot{m}_c + \dot{m}_g} \quad (2.1)$$

X : Fraction du fluide de refroidissement

$\dot{m}_c$ : débit du fluide de refroidissement (kg/s)

$\dot{m}_g$ : débit du fluide chaud (kg/s)

A la sortie de la turbine refroidie, l'air de refroidissement et le gaz chaud se mélangent avant d'entrer dans la seconde chambre de combustion. L'enthalpie du flux mélangé est obtenue en utilisant le bilan énergétique.

$$\dot{m}_g h_g + \dot{m}_c h_c = (\dot{m}_g + \dot{m}_c) h_{mix} \quad (2.2)$$

Le rendement du cycle IRReGT avec une turbine HP refroidie est calculée à partir de l'équation suivante :

$$\eta = \frac{W_{net}}{(1 - X) * q_{cc1} + q_{cc2}} \quad (2.3)$$

$W_{net}$ : Travail specific net (kJ/kg)

$q_{cc1}$ : Chaleur spécifique ajoutée dans la première chambre de combustion (kJ/kg)

$q_{cc2}$ : Chaleur spécifique ajoutée dans la seconde chambre de combustion (kJ/kg)

### 2.3.2. Résultats

Cette étude évalue l'influence du refroidissement des aubes de la turbine sur le rendement du cycle. Le rendement du cycle dépend des principales variables de la turbine : la température des aubes de la turbine, la température d'entrée de la turbine, le rendement de la turbine et l'efficacité du fluide de refroidissement. Les résultats suivants sont soumis à l'IRReGT avec seulement une turbine HP refroidie. Les mêmes conclusions peuvent être tirées pour les autres configurations en testant l'effet de ces paramètres sur la performance du cycle. L'analyse thermodynamique actuelle peut sous-estimer la perte d'efficacité de la turbine car elle est basée sur des corrélations et n'est pas directement appliquée aux paramètres de conception de la turbine.

En considérant deux températures de parois de turbine, 950 °C et 1100 °C, l'analyse thermodynamique est effectuée en faisant varier le TIT sur la turbine refroidie, comme le montre la Figure 2.14. Lorsque le TIT HP augmente, bien qu'une fraction du fluide de refroidissement plus élevée soit nécessaire pour

refroidir les aubes de la turbine, l'efficacité du cycle augmente également. Dans cette configuration, la TIT HP a une température maximale de 1470 °C en raison de la turbine LP non refroidie (discutée plus tard). Au fur et à mesure que la température de fusion du matériau augmente, la fraction massique du fluide de refroidissement nécessaire diminue et le rendement du cycle augmente. Lorsque le TIT atteint 1450 °C, la fraction massique du fluide de refroidissement est de 0.014 et le cycle GT atteint 51 % en considérant un matériau qui peut supporter des températures jusqu'à 1100 °C.

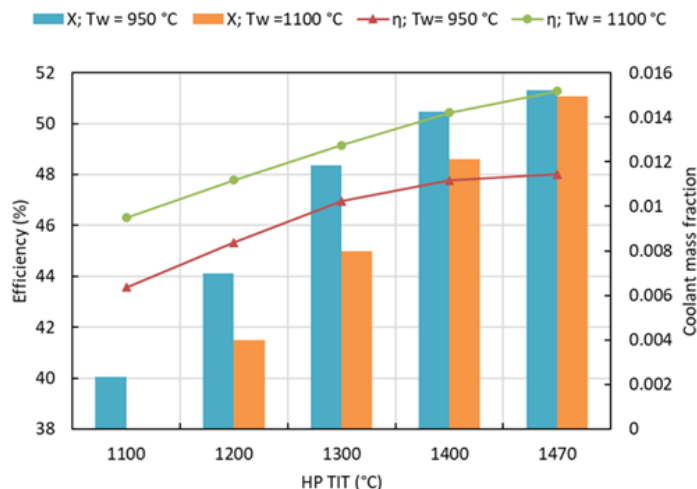


**Figure 2.14:** L'impact de la TIT HP sur le rendement du cycle et la fraction massique du fluide de refroidissement pour  $T_w = 950\text{ }^{\circ}\text{C}$  et  $T_w = 1100\text{ }^{\circ}\text{C}$ .

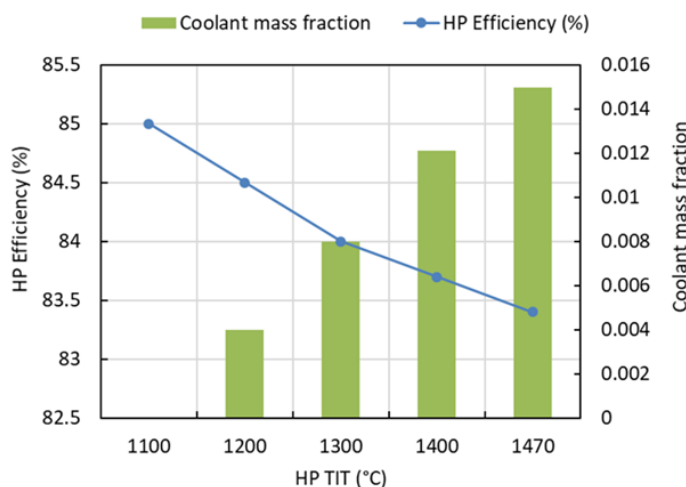


**Figure 2.15:** L'impact de l'augmentation de la TIT HP sur le rendement de la turbine HP.

La Figure 2.15 présente l'effet du refroidissement des aubes de la turbine sur le rendement de la turbine refroidie. À mesure que le TIT HP augmente, et que la fraction massique du liquide de refroidissement augmente, le rendement de la turbine refroidie passe de 0.85 pour une turbine non refroidie ( $T_w = 1100\text{ }^{\circ}\text{C}$ ) à 0.834 lorsque le TIT atteint 1470 °C.

Les résultats obtenus permettent de conclure que, bien que le refroidissement des aubes de la turbine par l'introduction d'air de refroidissement entraîne une diminution du rendement de la turbine, il améliore les performances globales du cycle en raison des températures d'entrée plus élevées de la turbine. Cette dernière permet généralement de surmonter la perte par le flux de liquide de refroidissement et d'améliorer le rendement du cycle.

## 2.4. Comparaison des Configurations de Turbine à Gaz

Quatre configurations de cycle de GT sont comparées dans cette section, leurs conditions de fonctionnement étant résumées dans le Tableau 2.1. Si l'on considère que la pression maximale admissible pour un compresseur centrifuge à un étage est de 3 bar, la pression de fonctionnement du cycle RGT est de 3 bar, tandis que les autres configurations fonctionnent à 9 bar. En raison de contraintes technologiques, la TIT de chaque architecture dépend du matériau de la turbine et du récupérateur. Le même matériau de turbine est utilisé dans toutes les architectures. La température maximale du récupérateur ne doit pas dépasser 900 °C, comme le recommande l'ASME pour les appareils sous pression, lorsqu'on utilise de l'acier inoxydable [221]. Cependant, la température de l'air chaud à l'entrée du récupérateur peut être un peu plus élevée car l'air chaud n'est pas soumis à une pression élevée et en raison de la présence d'un pincement. Par conséquent, les configurations proposées et leurs conditions de fonctionnement sont basées sur ces contraintes. Sur la base de ces affirmations, la première configuration est le cycle de référence, le cycle IRReGT. La deuxième configuration implique des aubes de turbine refroidies par RGT et fonctionnant à TIT = 1250 °C. La troisième configuration est le cycle IRReGT avec turbine HP refroidie fonctionnant à TIT = 1450 °C. La dernière configuration consiste en un cycle IRReGT avec une turbine HP refroidie et une turbine LP refroidie fonctionnant à TIT = 1700 °C.

Les résultats de l'analyse thermodynamique sont illustrés à la Figure 2.16. Parmi les cycles GT étudiés, plusieurs conclusions peuvent être tirées. Tout d'abord, en comparant le cycle IRReGT de base et le cycle IRReGT avec une turbine HP refroidie, on constate que la technique de refroidissement permet d'augmenter l'efficacité du cycle (4.1 points) et le travail spécifique net (80 kJ/kg) grâce à l'avantage d'atteindre une TIT plus élevée qui dépasse la température limite du matériau. De plus, alors que l'utilisation du refroidissement diminue l'efficacité de la turbine, l'augmentation de la TIT augmente l'efficacité globale du cycle. Cela explique l'efficacité accrue du cycle IRReGT avec refroidissement. Comme la turbine LP n'est pas refroidie, la TIT de la turbine HP est limitée à 1450 °C.

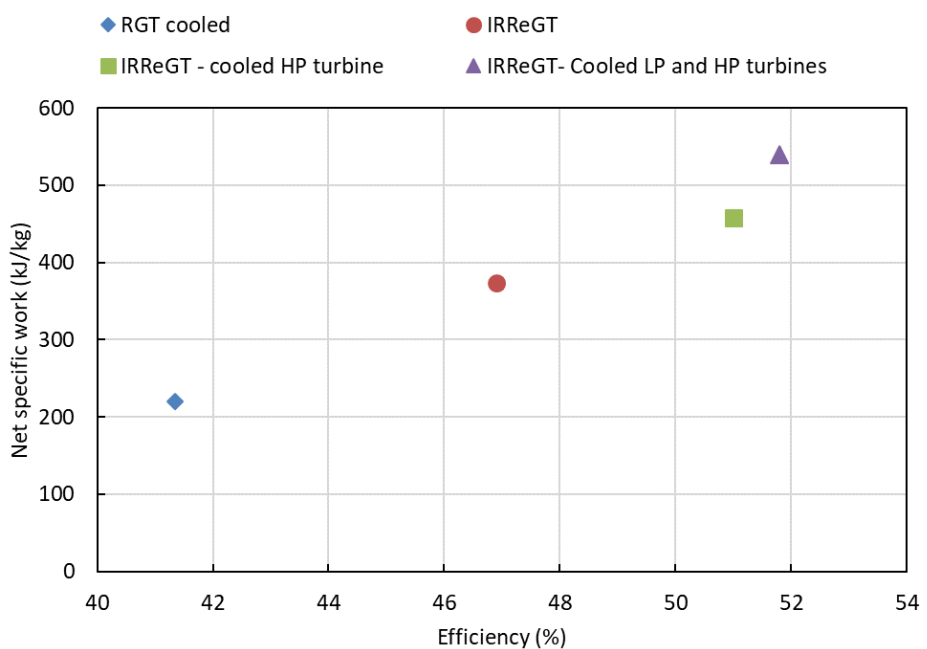


Figure 2.16 : Rendement et travail spécifique net pour différentes configurations de cycle GT refroidi.

En outre, le refroidissement intermédiaire et le réchauffage entre les étages du compresseur et de la turbine, offrent trois avantages importants : un rapport de pression plus élevé, un travail plus important et un potentiel de régénération plus important. Il en résulte une amélioration significative des performances du cycle et c'est ce qui rend le cycle IRReGT avec une turbine HP refroidie plus efficace. Enfin, en comparant le cycle IRReGT avec seulement une turbine HP refroidie et le cycle IRReGT avec deux turbines refroidies, on constate que ce dernier a de meilleures performances, en termes de rendement plus élevé (51.8 %), et de travail spécifique net (539 kJ/kg). Ce résultat est dû à l'augmentation supplémentaire de la TIT de la turbine HP sans limitation puisque la turbine LP est également refroidie. Cependant, l'amélioration du rendement du cycle est négligeable par rapport à la complexité technologique du cycle RGT refroidi (41.34 %).

**Table 2.1.: Conditions d'opérations des configurations.**

Configurations	Conditions d'opérations	Raisons
IRReGT cycle	P = 9 bar TIT = 1100 °C	Cycle de base.
RGT cycle refroidie	P = 3 bar TIT = 1100 °C	Le rapport de pression maximum pour un compresseur centrifuge est de 3.
IRReGT cycle avec HP turbine refroidie	P = 9 bar TIT HP turbine = 1450 °C TIT LP turbine = 1100 °C	Comme seule la turbine HP est refroidie, toute élévation supplémentaire du TIT HP entraîne un dépassement de 1100 °C du TIT turbine LP, ce qui n'est pas possible en raison des limitations des matériaux de la turbine. - La température maximale du récupérateur ne doit pas dépasser 900 °C en raison des limitations des matériaux. Cependant, la température de l'air chaud à l'entrée du récupérateur peut être un peu plus élevée, car l'air chaud n'est pas soumis à une pression élevée, et en raison du pincement. - L'ajout d'une deuxième chambre de combustion n'a pas de sens en raison de la limitation de la température du récupérateur.
IRReGT cycle with HP et LP turbines refroidies	P= 9 bar TIT HP turbine = 1700 °C	

## 2.5. Etude Technologique de la Conception des Composants du Système GT

Une évaluation technologique est réalisée pour les cycles de turbine à gaz afin de tenir en compte du poids du système ainsi que des contraintes techniques de chaque composant. Par conséquent, le système GT a été divisé en différents sous-systèmes qui sont : les turbomachines composées du compresseur centrifuge et de la turbine radiale refroidie et ses accessoires, le refroidisseur intermédiaire et le

régénérateur qui forment les échangeurs de chaleur, les chambres de combustion, le moteur électrique/générateur et les roulements.

### 2.5.1. Turbomachines

Un compresseur centrifuge et une turbine radiale sont généralement utilisés dans les microturbines. Comme nous l'avons vu dans les sections précédentes, l'augmentation de la température d'entrée de la turbine est bénéfique pour améliorer les performances du cycle en termes d'efficacité du cycle et de travail spécifique net. Comme la TIT est limitée par les contraintes des matériaux de la turbine, la technique de refroidissement des aubes est utilisée. Le moulage des roues de turbine radiales est un procédé traditionnel et peu coûteux utilisé depuis de nombreuses années. Si la technique de refroidissement est courante dans les turbomachines axiales, elle n'a pas été largement utilisée dans les turbines radiales en raison des diamètres plus petits des roues et de l'espace limité de l'aube. L'ajout de dispositifs de refroidissement aux turbines radiales pour augmenter la TIT est désormais possible grâce aux techniques de fabrication additive, qui permettent de fabriquer des géométries internes complexes sans étapes de fabrication supplémentaires. Par conséquent, cette section aborde d'abord les contraintes technologiques de la turbine refroidie en termes de complexité de fabrication et de génération de canaux de refroidissement, puis estime le poids du compresseur et de la turbine.

#### ➤ Impression 3D

L'impression 3D permet de générer des objets de tailles, de formes, de couleurs et de sévérité différentes en utilisant une approche de superposition.

Lors de la création de pièces en impression 3D, plusieurs recommandations de conception peuvent aider à améliorer la qualité de la pièce, la finition de la surface et la précision dimensionnelle. L'épaisseur minimale de la paroi est un paramètre important à aborder lors de l'utilisation de l'impression 3D, car une épaisseur de paroi très fine peut générer une déformation du corps du composant. Le diamètre du trou est un autre paramètre de conception important lorsque l'on envisage des géométries avec des gravures. Bien que les techniques d'impression 3D permettent la création de petites géométries, ces dernières peuvent affecter les propriétés physiques de l'écoulement, principalement sa vitesse, lorsqu'on envisage des diamètres réduits. Un canal très réduit entraîne une augmentation de la vitesse de l'écoulement, ce qui conduit à des pertes plus importantes dans le canal et peut-être à la transition de l'écoulement vers un comportement turbulent.

Par conséquent, le défi de cette thèse est de produire une turbine imprimée compacte, complexe et de petite taille avec des canaux de refroidissement. Il est important de considérer trois facteurs principaux: la taille de la turbine à intégrer dans le véhicule, et l'accommodation des canaux de refroidissement sans augmenter les pertes internes.

#### ➤ Canal de Refroidissement

Au sein de la communauté de conception des turbines axiales, les techniques de transfert de chaleur et les conceptions de refroidissement actif sont bien établies, et certaines de ces approches peuvent être appliquées avec succès aux turbomachines radiales. Le premier contact entre le fluide chaud et l'aube de la turbine se produit au niveau du bord d'attaque de l'aube, le point le plus chaud de la turbine. Par conséquent, le flux du fluide de refroidissement doit être dirigé vers le bord d'attaque de l'aube pour un maximum d'avantages. Lorsque le fluide traverse une aube de turbine, il se détende, ce qui entraîne une réduction de la température. Par conséquent, le refroidissement de l'aube de turbine est obligatoire uniquement dans la première partie de l'aube de turbine.

Le refroidissement de l'aube de la turbine et la génération de canaux de refroidissement impliquent des défis pour obtenir à la fois un refroidissement efficace de l'aube de la turbine et le respect de la contrainte du matériau. Zhang et al. [132] ont effectué une analyse d'optimisation de la topologie pour déterminer les zones qui peuvent être supprimées en toute sécurité de la turbine radiale sans compromettre la distribution des contraintes solides, comme présentées dans la Table 2.2.

**Table 2.2. : Régions possibles pour enlever la masse et introduire le canal de refroidissement.**

Local	Résultats
Entre l'arbre et la face arrière de la roue de turbine	Une région à forte contrainte
Entre le moyeu et l'aube	Une région à forte contrainte, la masse ne doit pas être retirée
Zone du bord de fuite	La majorité de la masse peut être retirée
Le corps principal de l'aube	La masse peut être retirée pour la génération de canaux
Connexion entre le canal de refroidissement et l'arbre creux	Région difficile mais nécessaire pour la connexion

### ➤ Dimensionnement

Reine et Bou Nader [227] ont établi une relation mathématique entre le débit massique et le rapport puissance/poids dans un turbocompresseur en se basant sur les turbocompresseurs de Garrett, Borgwarner et MTI.

Pour les configurations à double étage, on considère que la turbine HP entraîne le compresseur HP et forme un turbocompresseur, tandis que la turbine LP entraîne le compresseur LP et forme un autre turbocompresseur. Lorsque les techniques de refroidissement sont évaluées, on estime que le poids de la turbine est réduit de 22 % en raison de la réduction de la masse de la roue de la turbine, puisque la masse est retirée pour introduire le canal de refroidissement [210].

### 2.5.2. Echangeurs thermiques

Un HEX compact et très efficace est nécessaire pour améliorer les performances du groupe auxiliaire de puissance dans les applications automobiles. Ainsi, deux types de HEX sont utilisés : un refroidisseur intermédiaire et un récupérateur. Le premier est utilisé pour réduire le travail du compresseur, tandis que le second sert à récupérer les déchets des gaz d'échappement et à préchauffer l'air avant d'entrer dans la chambre de combustion.

Sur la base des résultats précédents, cette section présente d'abord la méthodologie de conception utilisée pour le refroidisseur intermédiaire et le récupérateur, puis l'estimation du poids de chaque HEX pour évaluer le poids total de la configuration du cycle GT.

### ➤ HEX Taille

La première étape de la conception d'un échangeur de chaleur consiste à déterminer les propriétés du fluide (densité, viscosité, chaleur spécifique  $C_p$ ) de chaque côté de l'échangeur de chaleur en utilisant les températures du fluide et la pression d'entrée. La méthodologie de conception et les corrélations utilisées sont les mêmes que celles adoptées par [99]. Le HEX est constitué d'une plaque à ailettes à

contre-courant. Les ailettes à bandes décalées sont considérées dans cette étude à la fois pour le récupérateur et l'intercooler en considérant une chute de pression de 100 mbar. Les principaux paramètres géométriques sont la hauteur (h), la longueur (x), l'épaisseur (t) et l'espacement (s) des ailettes.

### 2.5.3. Résultats

L'évaluation du poids consiste à additionner les poids des différents composants, notamment le système de turbomachines (compresseurs, turbines, arbres, roulements), les échangeurs de chaleur (refroidisseurs intermédiaires et récupérateurs), les chambres de combustion et le générateur électrique. Le poids de la chambre de combustion est estimé sur la base d'une chambre de combustion existante [258], en fonction de sa puissance et de son débit massique [87]. On estime que le rapport puissance/poids des générateurs électriques est de 3 kW/kg [243]. Par ailleurs, un package de 10 kg est considéré pour toutes les configurations. Il comprend les accessoires, les valves et l'inventeur électrique. De plus, un facteur de sécurité de 10 % est ajouté à toutes les configurations. Il faut noter que pour le cycle RGT refroidi et le cycle IRReGT avec deux turbines refroidies, l'air est extrait avant d'entrer dans le compresseur, donc un système externe est nécessaire pour forcer l'air à entrer dans l'arbre avec pression.

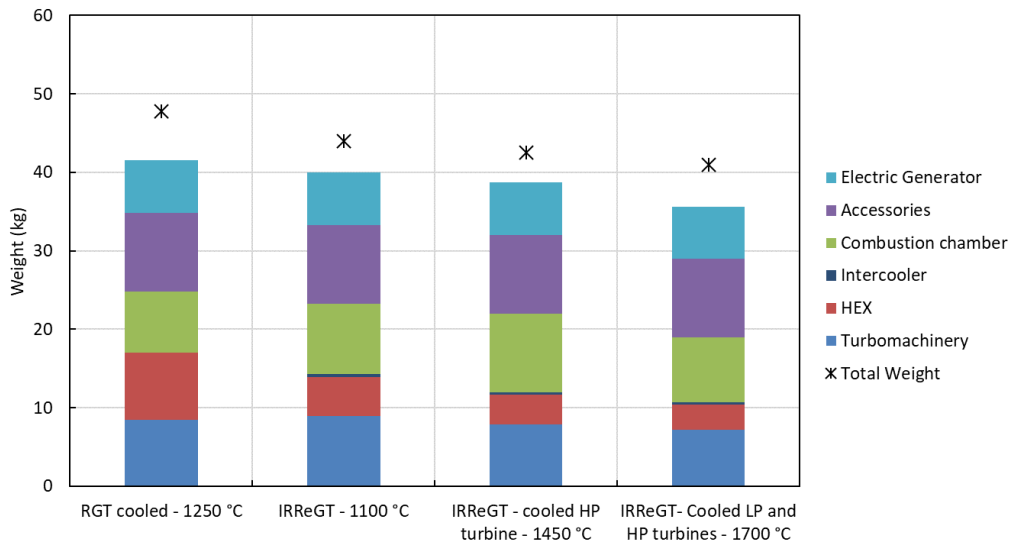


Figure 2.17: Comparaison entre le poids des composants pour les différents cycles étudiés.

La comparaison du poids, du rendement et du travail spécifique net des cycles considérés est présentée à la Figure 2.17. De nombreuses conclusions peuvent être tirées :

- Par rapport aux autres configurations, le cycle RGT refroidi est le plus mauvais, il a le travail spécifique net le plus faible, ce qui entraîne un débit massique élevé conduisant à des composants lourds et encombrants.
- Grâce à l'introduction de techniques de refroidissement, les configurations GT ont augmenté à la fois le travail spécifique net et l'efficacité en raison de la réduction du débit massique, ce qui entraîne des économies de poids. Par exemple, en comparant le cycle de base et l'IRReGT avec une turbine HP refroidie, on constate que l'efficacité du cycle augmente de 4 points, sans changement significatif du poids du système.
- Il n'y a pas de différence significative entre le cycle IRReGT avec une turbine HP refroidie et le cycle IRReGT avec deux turbines refroidies en termes de poids et d'efficacité.

Sur la base de ces résultats, le cycle IRReGT avec une turbine HP refroidie est le plus approprié. Tout d'abord, il présente un rendement plus élevé (51%) que le RGT, le cycle IRReGT standard, et un rendement relativement très proche du cycle IRReGT avec deux turbines refroidies. De même, le poids (42.5 kg) et le travail spécifique net (457.6 kJ/kg) suivent la même tendance. En outre, le cycle choisi est moins compliqué que le cycle IRReGT avec deux turbines refroidies puisqu'une seule turbine est refroidie et qu'il n'y a pas de système externe pour fournir de l'air avant l'entrée du compresseur dans l'arbre.

## 2.6. Conclusions

Les turbines à gaz sont des convertisseurs d'énergie potentiels pour les véhicules électriques hybrides en série. Ce sont des unités de puissance auxiliaires capables de recharger les batteries des voitures électriques une fois épuisées. De nombreuses étapes sont proposées pour améliorer le rendement des turbines à gaz, comme la sélection de la meilleure architecture de cycle, l'augmentation de la pression et l'augmentation de la température d'entrée de la turbine.

Par conséquent, ce chapitre présente une méthodologie pour choisir le cycle GT optimal et ses conditions optimales pour être utilisé comme prolongateur d'autonomie pour les SHEV. La première partie de ce chapitre consiste à réaliser une étude paramétrique pour le cycle GT avec récupérateur. L'analyse thermodynamique a identifié le cycle IRReGT avec deux étages de compression avec un intercooler, deux étages de détente avec réchauffage, et un récupérateur fonctionnant à une pression maximale de 9 bar comme le cycle le plus efficace.

Une analyse énergétique détaillée a déterminé que la chambre de combustion était responsable de la majorité des pertes d'énergie. L'augmentation de la TIT est une solution à la fois pour la destruction d'exergie dans la chambre de combustion et pour améliorer l'efficacité du cycle. En conséquence, de nouvelles configurations de GT sont suggérées ; elles consistent en des cycles GT avec des aubes de turbine refroidies basées sur le cycle IRReGT non refroidi. Le refroidissement par convection est appliqué pour atteindre une TIT plus élevée qui surmonte les limitations des matériaux de la turbine. L'analyse thermodynamique souligne l'impact du refroidissement des aubes de turbine sur l'efficacité du cycle par rapport au cycle IRReGT standard. D'après les résultats obtenus pour les différents cycles proposés avec refroidissement des pales, l'efficacité du cycle est affectée par la température des pales de la turbine, la TIT, l'efficacité de la turbine et l'efficacité du liquide de refroidissement. En outre, bien que le refroidissement de l'aube de la turbine diminue l'efficacité de la turbine, l'efficacité globale du cycle augmente en raison des températures d'entrée plus élevées de la turbine, ce qui permet généralement de surmonter la perte du flux de réfrigérant et d'améliorer l'efficacité du cycle.

Le groupe auxiliaire de puissance doit être très efficace, compact et de conception simple puisqu'il sera intégré au véhicule. Par conséquent, la troisième partie de ce chapitre met en lumière l'aspect technologique des cycles GT. Quatre cycles réalisables sont comparés en tenant compte des contraintes des matériaux de la turbine et du récupérateur. La technique d'impression 3D a été utilisée pour la turbine car elle permet de produire des géométries complexes dans un ensemble compact. Il convient toutefois de tenir compte des limites de l'impression 3D, telles que l'épaisseur minimale des parois (0.16 mm) et le diamètre minimal (0.5 mm). De plus, le poids des différents composants des cycles GT est évalué. Parmi les configurations testées, le cycle IRReGT avec une turbine HP refroidie et le cycle IRReGT avec deux turbines refroidies ont présenté le meilleur rendement et le poids le plus faible. Le premier cycle, le cycle IRReGT avec une turbine HP refroidie, est choisi car il est moins complexe et présente un poids et une efficacité très proches de ceux de l'autre cycle. L'analyse thermodynamique a montré que des températures de 1450 °C peuvent être atteintes avec une augmentation de l'efficacité du cycle

de 4.1 points (51 %) par rapport au cycle IRReGT de base (46.9 %) pour des températures de 1100 °C pour le matériau de fusion.

Comme la turbine refroidie HP est le composant le plus critique du cycle actuel, le chapitre suivant présente une méthodologie de conception pour la turbine refroidie. La procédure de conception consiste en une simulation 1D pour prédire la géométrie globale de la turbine, suivie d'une simulation 3D dans ANSYS CFX.



# **Chapter 3 Study of Fluid Flow Behavior of Radial Turbine Rotor Operating at High Temperature and High Pressure. Impact of Cooling.**

## **3.1. Introduction**

Radial turbines are commonly used in automotive turbochargers, aircraft power units, and all compact power sources. The cooled HP turbine is the key component in the IRReGT cooled cycles since its operating conditions and efficiency affect the cycle performance significantly. The radial-inflow turbine has received a lot of attention in terms of design and analysis mainly for applications in Organic Rankine Cycle and supercritical CO<sub>2</sub> cycle. Therefore, several studies have been carried out to assess the design methodology of radial turbines using one-dimensional (1D) preliminary design, three-dimensional (3D) simulation through computational fluid dynamics (CFD), and experimental validation. The following is an overview of the most relevant studies for turbine design methodology.

Numerous researches focused on developing preliminary design methods to estimate the performance of the radial turbine [245]. Vilim [246] developed a one-dimensional model for a radial-inflow turbine for supercritical carbon dioxide cycle applications. The developed model takes into account the different parts of the turbine stage including the volute, nozzle, and impeller, and the internal losses. A comparison was made between the predicted performance and the experimental results obtained at Sandia National Laboratories. As a result, two modifications were added to match the experimental results exactly. Additionally, the design methodology conducted in [247] for a radial turbine for the Organic Rankine cycle consists of a preliminary design followed by an optimization of critical parameters. The thermodynamics and aerodynamics elements of the preliminary design were developed using MATLAB. Afterward, an optimization code was used to enhance the main design parameters. Deligant et al. [248] implemented a meanline design model for a radial turbine for concentrated solar power in MODELICA. This turbine can be used in existing cycles by coupling the design code with an existing CO<sub>2</sub> supercritical cycle. The turbine conception will therefore vary based on the operation cycle.

On the other hand, other studies completed the 1D analysis with 3D simulations. Zhou et al. [249] first optimized the thermodynamic parameters of a supercritical Brayton cycle to select the parameters of a radial turbine. The preliminary design of the single-stage radial turbine was conducted with an estimation of the turbine loss. Then a CFD analysis of the designed turbine is performed for a detailed evaluation of the turbine performance. Simulated results are within a reasonable range of deviations from preliminary design results, indicating the reliability of the design method. Wei [250] developed a meanline design model for a radial inflow turbine followed by a CFD analysis. The results show compatible agreement between the 1D and the 3D simulation. Al Jubori et al. [251] carried out a complete design methodology for a small-scale turbine for Organic Rankine Cycle from 1D calculation, to 3D analysis, reaching the manufacturing stage and experimental validation. Another study conducted at Brunel University [111] investigated the design of a radial-inflow turbine for the Organic Rankine Cycle. Several codes were developed, ranging from meanline design to testing. The first step was to establish geometrical parameters and velocity triangles. The turbine was then simulated in 3D with ANSYS CFX before being tested. Optimization was also performed on MATLAB following an iterative approach to enhance its performance. A recent study assessed the development of a preliminary design of a rotor [252]. A loss model was also developed, and Computational fluid dynamics was used to validate the preliminary design model. Table 3.1 reports a review of the turbine design methodology approaches presented in the literature.

**Table 3.1: Review of the turbine design methodology.**

Authors	Research Approach
Vilim [246]	1D, experimental validation
Costall et al. [245]	1D
Han et al. [247]	1D
Zhou et al. [249]	1D, 3D
Deligant et al. [248]	1D coupled to the cycle
Wei [250]	1D, 3D
Al Jubori et al. [251]	1D, 3D, experimental
Alshammari [111]	1D, 3D, experimental
Da Silva et al. [252]	1D, 3D

Based on the surveyed studies, this chapter exposes a detailed design methodology, depicted in Figure 3.1 for the HP turbine of the IRReGT cycle. The chapter is divided into two main parts, Part I outlines the design methods for uncooled radial turbines operating at high pressure and temperature, and Part II outlines the design approach for cooled radial turbines operating at high temperature and pressure.

As a first step in the design process, a 1D approach is taken, known as the preliminary design. It determines the overall geometrical parameters of the radial inflow turbine and estimates the turbine performance based on input parameters. The 1D analysis is initially modeled in VBA Excel. The 1D model takes into consideration the losses at different parts of the turbine stage. Although 1D simulation gives an idea of the overall parameter of the designed turbine, it cannot capture the complex behavior in the radial turbine where the flow is 3D, viscous and turbulent. Therefore, the second step consists of a 3D geometry generation of the turbine blades, before realizing a 3D simulation using ANSYS CFD/CFX. Finally, the considered turbine is manufactured using 3D printing manufacturing technique to be validated experimentally.

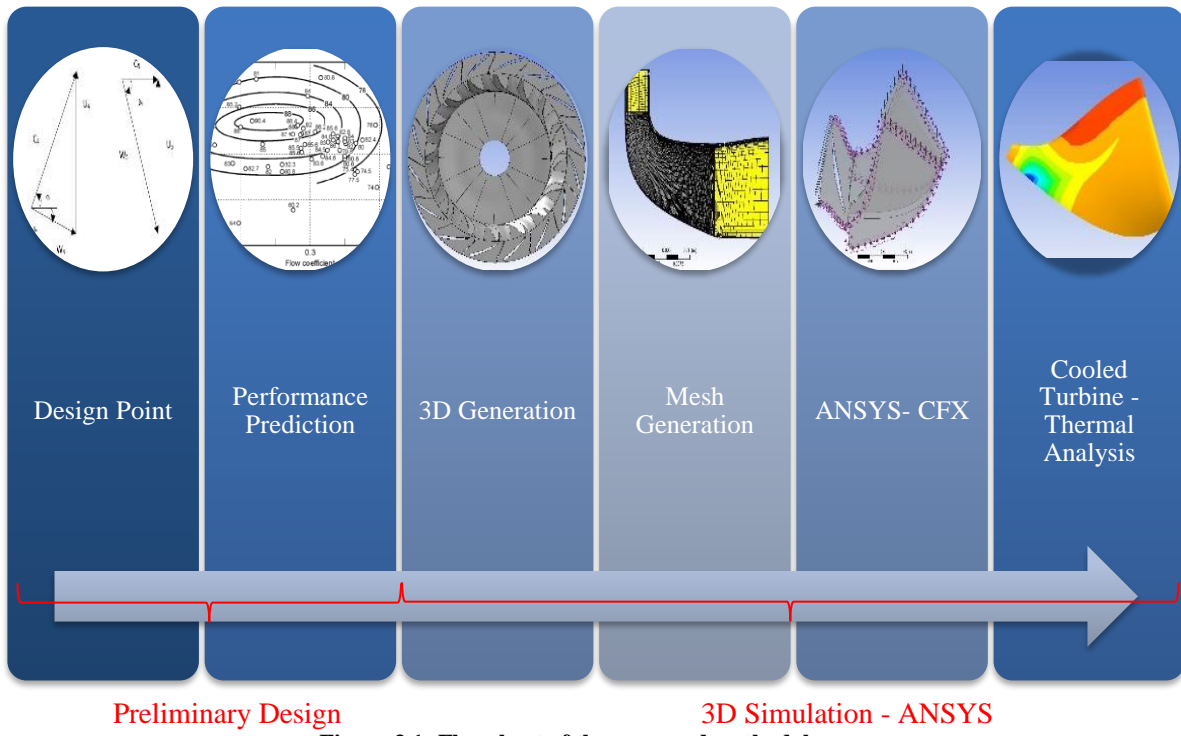


**Figure 3.1: Flowchart of the proposed methodology.**

### 3.2. Radial Turbine Architecture

The radial turbine contains mainly two parts: a fixed part (volute and stator vanes) and a rotating rotor, illustrated in Figure 3.2. The former leads to expanding the flow and giving a circumferential velocity about the axis of the machine. The passage of the flow in the latter leads to the production of work on the axis of the turbine. A diffuser can be added to recover the kinetic energy at the outlet of the turbine, and transform it into static pressure. This configuration is, however, subject to weight and installation constraints.

As the flow enters the volute, it is accelerated by the reduced cross-sectional area. Leaving at high speed, the flow is then spread evenly across the periphery before entering the stator vanes. In this manner, the flow is expanded and directed in an optimal direction toward the rotor. A vanless space (gap) separates the stator and the rotor. This space aims to further accelerate the flow before entering the rotor. Upon reaching the rotor, the flow is expanded and the kinetic energy is converted into shaft power

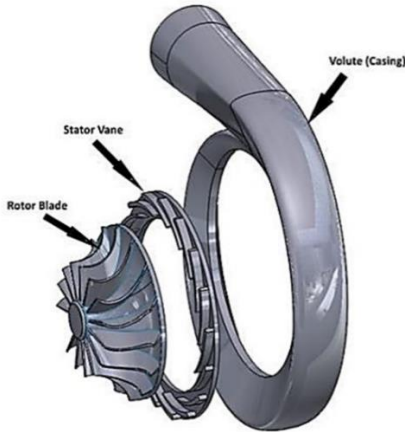


Figure 3.2: Radial turbine main components [111].

Figure 3.3 presents a schematic meridional view of a radial turbine with the different components, including the volute, the stator and the rotor. A tip clearance is present between the rotor blade and the shroud. The geometrical design parameters presented in this figure are: the volute radius ( $r_1$ ), the stator inlet diameter ( $r_2$ ), the stator exit diameter ( $r_3$ ), the rotor inlet diameter ( $r_4$ ), the exit hub radius ( $r_{h5}$ ), the exit shroud radius ( $r_{s5}$ ), the axial length ( $z_{Rotor}$ ), the stator blade height ( $b_3$ ), the rotor inlet blade height ( $b_4$ ), the rotor outlet blade height ( $b_5$ ).

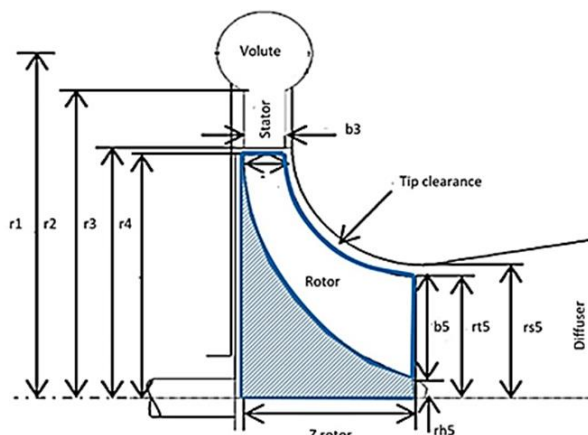


Figure 3.3: Meridional view of a turbine stage.

The turbine casing is divided into two categories depending on the section area: the collector or the volute. The former consists of a constant casing geometry whose aim is to distribute the flow without increasing the velocity. The presence of stator vanes is mandatory to accelerate and direct the flow before entering the rotor. The latter is a casing with a reduced cross-sectional area, seeking to accelerate the flow. In this case, the stator vanes are not required. This configuration is generally used in turbochargers [111].

After the flow exists the stator vanes, it passes through a radial gap to further increase its velocity. After that, the flow enters the rotating component, the rotor. This critical component determines the overall performance of the radial turbine.

### 3.3. Mollier Diagram of a Radial Turbine

Figure 3.4 presents the indices at the inlet and the outlet of the components: 1 refers to the volute inlet, 2 refers to the stator inlet, 3 refers to the stator exit (inlet of the vaneless space), 4 refers to the rotor inlet, 5 refers to the rotor outlet.

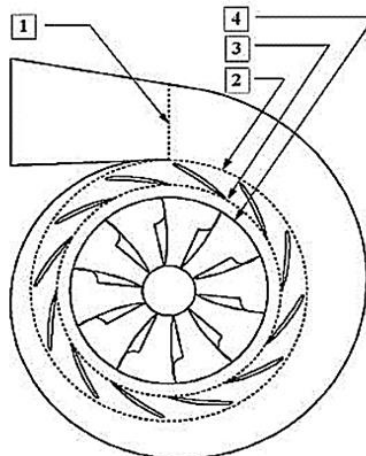


Figure 3.4: Turbine indices [253].

The thermodynamic expansion process in a radial turbine stage is illustrated in the Mollier diagram in Figure 3.5. The gas expands adiabatically in the volute and the stator. The stagnation enthalpy is assumed constant:  $h_{t1} = h_{t2} = h_{t3} = h_{t4}$  and the static enthalpy drop is related to the variation in absolute velocity  $C$ .

$$h_1 - h_2 = \frac{1}{2} (C_2^2 - C_1^2) \quad (3.1)$$

The specific work across the rotor is determined by Equation (3.2):

$$\Delta W_{net} = h_{t4} - h_{t5} \quad (3.2)$$

If a diffuser exists the stagnation enthalpy does not change, but the static enthalpy increases due to the conversion of velocity into pressure.

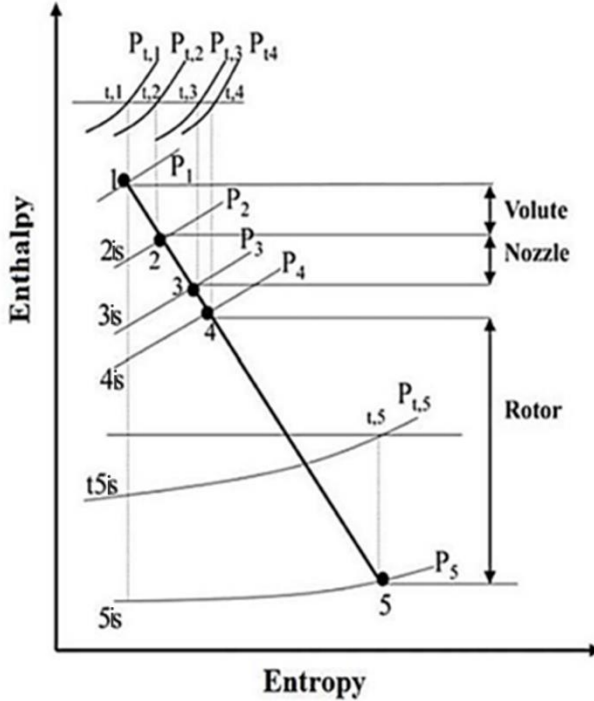


Figure 3.5: Enthalpy-Entropy diagram of the turbine stage [111].

### 3.4. Turbine Analysis

The velocity triangles of a radial turbine are similar to those of centrifugal compressors but in reverse directions. Figure 3.6 illustrates the velocity diagram at the inlet and the outlet of a radial turbine with an axial velocity at the exit. The following equations are conducted based on “Principles of Turbomachinery” [112].

The absolute velocity  $C$  is the sum of the relative velocity  $W$  and the blade velocity  $U$ .

$$C = W + U \quad (3.3)$$

$\alpha$  and  $\beta$  are respectively the absolute and the relative flow angles.

The work delivered by a radial turbine written in terms of the kinetic energies is given by:

$$W_{net} = h_{t4} - h_{t5} = h_4 - h_5 + \frac{1}{2}(C_4^2 - C_5^2) \quad (3.4)$$

$$W_{net} = \frac{1}{2}(C_4^2 - C_5^2) + \frac{1}{2}(U_4^2 - U_5^2) + \frac{1}{2}(W_5^2 - W_4^2) \quad (3.5)$$

Analyzing Equation (3.5), it can be seen that to increase the turbine work, the absolute velocity at the inlet of the rotor  $C_4$  should be increased. As a result, the flow angle should enter the rotor with a large angle  $\alpha_4$ . Additionally, decreasing the relative velocity value at the inlet of the rotor increases the turbine work. Another possibility to increase the turbine work is achieved by a reduced value of  $C_5$ , resulting in an axial velocity at the exit of the rotor.

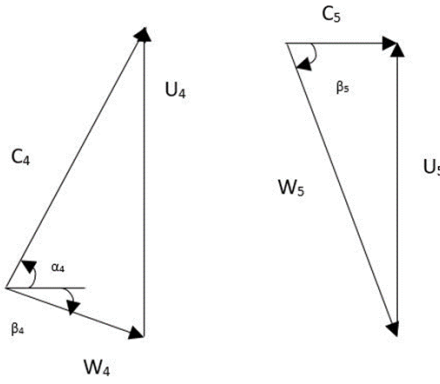


**Figure 3.6: Velocity triangle of a radial turbine at the inlet (left) and the outlet (right) with zero swirls at the exit.**

The Euler equation of turbomachinery Equation (3.6) leads to many conclusions, where  $C_{u4}$  is the tangential component of absolute velocity at the rotor inlet and  $C_{u5}$  is the tangential component of absolute velocity at the rotor exit :

$$W_{net} = U_4 C_{u4} - U_5 C_{u5} \quad (3.6)$$

Higher turbine work is obtained for small values of  $C_{u5}$  and  $U_5$  and large values  $C_{u4}$  and  $U_4$ . Therefore, the ratio  $\frac{r_5}{r_4}$  should be large.

In addition, the turbine work is increased for  $C_{u5}$  negative, but this will also increase the value of  $\beta_5$  and the exit relative Mach number might become so large and can cause the flow to choke [112]. Considering zero swirls at the exit of the turbine, the turbine work expression becomes:

$$W_{net} = U_4 C_{u4} \quad (3.7)$$

### 3.5. Moment of Momentum Balance

If we consider a control volume including the impeller of the rotor and the fluid, the acting forces on the control volume are the reaction forces of the blade and the pressure forces.

Applying the moment of momentum balance:

$$\vec{R} dt + (\vec{P}_4 + \vec{P}_5) \Omega dt = dm(\vec{C}_5 - \vec{C}_4) \quad (3.8)$$

The first term represents the forces acting from the blade on the flow and the second term represents the pressure forces on the surface  $\Omega$ , where  $\Omega$  is the area generated by the movement of the rotor blades.

Projecting this equation in the direction  $\vec{u}$  (blade velocity direction):

$$R_u' = G[C_5 \cos(\pi - \alpha_5) - C_4 \cos \alpha_4] \quad (3.9)$$

The force of the fluid on the rotor blade is given by:

$$R_u = -\dot{R}_u = G(C_4 \cos \alpha_4 + C_5 \cos \alpha_5) \quad (3.10)$$

With  $G = \frac{dm}{dt}$

Projecting the initial equation in the axial direction:

$$R_a = -\dot{R}_a = G(C_4 \sin \alpha_4 - C_5 \sin \alpha_5) + (P_4 - P_5)\Omega \quad (3.11)$$

The work from the turbine is obtained by multiplying  $R_u$  with the blade speed at the inlet and the outlet of the rotor.

The Euler equation is given by:

$$W_{net} (kW) = R_u * U = G * U * (C_4 \cos \alpha_4 + C_5 \cos \alpha_5) \quad (3.12)$$

$$W_{net} \left( \frac{kJ}{kg} \right) = U_4 C_{u4} - U_5 C_{u5} \quad (3.13)$$

In order to increase the work of the turbine,  $U_4 C_{u4} - U_5 C_{u5} > 0$  leading to  $U_4 > U_5$  and  $r_4 > r_5$ . However, for axial turbomachines,  $U_1 = U_2 = U$ . Thus, the work delivered is determined by:

$$W_{net} (kW) = R_u * U = G * U * (C_4 \cos \alpha_4 + C_5 \cos \alpha_5) \quad (3.14)$$

$$W_{net} \left( \frac{kJ}{kg} \right) = U * (C_{u4} - C_{u5}) \quad (3.15)$$

### 3.6. Radial-Inflow Turbine Performance Parameter

Radial-Inflow turbines are characterized by various non-dimensional parameters to evaluate their performance. The parameters are the velocity ratio, the specific speed, the specific diameter, the total-to-static and total-to-total efficiency, the degree of reaction, the flow coefficient, and the load coefficient.

#### 3.6.1. Velocity Ratio

The velocity ratio (Equation (3.16)) is the ratio between the rotor blade speed and the spouting velocity ( $C_0$ ). The spouting velocity is calculated as the velocity when the entire isentropic enthalpy is transformed into speed as depicted in Equation (3.17).

$$\nu_s = \frac{U_4}{C_0} \quad (3.16)$$

$$C_0 = \sqrt{2\Delta h_{is}} \quad (3.17)$$

Dixon et Hall [254] recommended a value of  $\nu_s$  between 0.68 and 0.71. Aungier [253] suggested a value of  $\nu_s$  between 0.6 and 0.7.

#### 3.6.2. Specific Speed and Specific Diameter

Balje [255] suggested a chart to evaluate the performance of the expansion machines representing the effect of the specific diameter, the specific speed, and the radius ratio on the turbine efficiency. The diagram is illustrated in Figure 3.7. The specific speed  $n_s$  and the specific diameter  $D_s$  are calculated respectively using Equation (3.18) and Equation (3.19).

$$n_s = \frac{\omega \sqrt{Q_5}}{\Delta h_{is}^{0.75}} \quad (3.18)$$

$$D_s = \frac{d_4 \Delta h_{act}^{0.25}}{\sqrt{Q}} \quad (3.19)$$

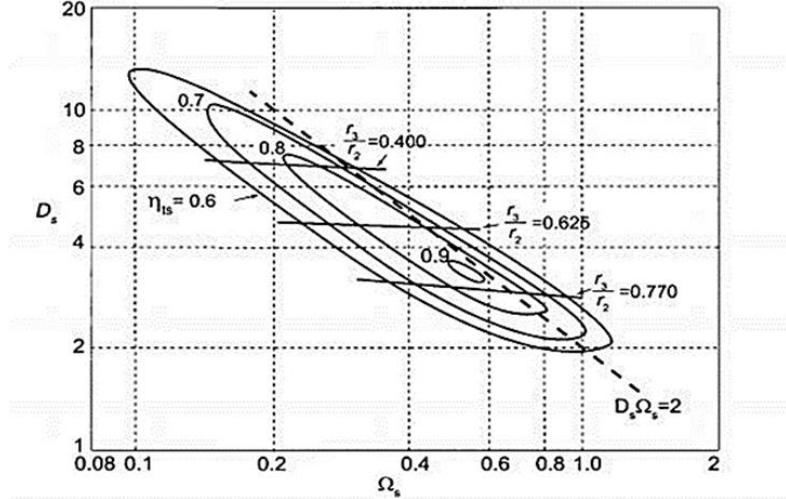


Figure 3.7: Balje diagram [112].

As shown in the Balje chart, the highest efficiency occurs for  $0.2 < n_s < 0.8$  and  $0.53 < \frac{r_5}{r_4} < 0.66$ .

### 3.6.3. Total-to-static Efficiency and Total-to-total Efficiency

The total-to-static efficiency ( $\eta_{ts}$ ) is defined by the ratio of the actual to the ideal work of the turbine stage Equation (3.20), where static enthalpy is taken at the outlet of the turbine. If a diffuser is used at the outlet of the turbine stage, a recovery of the kinetic energy is accomplished. Then, total-to-total efficiency ( $\eta_{tt}$ ) is used as seen in Equation (3.21).

$$\eta_{ts} = \frac{h_{t1} - h_{t5}}{h_{t1} - h_{5is}} \quad (3.20)$$

$$\eta_{tt} = \frac{h_{t1} - h_{t5}}{h_{t1} - h_{t5is}} \quad (3.21)$$

### 3.6.4. Degree of Reaction

The degree of reaction ( $R$ ) of a turbine stage describes the ratio of static enthalpy drop at the rotor to the total enthalpy change across the stage, as expressed in Equation (3.22).

$$R = \frac{h_4 - h_5}{h_{t1} - h_{t5}} \quad (3.22)$$

Aungier [253] recommended a stage reaction between  $0.45 < R < 0.65$ .

### 3.6.5. Flow $\varphi$ and Load $\psi$ Coefficient

The flow coefficient (Equation (3.23)) characterizes the mass flow behavior through the stage, a measure of the flow rate through the machine. It is defined by the ratio of the meridional velocity at the outlet of the rotor to the blade speed at the inlet of the rotor.

The load coefficient (Equation (3.24)) characterizes the work in the stage. It is defined by the ratio of the actual work of the stage to the square of the blade speed.

$$\varphi = \frac{Cm_5}{U_4} \quad (3.23)$$

$$\psi = \frac{\Delta h_{act}}{U_4^2} = \frac{Cu_4}{U_4} - \frac{r_5}{r_4} * \frac{Cu_5}{U_4} \quad (3.24)$$

The exit swirl of a radial turbine is generally small or equal to zero so the second term is negligible and the equation will be:

$$\psi = \frac{\Delta h_{act}}{U_4^2} = \frac{Cu_4}{U_4} \quad (3.25)$$

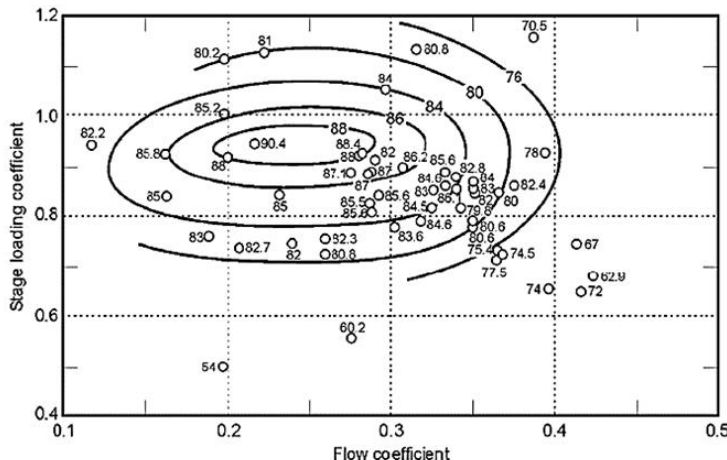


**Figure 3.8: Performance of a radial turbine in the function of the Flow and the Load coefficient [256].**

Figure 3.8 illustrates the efficiency of the radial turbine in function of the load and flow coefficient. It can be seen that the maximum efficiency occurs for a flow coefficient between 0.2 and 0.3, and a load coefficient between 0.9 and 1.

## 3.7. Preliminary Design Strategy of a Radial-Inflow Turbine

The meanline analysis is a one-dimensional approximation done on the mean radius of the turbomachinery stage. This study determines the overall performance of the turbine and the preliminary dimensions of the different components of the turbine stage. The meanline design is initially conducted in Visual Basic Applications (VBA) Excel. REFPROP, developed by the National Institute of Standards and Technology (NIST) is integrated into the procedure to obtain the gas properties.

Several applications for preliminary design methodologies are described in the literature. An aerodynamic design of a radial-inflow turbine stage was developed by Aungier [253]. The study considers three stage components: the volute, the stator, and the rotor. A vaneless space is added before

and after the nozzle vanes. No difference is made between the volute exit and the nozzle stations. Wei [250] also proposed a method for designing a radial turbine for a 250 kW pilot-scale supercritical carbon dioxide Brayton cycle, with loss correlations. In addition, Alshammari [111] suggested a modeling and testing procedure for a radial turbine for automotive organic Rankine cycle waste heat recovery. The meanline design approach incorporates loss estimation. Furthermore, Fiaschi et al. [257] discussed the design of radial turboexpanders for ORC applications for different organic fluids to small-size applications (50 kW). In the model, an estimation of losses is conducted based on correlations from the literature, based on which was concluded that the most significant losses come from the rotor. Based on these findings, the methodology conducted in this section is in agreement with the four cited approaches. The same approach will be used, including loss estimation.

This section concentrates on the preliminary design of the HP radial turbine of the IRReGT baseline cycle. Therefore, the designed turbine must match the operating conditions of the IRReGT cycle. The methodology conducted in this thesis is based on certain input parameters and empirical correlations from the literature. For simplicity, fluid properties are assumed to be constant in a plane normal to their direction of motion. They are therefore assumed to vary only along the mean streamline [258]. Meanline design determines the flow properties and geometric parameters at each station of the turbine stage. The meanline design modeling is an iterative process. Therefore, two meanline design codes are conducted assuming a zero swirl flow at the output of the rotor.

The input parameters for the first code ‘PMean’ are the operating conditions of the designed turbine, presented in Figure 3.9a: the stage inlet total temperature ( $T_{t1}$ ), the stage inlet total pressure ( $P_{t1}$ ), the total-to-total expansion ratio or the output total pressure ( $P_{t5}$ ), the stage mass flow rate ( $\dot{m}$ ), the rotational speed (N), and the velocity ratio ( $v_s$ ), and the power output. The second code has the same operating conditions input but with a total-to-static expansion ratio and without the power output as illustrated in Figure 3.9b. In addition, two geometrical parameters are considered for the two cases:  $r h_5 / r_4$  and  $r_3 / r_2$ .

An initial estimation of the cycle efficiency is needed and the velocity triangles at the inlet and the exit of the rotor and the stator are calculated. The losses are then estimated using correlations from the literature and a new cycle efficiency is calculated. The calculation will proceed until convergence for efficiency is achieved (residual for efficiency  $10^{-4}$ ).



**Figure 3.9: Methodology of meanline design of the radial turbine. (a) 'PMean' code, (b) 'Mean' code.**

### 3.7.1. Mathematical Equations for the Meanline Design Methodology

The specific speed is initially calculated using Equation (3.26) and taking:

$$\Delta h_{is} = h_{t1} - h_{5is} \quad (3.26)$$

$\Delta h_{is}$  is the isentropic expansion from the stage inlet conditions to the rotor exit

$\omega$  is the rotational speed of the turbine

$\dot{Q}_5$  is the volume flow defined from the mass flow rate and the density at the exit of the rotor

$$\dot{Q}_5 = \frac{\dot{m}}{\rho_{t5}} \quad (3.27)$$

$$\Delta h_{real} = h_{t1} - h_{t5} = \frac{Power}{\dot{m}} \quad (3.28)$$

$h_{t1}$  is the total enthalpy at the inlet of the turbine stage (kJ/kg)

$h_{t5}$  is the total enthalpy at the stage exit (kJ/kg)

The choices for  $n_s$  and  $v_s$  determine the performance of the turbine and in consequence the efficiency  $\eta_s$ . Many correlations are available in the literature providing recommended values of velocity ratio as a function of specific speed and estimating the cycle efficiency. Figure 3.10 is a stage performance chart extracted from [253], based on different correlations from the literature. Based on the chart, a specific speed should be between 0.45 and 0.75 and a velocity ratio should be between 0.6 and 0.7.

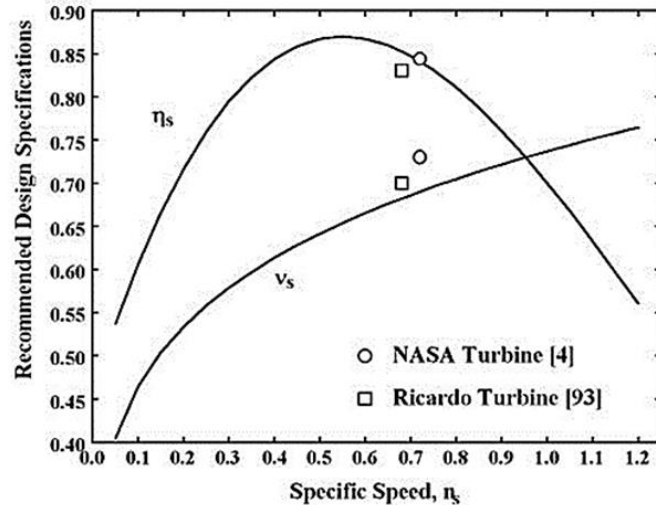


Figure 3.10: Generalized stage performance chart [253].

The curves shown in Figure 3.10 are obtained using the following analytical equations.

$$v_s = 0.737 n_s^{0.2} \quad (3.29)$$

$$\eta_s = 0.87 - 1.07(n_s - 0.55)^2 - 0.5(n_s - 0.55)^3 \quad (3.30)$$

The total inlet temperature and pressure are given, and the thermodynamic state at the inlet of the turbine stage is found. As well as, the parameters at the rotor exit are calculated.

### 3.7.2. Rotor Design

The rotor geometrical design parameters to be calculated are:

- The inlet flow angle  $\alpha_4$
- The inlet blade thickness  $t_{b4}$
- The exit blade thickness  $t_{b5}$
- The exit hub radius  $r_{h5}$
- The exit shroud radius  $r_{s5}$
- The axial length  $z_{Rotor}$
- The number of blades  $N_R$
- The inlet blade angle  $\beta_4$
- The rotor inlet blade height  $b_4$
- The rotor outlet blade height  $b_5$

The blades are assumed radial in any section of the rotor. The absolute velocity at the outlet of the rotor is axial and small in magnitude to reduce the exit losses ( $C_{u5} = 0$ ). Air is considered an ideal gas.

The rotor tip speed  $U_4$  and the tangential absolute velocity  $Cu_4$  and the inlet absolute angle  $\alpha_4$  at the rotor's inlet are calculated, after determining  $v_s$ . Then, the velocity triangle at the inlet of the rotor is obtained.

The discharge spouting velocity is calculated using Equation (3.31):

$$C_{0s} = \sqrt{2\Delta H_{is}} \quad (3.31)$$

The rotor inlet tip speed ( $U_4$ ) is calculated in Equation (3.32):

$$U_4 = v_s C_{0s} \quad (3.32)$$

The tangential component of absolute velocity at the rotor inlet ( $C_{u4}$ ) is determined by:

$$C_{u4} = \frac{U_4 \eta_{ts}}{2v_s^2} \quad (3.33)$$

Rohlik [259] recommends calculating the rotor inlet absolute flow angle ( $\alpha_4$ ) as a function of the specific speed as depicted in Equation (3.34).

$$\alpha_4 = 90 - (10.8 + 14.2n_s^2) \quad (3.34)$$

The absolute velocity at the rotor inlet ( $C_4$ ) is calculated based on mathematical analysis:

$$C_4 = \sqrt{C_{u4}^2 + C_{m4}^2} \quad (3.35)$$

Taking  $W_{m4} = C_{m4}$ , the relative velocity at the rotor inlet:

$$W_4 = \sqrt{W_{u4}^2 + W_{m4}^2} \quad (3.36)$$

The relative flow angle at the rotor inlet is determined using trigonometric analysis:

$$\beta_4 = \arctan\left(\frac{W_{u4}}{W_{m4}}\right) \quad (3.37)$$

Based on the previous equations, the velocity triangle at the inlet of the rotor is obtained.

The rotor inlet radius ( $r_4$ ) is calculated by considering the turbine rotational speed:

$$r_4 = \frac{U_4}{\omega} \quad (3.38)$$

The total enthalpy at the inlet of the rotor is equal to the total enthalpy at the inlet of the turbine stage  $h_{t1} = h_{t4}$ .

An estimation of the rotor total inlet pressure  $P_{t4}$  is calculated by Equation (3.39):

$$P_{t4} = P_{t1} - \rho_{t1} \Delta H_{is} (1 - \eta_s) / 4 \quad (3.39)$$

$\rho_{t1}$  is the total density of the fluid at the stage inlet.

The blade thicknesses at the leading ( $t_{b4}$ ) and the trailing edge ( $t_{b5}$ ), as well as the exit hub radius of the rotor ( $r_{h5}$ ), are determined using values suggested by [253] and presented in Equations (3.40) to (3.42).

$$t_{b4} = 0.04r_4 \quad (3.40)$$

$$t_{b5} = 0.02r_4 \quad (3.41)$$

$$r_{h5} = 0.3 r_4 \quad (3.42)$$

Applying the conservation of mass flow rate, the rotor inlet blade height ( $b_4$ ) is calculated using Equation (3.43).

$$b_4 = \frac{\dot{m}}{2\pi r_4 \rho_4 C_{m4}} \quad (3.43)$$

Considering  $h_4$  and  $s_4 = s_{t4}$ , the static density  $\rho_4$  is calculated.

The static enthalpy at the inlet of the rotor is obtained by Equation (3.44).

$$h_4 = h_{t4} - \frac{1}{2} C_4^2 \quad (3.44)$$

Numerous empirical correlations are suggested in the literature to determine the number of blades. Figure 3.11 plots the correlations proposed by Jamieson, Glassman, and Whitfield. A high number of blades are not used due to several reasons, including excessive flow blockage at the rotor exit, an unreasonably large surface area that causes high friction losses, and the weight and inertia of the rotor becoming relatively great.

Based on the previous statement, Glassman considered that Jamieson's result gave too many blades, and preferred to use an empirical relationship between  $N_R$  and  $\alpha_4$  as shown in Equation (3.45). The results obtained from Whitfield slightly match the results from Glassman at least for low blade numbers.

$$N_R = \frac{\pi}{30} (110 - \alpha_4) \tan \alpha_4 \quad (3.45)$$

The geometric parameters at the rotor inlet are defined. To minimize the leaving loss of the rotor,  $C_{u5}$  is assumed to be zero. Thus,  $C_5 = C_{m5}$ .

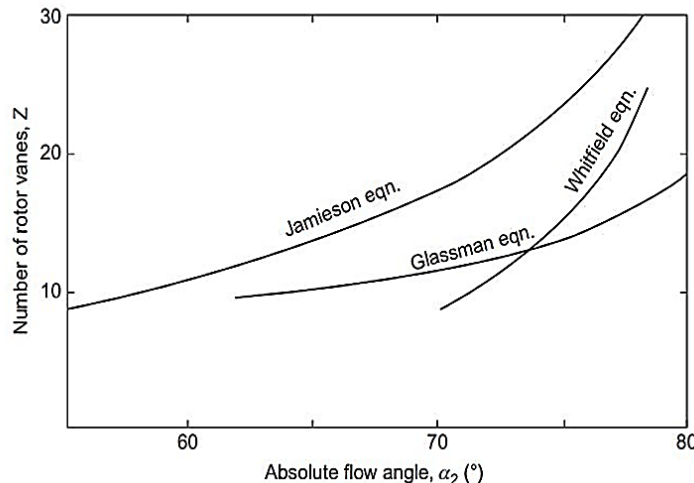


**Figure 3.11: Flow angle at rotor inlet as a function of the number of rotor blades [254].**

Aungier [253] proposed an initial estimation of the meridional speed  $C_{m5}$  using the correlation in Equation (3.46).

$$\frac{C_{m5}}{C_{m4}} = 1 + 5 \left( \frac{b_4}{r_4} \right)^2 \quad (3.46)$$

The velocity triangle at the outlet of the rotor is obtained using trigonometry rules. Hence, the thermodynamic state is calculated using the First Law of Thermodynamics.

The static enthalpy at the rotor outlet is determined by:

$$h_5 = h_{t5} - \frac{1}{2} C_5^2 \quad (3.47)$$

To finalize the rotor geometry, the rotor axial length ( $z_{Rotor}$ ) and the exit passage width ( $b_5$ ) are estimated respectively using Equation (3.48) and Equation (3.52) is estimated by:

$$z_{Rotor} = 1.5 * (r_{s5} - r_{h5}) \quad (3.48)$$

$$A_5 = \frac{\dot{m}}{\rho_5 C_{m5}} \quad (3.49)$$

$$r_{s5} = \sqrt{\frac{A_5}{\pi} + r_{h5}^2} \quad (3.50)$$

The mean radius at the rotor outlet:

$$r_5 = \frac{r_{h5} + r_{s5}}{2} \quad (3.51)$$

The exit passage width is given by:

$$b_5 = r_{s5} - r_{h5} \quad (3.52)$$

The blade speed at the rotor outlet ( $U_5$ ):

$$U_5 = r_5 \omega \quad (3.53)$$

The velocity triangle as well as the geometrical parameters at the inlet and the outlet of the rotor are obtained. The performance of the rotor is evaluated based on these findings.

### 3.7.3. Nozzle Blade Design

This section describes the procedure to design the nozzle blades. The velocity triangle is calculated in an iterative procedure from the continuity and radius ratios.

The rotor inlet passage width and the nozzle passage width are identical and determined in the previous section.

The blade angle of the nozzle is taken the same as the rotor inlet absolute flow angle:

$$\beta_2 = \beta_3 = \alpha_4 \quad (3.54)$$

The stator blade height ( $b_3$ ) is calculated using Equation (3.56).

$$\varepsilon_x = 0.04b_5 \quad (3.55)$$

$$b_3 = b_4 + \varepsilon_x \quad (3.56)$$

As discussed before, a radial gap exists between the rotor and the nozzle.

To estimate the distance of this gap ( $\Delta r$ ), Watanabe et al. [260] proposed the correlation in Equation (3.57):

$$\Delta r = 2b_4 \cos \alpha_4 \quad (3.57)$$

Hence, the radius at the nozzle exit ( $r_3$ ) is calculated:

$$r_3 = r_4 + \Delta r \quad (3.58)$$

The tangential velocity ( $C_{u3}$ ) at the nozzle exit is calculated using the conservation of angular momentum.

$$C_{u3} = \frac{C_{u4}r_4}{r_3} \quad (3.59)$$

The meridional component of absolute velocity at the nozzle outlet ( $C_{m3}$ ) is determined using Equation (3.60):

$$C_{m3} = \frac{C_{u3}}{\tan\alpha_3} \quad (3.60)$$

The tangential component of the absolute velocity at the nozzle inlet ( $C_{u2}$ ) is given by:

$$C_{u2} = C_{m2} * \tan\alpha_2 \quad (3.61)$$

Although the velocity triangle at the inlet of the nozzle is determined, the meridional velocity is based on an approximate estimate. Thus, an iterative process is used to determine the value of  $C_{m2}$  based on mass balance.

$$h_2 = h_{t2} - \frac{1}{2} C_2^2 \quad (3.62)$$

$$C_{m2} = \frac{\dot{m}}{2\pi r_2 \rho_2 b_2} \quad (3.63)$$

Where  $\rho_2$  is the static density at the nozzle inlet calculated from the static enthalpy  $h_2$  ( $h_{t2} = h_{t1}$ ) and the entropy  $s_2$  ( $s_2 = s_{t1}$ ).

At this step, both geometries for the rotor and the stator are defined, as well as the velocity triangles. However, this preliminary calculation does not take into consideration the losses at the different stages of the radial-inflow turbine.

### 3.7.4. Design Feasibility

The literature offers various recommendations for the design of the radial turbine. These recommendations are provided in Table 3.2, based on [253].

**Table 3.2: Recommendations for radial turbine design.**

---

Recommendations
$0.2 \leq C_{m5}/U_4 \leq 0.4$
$r_{s5}/r_4 \leq 0.78$
$\Delta Z_R \geq 1.5b_4$
$r_{s5}/r_4 = 1.29n_s$
$r_{s5}/r_4 \leq 0.7$
$1 \leq C_{m5}/C_{m4} \leq 1.5$
$0.45 \leq R \leq 0.65$

---

### 3.7.5. Loss Correlations

This assessment is based on well-established loss models for radial inflow turbines and is performed within an iterative loop. The loss correlations are outlined in [111].

Figure 3.12 illustrates the distribution of the losses in a turbine for an optimum geometry over the specific speed range. It can be seen that the majority of the turbine losses occur in the rotor. As the specific speed increases, the local Reynolds number increases as well. However, the boundary layer growth is reduced. As a result, the losses are decreased due to a reduction in the boundary layer growth. However, at high specific speeds, the kinetic exit losses are predominant due to higher exit velocities.

The rotor loss model ( $\Delta h_{loss,rotor}$ ) includes losses due to incidence ( $\Delta h_{incidence}$ ), passage ( $\Delta h_{passage}$ ), tip clearance ( $\Delta h_{tip}$ ), trailing edge ( $\Delta h_{trailing edge}$ ), windage ( $\Delta h_{windage}$ ), and exit energy ( $\Delta h_{exit}$ ), as shown in Equation (3.64).

$$\Delta h_{loss,rotor} = \Delta h_{incidence} + \Delta h_{passage} + \Delta h_{tip} + \Delta h_{trailing edge} + \Delta h_{windage} + \Delta h_{exit} \quad (3.64)$$

Due to the lack of data, the stator losses ( $\Delta h_{loss,stator}$ ) are estimated based on the chart in Figure 3.12.

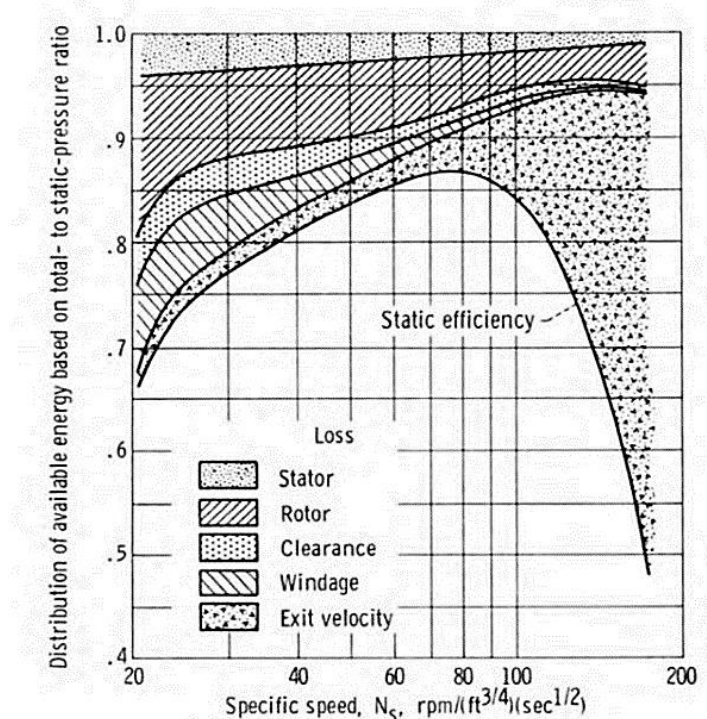


Figure 3.12: Distribution of losses in a radial turbine [259].

The losses are expressed in terms of an enthalpy drop as depicted in Equation (3.65):

$$\eta_s = \frac{\Delta h_0}{\Delta h_0 + \text{Losses}} \quad (3.65)$$

With

$$\text{Losses} = \Delta h_{loss,rotor} + \Delta h_{loss,stator} \quad (3.66)$$

#### 3.7.5.1 Incidence Loss

The incidence losses refer to the losses that occur when the flow enters the turbine at an angle different from the optimum direction. The incidence loss in Equation (3.67) is estimated based on a correlation loss when the incidence angle of the flow is different from the optimum incidence angle:

$$\Delta h_{incidence} = \frac{1}{2} W_4^2 \sin^2(\beta_4 - \beta_{4\ opt}) \quad (3.67)$$

The optimum relative flow angle ( $\beta_{4\ opt}$ ) is calculated based on the empirical correlation from Equation (3.68) [258].

$$\tan(\beta_{4\ opt}) = \frac{-1.98 \tan(\alpha_4)}{N_R(1 - \frac{1.98}{N_R})} \quad (3.68)$$

### 3.7.5.2 Passage Loss

The passage losses consist of all the losses in the blade passage. For a radial inflow turbine rotor, the main forms of passage losses include secondary flow, blockage, kinetic energy losses due to the growth of boundary layers, as well as flow separation in extreme cases.

The CETI model presented in Baines [261], is an improved loss model that combines the losses due to the secondary flow and the friction in the rotor passages. The correlation is:

$$\Delta h_{passage} = m_f * 0.11 * \left[ \left( \frac{L_h}{D_h} \right) + 0.68 * \left( 1 - \left( \frac{r_t}{r_4} \right)^2 * \frac{\cos(\beta_t)}{b_t} \right) * \frac{W_4^2 + W_t^2}{2} \right] \quad (3.69)$$

$$\text{if } \frac{r_4 - r_t}{b_t} \geq 0.2 ; m_f = 1$$

$$\text{if } \frac{r_4 - r_t}{b_t} \leq 0.2 ; m_f = 2$$

The symbol t represents the rotor throat where the flow separation takes place.

$$r_t = r_5 \quad \beta_t = 0.8\beta_5 \quad W_t = 0.7W_5 \quad b_t = o_t$$

The hydraulic length ( $L_h$ ) is calculated as an average as shown in Equation (3.70). The hydraulic diameter  $D_h$  is calculated as an average between the inlet and the exit diameter as presented in Equation (3.71).

$$L_h = \frac{\pi}{4} \left[ \left( \Delta Z_R - \frac{b_4}{2} \right) + \left( r_4 - r_t - \frac{b_t}{2} \right) \right] \quad (3.70)$$

$$D_h = \frac{1}{2} \left[ \left( \frac{4\pi r_4 b_4}{2\pi r_4 + N_R b_4} \right) + \left( \frac{2\pi * (r_{s5}^2 - r_{h5}^2)}{\pi(r_{s5} - r_{h5}) + N_R b_5} \right) \right] \quad (3.71)$$

$$c = \frac{\Delta Z_R}{\cos\beta} \quad (3.72)$$

$$\tan\beta = \frac{1}{2}(\tan\beta_4 + \tan\beta_5) \quad (3.73)$$

### 3.7.5.3 Tip Clearance Loss

In a radial inflow turbine, a gap exists between the rotor blade and the shroud. Leakage from the pressure surface to the suction surface of the turbine occurs. Figure 3.13 shows the radial and the axial clearances between the rotor and the casing. The accepted minimum clearance depends on the manufacturing procedure as well as the aerodynamics of the rotor [111]. Therefore, the tip clearance is included in the model and follows the empirical implementation suggested by [261], considering the effect of radial and axial clearances (Equation (3.74)).

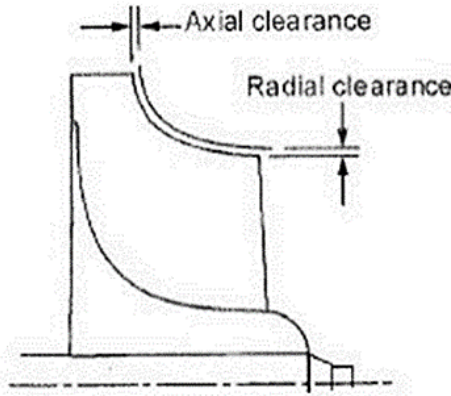


Figure 3.13: Tip clearances of a radial rotor [258].

$$\Delta h_{tip} = \frac{U_4^2 N_R}{8\pi} (k_a \varepsilon_a C_a + k_r \varepsilon_r C_r + k_{ar} \sqrt{\varepsilon_a C_a \varepsilon_r C_r}) \quad (3.74)$$

where  $k_a = 0.4$ ,  $k_r = 0.75$  and  $k_{ar} = -0.3$  were determined by experimental results.

$\varepsilon_a$  and  $\varepsilon_r$  are the axial and the radial clearances.

$C_a$  and  $C_r$  are calculated through Equation (3.75) and Equation (3.76), respectively:

$$C_a = \frac{1 - \frac{r_{s5}}{r_4}}{C_{m4} b_4} \quad (3.75)$$

$$C_r = \left( \frac{r_{s5}}{r_4} \right) \frac{N_R - b_4}{C_{m5} r_5 b_5} \quad (3.76)$$

### 3.7.5.4 Trailing Edge Loss

The trailing edge losses are calculated based on the relative total pressure presented in Equation (3.77) [262] and converted to a general loss coefficient as in Equation (3.78).

$$\Delta P_{t,rel} = \frac{\rho_5 W_5^2}{2g} \left( \frac{N_R t_{b5}}{\pi(r_{s5} + r_{h5}) \cos\beta_5} \right)^2 \quad (3.77)$$

$$L_t = \frac{2}{\gamma M_{5,rel}^2} * \frac{\Delta P_{t,rel}}{P_5(1 + \frac{W_5^2}{2T_5 C_p})^{(\frac{\gamma}{\gamma-1})}} \quad (3.78)$$

$C_p$  is the heat capacity at constant pressure,  $\gamma$  is ratio of constant volume and constant pressure heat capacity.

### 3.7.5.5 Windage Loss

Windage losses occur between the back-face and the housing of the rotor in a form of frictional losses as shown in Figure 3.14. Windage losses are calculated based on the empirical correlations for torque coefficient calculation.

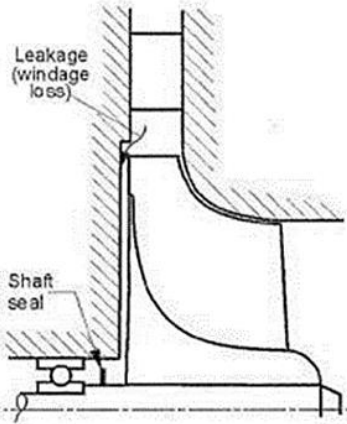


Figure 3.14: Windage losses due to the rotor backflow [250].

$$\Delta h_{windage} = k_f \frac{\bar{\rho} U_4^3 r_4^2}{2m} \quad (3.79)$$

Where  $k_f$  is a function of a Reynolds number.

If  $Re < 10^5$

$$k_f = \frac{3.7 * (\frac{\varepsilon_b}{r_4})^{0.1}}{Re^{0.5}} \quad (3.80)$$

If  $Re > 10^5$

$$k_f = \frac{0.102 * (\frac{\varepsilon_b}{r_4})^{0.1}}{Re^{0.2}} \quad (3.81)$$

$\varepsilon_b$  represents the clearance between the back face of the rotor and the turbine backplate. The Reynolds number is defined as:

$$Re = \frac{\bar{\rho} \bar{C} r_4}{\bar{\mu}} \quad (3.82)$$

Where  $\bar{\rho}$ ,  $\bar{C}$  and  $\bar{\mu}$  are the average fluid density, velocity, and viscosity between the rotor inlet and outlet.

### 3.7.5.6 Exit Energy Loss

The kinetic energy at the outlet of the rotor is treated as the exit energy loss and is calculated as in Equation (3.83). A diffuser can be added to convert a part of this kinetic energy into static pressure.

$$\Delta h_{exit} = \frac{C_5^2}{2} \quad (3.83)$$

### 3.7.6. Validation of the Meanline Design Code

This section shows the comparison between the developed models ‘Pmean’ and ‘mean’ and the one developed by [250]. The turbine is a radial turbine used for carbon dioxide with a mass flow rate of 1.8 kg/s. The total inlet temperature and the total inlet pressure are respectively 943 K and 106.92 bar. All the other input parameters are presented in Table 3.3.

**Table 3.3: Input parameters.**

Properties	Input Parameters
Working Fluid	Carbon Dioxide
Mass Flow Rate (kg/s)	1.8
Rotational Speed (rpm)	80 000
Total Inlet Temperature (K)	943
Total Inlet Pressure (bar)	106.92
Velocity Ratio	0.68
Output Power (kW)	84.076
Total-to-Static Expansion Ratio	1.364
Total-to-Total Expansion Ratio	1.376

Table 3.4 shows the results obtained with the codes with regard to the input operating parameters. The first set of results was obtained by running PMean Code. Hence, the output results are in good agreement with those obtained by [250], there is a maximum error of 3%. This implies that the code is valid for meanline design for a radial turbine with zero swirls at the exit of the rotor. On the other hand, the Mean code's error compared to [250] does not exceed 4%. Therefore, the Mean code can also be used to conduct the initial design estimation of a radial turbine. Therefore, both codes can be used to develop a preliminary radial turbine design.

**Table 3.4: Output design validation.**

Parameters	PMean Code	[250]	Error (%)	Mean Code	Error (%)
$U_4$	228.8	228.5	0.16	229.3	0.2
$Cu_4$	204.06	204.4	0.16	213	4.4
$Cm_4$	50.03	50.03	0	52.2	4.5
$\alpha_4$	76.26	76.24	0.02	76.2	0.04
$C_4$	210.1	210.4	0.16	219.7	4.3
$r_4$	0.027	0.0272	0.21	0.027	0.36
$b_4$	0.0039	0.004	0.16	0.004	2.7
$r_5$	0.0127	0.0127	0	0.0126	0.78
$b_5$	0.009	0.009	0	0.0088	2.22
$N_R$	14	14	0	14	0
$U_5$	106.56	106.47	0.08	105.68	0.93

$Cm_5$	55.37	55.42	0.078	57.41	3.5
$C_5$	55.37	55.42	0.078	57.41	3.5
$Cu_2$	149.68	154.8	3.3	156.72	1.29
$Cm_2$	36.7	37.37	1.657	38.38	2.65
$C_2$	154.12	159.23	3.2	161.3	1.25
$\alpha_2$	76.26	76.44	0.24	76.27	0.22
$r_3$	0.0292	0.0291	0.2	0.0292	0

### 3.8. Parametric Study for the Meanline Design Code

A parametric study was developed to investigate the effect of different input variables on turbine performance. Figure 3.15 shows the impact of rotational speed on both the rotor dimensions and the output work and efficiency. Increasing the turbine speed ( $N$ ) will significantly affect the rotor inlet diameter ( $d_4$ ).  $d_4$  substantially decreases with  $N$  increasing, falling from 566 mm for 20 000 rpm to 51.5 mm for 220 000 rpm. This results in a decrease in friction and exit losses with turbine size, leading to an increase in turbine efficiency as seen in Figure 3.15b. The rotor efficiency increases gradually with the turbine speed  $N$  reaching an efficiency up to 82 % for  $N = 220\,000$ . The turbine power output exhibits the same trend as the impeller efficiency with an increase of 1.2 kW from 20 000 rpm to 220 000 rpm as outlined in Euler Equation (3.15). The greater rotational speed, however, increases the centrifugal forces on the rotor, resulting in more solid stress. High rotating speeds are the reason why microscale turbomachines are not yet available in the market [263]. As a consequence, a compromise must be made to obtain a compact, efficient rotor with acceptable structural stresses.

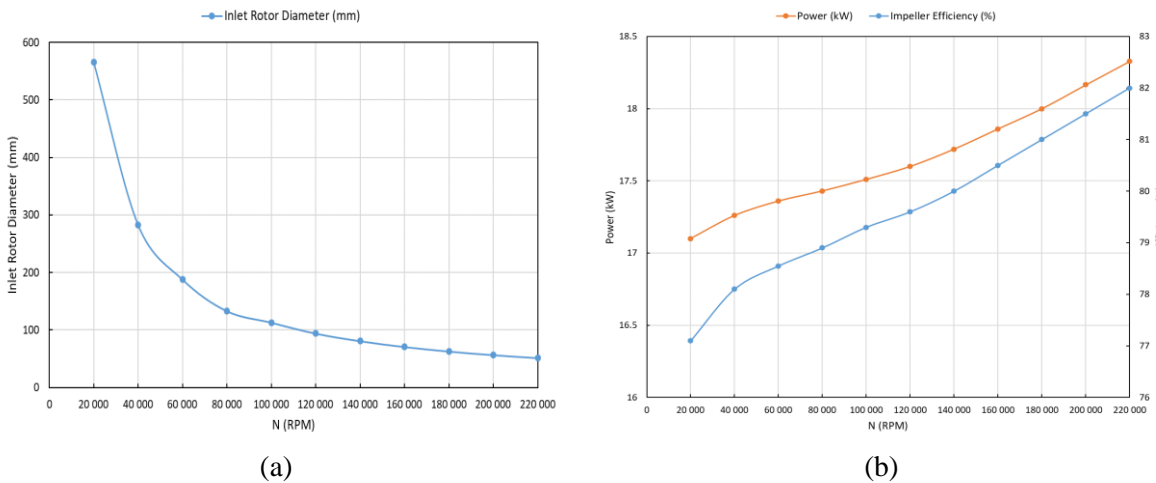
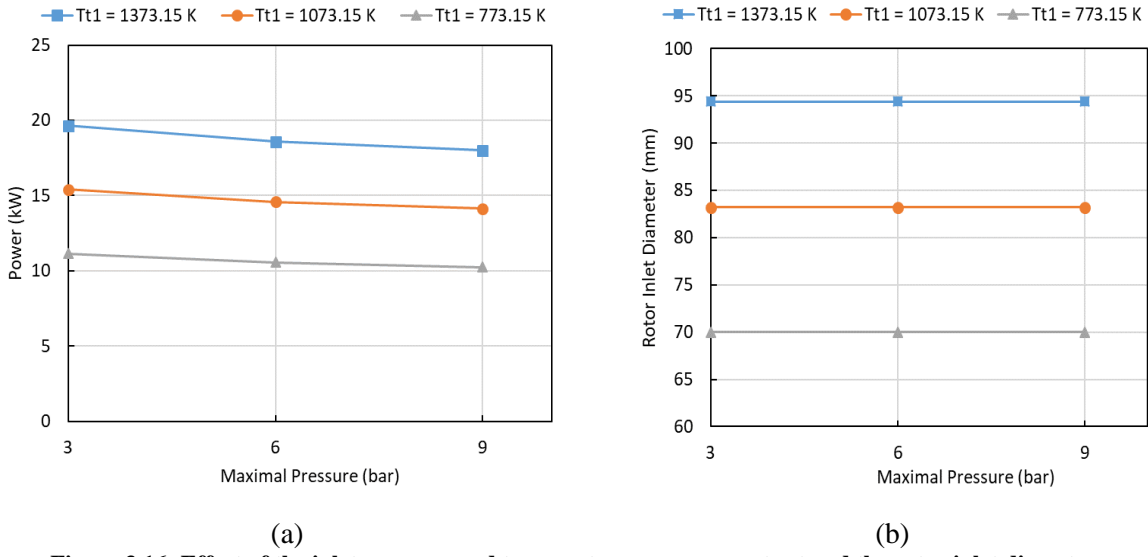


Figure 3.15: Impact of rotor rotational speed on (a) its diameter, (b) its efficiency, and power output.

Based on Figure 3.16, it is clear that the total inlet temperature ( $T_{t1}$ ) has a greater influence on the power output and rotor inlet diameter than the total inlet pressure ( $P_{t1}$ ). The variation of power output with the maximum pressure is insignificant, and the rotor inlet diameter is independent of the pressure. However, the power output for  $T_{t1} = 1373.15$  K is approximately twice the power output for  $T_{t1} = 773.15$  K. As well, the rotor diameter for  $T_{t1} = 1373.15$  K is higher by 25 % compared to  $T_{t1} = 773.15$  K. According to Equation (3.29), the velocity ratio and the expansion ratio are both fixed, so an increase in  $T_{t1}$  will result in an increase in  $U_4$ . Following Equation (3.38), the greater  $U_4$  corresponds to a larger  $r_4$ , and on that basis a greater  $d_4$  as well.



**Figure 3.16: Effect of the inlet pressure and temperature on power output and the rotor inlet diameter.**

Figure 3.17 shows the effect of changing the turbine inlet pressure on the leading edge height. When the pressure is higher, the leading edge height decreases. Comparing a turbine operating at 3 bar and 9 bar, the leading edge height is reduced to half. This occurs because when the pressure is increased, the air density increases too, thus reducing the volume required leading to a decrease in the leading edge height.



**Figure 3.17: Effect of maximum pressure on the rotor leading edge height.**

The power output and efficiency increase substantially with the mass flow rate of the working fluid as shown in Figure 3.18. The analysis has a direct relationship with the Euler equation, as shown in Equation (3.15). Increasing the mass flow rate from  $0.01\text{ kg/s}$  to  $0.09\text{ kg/s}$  respectively leads to an increase in the cycle efficiency and the power output by 2 points and 5 times. However, according to Figure 3.18b,  $d_4$  is independent of mass flow rate variation. Therefore, the variation of the mass flow rate has only an influence on the power output and the efficiency of the turbine, with no impact on the turbine geometry.

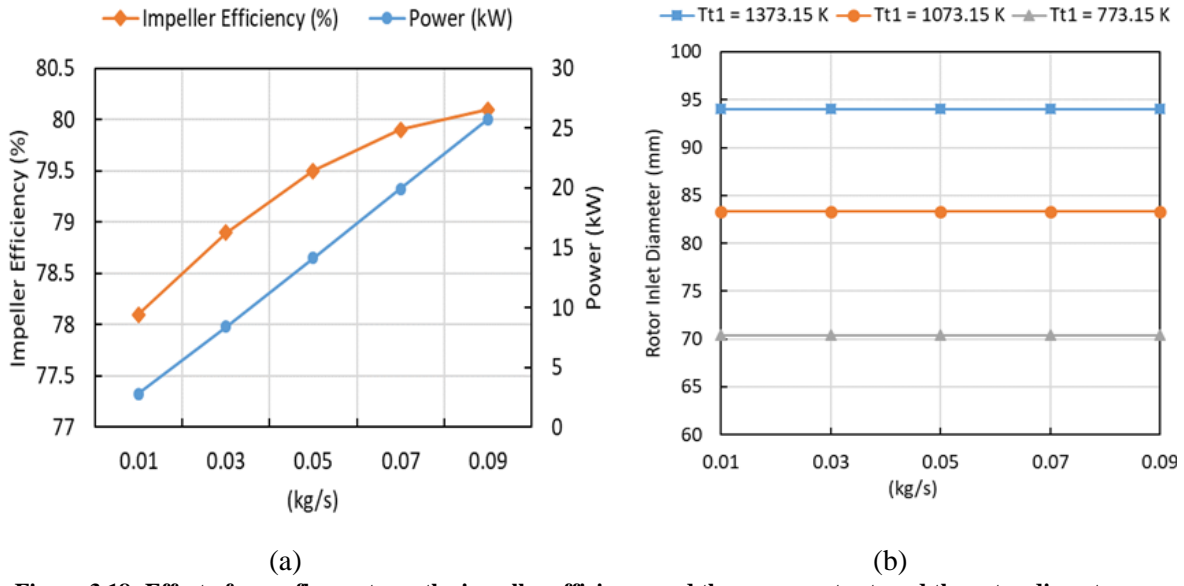


Figure 3.18: Effect of mass flow rate on the impeller efficiency and the power output, and the rotor diameter.

As seen in Figure 3.19a,  $d_4$  is affected by each of the velocity ratio and rotational speed in different ways. As the rotor rotational speed increases,  $d_4$  is reduced, while as the velocity ratio increases,  $d_4$  is increased. For instance,  $d_4$  increases by around 33 % when varying the velocity ratio from 0.6 to 0.9, reaching  $d_4 = 125$  mm for  $N = 120\,000$  rpm,  $d_4 = 187.5$  mm for  $N = 80\,000$  rpm, and  $d_4 = 375$  mm for  $N = 40\,000$  rpm. According to Figure 3.19b, there is an optimum velocity ratio between 0.65 - 0.75 that gives the highest power and efficiency. The results demonstrate that power and efficiency are strongly influenced by the velocity ratio, similar to what was discussed previously in Section 3.6.1.

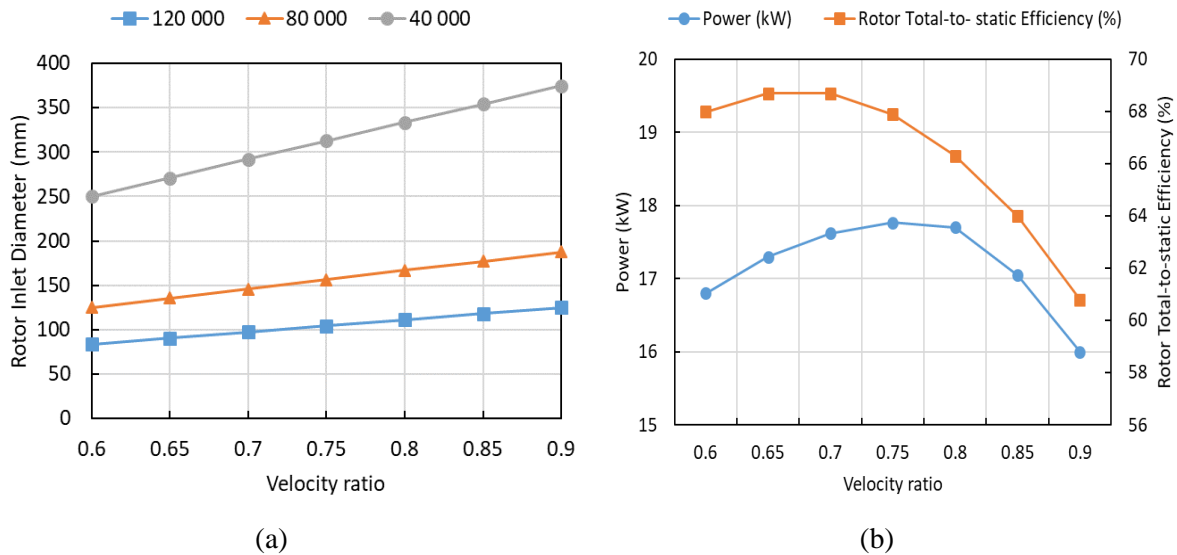


Figure 3.19: Impact of velocity ratio on the rotor inlet diameter, efficiency, and power output.

### 3.9. Computational Fluid Dynamics CFD- Uncooled Turbine

Although the 1D approach can predict the overall performance of the radial turbine, a 3D analysis is essential. It is necessary to perform a CFD study of the flow behavior in a turbomachine to predict any flow separation or shock wave that may occur. Due to this, CFD techniques have received a great deal of attention for modeling radial inflow turbines.

Several studies have focused on the design of a radial inflow turbine for the Organic Rankine cycle. Alshammari et al. [111] developed a 3D model for a radial inflow turbine for small-scale Organic Rankine cycle systems based on [253]. The stator geometry is developed in SolidWorks, While, the rotor is obtained using ANSYS BladeGen. The meshes are generated using ANSYS TurboGrid. Finally, the turbine stage is modeled in ANSYS CFX where the  $k-\omega$  SST is applied. The experimental results show good agreement with the simulation results. Sarmiento et al. [264] also investigated radial turbines for the organic Rankine cycle. First, a 1D design is developed using NIST REFPROP, followed by a CFD simulation. The geometry for both the nozzle and rotor was generated using ANSYS BladeGen. The mesh was generated using ANSYS TurboGrid with ATM optimized topology. The  $k-\omega$  SST turbulent model was selected with a convergence criterion of  $10^{-5}$ . The CFD results and the 1D approach match with a relative error of 1.091%. Furthermore, Da Silva et al. [252] proposed a design methodology for a radial turbine considering the R245fa fluid by the two approaches 1D and 3D modeling. CFX was used for the numerical calculation, TurboGrid was used for mesh generation, and BladeGen for modeling the rotor. Hexahedral mesh is applied near the wall and the residue was fixed to  $10^{-5}$ . The CFD simulations show acceptable agreement with the 1D design methodology in global terms.

Some studies have tackled the 3D design procedure of a radial turbine in other applications. Verma et al. [265] proposed a tool for designing a turboexpander for cryogenic refrigeration. The 3D model of the nozzle and the diffuser are generated using SolidWorks while BladeGen was used for the rotor geometry. The mesh was realized in ANSYS TurboGrid. CFD analysis revealed that the efficiency of the turbine matches the expected efficiency. Moreover, Chen et al. [266] conducted a study and an optimization of a centripetal turbine of 100 kW for ocean thermal energy conversion. The  $k-\epsilon$  model is the used turbulence model.

According to the review, CFD analysis allows the calculation of the flow field by considering the viscous effects that are not considered in 1D models. Additionally, CFD can be used to validate preliminary models. This section presents a complete CFD analysis of the 3D components of a 3D turbine stage model. The methodology presented in Figure 3.20, consists of importing input parameters from the VBA code to Vista RTD for both the stator and the rotor. Then, the geometry of the turbine stage is generated using ANSYS BladeGen. The mesh is obtained using ANSYS TurboGrid. Finally, both the stator and the rotor are imported into ANSYS CFX.

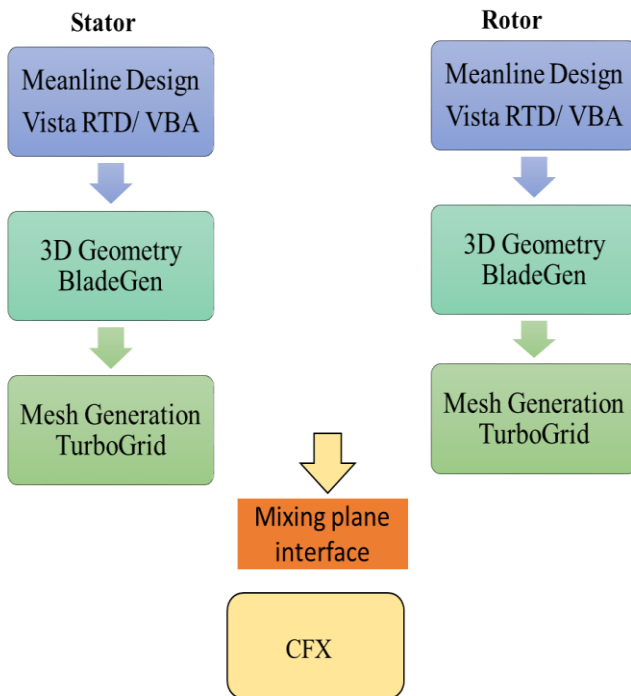


**Figure 3.20: Methodology for 3D simulation.**

### 3.9.1. ANSYS Vista RTD

Ansys-Vista RTD is used to conduct the meanline design of the studied radial turbine [267]. The required inputs are the inlet stagnation temperature and pressure, the mass flow rate, the total-to-total expansion ratio, the rotational speed, and the fluid properties. The geometrical inputs like the inlet and exit flow angles, the number of rotor blades, the diameter, and the axial length are conducted from the VBA code.

### 3.9.2. Comparison Between Vista RTD and VBA Code

The VBA code and the Vista RTD both develop a meanline analysis of the radial turbine. The difference between these two options is that the VBA code is used for a radial turbine with zero swirls at the exit; however, in Vista RTD the absolute velocity at the exit of the turbine is not necessary in the axial direction. Using the same input parameters for both, Figure 3.21 illustrates the velocity triangles at the inlet and outlet of the rotor. The velocity triangles in red are based on the VBA code, while the velocity triangles in black are based on the Vista RTD.

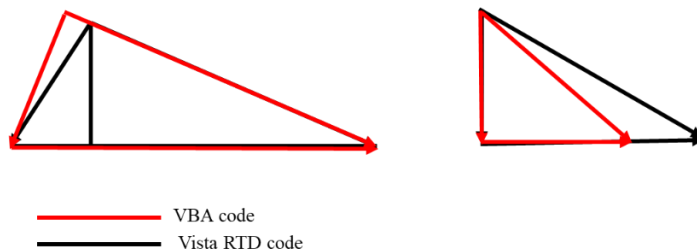


**Figure 3.21: Velocity triangles at the inlet (left) and the outlet (right) of the turbine with red for the VBA code and black for vista RTD.**

The velocity triangle at the inlet of the rotor obtained using the VBA code presents a lower relative blade angle comparing it with the Vista RTD. As a result, the rotor blades of the VBA code are slightly turned compared to the Vista RTD. There is an apparent mismatch between the velocity triangles at the outlet of the rotor. The reason is that Vista RTD shows the velocity triangle at the exit of the turbine at the turbine shroud radius, while in VBA, the velocity triangle is calculated at the mean outlet radius of the rotor. When computing the results at the same radius, the velocity triangles at the outlet of both codes match totally.

Based on these findings, for the rest of the study, some input parameters such as the number of blades and the angle of inlet velocity will be first computed in VBA, then introduced in Vista RTD as input parameters. Therefore, the preliminary design of the turbine will be a result of both codes.

### 3.9.3. 3D Model Generations

The 3D geometry of the nozzle and the rotor are created with ANSYS BladeGen. The inputs are imported from the meanline design and the blade profile is customized.

### 3.9.4. Computational Fluid Dynamics

CFD is a powerful tool that uses Navier-Stokes equations to solve the flow complexities in turbomachinery. Navier-Stokes equations describe the conservation of mass, momentum, and energy.

$$\frac{\partial \rho}{\partial t} + \frac{\partial}{\partial x_j} (\rho u_j) = 0 \quad (3.84)$$

$$\frac{\partial \rho u_i}{\partial t} + \frac{\partial (\rho \cdot u_j \cdot u_i)}{\partial x_j} = - \frac{\partial p}{\partial x_i} + \frac{\partial \tau_{ij}}{\partial x_j} + \rho f_i \quad (3.85)$$

$$\frac{\partial (\rho \cdot h)}{\partial t} + \frac{\partial (\rho \cdot u_j \cdot h)}{\partial x_j} = - \frac{\partial P}{\partial x_i} + u_j \frac{\partial P}{\partial x_j} + \tau_{ij} \frac{\partial u_i}{\partial x_j} - \frac{\partial q_j}{\partial x_j} + W_{ext} + q_H \quad (3.86)$$

$u_i, u_j$ : velocity,  $\rho$ : density,  $P$ : pressure,  $\tau$ : stress,  $q_H$ : heat flux,  $W_{ext}$ : work.

### 3.9.5. Turbulence Model

Navier-Stokes equations are discretized by RANS (Reynolds-averaged Navier-Stokes) equations. RANS equations are the time-averaged equation of motion for fluid flow. Their concept is based on decomposing the instantaneous quantity into mean and fluctuating quantities. This decomposition gives an extra term called Reynolds stress which is modeled using a turbulence model.

The main two turbulence models used are the k- $\varepsilon$  model and the k- $\omega$  model, in which  $\varepsilon$  is the turbulence dissipation rate and  $\omega$  is the specific dissipation rate. However, the k- $\varepsilon$  model cannot predict the flow separation in a turbulent model and the k- $\omega$  model cannot capture the free-stream turbulence effects. The k- $\omega$  SST model combines the two previous models. It is characterized by the robust behavior of the k- $\omega$  model near the wall and the ability of the k- $\varepsilon$  model to capture free stream turbulence far from the wall. Another advantage of using the k- $\omega$  SST is the ability to determine automatically the first node away from the wall  $Y^+$  and predict the flow separation.

Considering a flow over a plate in Figure 3.22, the boundary layer can be divided into laminar, transition, and turbulent boundary layer regions.

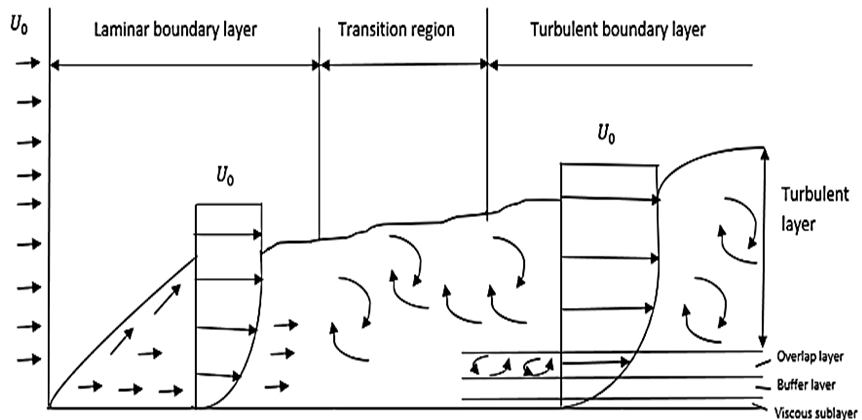


**Figure 3.22: Boundary layer over a flat plate.**

$U_0$  is the free stream velocity and  $\delta$  is the boundary layer thickness and  $y$  is the vertical distance measured from the wall.

In order to determine if the flow is laminar or turbulent, the Reynolds number is calculated.

$$Re = \frac{u L}{v} \quad (3.87)$$

$Re$ : the Reynolds number

$u$ : the velocity of the fluid (m/s)

$L$ : characteristic length (m)

$v$ : the kinematic viscosity of the fluid ( $m^2/s$ )

The turbulent boundary layer near the wall is decomposed into three layers, as seen in Figure 3.23:

- The inner layer, or sublayer, where the fluid is dominated by viscous shear in absence of the turbulent shear stress ( $y^+ < 5$ ), the relationship between  $u^+$  and  $y^+$  is linear.
- The buffer layer ( $5 < y^+ < 30$ )
- The overlap layer or log layer ( $5 < y^+ < 30$ ) where viscous and turbulent effects are both manifested. The relationship between  $y^+$  and  $u^+$  is logarithmic.

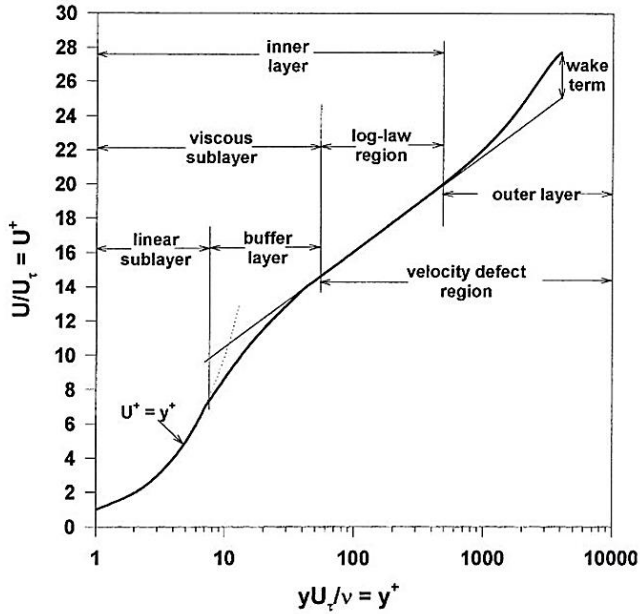


Figure 3.23 : $u^+$  in function of  $y^+$  [268].

A non-dimensional wall distance for a wall-bounded flow can be defined in the following way:

$$y^+ = \frac{u_* y}{v} \quad (3.88)$$

Where  $u_*$  is the friction velocity at the nearest wall,  $y$  is the distance to the nearest wall and  $v$  is the local kinematic viscosity of the fluid.

### 3.9.6. Mesh Generation

The mesh for both stator and rotor is generated by ANSYS Turbogrid where the Automatic Topology and Meshing (ATM Optimized) option was used.

An evaluation of the mesh quality is performed by measuring the maximum and minimum face angle elements, volume ratios, edge length ratios, and the number of connections. An improvement in mesh quality is possible if the mesh quality is poor in a certain region.

### 3.9.7. Physical Domain and Boundary Conditions

The generated mesh is imported to ANSYS CFX, where two models of boundary conditions are available. In the first model, the total inlet stagnation temperature and pressure, as well as the static outlet pressure, are specified. While the second model defines the mass flow rate at the inlet and the static pressure at the outlet. Through the use of the total energy model, heat transfer is included. In this simulation, the first model is applied.

To simulate the rotor (rotating) and the stator (stationary), a domain interface is required to provide communication between the stationary and rotating blades. Two major interfaces exist in ANSYS CFX: the mixing plane and the frozen rotor. In the mixing plane approach, flow data are averaged over the stator outlet and the rotor inlet (rotor-stator interface), and then boundary conditions are updated. In contrast, the frozen rotor uses a rotating reference so that the true flow passes downstream at one position. This study will use the mixing plane approach. The convergence is achieved when the Root-Mean-Square is less than  $10^{-6}$  for mass and momentum.

### 3.9.8. Validation of the Current Method

The validation of the current design procedure is achieved by comparing the results with a commercially existing turbine. Odabaee et al. [267] and Sauret [269] carried out two papers consisting of reproducing the same geometry of an existing radial inflow turbine used in Sundstrand Power Systems T-100 Multipurpose Small Power Unit. The former consists of a stator, a rotor, and a diffuser designed via Vista RTD and ANSYS CFX. The latter design comprises a stator, a rotor, and a diffuser designed via RITAL and Axcent as shown in Table 3.5.

**Table 3.5: Summary of the design procedure in two publications.**

Reference	Components	Softwares
Odabaee et al. [267]	Stator + Rotor + Diffuser	Vista RTD + CFX
Sauret [269]	Stator + Rotor + Diffuser	Rital + Axcent
Current code	Stator + Rotor	Vista RTD + CFX

To validate the compatibility of the developed code, the results are compared with the simulation and experimental results of [267] and [269] for the same operating conditions in Table 3.6. The input parameters are the rotational speed N, the inlet total pressure  $P_{t4}$ , the outlet static pressure  $P_5$ , and the outlet static temperature  $T_5$ .

**Table 3.6: Operating conditions.**

Operating Conditions	Values	Rig Conditions
N (RPM)	106 588	71 700
$P_{t4}$ (kPa)	580.4	413.6
$P_5$ (kPa)	94	63
$T_5$ (K)	1056.5	477.6

At first, the preliminary design of the turbine is compared in terms of efficiency, velocity triangles, and geometrical parameters. The comparison between the turbines' efficiency is presented in Table 3.7. It can be seen that the results are very close. The total-to-total efficiency of the designed turbine is the same in the validation code and [267], but higher by 0.4 points compared to [269]. The difference is justified because of two different software Vista RTD and Rital.

**Table 3.7: Preliminary design validation.**

Parameters	Odabaee et al. [267]	Sauret [269]	Validation Code
$\eta_{tt}$	86.4	86.8	86.4
$\eta_{ts}$	86	86.05	86.2
Power (kW)	-	120.8	119.99

The velocity triangles at the inlet and the outlet of the rotor are only depicted by [269]. Figure 3.24 illustrates a comparison of both the velocity triangles at the inlet (left) and the outlet (right) of the rotor. The blue lines correspond to the code developed by [269] and the red lines are those for the validation code.

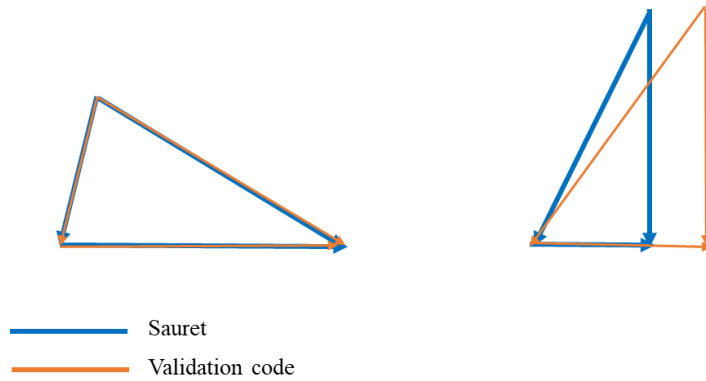


**Figure 3.24: Comparison of velocity triangles at the inlet (left) and the outlet (right) of the rotor between [269] (blue) and the validation code (red).**

It can be seen that the velocity triangles at the rotor inlet match unlike the velocity triangles at the outlet of the rotor. The exit velocity triangle is conducted on the mean radius of the turbine rotor ( $\frac{r_{s5}+r_{h5}}{2}$ ) in [269]. While in the validation code, the exit velocity triangle is calculated at the shroud radius ( $r_{s5}$ ).

**Table 3.8: Rotor geometry design validation.**

Parameters	Sauret [269]	Validation Code	Error (%)
$r_4$ (mm)	58.2	57.1	1
$r_{h5}$ (mm)	15.2	15	1.3
$r_{s5}$ (mm)	36.8	36.2	1.6
$T_5$ (K)	711.2	705.5	0.8
$T_{t5}$ (K)	728.6	726	0.35
$P_5$ (kPa)	96.1	93.14	3
$P_{t5}$ (kPa)	105.8	103.64	2
$M_4$	0.986	0.984	0.2
$M_5$	0.384	0.399	3

Then, the geometric and aerodynamic performance of the rotor is conducted by comparing the rotor inlet and outlet radius, the pressure and temperature, and the Mach number at different stations as summarized in Table 3.8. It can be seen that the error does not exceed 3 %. Therefore, the results are compatible and in good agreement.

The last step of validation is the 3D simulation using ANSYS CFX. The results are compared with both the simulation and the experimental results from [267] because the two simulations use the same software. The total-to-static efficiency (Table 3.9) and the total-to-total efficiency (Table 3.10) display almost identical values.

**Table 3.9: Comparison of the total-to-static efficiency.**

$\eta_{ts}$	Odabaee et al. [267]	Validation Code
Preliminary	85.9	86.2
3D simulation	86.2	87.6
Experiment	86.2	-

**Table 3.10: Comparison of the total-to-total efficiency.**

$\eta_{tt}$	Odabaee et al. [267]	Validation Code
Preliminary	86.4	86.4
3D simulation	86.2	87.6
Experiment	87.5	-

The validation of the developed approach is done by comparing the temperature variation on different parts of the turbine components. Figure 3.25 shows that the temperature distribution is slightly the same in both cases, with no significant difference.

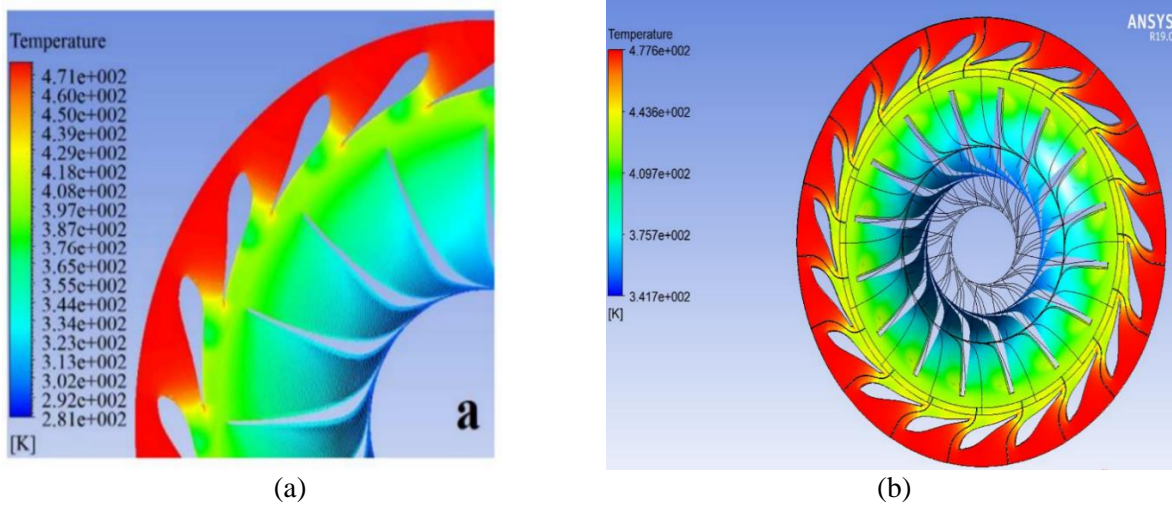


**Figure 3.25: Comparison of the temperature variation map, (a) Odabaee et al. [267], (b) Validation Code.**

Based on these findings, it can be concluded from this section, that the CFX code is valid and can be used to evaluate the performance of the microturbine for the range-extended electric vehicle.

### 3.9.9. Modeling of the Uncooled HP Turbine for IRReGT Cycle

This section develops the design of the uncooled HP turbine of the standard IRReGT cycle. It is composed of two compression stages with an intercooler, where the maximum pressure is 9 bar, then two expansion stages with reheating and a recuperator. The two turbines are uncooled, handling temperatures up to 1373.15 K. The operating conditions of the HP turbine are obtained from the thermodynamic analysis conducted in Chapter 2 and presented in Table 3.11. Since centrifugal forces and stresses on the turbine wheel increase at higher rotational speeds, 120 000 rpm is chosen for the rotational speed of the turbine.

**Table 3.11: HP turbine properties.**

Parameters	Operating conditions
Fluid	Air
Total Inlet Pressure	9 bar
Total Inlet Temperature	1373.15 k
Total-to-total expansion ratio	3
Mass flow rate	0.054 kg/s
Rotational speed	120 000 rpm

To perform the preliminary design, VBA is first used to determine input parameters such as the number of blades and the absolute inlet angle which are then inserted into Vista RTD. The results from Vista RTD are aerodynamic and geometric parameters presented in Table 3.12.

**Table 3.12: Preliminary design results from Vista RTD.**

Parameters	Operating conditions
$U_4$ (m/s)	558.3
$C_4$ (m/s)	633.48
$W_4$ (m/s)	140.86
$\alpha_4$ ( $^{\circ}$ )	78.5
$\beta_4$ ( $^{\circ}$ )	26.28
$N_R$	16
$U_5$ (m/s)	446
$C_5$ (m/s)	228.8
$W_5$ (m/s)	159.5
$d_4$ (mm)	88.9
$d_{h5}$ (mm)	19.5
$d_{s5}$ (mm)	71
$d_2$ (mm)	102
Stage Efficiency $\eta$ (%)	75
Impeller $\eta$ (%)	79.5

The results from the preliminary design of Table 3.12 are transmitted to ANSYS BladeGen to generate the 3D geometry of both the rotor and the stator, as illustrated in Figure 3.26.

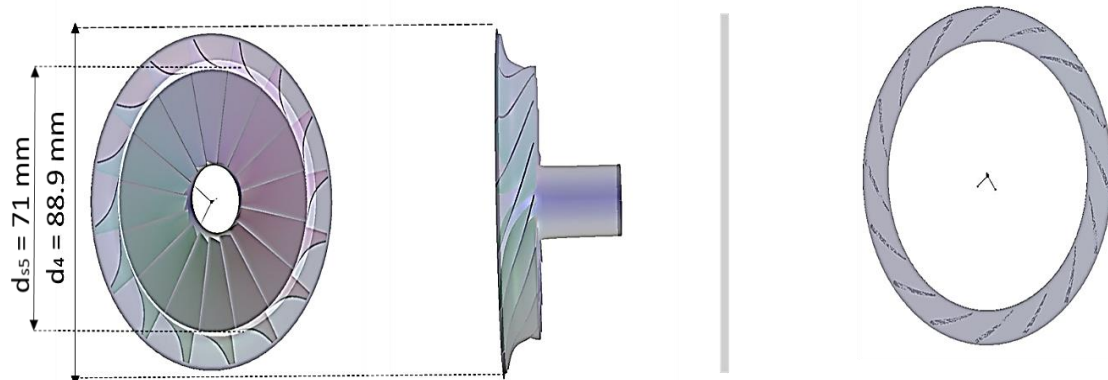


**Figure 3.26: (a) Rotor 3D geometry, (b) Stator 3D geometry.**

The geometries are imported to ANSYS TurboGrid to generate the mesh using the Automatic Topology and Meshing (ATM Optimized). A grid independence analysis was conducted by adding more elements to the mesh of the rotor and stator. The number of mesh elements increases the computational time of the simulation, but it ensures convergence. Hence, a compromise must be made between the number of elements and the processing time.

**Table 3.13: Grid sensitivity study results.**

	Number of elements	stator	Number of rotor elements	$\eta$ (%)	Rotor outlet temperature (K)
1	95 656		112 863	78.46	1086.21
2	192 444		204 350	79.27	1085.83
3	297 600		297 700	79.89	1085.64
4	371 840		640 800	80	1085.57
5	752 130		640 800	80.62	1085.58

Among the investigated grid result shown in Table 3.13, and as a compromise between accuracy, grid independence, and computational time, grid size number 4 was selected. The global imbalances are much less than 1%, which confirms proper solver convergence. The rotor and the stator mesh are illustrated respectively in Figure 3.27 and Figure 3.28.

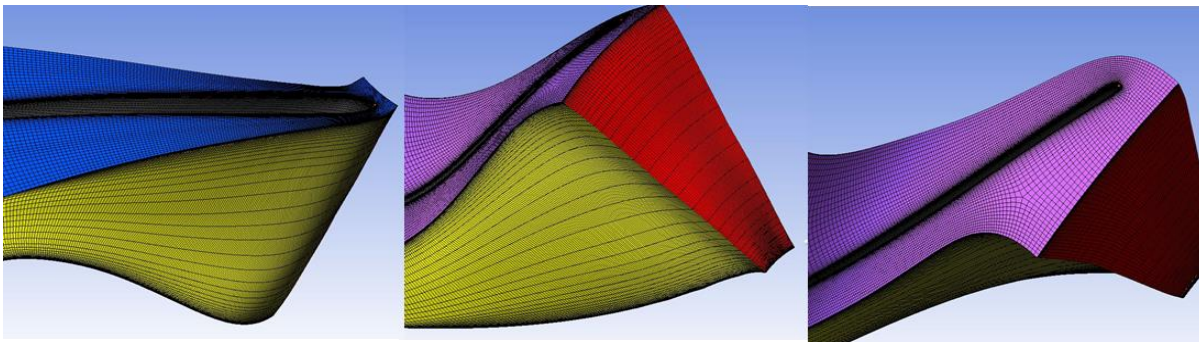


**Figure 3.27: Rotor mesh generation.**

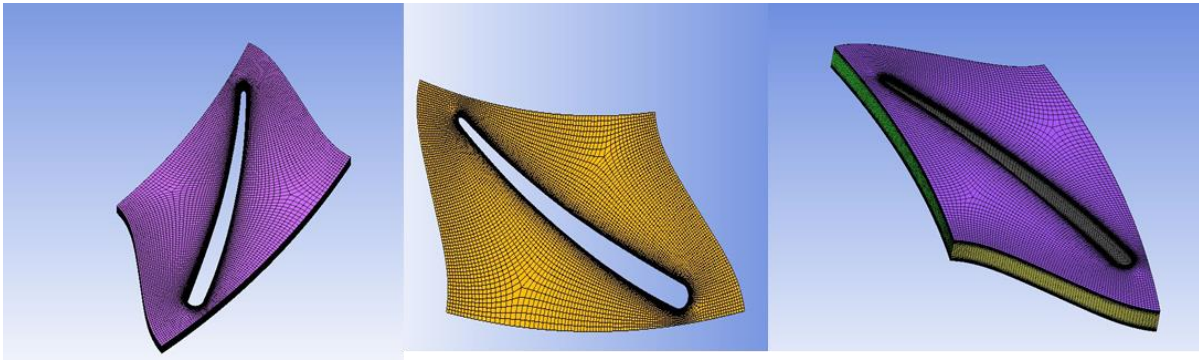


**Figure 3.28: Stator mesh generation.**

Both the stator and rotor are imported into ANSYS CFX. The boundary conditions are the total inlet temperature and the total inlet pressure at the nozzle inlet and the outlet static pressure at the rotor exit. The flow at the nozzle inlet is assumed in the perpendicular direction (radial direction). A Mixing plane model is applied at the stator-rotor interface to ensure the connection between the stationary and the rotating blade domain. The simulation is carried out for one stator blade passage and one rotor blade passage and the periodicity model is used to determine the result on the overall stage. Additionally, all the walls are assumed to be smooth, and adiabatic with no-slip conditions. The k- $\omega$  SST turbulence model is used. The convergence is adjusted at  $10^{-6}$  for all the residuals (pressure, mass flow, temperature). All the computational fluid domain details are depicted in Figure 3.29.

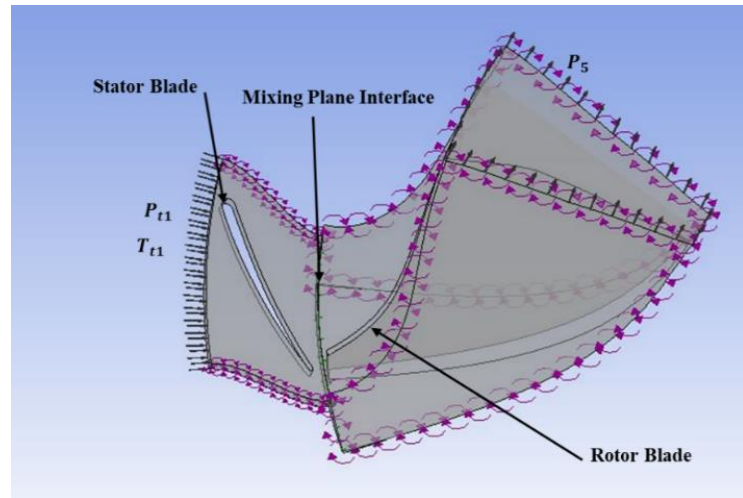


**Figure 3.29: Computational fluid domain for stator and rotor.**

Figure 3.30 represents the stator and the rotor combined in 3D to be simulated in ANSYS CFX.

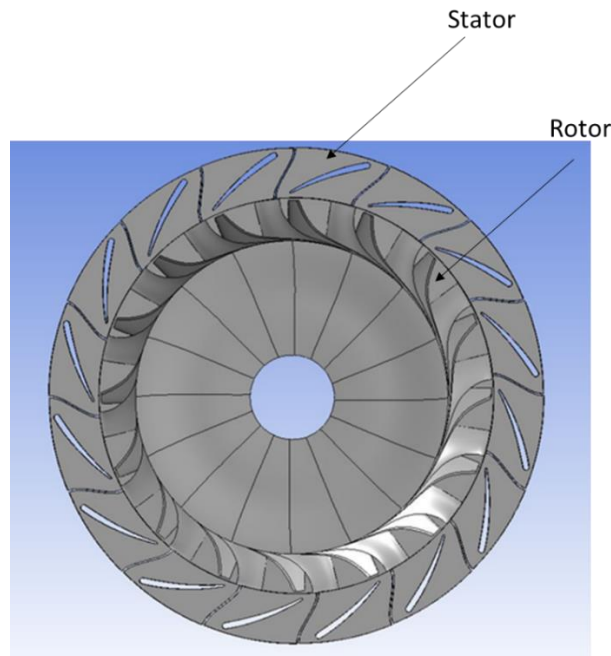


**Figure 3.30: Stator and rotor in 3D.**

### 3.9.10. CFD Results

The results in this section are based on the turbine operating conditions in Table 3.11.

The contours of the temperature and pressure through the turbine stage at a span of 50 % are presented respectively in Figure 3.30 and Figure 3.32. The temperature at the inlet of the stator is 1373 K, it decreases through the turbine stage to reach 990 K at the stator exit.

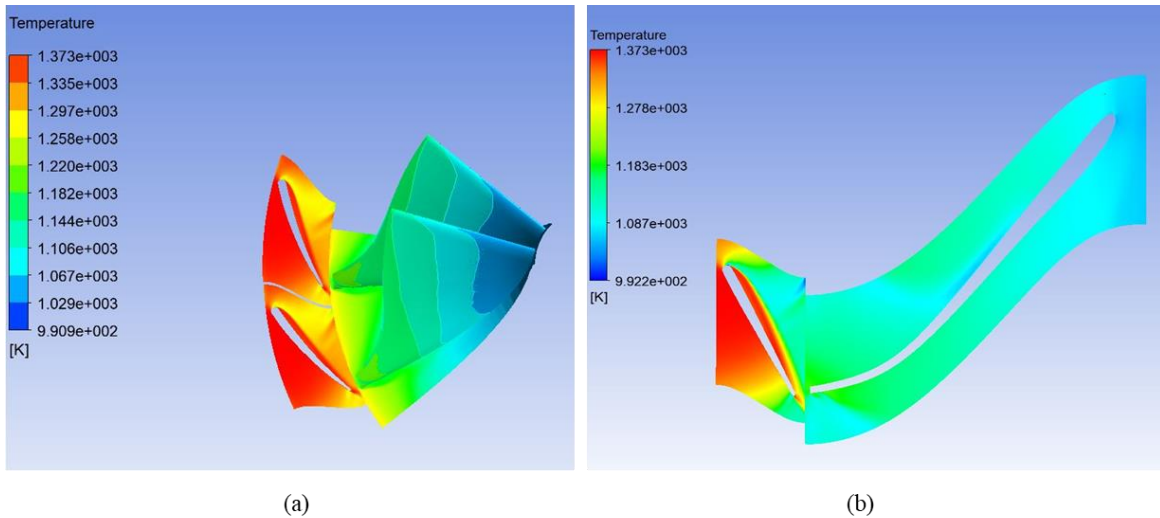


**Figure 3.31: Temperature distribution in the turbine stage (a) 3D view, (b) Blade-to-blade view.**

In addition, the pressure through the turbine stage decreases from 9 bar to 2.9 bar at the exit of the stator. It can be seen that the pressure drop through the stator and the rotor is in good agreement with the design requirement.

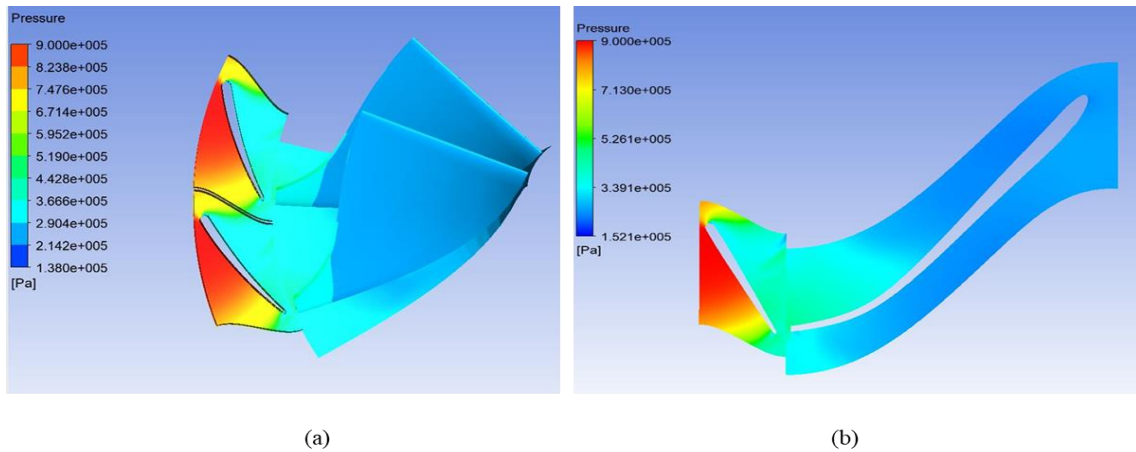


**Figure 3.32: Pressure distribution in the turbine stage (a) 3D view, (b) Blade-to-blade view.**

The distribution of the Mach number value through the turbine stage, as illustrated in Figure 3.33, shows that a maximum value of the Mach number approaching 1 is reached at the stator exit. This value is expected because the flow is accelerated through the stator blades before entering the rotor.

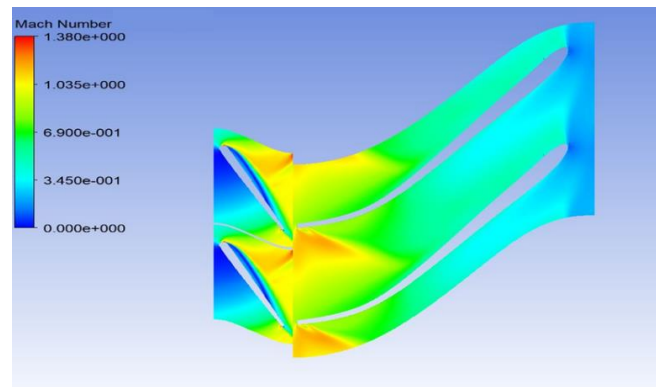


**Figure 3.33: Mach number distribution in the turbine stage.**

The flow streamlines through the turbine stage are visualized in Figure 3.34 at a span of 50 %. There is no turbulent flow at the leading edge of the rotor, implying that the inlet incidence angle is optimal. There is, however, some diffusion on the pressure side of the rotor blade, which indicates flow separation. These recirculations occur as a result of a difference between the actual and the ideal flows in the blade passage.

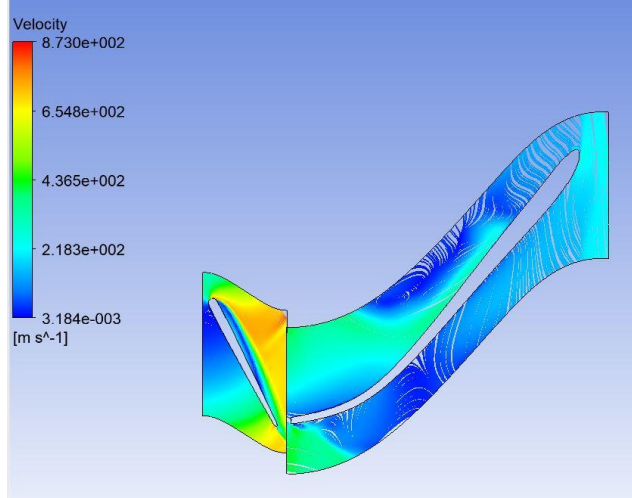


**Figure 3.34:** Velocity streamline at 50% span at  $N = 120\,000$  rpm,  $P_{max} = 9$  bar.

The preliminary 1D results and the CFD results were compared as shown in Table 3.14. Overall, the parameters are in good agreement for the majority of the parameters. The designed HP turbine for the standard IRReGT cycle operating at 9 bar, has an efficiency of 75 % based on 1D results and 80 % based on the CFD results. Thus, the proposed methodology can accurately predict the HP radial turbine performance and flow characteristics.

**Table 3.14: Comparison between the proposed methodology and CFD results.**

Parameter	1D Results	CFD Results
$P_{01}$ (bar)	9	9
$T_{01}$ (K)	1373.15	1373.15
$P_5$ (bar)	2.9	2.94
$T_{05}$ (K)	1113.15	1110.6
$P_5$ (bar)	2.58	2.57
$T_5$ (K)	1090.3	1083.6
$C_4$ (m/s)	673.32	660.4
$C_5$ (m/s)	300	224.69
$\eta$ (%)	75	80

### 3.10. Discussions

The benefit of choosing a turbine operating at 9 bar is due to its contribution to increasing the efficiency of the IRReGT cycle, as determined in Chapter 2. The majority of the turbines on the market are turbines with an inlet pressure limited to 3 bar. To the authors' knowledge, there is no turbine designed to operate at 9 bar. Although a turbine's performance is mainly determined by its expansion ratio, some geometrical parameters (mainly velocity triangles) change when considering different inlet pressures when designing a turbine from scratch.

The optimal rotational speed for a turbine operating at 9 bar is 220 000 - 240 000 rpm. Since the rotational speed is fixed to 120 000 rpm in this application due to stress constraints, a turbine operating at 3 bar will have higher efficiency at 120 000 rpm.

On the other hand, for the same operating conditions (rotational speed, inlet temperature, expansion ratio), the blade geometrical parameters for a turbine operating at 9 bar differ from the one operating at 3 bar, as depicted in Table 3.15. As the inlet pressure increases, the relative flow angle increases too, resulting in a more deflected turbine blade and an excessive blade curvature. In addition, since the inlet pressure is higher, the density of its inlet gas is also higher resulting in a reduction in the gas volume. In this way, the height of the leading edge and trailing edge of the turbine decreases as the pressure increases. For instance, the leading edge height when the turbine operates at 3 bar is approximately 2.5 times the one for a turbine operating at 9 bar. As well, the increase in the inlet pressure reduces the axial length of the turbine. Thus, the axial length of the turbine decreases by 1.5 when the inlet pressure increases from 3 bar to 9 bar. Based on the above statements, the 9 bar turbine presents a more deflected blade, with a reduced blade height as well as a reduced axial length compared to a 3 bar. This makes the 9 bar turbine more complex technologically.

Blade tip clearance is another important parameter that affects the operating behavior of a turbine. Clearance changes during operation occur due to strain on the engine, mechanical, and centrifugal forces, and changes in thermal and mechanical loads between the rotating wheel and the stationary casing. Choosing the clearance gap correctly is crucial since too much clearance can cause internal leaks and efficiency loss, while too little clearance can cause blades to rub against housings. As the turbine operating at 9 bar is subjected to higher pressure, thus, higher strain and mechanical loads, the clearance gap is higher than for the one operating at 3 bar. The efficiency of a turbine decreases by up to 8% when the tip clearance increases from 0 % to 4 % [270].

**Table 3.15: Comparison between 9 bar and 3 bar.**

Parameters	3 bar	9 bar
$\beta_4$ (°C)	30	49
$\beta_5$ (°C)	64.8	65
$b_4$ (mm)	0.0027	0.0011
$\Delta z_R$ (mm)	0.0165	0.00839

In conclusion, although the use of a turbine operating at 9 bar enhances the IRReGT cycle efficiency significantly, it is coupled with technological complexities. Compared to a turbine operating at 3 bar and with the same operating conditions, the blade of a 9 bar turbine is in excessive curvature, with the lowest edges height and reduced axial length.

### 3.11. 3D Simulation of a Cooled Turbine

This section outlines the design of the cooled radial turbine from the coolant channel generation to the CFD analysis. The purpose of this section is two-fold: the first is to validate the thermodynamic model in Chapter 2 that determines the mass of coolant required, while the second objective is to assess the CFD simulation of a HP cooled compact radial turbine. This thesis considered only the cooling of the rotor blade, the cooling of the stator blade is not in the scope of this study. As explained before, the convection cooling technique is selected since it consists of simple, and suitable small-scale turbine blades.

The thermodynamic analysis conducted in Chapter 2 made it possible to determine the mass of coolant needed to protect the turbine blade from the hot gas. It can be seen that for a TIT of 1450 °C, the fraction of coolant from the total mass of air is 1.41 % when the material can handle a maximum temperature of 1100 °C.

The design approach of the cooled turbine consists of initially determining the hottest areas of the turbine blade to identify the zones that should be cooled. Then, the cooling channel is generated based on both the cooling necessity and the 3D printing constraints. Finally, 3D analyses are conducted to evaluate the impact of cooling on the turbine behavior. Figure 3.35 defines the considered design methodology.

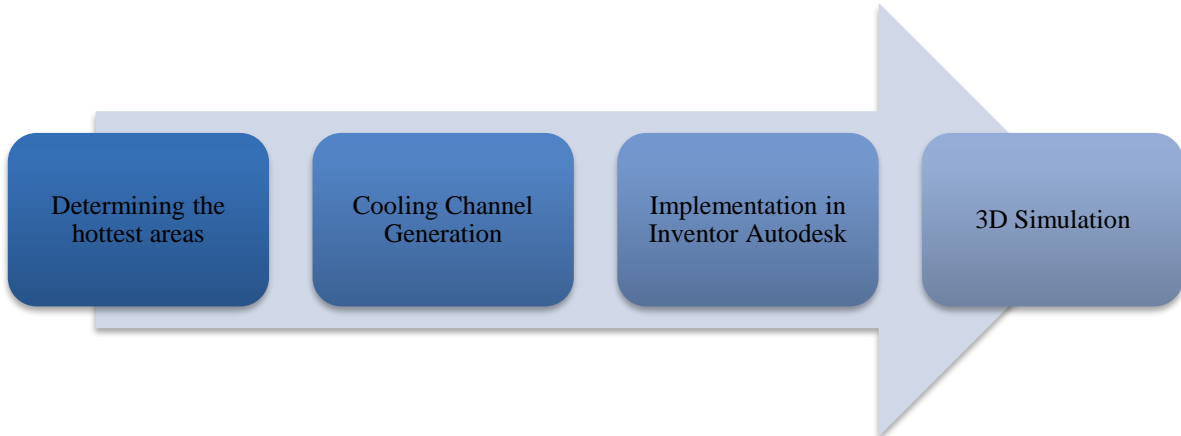


**Figure 3.35:** Design methodology for the cooled turbine.

#### ➤ Cooling Channel Generation

The channels in the turbine blades are designed to reach the hottest spots of the turbine blade taking into consideration the material stresses. The leading edge of the turbine rotor is the most critical as it is the most affected by the hot gas temperature. As it flows into the turbine blade, the hot gas expands, so its temperature decreases. Figure 3.36 presents the temperature variation on a rotor blade for an uncooled turbine operating at 9 bar and TIT = 1450 °C. The red outline delimits the area with the highest temperature. Therefore, the coolant channel should pass through this region to ensure its cooling.

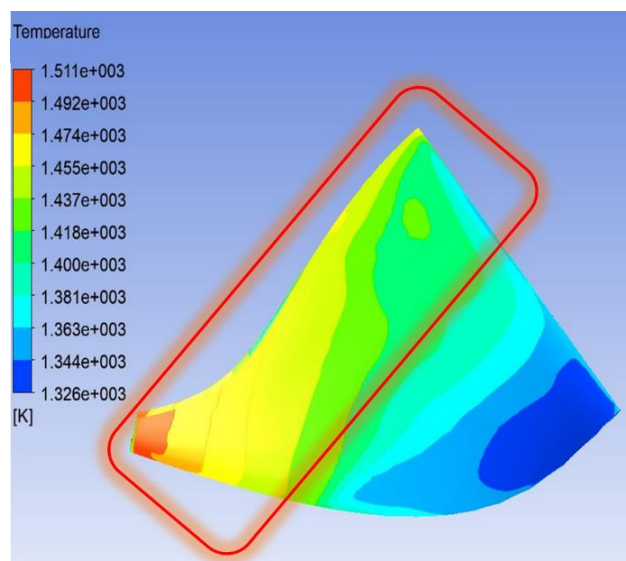


**Figure 3.36:** Zone with the highest temperature for an uncooled turbine operating at 9 bar and TIT = 1450 °C.

A preliminary study has been conducted for the design of the cooling channel. The cooling circuit is considered a cylindrical channel that runs from the leading edge of the turbine to its trailing edge. The cooling channel is designed to be able to introduce the calculated mass of coolant air into the turbine blade. The study takes into account the acceptable pressure drops into the cooling channel, as well as the limitations of 3D printing including the minimum wall thickness (0.16 mm).

Based on this study, a coolant channel of a diameter of 0.5 mm is implemented into the turbine blade. The proposed configuration is an acceptable compromise for pressure drops, 3D printing limitations, and heat transfer constraints.

### **3.12. Numerical Simulation Methodology of a Cooled Turbine Blade**

An overview of the most relevant studies in the literature investigating numerical simulation methods for the cooled turbine blade using different cooling techniques. Based on the surveyed studies and the author's knowledge, very few presented a detailed methodology for internal convection in a smooth cooling channel.

Al-Kayiem et al. [271] performed an analysis of an internal ribbed rectangular cooling channel of the turbine blade. The blade geometry is supplied by Lumut Power plant-Malaysia. Hence, it was initially exported in Autocad, then discretized in GAMBIT, and finally simulated using ANSYS Fluent. Comparison between the analytical and the numerical methods showed a good agreement, where the temperature difference does not exceed 10 %. Do et al. [272] conducted a numerical study for the heat transfer of pin fins in gas turbine blade internal cooling. The flow characteristics and heat transfer were solved in ANSYS CFX using continuity, RANS, and energy equations. The meshes were generated in ANSYS ICEM. The convergence condition was set so that the root-mean-square values of the continuity, momentum, energy and turbulent kinetic energy equations are less than  $10^{-6}$ . Irfan Ahmed et al. [273] investigated the internal cooling and the film cooling of a turbine blade by comparing two different materials Nickel Chromium and Titanium carbide. The turbine blade was designed in CATIAV5-6R. Then, Fluent was used to determine the temperature distribution and the heat transfer through the turbine blade. Results show that the heat transfer depends on the turbine blade melting temperature.

Other researchers proposed to solve the cooling technology by using novel coolants such as liquid metals, especially to cool the stator vanes of the gas turbine. Zhang et al. [274] studied the thermal behavior of liquid metal in internal cooling using a U-shaped cooling channel on the gas turbine performance. The k- $\omega$  SST turbulence model and total energy equation are used to solve the heat transfer and the 3D steady-state turbulent flow. Results show that the heat transfer performance depends mainly on the coolant inlet temperature. Increasing the coolant inlet temperature results in a decrease in the heat transfer performance and an increase in the external blade temperature.

Zhang et al. [132] developed a study on a compact radial turbine rotor cooled by convection. CFD analysis of GT components, including the compressor from which coolant is extracted, was conducted using Star-CCM+. In a turbine body, there are two main parts: a solid part and a fluid part. The k- $\omega$  SST turbulence model is applied in the conjugate heat transfer simulation, with no other turbulence models. Both the mainstream and the coolant are considered ideal gas, and the rotor was taken in CM247 LC. An unstructured polyhedral mesh configuration was applied and generated in Star CCM+. There are three main interfaces: mainstream flow/turbine wheel, coolant/turbine wheel, and compressor wheel/mainstream flow. When comparing the uncooled and cooled turbine configurations, it can be seen that the cooled turbine blade's leading edge temperature is less than 110 K.

Based on these findings, this section proposes a detailed methodology to study the 3D simulation of a cooled turbine rotor. The cooling scheme is the same as the one carried out in [132]. It consists of a smooth cooling channel accommodated in a compact turbine rotor. The same procedure is applied to capture the 3D flow and heat transfer. The simulation is conducted in ANSYS CFX by dividing the turbine blade into three main parts and by using the  $k-\omega$  SST turbulence model. The detailed procedure is explained in the following sections.

### 3.12.1. 3D Generation of the Cooled Blade

The uncooled turbine blade generated in ANSYS BladeGen (Figure 3.26a), was exported in Inventor to accommodate the cooling channel. The cooling channel architecture and placement match the topology optimization suggested for HiETA [132]. The coolant enters the leading edge, the hottest part of the turbine, and flows through the turbine blade as close as possible to the shroud, following the pathway delimited in Figure 3.36. Figure 3.37 illustrates the turbine blade with the generated cooling channel of a diameter of 0.5 mm.

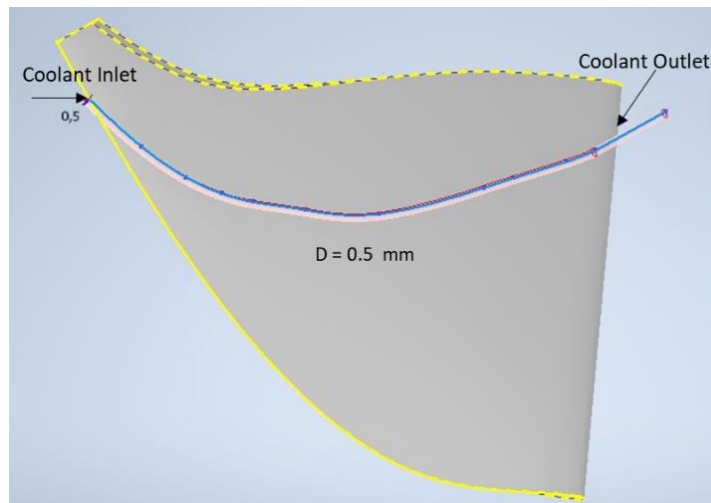


Figure 3.37: Cooled turbine blade configuration from 3D Inventor.

As explained before, the coolant passes through a hollow shaft, reaches the leading edge then exists through the trailing edge to mix with the mainstream flow. Figure 3.38 represents both the cross-sectional area of the designed cooled turbine and the entire geometry.

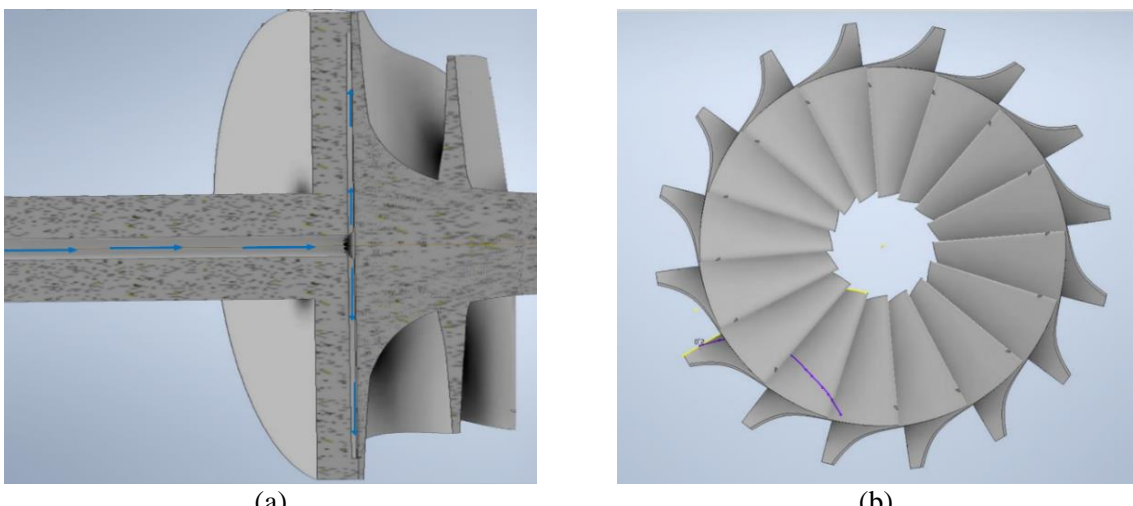


Figure 3.38: Cooled turbine geometry (a) cross-sectional configuration, (b) complete turbine.

The overall blade is then imported to ANSYS Design Modeler, as shown in Figure 3.39. The characteristics of the cooled blade are determined as follows: the fluid part is composed of the hot gas and the coolant, and the solid part consists of the turbine blade.

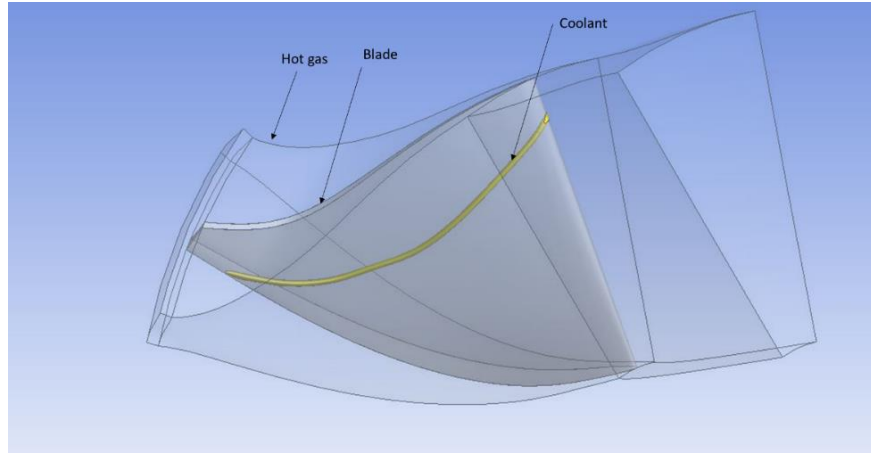


Figure 3.39: The three bodies of the cooled turbine blade in Design Modeler.

### 3.12.2. Mesh Generation

The turbine meshing is realized in ANSYS Meshing. Accurate mesh quality is determined by taking a smooth meshing and checking its skewness. Skewness refers to the deviation between the optimal cell size and the current cell size. A skewness of 0 indicates ideal meshing, while a skewness of 1 indicates that the meshing is far from optimal. Using grid independence, the optimal number of mesh elements was chosen for the cooled turbine blades, as shown in Figure 3.40. On the left, is the mesh generation of the turbine blade and the coolant channel, and on the right is the hot gas volume. A major challenge in meshing was caused by the difference in scale across the geometry. The mainstream mesh size scale is larger than the coolant mesh size scale.

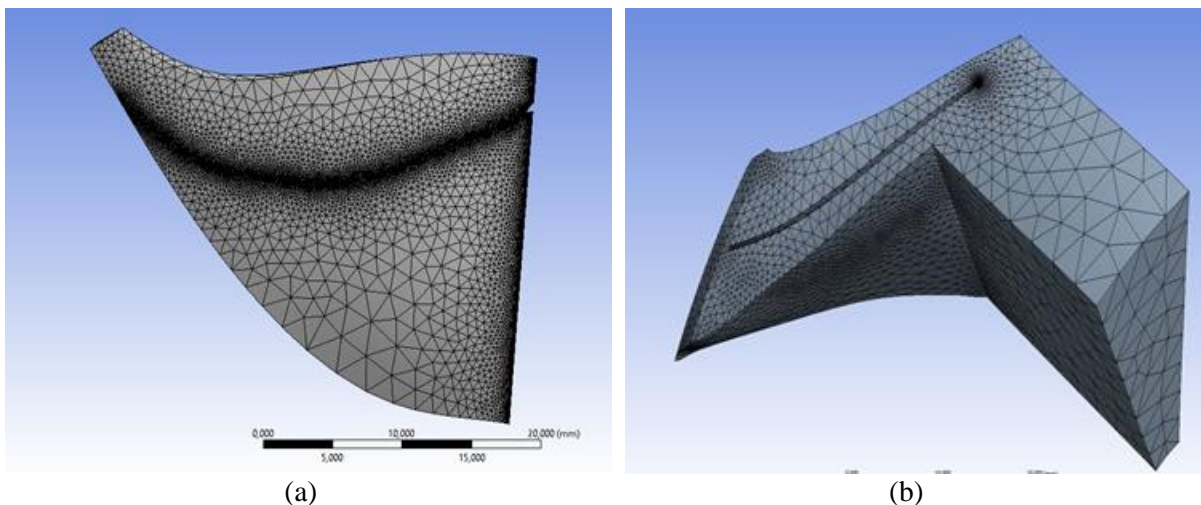
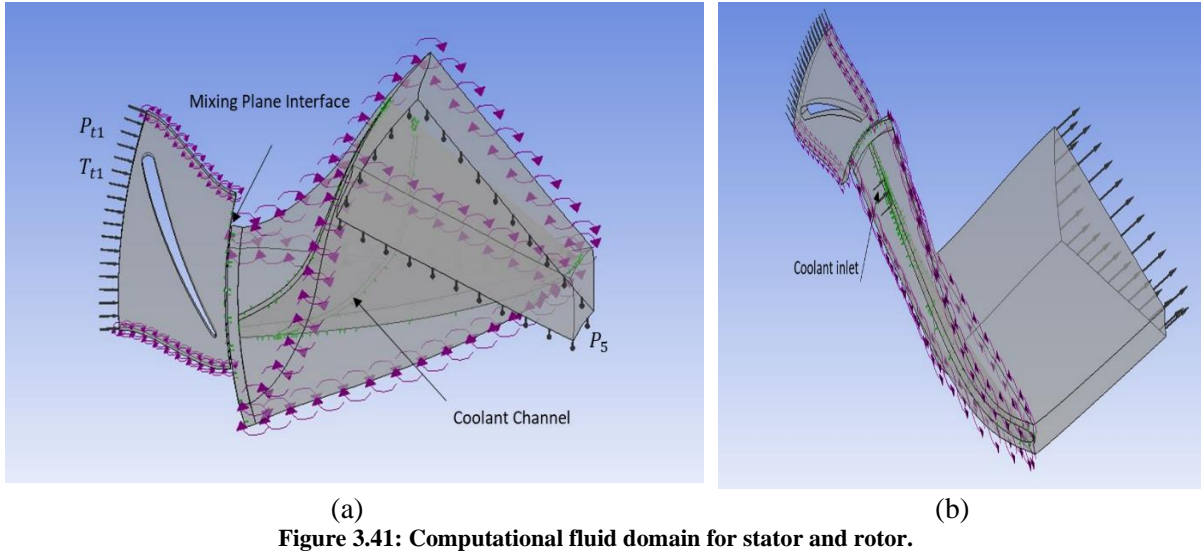


Figure 3.40: Mesh generation for (a) the blade and the coolant, and (b) the hot gas body.

### 3.12.3. Cooled Turbine Setup

Both the stator and rotor are imported into ANSYS CFX. The boundary conditions are the total inlet temperature and the total inlet pressure at the nozzle inlet and the outlet static pressure at the rotor exit. The flow at the nozzle inlet is assumed in the perpendicular direction (radial direction). Aerodynamics

and heat transfer calculations rely heavily on interface surfaces in simulations. Therefore, a mixing plane model is applied at the stator-rotor interface to ensure the connection between the stationary and the rotating blade domain. A second interface is added between the solid blade and the coolant flow. Additionally, an interface is applied between the blade and the hot gas. At the coolant inlet boundary, mass and temperature are fixed as a result of the thermodynamic calculation obtained in Chapter 2. The detailed boundary conditions are listed in Table 3.16. All the computational fluid domain details are illustrated in Figure 3.41. The temperature distribution and the heat transfer through the turbine blade depend on the material conductivity. As a result, steel is chosen as the material for turbine blades. The mainstream flow and the coolant are considered ideal gas.



**Figure 3.41: Computational fluid domain for stator and rotor.**

**Table 3.16: Boundary conditions.**

Boundary conditions	Operating conditions
Inlet Total Pressure (bar)	9
Inlet Total Temperature (K)	1723.15
Outlet Static Pressure (bar )	2.9
N (rpm)	120 000
Coolant Inlet Temperature (K)	443.15
Coolant Mass Fraction	1.41 %

The simulation is carried out for one stator blade passage and one rotor blade passage and the periodicity model is used to determine the result on the overall stage. Additionally, all the walls are assumed to be smooth, with no-slip conditions. The k- $\omega$  SST turbulence and the total energy equation model are employed to calculate the heat transfer and 3D flow. The convergence is adjusted at  $10^{-6}$  for all the residuals.

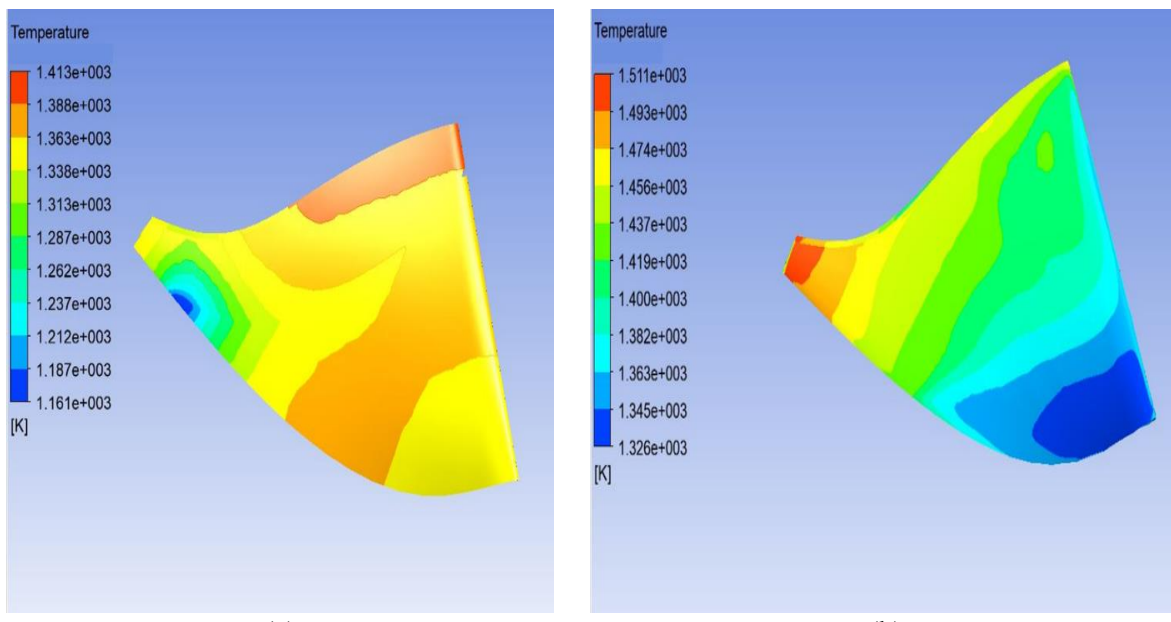
### 3.12.4. Comparison Between Cooled and Uncooled Turbine Blade For The Same TIT- Case Study

#### ➤ Temperature and Pressure Variation

In order to evaluate the impact of the turbine cooling on the temperature distribution at the turbine surface, two turbines were compared under similar operating conditions: TIT = 1723.15 K (1450 °C)

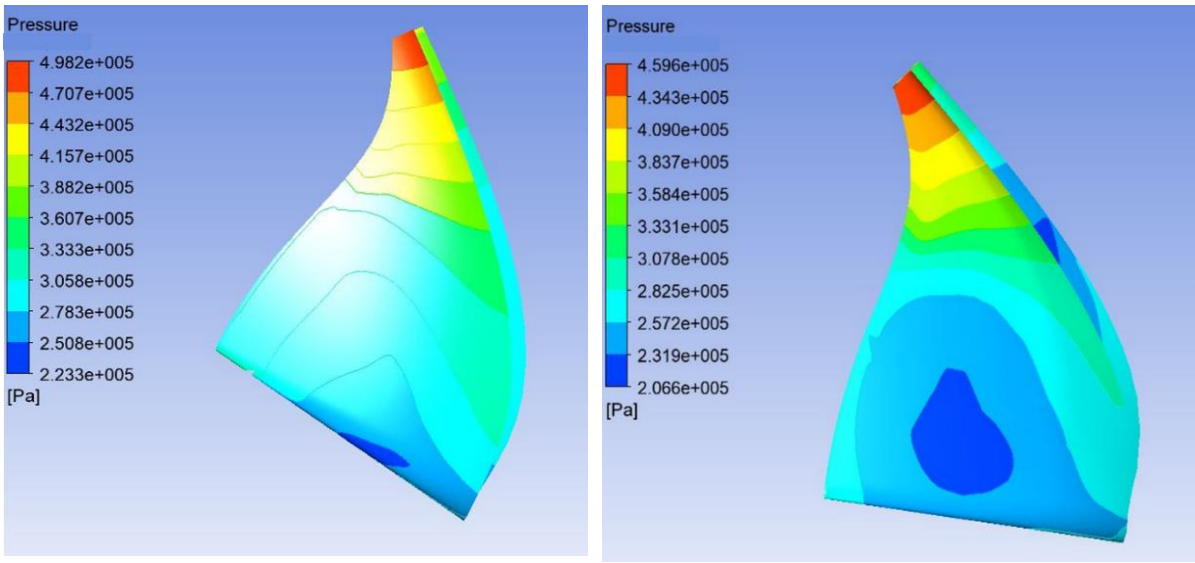
and  $P_{max} = 9$  bar. The first turbine is uncooled, while the second turbine is cooled, where the inlet temperature of the coolant is 443.15 K (as the temperature at the exit of the LP compressor) and its fraction is 1.41% of the total mass flow rate. This section aims to first validate the thermodynamic analysis of Chapter 2 by verifying that the fixed mass of coolant is enough to cool the turbine blade ( $T_w = 1373.15$  K) and to confirm that the cooling design is successful in cooling the blade.

Figure 3.42 illustrates the result of the CFD simulation of a cooled turbine (on the left) and an uncooled turbine (on the right) both operating at a TIT of 1723.15 K and an inlet total pressure of 9 bar. Only the rotor of the turbine is cooled, so since the stator is uncooled, the rotor only is presented. The temperature distributions on the rotor surface of the baseline and cooled turbine indicate a difference in heat transfer; the cooling design has achieved successful cooling of the blade surface. The leading edge temperature of the cooled turbine is 150 K lower than the reference turbine. The results are very close to those obtained by HiETA when comparing their cooled and uncooled radial turbine, where the blade leading edge temperature was 110 K lower than the uncooled model [133]. There is also a considerable difference in the temperature between other parts of the turbine wheel compared to the uncooled geometry. Based on the fact that the turbine material can handle temperatures up to 1373.15 K (1100 °C), it can be seen that in the case of the cooled rotor, the blade temperature does not exceed this limit except for a little area at the trailing edge where the temperature exceeds by 20 K. As a result, it can be concluded that the thermodynamic analysis succeeds in predicting the required mass of coolant and the cooling channel is effective in reducing the blade temperature along the surface. When comparing the two methods of calculation, it is apparent that the temperature of the hot gas decreases by 10 K in the 1D approach, whereas it decreases by 150 K in the 3D approach. This implies that the heat transfer occurring in the 3D simulation is more significant than in the 1D simulation.



**Figure 3.42: Distribution of temperature on the turbine blade for the same TIT and  $P_{max}$  (a) cooled rotor, (b) uncooled rotor.**

The pressure variation on the blade of both turbines is compared as shown in Figure 3.43. It can be seen that the pressure distribution on both configurations is practically the same. The turbine is designed to ensure an expansion ratio equal to 3.



**Figure 3.43: Distribution of pressure on the turbine blade for the same TIT and Pmax (a) cooled rotor, (b) uncooled rotor.**

Considering Figure 3.44, as the coolant passes through the channel, its temperature increases, reaching a temperature of 1200 K at the exit of the coolant channel. This is due to the heat transfer between the coolant air and the turbine blade. It should be noted that the blade temperature is the maximum temperature the coolant can reach. Also, comparing the results with the 1D approach, it can be seen that the coolant temperature at the exit of the coolant channel is higher than the predicted temperature in the 1D approach.

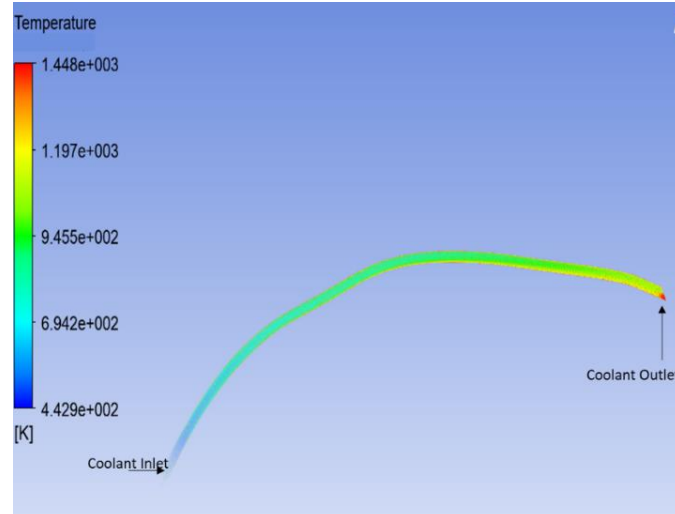


**Figure 3.44: Temperature variation of the coolant in the cooling channel.**

### ➤ Heat Transfer Coefficient

The overall heat transfer coefficient  $U$  of the cooled turbine is calculated using an analytical method and using a 3D simulation. The results from the two methods are compared. The operating conditions used for the analytical LMSTD method are listed in Table 3.17.

**Table 3.17: Parameters applied for the LMTD method, and the obtained U for both the analytical and the 3D simulation analysis.**

Parameters	Operating conditions	
Coolant Inlet Temperature (K)	443.15	
Coolant mass flow (kg/s)	$4 \times 10^{-5}$	
Coolant Heat Exchange Area ( $\text{m}^2$ )	$2.042 \times 10^{-5}$	
LMTD (K)	864.91	
Results	Analytical Analysis	ANSYS CFX
Overall Heat Transfer Coefficient U ( $\text{W} \cdot \text{m}^{-2} \cdot \text{K}^{-1}$ )	1245	1421.24

Using LMTD Equation, the overall heat transfer coefficient U is equal to  $1245 \text{ W} \cdot \text{m}^{-2} \cdot \text{K}^{-1}$ . However, the heat transfer coefficient obtained from ANSYS CFX-post is equal to  $1421.24 \text{ W} \cdot \text{m}^{-2} \cdot \text{K}^{-1}$ . Thus, it can be concluded that both the analytical and the 3D simulation results are in a good agreement where the relative error does not exceed 12%.

### ➤ Turbine Efficiency

A further aspect that needs to be addressed is the effect of turbine cooling on the turbine efficiency. The thermodynamic analysis developed in Chapter 2 has suggested a method to calculate the efficiency of the cooled turbine. The goal of this section is to evaluate the impact of cooling the turbine blade on its efficiency.

In Section 3.9.10, it was shown through CFD simulations that the efficiency of the designed uncooled turbine when operating at its designed conditions (9 bar pressure and TIT = 1373.15 K), is 80 %. The study of the impact of TIT on the uncooled turbine efficiency is illustrated in Figure 3.45. Significant changes in turbine efficiency are obtained as TIT varies. The highest efficiency is achieved when the turbine operates at its designed TIT (1373.15 K). For instance, the efficiency of the uncooled turbine when operating at 9 bar and TIT = 1723.15 K decreases to 78 %. In other words, the efficiency of the designed uncooled turbine decreases by 2 points when operating at 1723.15 K. However when carrying on the study of the cooled turbine operating at TIT = 1723.15 K, the efficiency appears to decrease to 72 %.

Two factors contribute to the decrease in turbine efficiency:

- Operating the turbine at a different TIT (1723.15 K) than the designed TIT (1373.15 K)
- The factor of cooling the blades

As operating the turbine on different TIT reduces efficiency by about 2 points, it is estimated that cooling decreases efficiency by 6 efficiency points. Based on these factors, it can be predicted that the efficiency of the cooled turbine will be around 74 % if the turbine is designed at the optimal operating temperature.

In Table 3.18, turbine efficiency is calculated from 1D and ANSYS simulations for different configurations. The efficiency of the cooled turbine calculated using the ANSYS model is lower than the one calculated using the 1D model. The reason behind this difference is that in the 1D formulation, the calculation does not take into consideration the 3D behavior and the separation of the flow. It is based on empirical correlations and does not account for the exact geometry of the turbine blade.

**Table 3.18: Turbine Efficiency for the different turbine configurations.**

	CFD Results	1D Analysis	CFD Results	
Operating Conditions Efficiency (%)	Uncooled Turbine TIT = 1373.15 K 80	Uncooled Turbine TIT = 1723.15 K 78	Cooled Turbine TIT = 1723.15 K 77.5	74

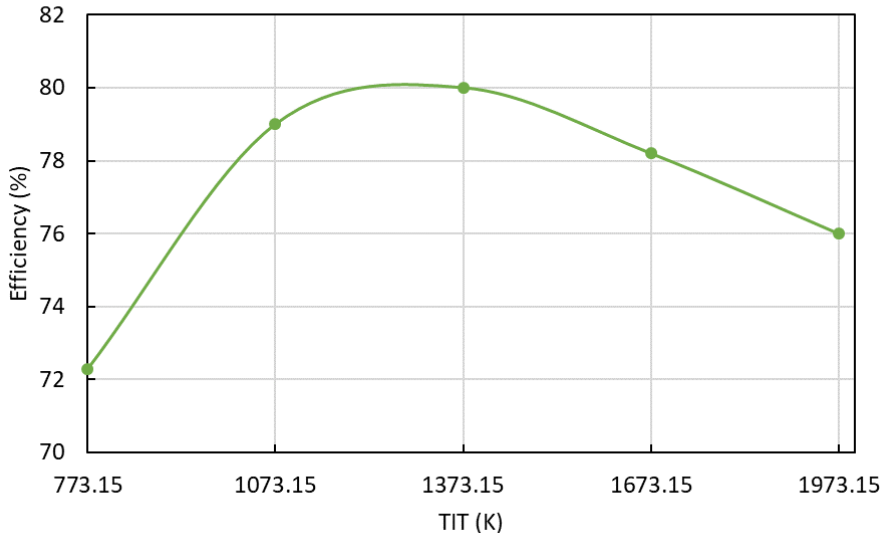


**Figure 3.45: The efficiency of the designed turbine at different TIT.**

## ➤ Discussions

Based on the preceding findings, the following statements can be drawn. First, the estimated mass of coolant using the 1D approach is sufficient to reduce the temperature of the turbine blade compared with the uncooled case. A comparison of the thermodynamic (1D) formulation with the 3D simulation, however, revealed that the thermodynamic (1D) formulation underestimated the heat transfer. On the other hand, the turbine efficiency depends on the inlet temperature. An efficiency drop of 2 points was observed when the turbine was operated at a different TIT (1723.15 K). However, the efficiency of the turbine decreased to 72 % when the cooling method was applied. The decrease in efficiency is attributed to both a geometry adjustment needed to adapt to the new TIT and the introduction of cooling channels. The geometry of the turbine was seen to reduce its efficiency by around two efficiency points, and thus, it was assumed that cooling reduced the efficiency by six points. Therefore, if the cooled turbine was designed at the optimal temperature, its efficiency would be 74 %.

### 3.13. Impact of Turbine Efficiency on The Cycle Performance

The standard IRReGT cycle is the baseline cycle. To test the influence of the cooled and the uncooled turbine on the range extender efficiency, the thermodynamic analysis of Chapter 2 is conducted but considering the efficiencies of the designed HP uncooled turbine and the designed HP cooled turbine from the ANSYS CFX. This section consists of comparing these two cycles: the IRReGT baseline cycle, and the IRReGT with a cooled HP turbine considering the CFD efficiency.

Two scenarios are investigated taking as a reference the designed uncooled HP turbine operating at 9 bar and TIT = 1100 °C (1373.15 K), which isentropic efficiency is 80 % (ANSYS CFX). The first scenario is the baseline cycle where the temperature at the inlet of both turbines is limited by the material melting temperature considered equal to 1100 °C (1373.15 K). The second configuration is the worst-case scenario that consists of the current cycle with a cooled HP turbine taking the turbine efficiency as obtained in the 3D simulation (74 %). Therefore, the efficiency of the uncooled turbines is taken equal to 80 %, while the efficiency of the cooled HP turbine is taken equal to 74 %. The operating conditions are presented in Table 3.19.

**Table 3.19: Operating conditions.**

Operating Conditions	IRReGT baseline cycle	IRReGT cycle with a cooled HP turbine
HP turbine	uncooled	cooled
HP turbine efficiency (%)	80	74
LP turbine	uncooled	uncooled
LP turbine efficiency (%)	80	80

A thermodynamic analysis and an exergetic study are conducted for both cycles. The results of the standard IRReGT cycle and the cooled IRReGT are illustrated in Figure 3.46 and Figure 3.47. Compared to the baseline cycle, the IRReGT cycle with cooled turbines yields higher net output work, resulting in a decrease in air mass by 17 % for a power of 20 kW. Thus, the system is less bulky and more compact. In addition, although the HP cooled turbine efficiency is decreased by 6 points, the overall efficiency of the IRReGT cycle with a cooled turbine (47 %) is still higher than the baseline IRReGT cycle (43.6 %).

Based on the parametric study conducted in Chapter 2 , increasing the inlet temperature of the HP turbine from 1100 °C to 1450 °C leads to a 5.5 points increase in overall cycle efficiency. Meanwhile, the reduction in turbine efficiency by 6 points from 80 % to 74 % reduces cycle efficiency by around 3.5 points. On another note, the exergetic study has shown that the exergy destruction in both cycles is very close.

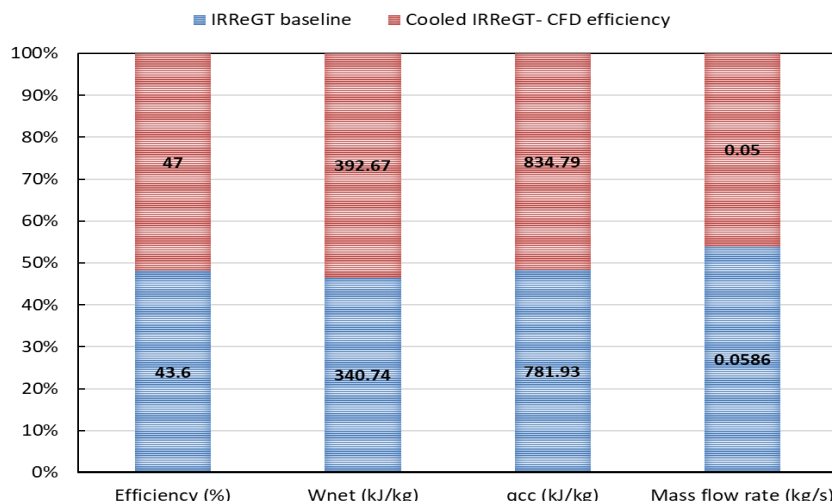


**Figure 3.46: Comparison of different output parameters between the uncooled standard IRReGT cycle and the IRReGT cycle with a cooled turbine.**

By comparing the exergy destruction of each component of both cycles, many conclusions are obtained.

- The exergy destruction of the compressors and the LP uncooled turbine is the same in both cases.
- The exergy destruction of the cooled turbine is higher by 35 % compared to the uncooled cycle due to the decrease in efficiency.
- The exergy destruction of both combustion chambers in the baseline cycle is higher than the exergy destruction in the cooled cycle.
- The exergy destruction of the regenerator is higher in the baseline cycle than in the cooled case since the temperatures at the inlet of the regenerator (mainly hot gas temperature) is higher.

In light of these findings, it can be concluded that while cooling turbine blades are associated with a reduction in the turbine efficiency and complexity in the turbine geometry and structure, it increases the overall efficiency of the cycle and reduces the amount of mass of air required to produce the same amount of power. This results in a more compact, efficient range extender system to boost the autonomy of electric cars.

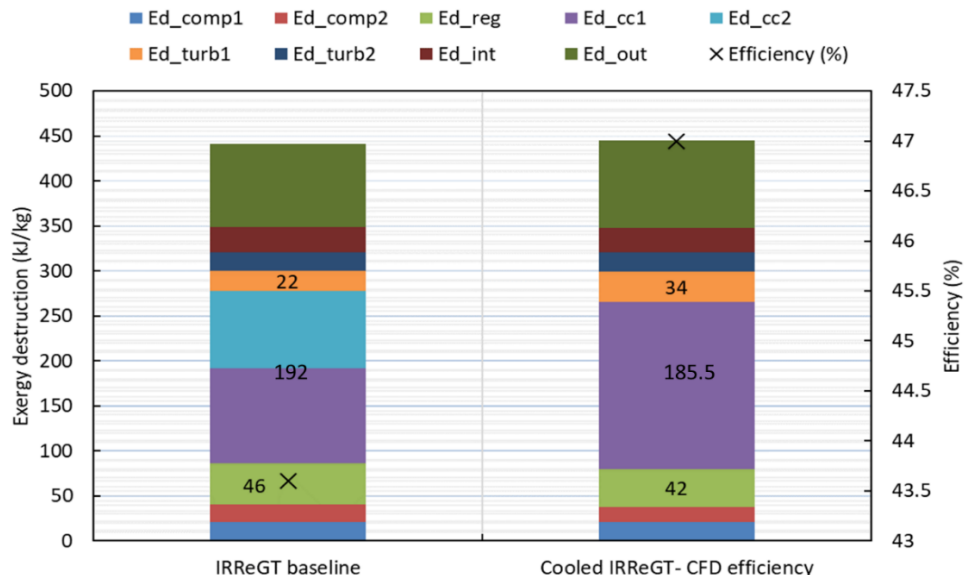


**Figure 3.47: Exergy destruction of different components of the two cycles.**

### 3.14. Conclusion

The cooled HP turbine of the cooled IRReGT cycle is the most critical component. Thus, this chapter presents a detailed methodology procedure to design a cooled radial turbine operating at high temperature and high pressure and manufactured using 3D printing.

The first part of this chapter is a design tool for an uncooled turbine. The design procedure consists of a preliminary design to determine the overall geometrical parameters and the overall performance of the current turbine. The 1D analysis is based on correlations from the literature to generate the velocity triangles at the inlet and the outlet of each component of the turbine stage using VBA. Although this technique is efficient to evaluate the overall performance of the turbine wheel, the 3D simulation using ANSYS CFX is mandatory to predict the flow separation and the 3D behavior of the system. The proposed design methodology was then validated by comparing the results with a real commercial turbine. The results agreed on the effectiveness of this procedure in predicting the turbine performance

and design. Therefore, an uncooled turbine operating at a temperature of 1100 °C, a pressure of 9 bar, and a rotational speed of 120 000 rpm was designed to offer an efficiency of 80 %.

The second part of this chapter is a design tool of the cooled turbine taking into consideration challenges related to the small-scale turbine and the 3D printing limitations. A cooling channel was integrated into the rotor blade of the designed turbine taking into consideration a minimum wall thickness of 0.16 mm, and a minimum hole diameter of 0.5 mm. The coolant channel trajectory should pass through the rotor blade zone that is subjected to the highest temperature. The 3D simulation confirmed that the mass of coolant determined from the thermodynamic analysis was sufficient to cool the turbine blade. First, the temperature along the turbine blade was less than the fixed temperature for material limitations. Second, compared to the uncooled turbine operating under the same conditions, the temperature at different parts of the cooled turbine was less than in the uncooled case, for example, the temperature at the leading edge was reduced by 150 K. Compared to the 1D approach, the estimated decrease in temperature of the hot gas is around 10 K, this implies that the 1D approach underestimated the heat transfer compared to the 3D model. Therefore, the efficiency of the cooled turbine was estimated to reach 74 % in ANSYS CFX, compared to 77.5 % from the 1D approach.

The final step of this chapter was to reevaluate the overall cycle efficiency of the IRReGT cooled cycle considering the efficiency of the designed turbine in ANSYS CFX. The thermodynamic analysis showed that the performance of the current cycle with a cooled HP turbine is still more beneficial than the uncooled IRReGT cycle. Although the decrease in turbine efficiency results in a decrease in cycle efficiency, the increase in turbine inlet temperature affects the overall cycle positively and significantly. For instance, the efficiency of the proposed cycle was higher by 3 points than the baseline reference cycle.

# **Chapitre 3: Etude du Comportement de l'Ecoulement des Fluides dans un Rotor de Turbine Radiale Fonctionnant à Haute Température et Haute Pression. Impact du Refroidissement.**

## **3.1. Introduction**

Les turbines radiales sont généralement utilisées dans les turbocompresseurs pour les automobiles et comme unité de puissance pour les avions, et toutes les sources d'énergie compactes. Ce chapitre expose une méthodologie de conception détaillée pour la turbine HP du cycle IRReGT, il est divisé en deux parties. La première partie décrit la méthodologie de conception d'une turbine radiale non refroidie fonctionnant à haute pression et à haute température. La première étape du processus de conception consiste à adopter une approche unidimensionnelle (1D), appelée conception préliminaire. Elle détermine les paramètres géométriques globaux de la turbine à flux radial et estime les performances de la turbine en fonction des paramètres d'entrée. Bien que la simulation 1D donne une idée du fonctionnement global de la turbine conçue, elle ne peut pas capturer le comportement complexe dans la turbine radiale où l'écoulement est 3D, visqueux et turbulent. Par conséquent, la deuxième étape consiste à générer une géométrie 3D des pales de la turbine, avant de réaliser une simulation 3D à l'aide d'ANSYS CFD/CFX. La deuxième partie de ce chapitre présente la méthode de conception d'une turbine radiale refroidie fonctionnant à haute température et à haute pression.

## **3.2. Composants d'Une Turbine Radiale**

La turbine radiale comprend principalement deux parties : une partie fixe (volute et aubes du stator) et un rotor rotatif, illustré à la Figure 3.1. La première partie conduit à dilater le flux et à lui donner une vitesse circonférentielle autour de l'axe de la machine. Le passage du flux dans le second conduit à la production de travail sur l'axe de la turbine. Un diffuseur peut être ajouté pour récupérer l'énergie cinétique à la sortie de la turbine, et la transformer en pression statique. Cette configuration est cependant soumise à des contraintes de poids et d'installation.

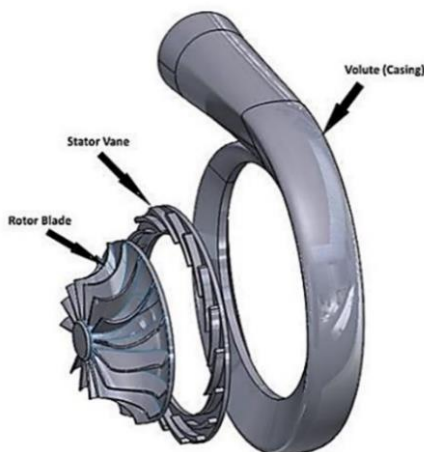


**Figure 3.1: Composants d'une turbine radiale.**

Lorsque le flux entre dans la volute, il est accéléré par la section transversale réduite. En sortant à grande vitesse, le flux est ensuite réparti uniformément sur la périphérie avant de pénétrer dans les aubes du stator. De cette manière, le flux est dilaté et dirigé dans une direction optimale vers le rotor. Un espace sans ailettes sépare le stator et le rotor. Cet espace vise à accélérer davantage l'écoulement avant de pénétrer dans le rotor. Lorsqu'il atteint le rotor, le flux est détendu et l'énergie cinétique est convertie en puissance sur l'arbre.

### 3.3. Stratégie de conception préliminaire d'une turbine radiale

La conception préliminaire de la turbine radiale consiste en une approximation unidimensionnelle faite sur le rayon moyen de l'étage de la turbine. Cette étude permet de déterminer les performances globales de la turbine et les dimensions préliminaires des différents composants de l'étage de turbine. La conception de la ligne moyenne est initialement réalisée dans Visual Basic Applications (VBA) Excel. REFPROP, développé par le National Institute of Standards and Technology (NIST) est intégré à la procédure pour obtenir les propriétés des gaz.

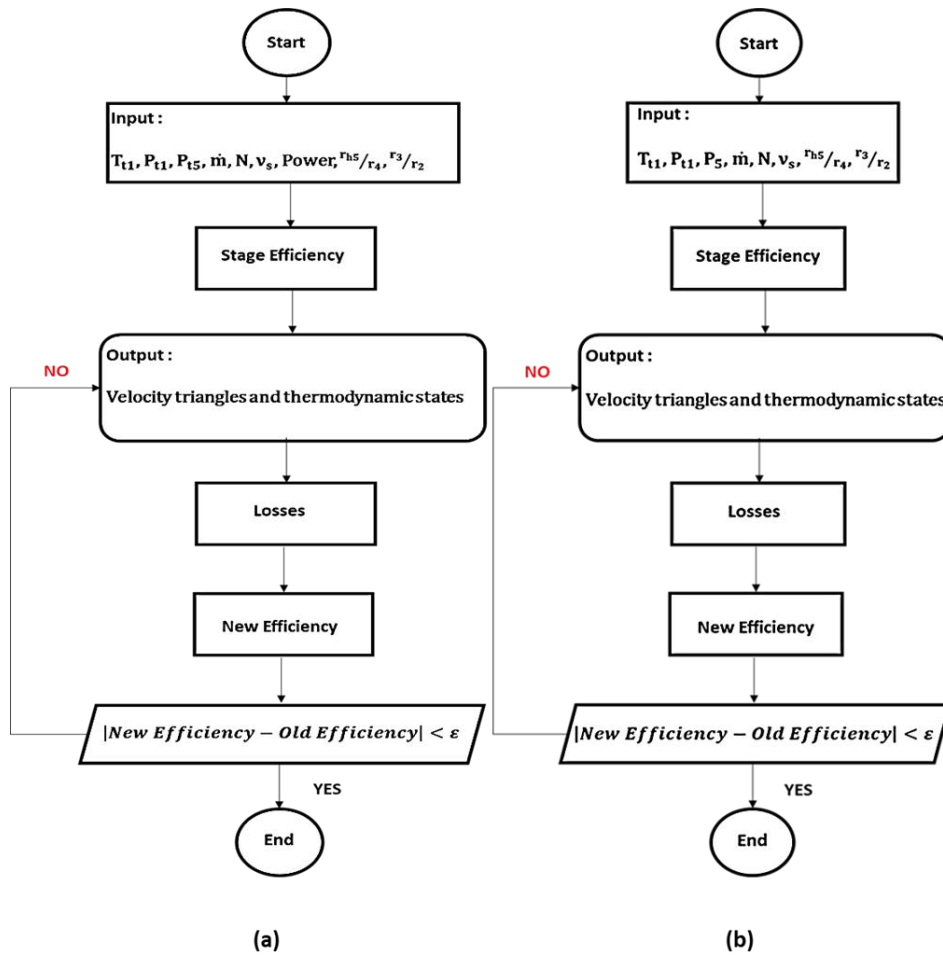


Figure 3.2: Methodologie de la conception préliminaire de la turbine radiale (a) 'PMean' code, (b) 'Mean' code.

Le présent travail se concentre sur la conception préliminaire de la turbine radiale HP refroidie du cycle IRReGT. La turbine conçue doit donc correspondre aux conditions de fonctionnement du cycle IRReGT refroidi. La méthodologie menée dans cette thèse est basée sur certains paramètres d'entrée et des corrélations empiriques issues de la littérature. Pour des raisons de simplicité, les propriétés du fluide sont supposées être constantes sur un plan normal à sa direction de mouvement. Par conséquent, les

propriétés du fluide sont supposées varier uniquement le long de la ligne de courant moyenne [258]. La conception de la ligne moyenne détermine les propriétés de l'écoulement et les paramètres géométriques à chaque station de l'étage de turbine. La modélisation de l'étude préliminaire est un processus itératif. Par conséquent, deux codes de conception sont réalisés.

Les paramètres d'entrée du premier code "PMean" sont les conditions de fonctionnement de la turbine conçue, présentées à la Figure 3.2a : la température totale d'entrée de l'étage ( $T_{t1}$ ), la pression totale d'entrée de l'étage ( $P_{t1}$ ), le rapport de détente totale à totale ou la pression totale de sortie ( $P_{t5}$ ), le débit massique de l'étage ( $m$ ), la vitesse de rotation (N) et le rapport de vitesse ( $v_s$ ), et la puissance de sortie. Le second code a les mêmes conditions de fonctionnement en entrée, mais avec un rapport de dilatation totale/statique et sans la puissance de sortie, comme illustré à la Figure 3.2b. En outre, deux paramètres géométriques sont considérés pour les deux cas :  $r h_5 / r_4$  et  $r_3 / r_2$ .

Une première estimation du rendement du cycle est nécessaire et les triangles de vitesse à l'entrée et à la sortie du rotor et du stator sont calculés. Les pertes sont ensuite estimées en utilisant les corrélations de la littérature et une nouvelle efficacité du cycle est calculée. Le calcul se poursuit jusqu'à ce que la convergence pour l'efficacité soit atteinte (résidu pour l'efficacité  $10^{-4}$ ).

### 3.4. Validation de l'étude préliminaire

Cette section montre la comparaison entre les modèles développés 'Pmean' et 'mean' et celui développé par [250]. La turbine est une turbine radiale utilisée pour le dioxyde de carbone avec un débit massique de 1.8 kg/s. La température totale d'entrée et la pression totale d'entrée sont respectivement de 943 K et 106.92 bar. Tous les autres paramètres d'entrée sont présentés dans le tableau 3.1.

**Table 3.1: Condition d'opération de la turbine à valider.**

Propriétés	Conditions d'opération
Fluide de travail	Dioxyde de Carbone
Débit (kg/s)	1.8
Vitesse de rotation (rpm)	80 000
Température totale à l'entrée (K)	943
Pression totale à l'entrée (bar)	106.92
Rapport de vitesse	0.68
Puissance de sortie (kW)	84.076
Rapport de détente statique	1.364
Rapport de dilatation total-total	1.376

Le premier ensemble de résultats a été obtenu en exécutant le code PMean. Les résultats de sortie sont en bon accord avec ceux obtenus par [250], il y a une erreur maximale de 3%. Ceci implique que le code est valide pour la conception préliminaire de la turbine radiale. D'autre part, l'erreur du code Mean par rapport à [250] ne dépasse pas 4 %. Par conséquent, le code Mean peut également être utilisé pour effectuer l'estimation initiale de la conception d'une turbine radiale. On peut conclure que les deux codes peuvent être utilisés pour développer une conception préliminaire d'une turbine radiale.

### 3.5. Dynamique des Fluides Numériques

Bien que l'approche 1D puisse prédire la performance globale de la turbine radiale, une analyse 3D est essentielle. La CFD est nécessaire pour étudier le comportement de l'écoulement dans la turbomachine, et prévoir toute séparation de l'écoulement ou onde de choc. Par conséquent, l'application des techniques de CFD pour la modélisation d'une turbine radiale a reçu une grande attention.

La CFD est un outil puissant qui utilise les équations de Navier-Stokes pour résoudre les complexités de l'écoulement dans les turbomachines. Les équations de Navier-Stokes décrivent la conservation de la masse, de la quantité de mouvement et de l'énergie.

$$\frac{\partial \rho}{\partial t} + \frac{\partial}{\partial x_j} (\rho u_j) = 0 \quad (3.1)$$

$$\frac{\partial \rho u_i}{\partial t} + \frac{\partial (\rho \cdot u_j \cdot u_i)}{\partial x_j} = - \frac{\partial p}{\partial x_i} + \frac{\partial \tau_{ij}}{\partial x_j} + \rho f_i \quad (3.2)$$

$$\frac{\partial (\rho \cdot h)}{\partial t} + \frac{\partial (\rho \cdot u_j \cdot h)}{\partial x_j} = - \frac{\partial P}{\partial x_i} + u_j \frac{\partial P}{\partial x_j} + \tau_{ij} \frac{\partial u_i}{\partial x_j} - \frac{\partial q_j}{\partial x_j} + W_{ext} + q_H \quad (3.3)$$

$u_i, u_j$ : vitesse,  $\rho$ : densité,  $P$ : pression,  $\tau$ : stress,  $q_H$ : chaleur,  $W_{ext}$ : travail.

Selon la synthèse effectuée, l'analyse CFD permet de calculer le champ d'écoulement en tenant compte des effets visqueux qui ne sont pas pris en compte dans les modèles 1D. De plus, la CFD peut être utilisée pour valider les modèles préliminaires. Dans cette section, la construction d'un modèle 3D de l'étage de turbine et une analyse CFD complète des composants 3D sont présentées. La méthodologie présentée à la Figure 3.3, consiste à importer les paramètres d'entrée du code VBA de Vista RTD pour le stator et le rotor. Ensuite, la géométrie de l'étage de turbine est générée à l'aide d'ANSYS BladeGen. Le maillage est obtenu à l'aide de ANSYS TurboGrid. Enfin, le stator et le rotor sont importés dans ANSYS CFX.

Ansys-Vista RTD développé par PCA Engineers est utilisé pour effectuer la conception préliminaire de la turbine radiale étudiée [267]. Les données requises sont la température et la pression de stagnation à l'entrée, le débit massique, le rapport d'expansion totale, la vitesse de rotation et les propriétés du fluide. Les données géométriques telles que les angles d'entrée et de sortie, le nombre de pales du rotor, le diamètre et la longueur axiale sont effectuées à partir du code VBA.

La géométrie 3D du stator et du rotor sont créées avec ANSYS BladeGen. Les entrées sont importées à partir de l'étude préliminaire et le profil de la pale est personnalisé.

Les équations de Navier-Stokes sont discrétisées par RANS (Reynolds-averaged Navier-Stokes equations). Les équations RANS sont les équations de mouvement de l'écoulement des fluides moyennées dans le temps. Leur concept est basé sur la décomposition de la quantité instantanée en quantités moyenne et fluctuante. Cette décomposition donne un terme supplémentaire appelé contrainte de Reynolds qui est modélisé à l'aide d'un modèle de turbulence.

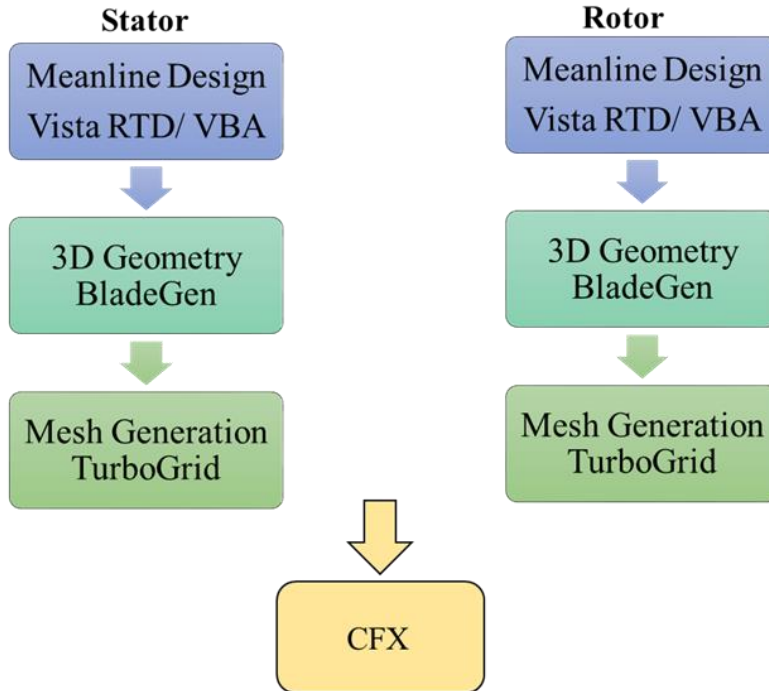


Figure 3.3: Méthodologie pour la simulation 3D.

Les deux principaux modèles de turbulence utilisés sont le modèle  $k-\varepsilon$  et le modèle  $k-\omega$ , dans lesquels  $\varepsilon$  est le taux de dissipation de la turbulence et  $\omega$  est le taux de dissipation spécifique. Cependant, le modèle  $k-\varepsilon$  ne peut pas prédire la séparation de l'écoulement dans un modèle turbulent et le modèle  $k-\omega$  ne peut pas capturer les effets de la turbulence en écoulement libre. Le modèle  $k-\omega$  SST combine les deux modèles précédents. Ce modèle a été initialement proposé par Menter [275]. Il est caractérisé par le comportement robuste du modèle  $k-\omega$  près de la paroi et la capacité du modèle  $k-\varepsilon$  à capturer la turbulence en écoulement libre loin de la paroi. Un autre avantage de l'utilisation du  $k-\omega$  SST est la possibilité de déterminer automatiquement le premier nœud éloigné de la paroi  $Y+$  et de prédire la séparation des flux.

Le maillage pour le stator et le rotor est réalisé dans ANSYS Turbogrid où l'option Topologie et Maillage Automatique (ATM Optimisé) a été utilisée.

Une évaluation de la qualité du maillage est effectuée en mesurant les éléments d'angle de face maximum et minimum, les rapports de volume, les rapports de longueur d'arête et le nombre de connexions. Une amélioration de la qualité du maillage est possible si la qualité du maillage est mauvaise dans une certaine région.

Le maillage généré est importé dans ANSYS CFX où deux modèles de conditions limites sont disponibles. Dans le premier modèle, la température et la pression de stagnation totale à l'entrée, ainsi que la pression statique à la sortie, sont spécifiées. Tandis que le second modèle définit le débit massique à l'entrée et la pression statique à la sortie. Grâce à l'utilisation du modèle d'énergie totale, le transfert de chaleur est inclus. Dans cette simulation, le premier modèle est appliqué.

Pour simuler le rotor (en rotation) et le stator (stationnaire), une interface de domaine est nécessaire pour assurer la communication entre les pales stationnaires et en rotation. Deux interfaces principales existent dans ANSYS CFX : mixing plane et frozen rotor. Dans la première approche, les données d'écoulement sont moyennées sur la sortie du stator et l'entrée du rotor (interface rotor-stator), puis les conditions limites sont mises à jour. En revanche, le deuxième cas utilise une référence rotative de sorte que le

véritable écoulement passe en aval à une position. Dans notre étude on utilise la première approche. La convergence est atteinte lorsque le Root-Mean-Square est inférieur à  $10^{-6}$  pour la masse et la quantité de mouvement.

### 3.5.1. Conception d'une turbine radiale non refroidie

Cette section développe la conception de la turbine HP non refroidie du cycle standard IRReGT. Elle est composée de deux étages de compression avec un intercooler, où la pression maximale est de 9 bar, puis de deux étages de détente avec réchauffage et d'un récupérateur. Les deux turbines ne sont pas refroidies et supportent des températures allant jusqu'à 1373.15 K. Les conditions de fonctionnement de la turbine HP sont obtenues à partir de l'analyse thermodynamique réalisée au Chapitre 2 et présentées dans le tableau 3.2. Comme les forces centrifuges et les contraintes sur la roue de la turbine augmentent à des vitesses de rotation plus élevées, 120 000 tr/min est choisi pour la vitesse de rotation de la turbine.

**Tableau 3.2. Conditions d'opération de la turbine.**

Parameters	Operating conditions
Fluide	air
Pression Totale Entrée	9 bar
Temperature Totale Entrée	1373.15 k
Taux de détente	3
Debit massique	0.054 kg/s
Vitesse de rotation	120 000 rpm

Afin d'effectuer la conception préliminaire, VBA est d'abord utilisé pour déterminer les paramètres d'entrée tels que le nombre de pales et l'angle d'entrée absolu, qui sont ensuite insérés dans Vista RTD. Les résultats de Vista RTD sont des paramètres aérodynamiques et géométriques.

Les résultats de la conception préliminaire sont transmis dans ANSYS BladeGen pour générer la géométrie 3D du rotor et du stator, comme illustré à la Figure 3.4.

Les géométries sont importées dans ANSYS TurboGrid pour générer le maillage à l'aide de la topologie et du maillage automatiques (ATM optimisé). Une analyse d'indépendance de la grille a été réalisée en ajoutant davantage d'éléments au maillage du rotor et du stator. Le nombre d'éléments de maillage augmente le temps de calcul de la simulation, mais il assure la convergence. Par conséquent, un compromis doit être fait entre le nombre d'éléments et le temps de traitement.

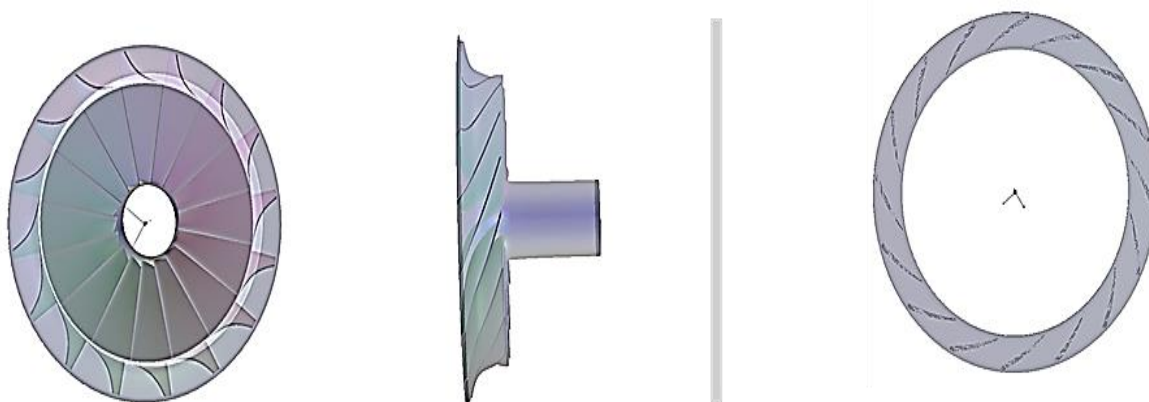


**Figure 3.4: (a) Géométrie 3D du rotor, (b) Géométrie 3D stator.**

Le stator et le rotor sont importés dans ANSYS CFX. Les conditions aux limites sont la température totale d'entrée et la pression totale d'entrée à l'entrée de la buse et la pression statique de sortie à la sortie du rotor. L'écoulement à l'entrée est supposé dans la direction perpendiculaire (direction radiale). La simulation est effectuée pour un passage de pale de stator et un passage de pale de rotor et le modèle de périodicité est utilisé pour déterminer le résultat sur l'ensemble de la roue. De plus, toutes les parois sont supposées être lisses, et adiabatiques avec des conditions sans glissement. Le modèle de turbulence k- $\omega$  SST est utilisé. La convergence est ajustée à  $10^{-6}$  pour tous les résidus. Tous les détails du domaine de fluide de calcul sont illustrés à la Figure 3.5. En outre, la Figure 3.6 montre le stator et le rotor combinés en 3D.

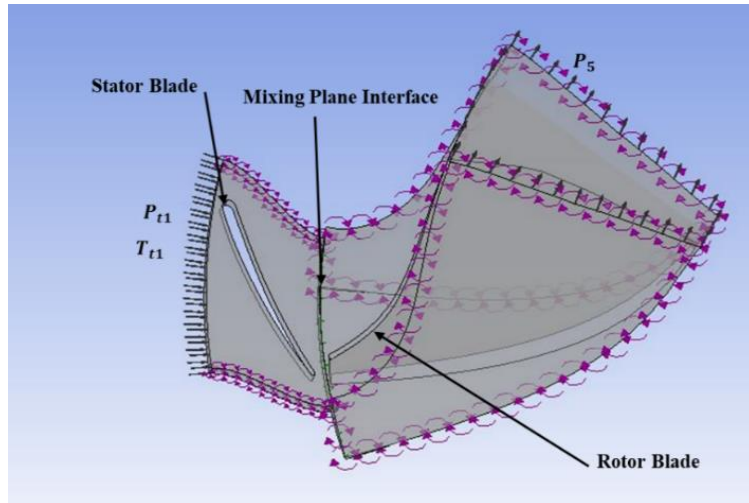


Figure 3.5 : Rotor et stator dans ANSYS CFX.

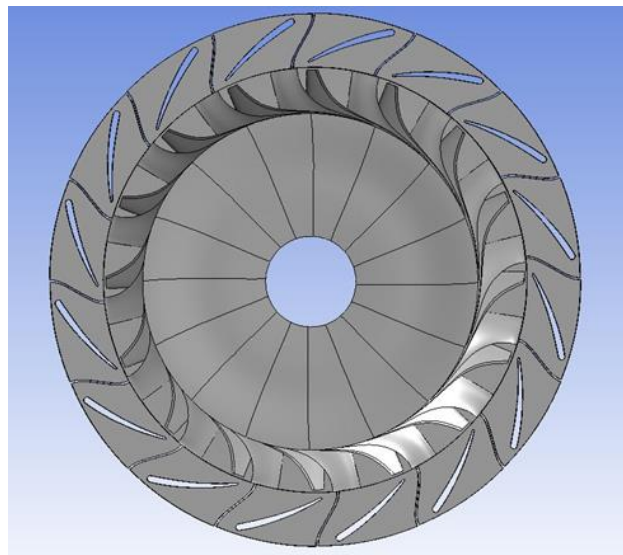
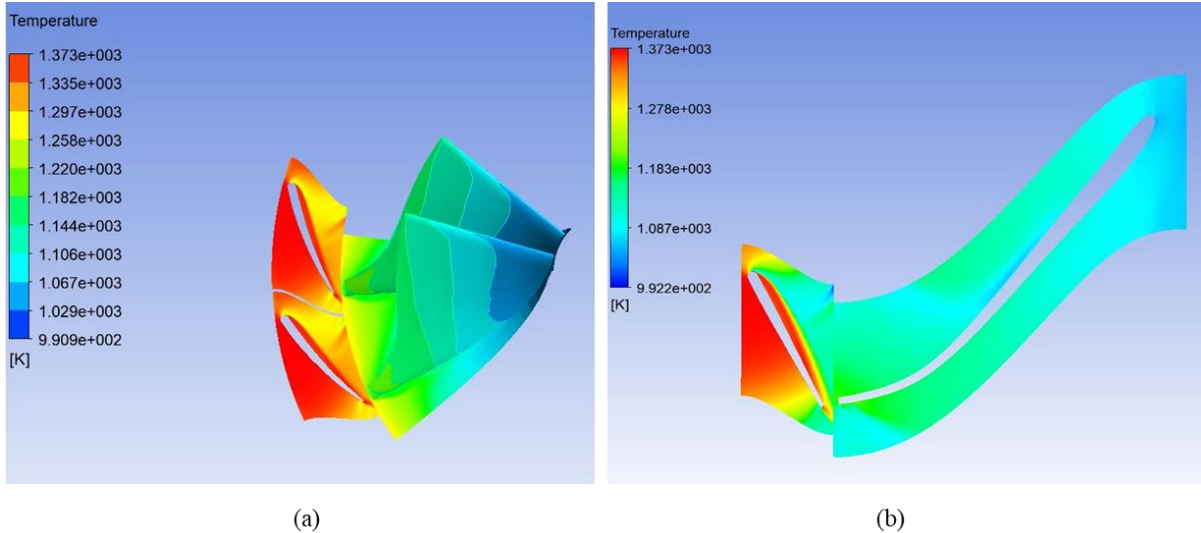


Figure 3.6 : Stator et rotor en 3D.

### 3.5.2. Résultats

Les résultats de cette section sont basés sur les conditions de fonctionnement de la turbine du tableau 3.2. Les contours de la température et de la pression à travers l'étage de turbine à une portée de 50 % sont présentés respectivement à la Figure 3.7 et à la Figure 3.8. La température à l'entrée du stator est de 1373.15 K, elle diminue à travers l'étage de turbine pour atteindre 990 K à la sortie du stator. De plus,

la pression à travers l'étage de turbine diminue de 9 bar à 2.9 bar à la sortie du stator. On peut voir que la chute de pression à travers le stator et le rotor est en bon accord avec l'exigence de conception.



**Figure 3.7 : Variation de la température (a) Vue en 3D, (b) Vue de deux aubes.**

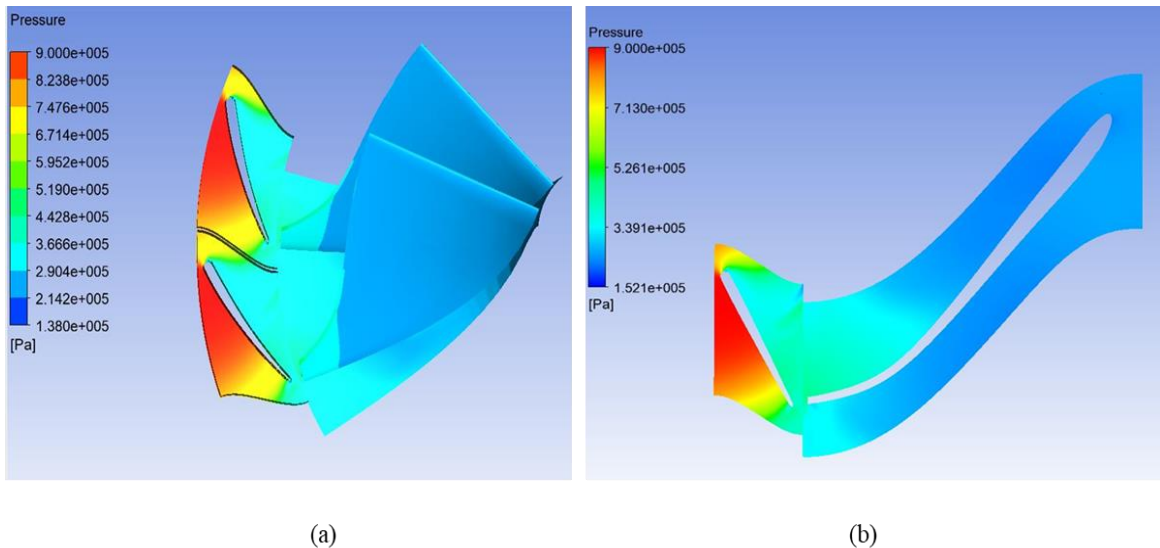


**Figure 3.8 : Variation de la pression (a) Vue en 3D, (b) Vue des deux aubes.**

**Tableau 3.3 : Comparaison entre les résultats de l'étude préliminaire et CFD.**

Paramètre	Résultats 1D	Résultats CFD
$P_{01}$ (bar)	9	9
$T_{01}$ (K)	1373.15	1373.15
$P_5$ (bar)	2.9	2.94
$T_{05}$ (K)	1113.15	1110.6
$P_5$ (bar)	2.58	2.57
$T_5$ (K)	1090.3	1083.6
$C_4$ (m/s)	673.32	660.4
$C_5$ (m/s)	300	224.69
$\eta_{tt}$ (%)	75	80

Les résultats préliminaires 1D et les résultats CFD ont été comparés comme indiqué dans le tableau 3.3. Globalement, ils sont en bon accord pour la majorité des paramètres. La turbine HP conçue pour le cycle standard IRReGT fonctionnant à 9 bars, a un rendement de 75 % sur la base des résultats 1D et de 80 % sur la base des résultats CFD. Ainsi, la méthodologie proposée peut prédire avec précision les performances de la turbine radiale HP et les caractéristiques d'écoulement.

### 3.6. Conception d'une turbine radiale refroidie

Cette section décrit la conception de la turbine radiale refroidie, depuis la génération du canal de refroidissement jusqu'à l'analyse CFD. L'objectif de cette section est de deux ordres : le premier est de valider le modèle thermodynamique du chapitre 2 qui détermine la masse de fluide de refroidissement nécessaire, tandis que le second objectif est d'évaluer la simulation CFD d'une turbine radiale compacte refroidie par HP. Cette thèse ne porte que sur le refroidissement de la roue du rotor, le refroidissement de la roue du stator n'est pas dans le cadre de cette étude. Comme expliqué précédemment, la technique de refroidissement par convection est choisie car elle consiste en un procédé simple et adapté aux aubes de turbine à petite échelle.

L'analyse thermodynamique réalisée dans le Chapitre 2 a permis de déterminer la masse de fluide de refroidissement nécessaire pour protéger l'aube de turbine du gaz chaud. On constate que pour une TIT de 1450 °C, la fraction de liquide de refroidissement par rapport à la masse totale d'air est de 1.41 % alors que le matériau peut supporter une température maximale de 1100 °C.

#### 3.6.1. Génération du canal de refroidissement

Les canaux dans les aubes de turbine sont conçus pour atteindre les points les plus chauds de l'aube de turbine en tenant compte des contraintes du matériau. Le bord d'attaque du rotor de la turbine est le plus critique car il est le plus affecté par la température du gaz chaud. Lorsqu'il pénètre dans l'aube de la turbine, le gaz chaud se dilate et sa température diminue. La Figure 3.9 présente la variation de température sur une aube de turbine pour une turbine non refroidie fonctionnant à 9 bar et TIT = 1450 °C. Le contour rouge délimite la zone où la température est la plus élevée. Par conséquent, le canal du liquide de refroidissement doit passer par cette région pour assurer son refroidissement.

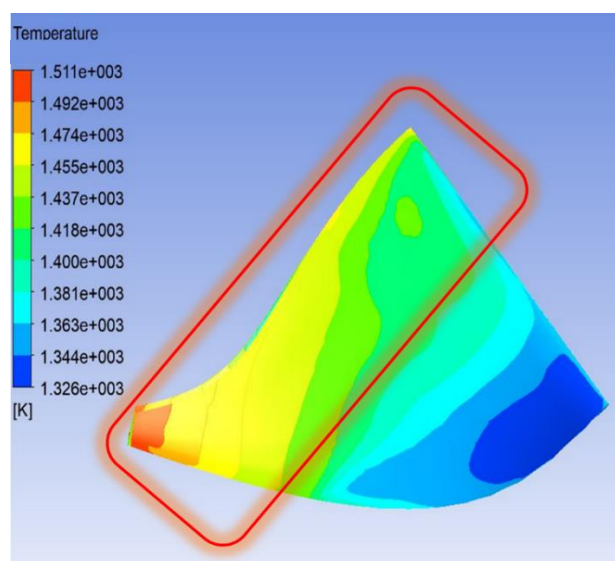


**Figure 3.9 : Zone présentant la température la plus élevée pour une turbine non refroidie fonctionnant à 9 bar et TIT =1450 °C.**

### 3.7. Simulation de la turbine refroidie

Cette section propose une méthodologie détaillée pour étudier la simulation 3D d'un rotor de turbine refroidi. Le schéma de refroidissement est le même que celui réalisé dans [132]. Il consiste en un canal de refroidissement lisse logé dans un rotor de turbine compact. La même procédure est appliquée pour capturer l'écoulement et le transfert de chaleur en 3D. La simulation est réalisée dans ANSYS CFX en plongeant la pale de turbine en trois parties principales et en utilisant le modèle de turbulence k- $\omega$  SST. La procédure détaillée est expliquée dans les sections suivantes.

#### 3.7.1. Génération de la géométrie de la turbine refroidie

L'aube de turbine non refroidie générée dans ANSYS BladeGen (Figure 3.11) a été exportée dans Inventor pour intégrer le canal de refroidissement. L'architecture et le placement du canal de refroidissement correspondent à l'optimisation de la topologie suggérée pour HIETA [132]. Le fluide de refroidissement pénètre dans le bord d'attaque, la partie la plus chaude de la turbine, et traverse l'aube de la turbine aussi près que possible du shroud, en suivant le chemin délimité à la Figure 3.9. La Figure 3.11 illustre l'aube de la turbine avec le canal de refroidissement généré d'un diamètre de 0.5 mm.

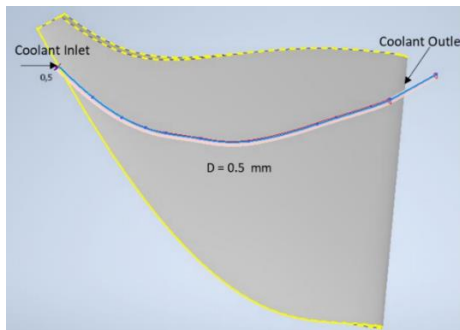


Figure 3.11: Configuration d'une pale de turbine refroidie à partir de 3D Inventor.

Comme expliqué précédemment, le fluide de refroidissement passe par un arbre creux, atteint le bord d'attaque puis sort par le bord de fuite pour se mélanger à l'écoulement principal. La Figure 3.12 représente à la fois la section transversale de la turbine refroidie et la géométrie complète.

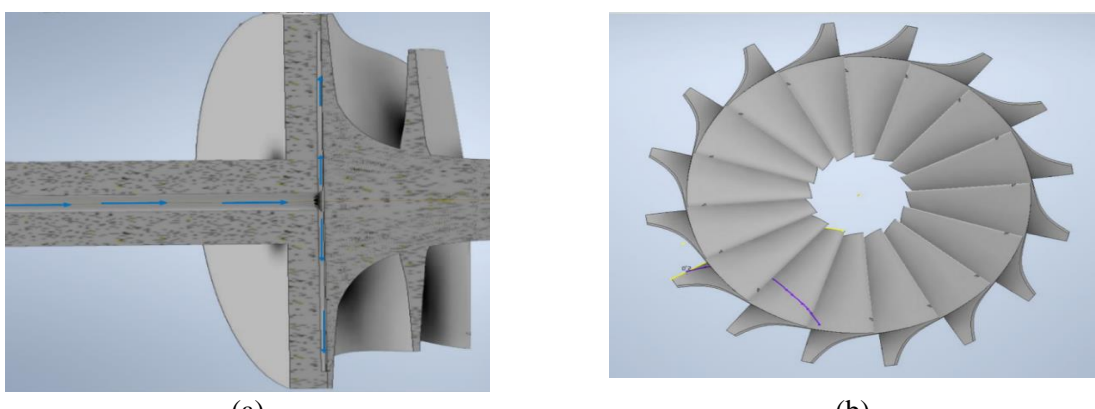


Figure 3.12: Géométrie de la turbine refroidie (a) configuration en coupe transversale, (b) turbine complète.

L'aube refroidie est ensuite importée dans ANSYS Design Modeler, comme le montre la Figure 3.13. Les caractéristiques de l'aube refroidie sont déterminées comme suit : la partie fluide est composée du gaz chaud et du fluide de refroidissement, et la partie solide est constituée de l'aube de la turbine.

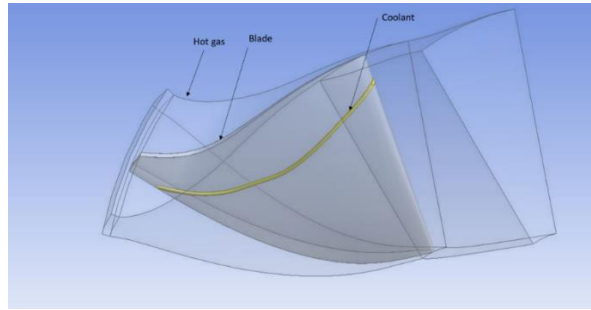


Figure 3.13: Les trois corps de la pale de turbine refroidie dans Design Modeler.

### 3.7.2. Génération du maillage

Le maillage de la turbine est réalisé dans ANSYS Meshing. La qualité du maillage est déterminée en prenant un maillage lisse et en vérifiant sa qualité. En utilisant l'indépendance de la grille, le nombre optimal d'éléments de maillage a été choisi pour les aubes de turbine refroidies, comme le montre la Figure 3.14. À gauche, on voit le maillage de l'aube de turbine et du canal de refroidissement, et à droite, le volume de gaz chaud. L'un des principaux défis du maillage a été causé par la différence d'échelle dans la géométrie. L'échelle de maillage du courant principal est plus grande que l'échelle de maillage du fluide de refroidissement.

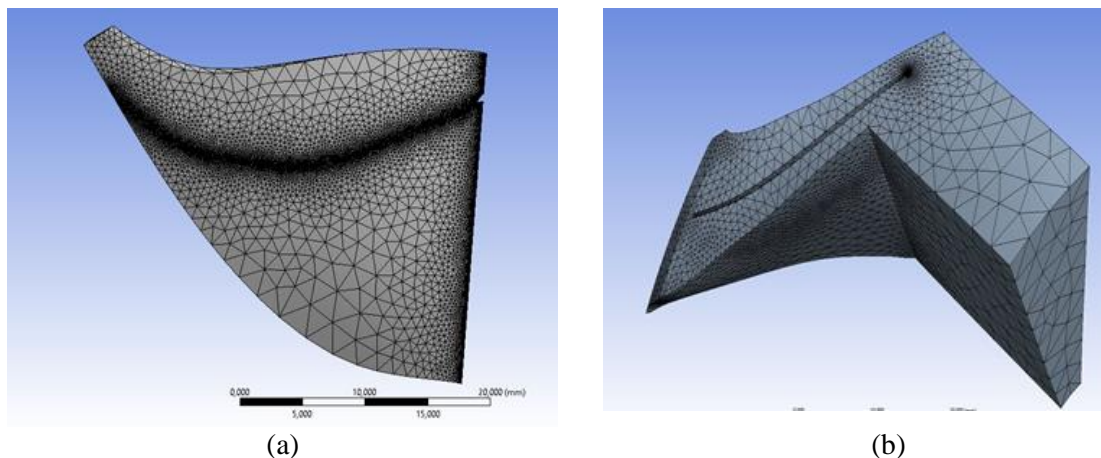


Figure 3.14 : Génération de maillage pour (a) la pale et le fluide de refroidissement, et (b) le corps de gaz chaud.

### 3.7.3. Configuration de la turbine refroidie

Le stator et le rotor sont importés dans ANSYS CFX. Les conditions aux limites sont la température totale d'entrée et la pression totale d'entrée à l'entrée de la tuyère et la pression statique de sortie à la sortie du rotor. L'écoulement à l'entrée est supposé dans la direction perpendiculaire (direction radiale). Les calculs d'aérodynamique et de transfert de chaleur reposent fortement sur les surfaces d'interface dans les simulations. Par conséquent, un modèle de Mixing plane est appliqué à l'interface stator-rotor pour assurer la connexion entre le domaine des pales stationnaires et celui des pales en rotation. Une deuxième interface est ajoutée entre la pale solide et le flux de fluide de refroidissement. De plus, une interface est appliquée entre la pale et le gaz chaud. À la limite de l'entrée du fluide de refroidissement, la masse et la température sont fixées comme résultat du calcul thermodynamique obtenu au chapitre 2. Tous les détails du domaine de fluide de calcul sont illustrés à la Figure 3.15. La distribution de la température et le transfert de chaleur à travers l'aube de la turbine dépendent de la conductivité du matériau. Par conséquent, l'acier est choisi comme matériau pour les aubes de turbine. L'écoulement principal et le fluide de refroidissement sont considérés comme des gaz idéaux.

La simulation est effectuée pour un passage d'aube de stator et un passage d'aube de rotor et le modèle de périodicité est utilisé pour déterminer le résultat sur l'étage global. De plus, toutes les parois sont supposées être lisses, sans conditions de glissement. La turbulence k- $\omega$  SST et le modèle d'équation d'énergie totale sont employés pour calculer le transfert de chaleur et l'écoulement 3D. La convergence est ajustée à  $10^{-6}$  pour tous les résidus.

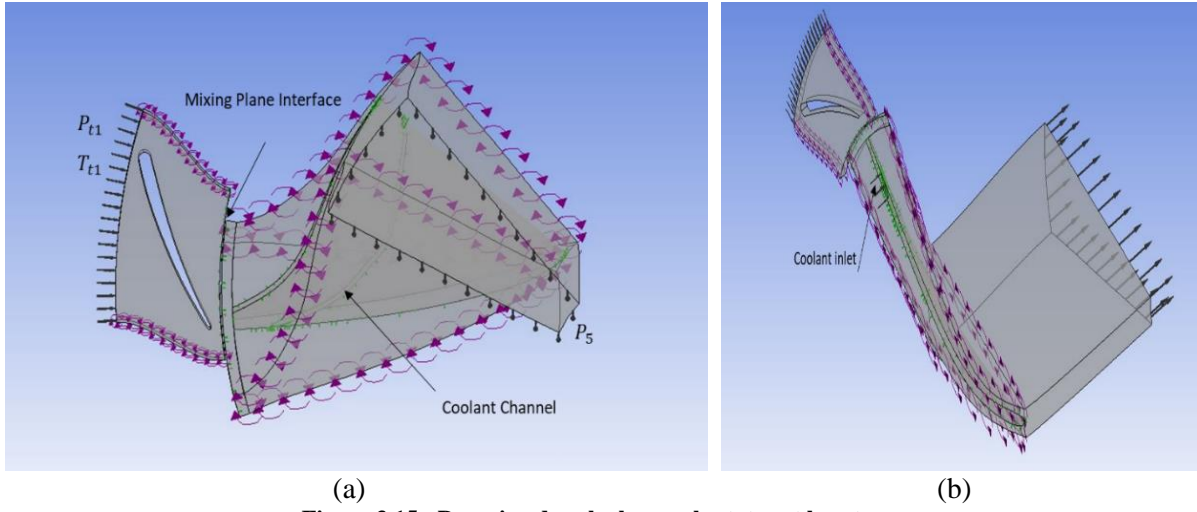
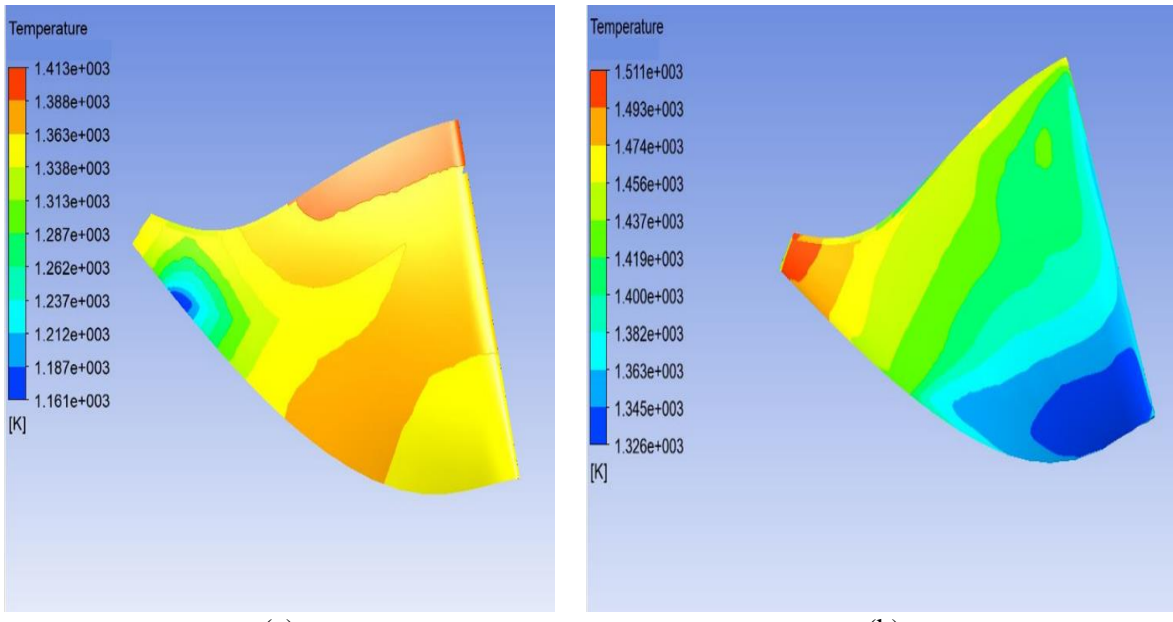


Figure 3.15 : Domaine de calcul pour le stator et le rotor.

### 3.7.4. Comparaison des turbines refroidies et non refroidies

Afin d'évaluer l'impact du refroidissement de la turbine sur la distribution de la température à la surface de la turbine, deux turbines ont été comparées dans des conditions de fonctionnement similaires : TIT = 1723.15 K et Pmax = 9 bar. La première turbine n'est pas refroidie, tandis que la seconde est refroidie, où la température d'entrée du liquide de refroidissement est de 170 °C (comme la température à la sortie du compresseur BP) et sa fraction est de 1.41% du débit massique total. Cette section vise d'abord à valider l'analyse thermodynamique du Chapitre 2 en vérifiant que la masse fixe de fluide de refroidissement est suffisante pour refroidir l'aube de la turbine ( $T_w = 1100$  °C) et à confirmer que la conception du refroidissement réussit à refroidir l'aube.

Les Figures 3.16 et 3.17 illustrent le résultat de la simulation CFD d'une turbine refroidie (à gauche) et d'une turbine non refroidie (à droite), toutes deux fonctionnant à une TIT de 1723.15 K et à une pression totale d'entrée de 9 bars. Seul le rotor de la turbine est refroidi, donc comme le stator n'est pas refroidi, seul le rotor est présenté. Les distributions de température sur la surface du rotor de la turbine de base et de la turbine refroidie indiquent une différence dans le transfert de chaleur; la conception du refroidissement a réussi à refroidir la surface de la pale. La température du bord d'attaque de la turbine refroidie est inférieure de 150 K à celle de la turbine de référence. Il existe également une différence considérable dans la température des autres parties de la roue de la turbine par rapport à la géométrie non refroidie. En se basant sur le fait que le matériau de la turbine peut supporter des températures allant jusqu'à 1373.15 K, on peut voir que dans le cas du rotor refroidi, la température de l'aube ne dépasse pas cette limite, à l'exception d'une petite zone au niveau du bord de fuite où la température dépasse de 20 K. Par conséquent, on peut conclure que l'analyse thermodynamique réussit à prédire la masse nécessaire de fluide de refroidissement et que le canal de refroidissement est efficace pour réduire la température de l'aube le long de la surface.

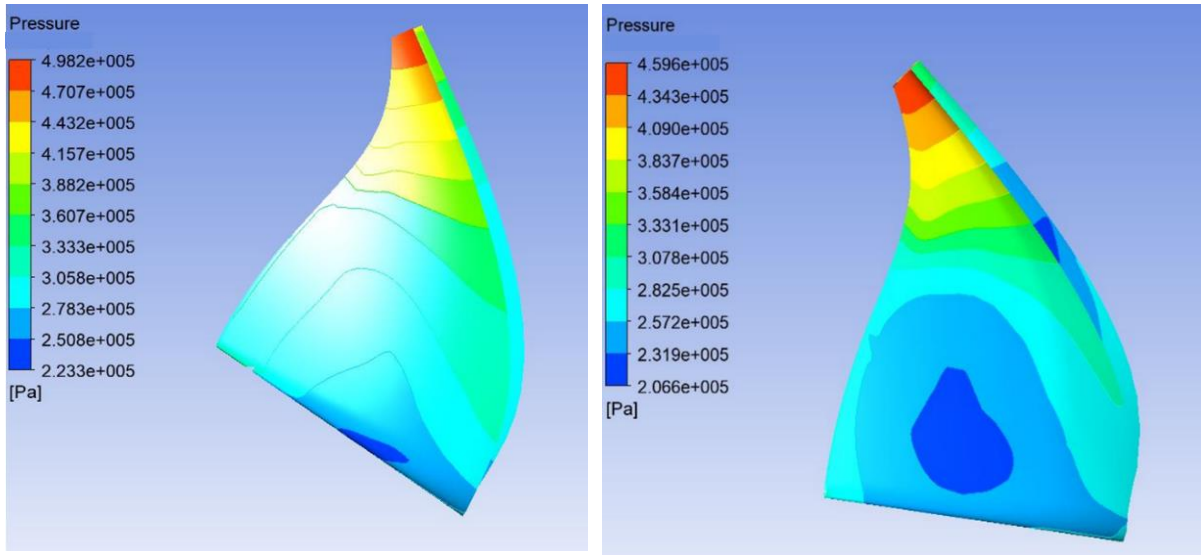


(a)

(b)

**Figure 3.16 : Distribution de la température sur la pale de la turbine pour la même TIT et Pmax (a) rotor refroidi, (b) rotor non refroidi.**

La variation de la pression sur la pale des deux turbines est comparée comme le montre la Figure 3.17. On peut constater que la distribution de la pression sur les deux configurations est pratiquement la même. La turbine est conçue pour assurer un taux d'expansion égal à 3. Si l'on considère la Figure 3.18, la température du fluide de refroidissement augmente au fur et à mesure qu'il passe dans le canal, pour atteindre une température de 1200 K à la sortie du canal de refroidissement. Ceci est dû au transfert de chaleur entre l'air de refroidissement et l'aube de la turbine. Il convient de noter que la température de l'aube est la température maximale que le fluide de refroidissement peut atteindre.



(a)

(b)

**Figure 3.17 : Distribution de la pression sur la pale de la turbine pour la même TIT et Pmax (a) rotor refroidi, (b) rotor non refroidi.**

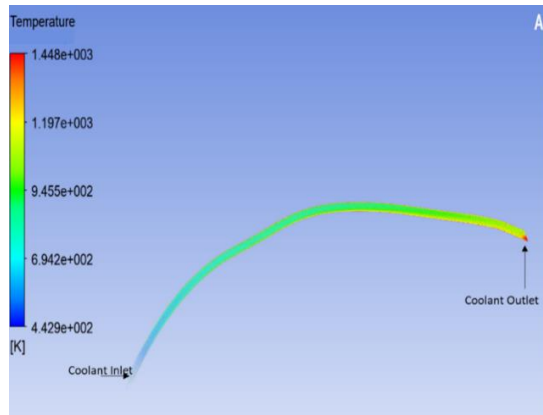


**Figure 3.18 : Variation de la température du liquide de refroidissement dans le canal de refroidissement.**

Un autre aspect qui doit être abordé est l'effet du refroidissement de la turbine sur son rendement. L'analyse thermodynamique développée au Chapitre 2 a proposé une méthode pour calculer le rendement de la turbine refroidie. L'objectif de cette section est d'évaluer l'impact du refroidissement de la pale de la turbine sur son efficacité. Le rendement de la turbine non refroidie conçue, lorsqu'elle fonctionne dans les conditions prévues (pression de 9 bars et TIT = 1373.15 K), est de 80 %. Des changements significatifs du rendement de la turbine sont obtenus lorsque le TIT varie. Le rendement le plus élevé est obtenu lorsque la turbine fonctionne à son TIT nominal. Par exemple, l'efficacité de la turbine actuelle, lorsqu'elle fonctionne à 9 bar et à un TIT = 1723.15 K, diminue à 78 %. En d'autres termes, l'efficacité de la turbine conçue diminue de 2 points lorsqu'elle fonctionne à 1723.15 K. Selon ANSYS CFX, l'efficacité de la turbine refroidie est de 72 % lorsqu'elle fonctionne à 1723.15 K. Deux facteurs contribuent à la diminution de l'efficacité de la turbine : le fonctionnement de la turbine à un TIT différent de celui qui a été conçu et le refroidissement des pales. Comme la géométrie de la turbine réduit le rendement d'environ 2 points, on estime que le refroidissement diminue le rendement de 6 points. Sur la base de ces facteurs, on peut prévoir que l'efficacité de la turbine refroidie sera d'environ 74 % si la turbine est conçue à la température de fonctionnement optimale.

Le coefficient global de transfert de chaleur U de la turbine refroidie est calculé à l'aide d'une méthode analytique et d'une simulation 3D. Les résultats des deux méthodes sont comparés. Les conditions de fonctionnement utilisées pour la méthode analytique LMTD sont énumérées dans le tableau 3.5. Le coefficient de transfert de chaleur global U est égal à  $1245 \text{ W.m}^{-2} \cdot \text{K}^{-1}$ . Cependant, le coefficient de transfert de chaleur obtenu à partir de ANSYS CFX-post est égal à  $1421.24 \text{ W.m}^{-2} \cdot \text{K}^{-1}$ . On peut donc conclure que les résultats de l'analyse et de la simulation 3D sont en bon accord, l'erreur relative ne dépassant pas 12 %.

**Table 3.20: Paramètres appliqués pour la méthode LMTD, et les U obtenus pour l'analyse et la simulation 3D.**

Paramètres	Conditions de fonctionnement	
Température d'entrée du fluide de refroidissement (K)	443.15	
Débit massique du fluide de refroidissement (kg/s)	$4 \times 10^{-5}$	
Zone d'échange thermique du fluide de refroidissement (m <sup>2</sup> )	$2.042 \times 10^{-5}$	
LMTD (K)	864.91	
Resultats	Analyse Analytique	ANSYS CFX
Coefficient de transfert de chaleur U (W.m <sup>-2</sup> .K <sup>-1</sup> )	1245	1421.24

Plusieurs conclusions peuvent être tirées de ces résultats. Tout d'abord, la masse estimée du fluide de refroidissement en utilisant l'approche 1D est efficace pour réduire la température de la pale de la turbine par rapport au cas non refroidi. De plus, on peut conclure que l'efficacité de la turbine dépend de la température d'entrée, par conséquent, lorsque la turbine fonctionne à différentes TIT, une diminution de l'efficacité de 2 points est obtenue. Lorsque la méthode de refroidissement est appliquée, l'efficacité de la turbine diminue à 72 %. La diminution du rendement est attribuée à la fois à un ajustement de la géométrie nécessaire pour s'adapter à la nouvelle TIT et à l'introduction de canaux de refroidissement. La géométrie de la turbine réduit son rendement d'environ deux points de rendement, et donc le refroidissement réduit le rendement de six points de rendement. En outre, on peut conclure que la formulation thermodynamique sous-estime le transfert de chaleur et la perte d'efficacité dans la turbine refroidie par rapport à la simulation 3D, puisque la diminution de température dans la simulation 3D est de 150 K, alors qu'elle n'est que de 10 K dans l'approche 1D. Par conséquent, si la turbine refroidie est conçue à la température optimale, son efficacité serait de 74 %.

### 3.8. Impact de la turbine refroidie sur le rendement du cycle

Le cycle standard IRReGT est le cycle de référence. Pour tester l'influence de la turbine refroidie et de la turbine non refroidie sur l'efficacité du prolongateur d'autonomie, l'analyse thermodynamique du chapitre 2 est réalisée mais en considérant les efficacités de la turbine HP non refroidie conçue et de la turbine HP refroidie conçue à partir de l'ANSYS CFX. Cette section consiste à comparer ces deux cycles: le cycle IRReGT de base, et le cycle IRReGT avec une turbine HP refroidie en considérant l'efficacité obtenue par la CFD. Une analyse thermodynamique et une étude exergétique sont menées pour les deux cycles. Les résultats du cycle IRReGT standard et du cycle IRReGT refroidi. Par rapport au cycle de base, le cycle IRReGT avec une turbine refroidie donne un travail de sortie net plus élevé, ce qui entraîne une diminution de la masse d'air de 17 % (scénario le plus défavorable) pour une puissance de 20 kW. Ainsi, le système est moins encombrant et plus compact. En outre, bien que le rendement de la turbine refroidie HP soit diminué de 6 points, le rendement global du cycle IRReGT avec turbine refroidie (47 %) est toujours supérieur à celui du cycle IRReGT de base (43.6 %).

D'après l'étude paramétrique réalisée au chapitre 2, l'augmentation de la température d'entrée de la turbine HP de 1100 °C à 1450 °C entraîne une augmentation de 6 points de l'efficacité globale du cycle. Parallèlement, la réduction du rendement de la turbine de 4 points, de 80 % à 74 %, réduit le rendement du cycle d'environ 3.6 points. Par ailleurs, l'étude exergétique a montré que la destruction d'énergie du cycle IRReGT avec une turbine refroidie est plus importante que dans le cas du cycle de base.

En comparant la destruction d'énergie de chaque composant des deux cycles, plusieurs conclusions sont obtenues.

- La destruction d'énergie dans les deux cycles est très proche.
- La destruction d'énergie de la turbine refroidie est supérieure de 35 % par rapport au cycle non refroidi en raison de la diminution de l'efficacité.
- La destruction d'énergie du régénérateur est plus élevée dans le cycle de base que dans le cas refroidi car les températures à l'entrée du régénérateur (principalement la température des gaz chauds) sont plus élevées.

À la lumière de ces résultats, on peut conclure que, bien que le refroidissement des aubes de turbine soit associé à une réduction du rendement de la turbine et à une complexité de sa géométrie et de sa structure, il augmente le rendement global du cycle et réduit la quantité de masse d'air nécessaire pour produire la

même quantité de puissance. Il en résulte un système de prolongateur d'autonomie plus compact et plus efficace pour accroître l'autonomie des voitures électriques.

### 3.9. Conclusion

La turbine HP refroidie du cycle IRReGT refroidi est le composant le plus critique. Ainsi, ce chapitre présente une procédure méthodologique détaillée pour concevoir une turbine radiale refroidie fonctionnant à haute température et haute pression et fabriquée par impression 3D.

La première partie de ce chapitre est un outil de conception pour une turbine non refroidie. La procédure de conception consiste en une conception préliminaire pour déterminer les paramètres géométriques globaux et la performance globale de la turbine actuelle. L'analyse 1D est basée sur des corrélations de la littérature pour générer les triangles de vitesse à chaque étape de la turbine. Bien que cette technique soit efficace pour évaluer la performance globale de la roue de la turbine, la simulation 3D à l'aide d'ANSYS CFX est obligatoire pour prédire la séparation des flux et le comportement 3D du système. La méthodologie de conception proposée est ensuite validée en comparant les résultats avec une turbine commerciale. Les résultats confirment l'efficacité de cette procédure pour prédire les performances et la conception de la turbine. Par conséquent, une turbine non refroidie fonctionnant à une température de 1100 °C, une pression de 9 bars et une vitesse de rotation de 120 000 tr/min est conçue pour offrir un rendement de 80 %.

La deuxième partie de ce chapitre est un outil de conception de la turbine refroidie prenant en compte les défis liés à la turbine à petite échelle et les limitations de l'impression 3D. Un canal de refroidissement est intégré dans la pale du rotor de la turbine conçue en tenant compte d'une épaisseur de paroi minimale de 0.16 mm, et d'un diamètre de trou minimal de 0.5 mm. La trajectoire du canal de refroidissement passe par la zone de la pale de rotor qui est soumise à la température la plus élevée. La simulation 3D a permis de vérifier que la masse de fluide de refroidissement déterminée à partir de l'analyse thermodynamique est suffisante pour refroidir l'aube de la turbine. Premièrement, la température le long de l'aube de la turbine est inférieure à la température fixée pour des raisons de limitation des matériaux. Deuxièmement, par rapport à la turbine non refroidie fonctionnant dans les mêmes conditions, la température de différentes parties de la turbine refroidie est inférieure à celle du cas non refroidi, par exemple, la température du bord d'attaque est réduite de 150 K. Par rapport à l'approche 1D, la diminution estimée de la température du gaz chaud est d'environ 10 K, ce qui implique que l'approche 1D sous-estime le transfert de chaleur par rapport au modèle 3D. Par conséquent, l'efficacité de la turbine refroidie est estimée à 74 % dans ANSYS CFX, contre 77.5 % dans l'approche 1D.

L'étape finale de ce chapitre consiste à réévaluer l'efficacité globale du cycle refroidi IRReGT en tenant compte de l'efficacité de la turbine conçue dans ANSYS CFX. L'analyse thermodynamique a vérifié que les performances du cycle actuel avec une turbine HP refroidie sont toujours plus avantageuses que celles du cycle IRReGT non refroidi. Ainsi, l'efficacité du cycle proposé est supérieure de 3 points à celle du cycle de référence de base. La diminution de l'efficacité de la turbine entraîne une diminution de l'efficacité du cycle, mais l'augmentation de la TIT a un effet positif et significatif sur le cycle global.

## General Conclusion and Perspectives

In July 2009, European Union (EU) and G8 leaders agreed to reduce greenhouse gas (GHG) emissions by 80 % from 1990 levels by 2050. The transportation sector is responsible for the majority of these nocive emissions. Therefore, new regulations are enforced to replace the internal combustion engine with new powertrains. With the development of series hybrid electric vehicles architecture, the gas turbine cycle is selected as the most suitable powertrain for electric cars. The system consists of a gas turbine cycle coupled to an alternator that transforms the mechanical power of the turbine into electric power, and charges the battery of the electric car.

According to the literature review, three major steps are required to enhance the performance of the gas turbine (GT) cycle: choosing the optimal architecture, increasing the pressure, and increasing the turbine inlet temperature. Based on the optimal architecture criteria, a previous study conducted by Bou Nader [1] in MINES Paristech has selected the IRReGT cycle consisting of a double compression stage with intercooler, a double turbine stage with reheating, and a recuperator as the most suitable cycle in terms of higher efficiency and higher specific output. Regarding the pressure criteria, it was shown that there is an optimum pressure above which the cycle efficiency will decrease. However, considering the turbine inlet temperature parameter, material constraints such as melting temperature and cost should be taken into consideration. Therefore, cooling techniques were introduced to operate at higher temperatures beyond the material limits. Among the wide techniques of cooling, convection cooling was selected since it is simple and compatible with microscale turbines. This method consists of a smooth coolant channel introduced in the turbine blade where the heat transfer occurs between the coolant and the turbine material. However, such complex small-scale components require new methods to produce them such as the 3D printing technique.

In this thesis, four consecutive studies were carried out to design high efficient, compact range extender for series hybrid electric cars:

- A parameter study
- A thermodynamic analysis
- A technological assessment
- A CFD analysis

First, a parametric study was conducted to determine the optimal operating conditions in terms of higher efficiency and higher specific work. The parametric study showed that the optimal pressure is 9 bar while increasing the pressure above this value leads to a decrease in the cycle efficiency and an increase in the stress and loss on the turbine wheel. Secondly, a thermodynamic analysis was performed to study the impact of cooling the turbine blades on the cycle performance. The thermodynamic analysis determines the required mass of coolant to cool the turbine which is considered a heat exchanger with a constant wall temperature. As well, in this section, a new definition of ‘cooled turbine efficiency’ was proposed to evaluate the effect of cooling on the radial turbine efficiency. The results showed that the cooling technique was beneficial in increasing the cycle efficiency (4.1 points) compared to the baseline cycle due to the advantage of a further increase in TIT. As well, it was shown that while cooling was disadvantageous to the turbine efficiency, it increases the efficiency of the overall cycle. A comparison of multiple GT architectures with cooling turbine blades was conducted to study the effects of cooling on GT configurations. Four realistic GT architectures were compared involving either one cooled turbine or two cooled turbines, taking into account the turbine and recuperator operating temperatures. Because the extender is incorporated into the vehicle, the cycle should be compact, efficient, and simple.

Therefore, a technological assessment was carried out to consider the system weight and the technical constraints of each component. Among the investigated configurations, the IRReGT cycle with only a cooled HP turbine was selected. When operating at 9 bar, it was observed to offer high efficiency of 51 %, a high net specific work (457.6 kJ/kg), and the lowest weight (42.5 kg).

Based on the previously selected cycle, this work was further developed to design the HP cooled turbine from the 1D approach, geometry generation, and meshing to 3D simulation. The cooled HP turbine is the most critical part. It is a small-scale cooled radial turbine manufactured using 3D printing. A detailed design methodology was presented: the first approach aimed to design an uncooled turbine. Therefore, a preliminary design was performed in VBA to determine the overall geometry and performance of the uncooled turbine. The meanline was followed by a 3D simulation using ANSYS CFX to study the interaction between the fluid flow and the uncooled turbine blade. For this reason, stator and rotor geometry was generated using ANSYS BladeGen, and meshes were generated using ANSYS TurboGrid. Afterward, both the stator and the rotor were imported into ANSYS CFX to conduct the 3D simulation. Results showed that the designed uncooled turbine operating at 9 bar and TIT= 1100 °C, achieved an efficiency of 80 %. After the validation of the current proposed design approach, the second step was to design the cooled turbine blade taking 3D printing limitations, previously concluded, into account. These limitations include the minimum wall thickness (0.16 mm) and minimum hole diameter (0.5 mm). To accomplish the cooling of the turbine blade, the coolant channel should pass through the areas subjected to the highest temperatures, as the leading edge. It was observed that the results of the 3D simulation were in good agreement with the 1D analysis. The required mass of coolant was sufficient to cool the turbine blade since the temperature of the leading edge was reduced by 150 K compared to the uncooled case. Nevertheless, the 3D analysis showed that the 1D analysis underestimated the loss in turbine efficiency by 3.5 points. Therefore, it was assumed that the cooled turbine efficiency is 74 %. Finally, a reevaluation of the efficiency of the IRReGT cycle with a cooled turbine showed that the current cycle is still more beneficial than the uncooled IRReGT cycle even with a reduced turbine efficiency. An increase of cycle efficiency by 3 points to the baseline reference cycle was obtained.

For future work, it is first important to develop an experimental setup that allows the visualization of the behavior of the cooled turbine (Appendice A: Experimental Setup). The experimental study has various objectives. The first one consists of the verification of the feasibility of the turbine in terms of 3D printing manufacturing. The second objective is the validation of the 3D developed model. This imposes the verification that the required mass of coolant is sufficient to cool the turbine blade. As well, this allows the evaluation of the cooled turbine performance and the turbine efficiency.

The obtained results are encouraging to further enhance the performance of the cooling turbine concept. Therefore, the optimization of the cooled turbine is a crucial step that allows the obtention of an optimum design offering a compromise between high efficiency and simple feasibility. An additional point to consider is to analyze several geometries of the cooling channel. This includes the trajectory of the coolant channel into the turbine blade, as well as the shape of the coolant channel including round, rectangular sections. Moreover, the study should consider other cooling techniques, their design complexity, and the manufacturing feasibility.

Another perspective for future work is to develop new correlations for the 1D approach that takes into consideration the heat transfer in generating the turbine blade profile. The heat transfer should be included in the correlations to assess the heat extraction at different steps of the turbine stage, to account for the best turbine blade geometry. In addition, it is proposed to develop an optimization tool for the cooled turbine design and re-evaluate the turbine efficiency variation.

## Conclusion Générale et Perspectives

En juillet 2009, les dirigeants de l'Union européenne (UE) et du G8 ont décidé de réduire les émissions de gaz à effet de serre (GES) de 80 % par rapport aux niveaux de 1990 d'ici à 2050. Le secteur des transports est responsable d'une grande partie de ces émissions nocives. C'est pourquoi de nouvelles réglementations sont mises en œuvre pour remplacer le moteur à combustion interne par de nouveaux groupes motopropulseurs. Avec le développement de l'architecture des véhicules électriques hybrides de série, le cycle de la turbine à gaz est sélectionné comme le groupe motopropulseur le plus approprié pour les voitures électriques. Le système consiste en un cycle de turbine à gaz couplé à un alternateur, qui transforme l'énergie mécanique de la turbine en énergie électrique et charge la batterie de la voiture électrique.

Selon la littérature, trois étapes majeures sont nécessaires pour améliorer les performances du cycle de la turbine à gaz (GT) : le choix de l'architecture optimale, l'augmentation de la pression et l'augmentation de la température d'entrée de la turbine. Sur la base des critères d'architecture optimale, une étude précédente menée par Bou Nader [1] à MINES ParisTech a permis de sélectionner le cycle IRReGT composé d'un double étage de compression avec intercooler, d'un double étage de turbine avec réchauffage, et d'un récupérateur comme étant le cycle le plus approprié en termes d'efficacité et de rendement spécifique plus élevés. En ce qui concerne la pression, il a été démontré qu'il existe une pression optimale au-dessus de laquelle l'efficacité du cycle diminue. Cependant, si l'on considère le paramètre de la température d'entrée de la turbine, les contraintes liées aux matériaux, telles que la température de fusion et le coût, doivent être prises en compte. Par conséquent, des techniques de refroidissement ont été introduites pour fonctionner à des températures plus élevées au-delà des limites des matériaux. Parmi les nombreuses techniques de refroidissement, le refroidissement par convection a été choisi car il est simple et compatible avec les turbines à micro-échelle. Cette méthode consiste en un canal de refroidissement lisse introduit dans l'aube de la turbine où le transfert de chaleur se produit entre le fluide de refroidissement et le matériau de la turbine. Cependant, ces composants complexes à petite échelle nécessitent de nouvelles méthodes pour les produire, comme la technique d'impression 3D.

Dans cette thèse, quatre études consécutives ont été menées pour concevoir un prolongateur d'autonomie compact et hautement efficace pour les voitures électriques hybrides en série :

- Une étude paramétrique
- Une analyse thermodynamique
- Une évaluation technologique
- Une analyse CFD

Tout d'abord, une étude paramétrique a été menée pour déterminer les conditions de fonctionnement optimales en termes de rendement et de travail spécifique plus élevés. L'étude paramétrique a montré que la pression optimale est de 9 bar alors que l'augmentation de la pression au-delà de cette valeur conduit à une diminution de l'efficacité du cycle et à une augmentation des contraintes et des pertes sur la roue de la turbine. Deuxièmement, une analyse thermodynamique a été réalisée pour étudier l'impact du refroidissement des pales de la turbine sur les performances du cycle. L'analyse thermodynamique détermine la masse du fluide de refroidissement nécessaire pour refroidir la turbine qui est considérée comme un échangeur de chaleur avec une température de paroi constante. De plus, dans cette section, une nouvelle définition de " l'efficacité de la turbine refroidie " a été proposée pour évaluer l'effet du refroidissement sur l'efficacité de la turbine. Les résultats ont montré que la technique de refroidissement

a permis d'augmenter le rendement du cycle (4.1 points) par rapport au cycle de base grâce à l'avantage d'une augmentation supplémentaire de la TIT. De même, il a été démontré que si le refroidissement est désavantageux pour l'efficacité de la turbine, il augmente l'efficacité du cycle global. Une comparaison de plusieurs architectures de turbine à gaz avec aubes refroidies a été réalisée pour étudier les effets du refroidissement sur les configurations de GT. Quatre architectures réalistes de GT ont été comparées, impliquant soit une turbine refroidie, soit deux turbines refroidies, en tenant compte des températures de fonctionnement de la turbine et du récupérateur. Comme le prolongateur est incorporé au véhicule, le cycle doit être compact, efficace et simple. Par conséquent, une évaluation technologique a été réalisée pour prendre en compte le poids du système et les contraintes techniques de chaque composant. Parmi les configurations étudiées, le cycle IRReGT avec seulement une turbine HP refroidie a été sélectionné. En fonctionnant à 9 bars, il a été observé qu'il offrait un rendement élevé de 51 %, un travail spécifique net élevé (457.6 kJ/kg) et le poids le plus faible (42.5 kg).

Sur la base du cycle sélectionné précédemment, ce travail a été approfondi pour concevoir la turbine HP refroidie à partir d'une approche 1D, suivie d'une génération de la géométrie et du maillage et d'une simulation 3D. La turbine HP refroidie est le composant le plus critique. Il s'agit d'une turbine radiale refroidie à petite échelle fabriquée par impression 3D. Une méthodologie de conception détaillée a été présentée. La première approche visait à concevoir une turbine non refroidie. Par conséquent, une conception préliminaire a été réalisée en VBA pour déterminer la géométrie globale et les performances de la turbine non refroidie. L'étude préliminaire a été suivie d'une simulation 3D à l'aide d'ANSYS CFX pour étudier l'interaction entre l'écoulement du fluide et la pale de la turbine non refroidie. Pour cette raison, la géométrie du stator et du rotor a été générée à l'aide de ANSYS BladeGen, et les mailles ont été générées à l'aide de ANSYS TurboGrid. Ensuite, le stator et le rotor ont été importés dans ANSYS CFX pour effectuer la simulation 3D. Les résultats ont montré que la turbine non refroidie conçue, fonctionnant à 9 bar et  $TIT = 1100^\circ\text{C}$ , a atteint un rendement de 80 %. Après la validation de l'approche de conception proposée actuellement, la deuxième étape a consisté à concevoir l'aube de turbine refroidie en tenant compte des limites de l'impression 3D, conclues précédemment. Ces limites comprennent l'épaisseur minimale de la paroi (0,16 mm) et le diamètre minimal des trous (0,5 mm). Pour réaliser le refroidissement de l'aube de turbine, le canal de refroidissement doit passer par les zones soumises aux plus hautes températures, comme le bord d'attaque. Il a été observé que les résultats de la simulation 3D étaient en bon accord avec l'analyse 1D. La masse du fluide de refroidissement requise était suffisante pour refroidir l'aube de la turbine puisque la température du bord d'attaque a été réduite de 150 K par rapport au cas non refroidi. Néanmoins, l'analyse 3D a montré que l'analyse 1D sous-estimait la perte d'efficacité de la turbine de 3.5 points. Par conséquent, on a supposé que l'efficacité de la turbine refroidie était de 74 %. Enfin, une réévaluation de l'efficacité du cycle IRReGT avec une turbine refroidie a montré que le cycle actuel est toujours plus avantageux que le cycle IRReGT non refroidi, même avec une efficacité réduite de la turbine. Une augmentation de l'efficacité du cycle de 3 points par rapport au cycle de référence de base a été obtenue.

Pour les futurs travaux, il est d'abord important de développer un montage expérimental qui permette de visualiser le comportement de la turbine refroidie. L'étude expérimentale a plusieurs objectifs. Le premier consiste en la vérification de la faisabilité de la turbine en termes de fabrication par impression 3D. Le second objectif est la validation du modèle développé en 3D. Cela impose de vérifier que la masse du fluide de refroidissement déterminée est suffisante pour refroidir les aubes de la turbine. De plus, cela permet d'évaluer les performances de la turbine refroidie et son efficacité.

Les résultats obtenus sont encourageants pour améliorer encore les performances du concept de turbine refroidie. Par conséquent, l'optimisation de la turbine refroidie est une étape cruciale qui permet l'obtention d'une conception optimale offrant un compromis entre un rendement élevé et une faisabilité

simple. Un point supplémentaire à considérer est d'analyser plusieurs géométries du canal de refroidissement. Cela inclut la trajectoire du canal de refroidissement dans la pale de la turbine, ainsi que la forme du canal de refroidissement, y compris les sections rondes et rectangulaires. De plus, l'étude devrait prendre en compte d'autres techniques de refroidissement, la complexité de leur conception et la faisabilité de leur fabrication.

Une autre perspective pour le travail futur est de développer de nouvelles corrélations pour l'approche 1D qui prend en considération le transfert de chaleur dans la génération du profil de l'aube de la turbine. Le transfert de chaleur devrait être inclus dans les corrélations pour évaluer l'extraction de chaleur à différentes étapes de l'étage de la turbine, afin de tenir compte de la meilleure géométrie des aubes de la turbine. En outre, il est proposé de développer un outil d'optimisation pour la conception de la turbine refroidie et de réévaluer la variation de l'efficacité de la turbine.

## Appendice A: Experimental Setup

This appendix presents the test bench setup under preparations to perform the experiments. The goal of the experiment is to demonstrate the success of the cooling technology, as well as the manufacturing of the 3D turbine, and the validation of the developed models. The experimentation is realized for a cooled turbine operating at 3 bar since the casing of the turbine is already provided from a variable geometry turbocharger, illustrated in Figure A.1a. The uncooled turbine rotor of this turbocharger is available and is taken as a reference to evaluate the impact of cooling on the temperature distribution and the turbine performance (Figure A.1).

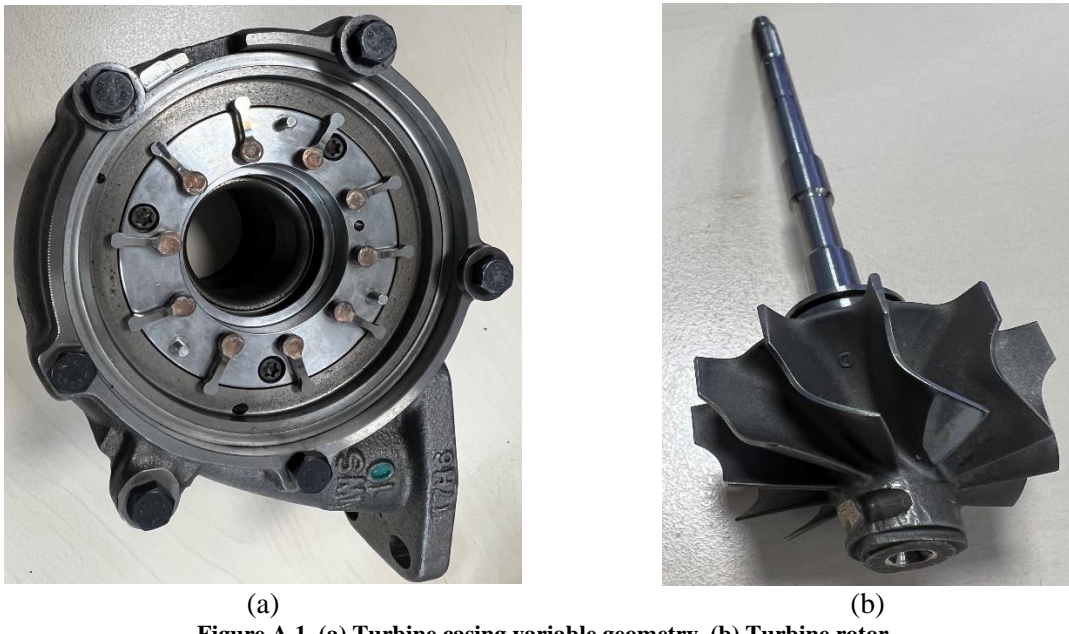
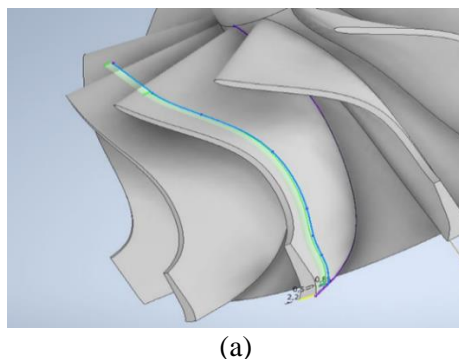


**Figure A.1. (a) Turbine casing variable geometry, (b) Turbine rotor.**

A new turbine operating at a pressure of 3 bar and a TIT = 1100 °C is designed based on the presented design tool in Chapter 3. The designed turbine should be similar to the uncooled turbine, mainly in the diameter to fit into the available casing.

Considering the same limitations of 3D printing, a cooling channel is also incorporated into the turbine blade. The turbine is imported into Inventor Autodesk to generate the cooling channel. At the rotor shaft, several holes are responsible to introduce the coolant air into the shaft. The coolant air passes through the shaft of the rotor and then enters each blade at the leading edge. The flow exits at the trailing edge of the turbine blade to mix with the mainstream. The cooling channel in the turbine blade, a cross-section of the shaft and rotor, and overall turbine geometry are shown in Figure A.2. The designed turbine is converted into an STL file and sent to be printed in Steel 316 L.



(a)

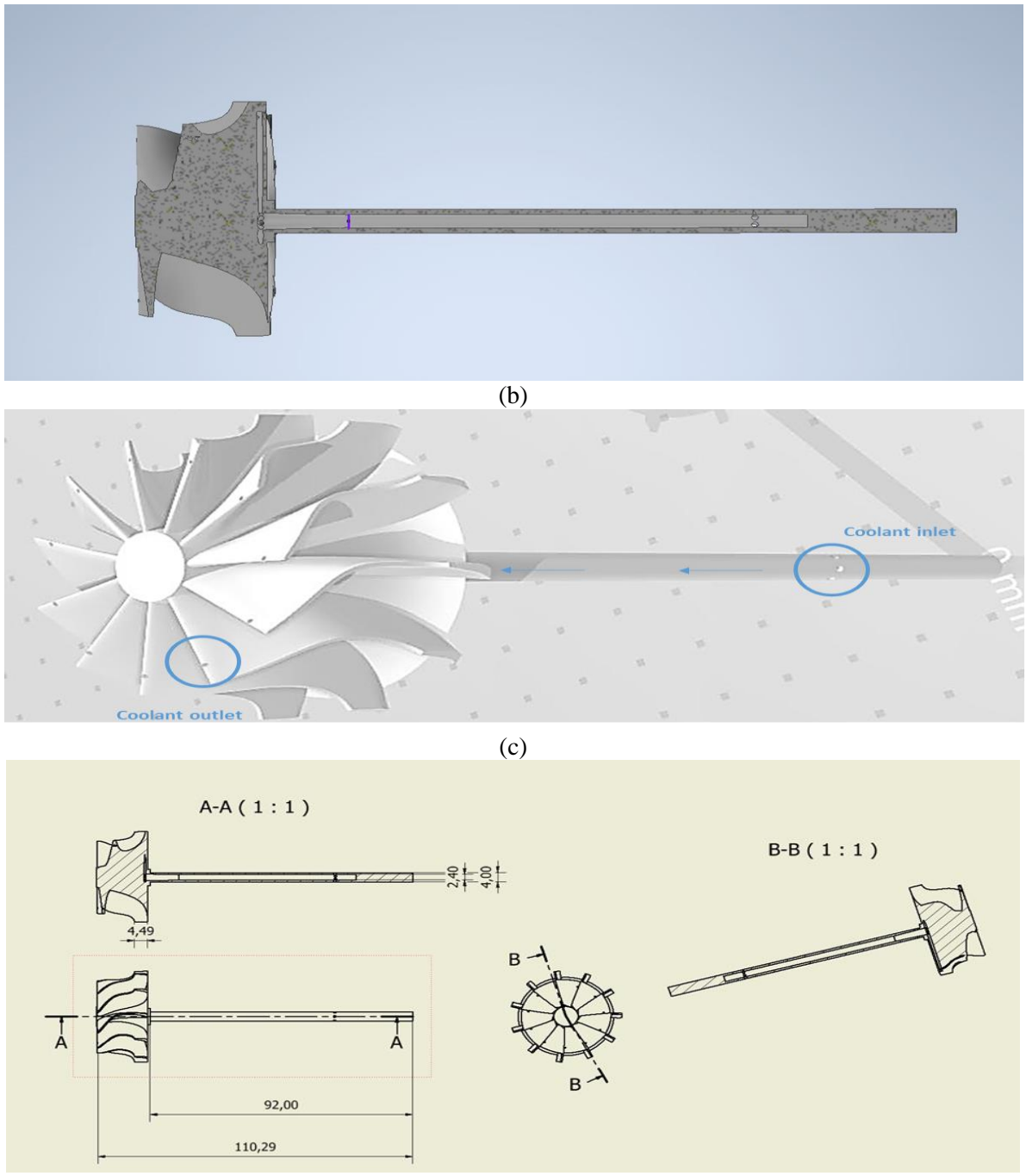


**Figure A.2. (a) cooling channel, (b) cross section of the shaft and turbine rotor, (c) overall geometry of the designed turbine, (d) Drawing of the designed cooled turbine rotor.**

The test bench is presented in Figure A.3. The schematic presentation shows that an air tank with compressed air is responsible for providing air at 3 bar. A part of air is inserted directly into the shaft and used as a coolant for the turbine blade, while the remaining steam enters a heater where the temperature of the air is increased similarly to the hot gas. The turbine is coupled to a generator to measure the power at its outlet. At each step of the test bench, pressure and temperature sensors are implemented.

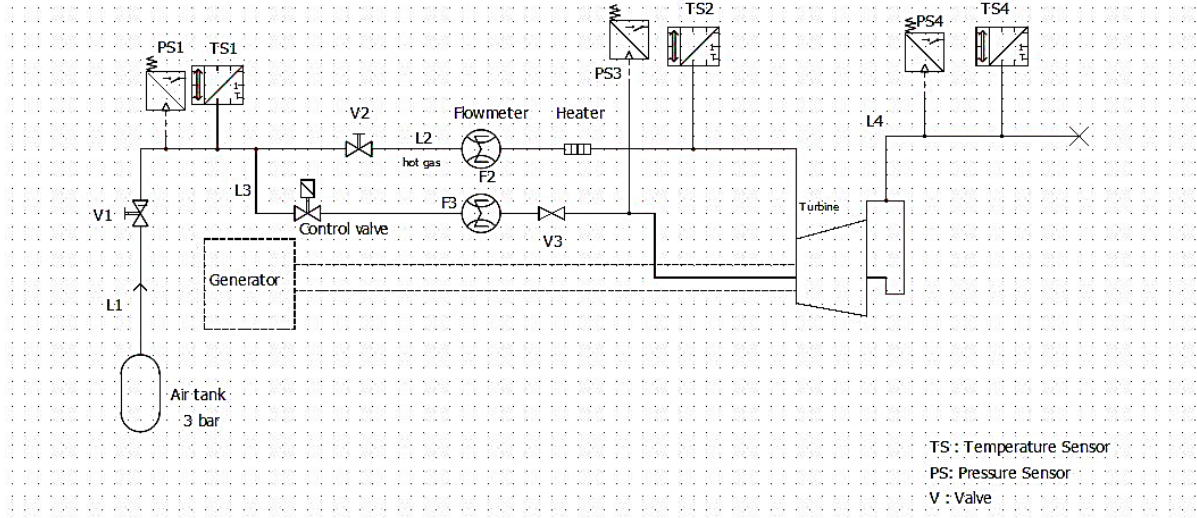


**Figure A.3. Test bench setup.**

The turbine wheel was painted with thermal history paint to determine the temperature distribution along the turbine surface. The paint was sprayed on the turbine before the test. When this spray is subjected to hot gas the color of the paint changes due to the oxidation process. Therefore, a temperature map can be drawn on the surface of the rotor blade.

The same test setup is reproduced as well for the uncooled turbine case but without the presence of the cooling air. Finally, comparing the two cases, the impact of turbine cooling on the turbine efficiency and the turbine temperature variation is evaluated.

## References

1. Bou Nader W. Methodology for the selection and optimization of energy converters for automotive powertrain applications. [France]: PSL Université; 2019.
2. EUROPEAN UNION/EUROPEAN COMMISSION. RoadMAP 2050 - A practical Guide To A Prosperous, Low-Carbon Europe. 2010 Apr. Report No.: Volume 1.
3. The International Council On Clean Transportation. Zero-emission vehicles [Internet]. International Council on Clean Transportation. [cited 2022 May 10].
4. 2017 Global update: Light-duty vehicle greenhouse gas and fuel economy standards [Internet]. International Council on Clean Transportation. [cited 2022 May 11]. /
5. Nations U. COP26 : ensemble pour notre planète | Nations Unies [Internet]. United Nations. United Nations; [cited 2022 May 11].
6. Asthana S, Bansal S, Jaggi S, Kumar N. A Comparative Study of Recent Advancements in the Field of Variable Compression Ratio Engine Technology. SAE Tech Pap. 2016 Apr 5.
7. Doric J, Klinar I. Efficiency of a new internal combustion engine concept with variable piston motion. *Therm Sci.* 2014;18(1):113–27.
8. Mahmoudi AR, Khazaee I, Ghazikhani M. Simulating the effects of turbocharging on the emission levels of a gasoline engine. *Alex Eng J.* 2017 Dec 1;56(4):737–48.
9. Gupta S, Chaube A, Verma P. Review on Heat Transfer Augmentation Techniques: Application in Gas Turbine Blade Internal Cooling. 2012;5(1).
10. Wang Y, Sicot C, Borée J, Grandemange M. Experimental study of wheel-vehicle aerodynamic interactions. *J Wind Eng Ind Aerodyn.* 2020 Mar 1;198:104062.
11. Sankar Mohanta B, Kumar A. A parametric analysis on the performance of vehicle tires. *Mater Today Proc.* 2021 May 22.
12. Mansour C, Bou Nader W, Breque F, Haddad M, Nemer M. Assessing additional fuel consumption from cabin thermal comfort and auxiliary needs on the worldwide harmonized light vehicles test cycle. *Transp Res Part Transp Environ.* 2018 Jul 1;62:139–51.
13. Martins J, Brito FP. Alternative Fuels for Internal Combustion Engines. *Energies.* 2020 Jan;13(16):4086.
14. Honeywell's UOP breaks ground on plant to convert biomass to green transportation fuels. *Focus Catal.* 2011 Oct;2011(10):6.
15. Carslaw DC, Fricker N. Natural gas vehicles - A realistic alternative. *Fuel Energy Abstr.* 1995;5(36):358.
16. Bongartz D, Doré L, Eichler K, Grube T, Heuser B, Hombach LE, et al. Comparison of light-duty transportation fuels produced from renewable hydrogen and green carbon dioxide. *Appl Energy.* 2018 Dec 1;231:757–67.
17. Nouni MR, Jha P, Sarkhel R, Banerjee C, Tripathi AK, Manna J. Alternative fuels for decarbonisation of road transport sector in India: Options, present status, opportunities, and challenges. *Fuel.* 2021 Dec 1;305:121583.
18. Ma F, Wang Y, Liu H, Li Y, Wang J, Ding S. Effects of hydrogen addition on cycle-by-cycle variations in a lean burn natural gas spark-ignition engine. *Int J Hydrg Energy.* 2008 Jan 1;33(2):823–31.
19. White CM, Steeper RR, Lutz AE. The hydrogen-fueled internal combustion engine: a technical review. *Int J Hydrg Energy.* 2006 Aug 1;31(10):1292–305.
20. Verger T, Azimov U, Adeniyi O. Biomass-based fuel blends as an alternative for the future heavy-duty transport: A review. *Renew Sustain Energy Rev.* 2022 Jun 1;161:112391.
21. Shamami MS, Alam MS, Ahmad F, Shariff SM, AlSaidan I, Rafat Y, et al. Artificial Intelligence-Based Performance Optimization of Electric Vehicle-to-Home (V2H) Energy Management System. *SAE Int J Sustain Transp Energy Environ Policy.* 2020 Sep 22;1(2):115–25.
22. Tran MK, Fowler M. Sensor Fault Detection and Isolation for Degrading Lithium-Ion Batteries in Electric Vehicles Using Parameter Estimation with Recursive Least Squares. *Batteries.* 2020 Mar;6(1):1.
23. Mevawalla A, Panchal S, Tran MK, Fowler M, Fraser R. Mathematical Heat Transfer Modeling and Experimental Validation of Lithium-Ion Battery Considering: Tab and Surface Temperature,

- Separator, Electrolyte Resistance, Anode-Cathode Irreversible and Reversible Heat. Batteries. 2020 Dec;6(4):61.
24. Sanguesa JA, Torres-Sanz V, Garrido P, Martinez FJ, Marquez-Barja JM. A Review on Electric Vehicles: Technologies and Challenges. Smart Cities. 2021 Mar;4(1):372–404.
  25. Range & Charging & Saving | Nissan LEAF - Electric Family Car [Internet]. Nissan. [cited 2022 May 11].
  26. Supercharger [Internet]. Tesla. [cited 2022 May 13].
  27. Mutarraf MU, Guan Y, Xu L, Su CL, Vasquez JC, Guerrero JM. Electric cars, ships, and their charging infrastructure – A comprehensive review. Sustain Energy Technol Assess. 2022 Aug 1;52:102177.
  28. Berjoza D, Jurgena J. Effects of change in the weight of electric vehicles on their performance characteristics. In 2017. p. 952–63.
  29. Heron A, Rinderknecht F. Comparison of range extender technologies for battery electric vehicles. In: 2013 Eighth International Conference and Exhibition on Ecological Vehicles and Renewable Energies (EVER). 2013. p. 1–6.
  30. Tran MK, Bhatti A, Vrolyk R, Wong D, Panchal S, Fowler M, et al. A Review of Range Extenders in Battery Electric Vehicles: Current Progress and Future Perspectives. World Electr Veh J. 2021 Jun;12(2):54.
  31. Scuderi CJ. Split Four Stroke Cycle Internal Combustion Engine. International Patent WO 03/008785 A1.
  32. Phillips F, Gilbert I, Pirault JP, Megel M. Scuderi Split Cycle Research Engine: Overview, Architecture and Operation. SAE Int J Engines. 2011 Apr 12;4(1):450–66.
  33. Patil SG, Martin AJ, Ananthesha. Study on Performance Characteristics of Scuderi – Split Cycle Engine.
  34. Scuderi SC, Scuderi SP. Split-cycle air hybrid engine [Internet]. CA2634193A1, 2007 [cited 2022 Aug 16].
  35. Diakunchak I, Kiesow HJ, McQuiggan G. The History of the Siemens Gas Turbine. 2008.
  36. Chrysler Corporation. History of Chrysler Corporation Gas Turbine Vehicles. Michigan, USA; 1979 Jan. (Technical Information Engineering office).
  37. Corporation B. Popular Science. 1974 May.
  38. Norbye J. Turbine Drives Chevy Truck. Popular science. 1965 Oct.
  39. Cunha HE, Kyprianidis KG. Investigation of the Potential of Gas Turbines for Vehicular Applications. In American Society of Mechanical Engineers Digital Collection; 2013. p. 51–64.
  40. Cheverton MrB. On the use of heated air as a motive power. J Frankl Inst. 1853 Jun 1;55(6):365–8.
  41. Postma ND, Van Giessel R, Reinink F. The Stirling Engine for Passenger Car Application. In 1973. p. 730648.
  42. Van Giessel R, Reinink F. Design of the 4-215 D.A. Automotive Stirling Engine. In 1977. p. 770082.
  43. Gheith R, Aloui F, Tazerout M, Ben Nasrallah S. Experimental investigations of a gamma Stirling engine. Int J Energy Res. 2012;36(12):1175–82.
  44. Endo T, Kawajiri S, Kojima Y, Takahashi K, Baba T, Ibaraki S, et al. Study on Maximizing Exergy in Automotive Engines. In 2007. p. 2007-01–0257.
  45. Freymann P, Ringler DiplP, Seifert D, Horst DiplII. The Second Generation Turbosteamer. MTZ Worldw. 2012 Feb 1;73:18–23.
  46. Touré A, Stouffs P. Modeling of the Ericsson engine. Energy. 2014 Nov 1;76:445–52.
  47. Ngangué MN, Stouffs P. Dynamic simulation of an original Joule cycle liquid pistons hot air Ericsson engine. Energy. 2020 Jan 1;190:116293.
  48. Ferro B, Bannwart F. Modeling a thermoacoustic engine under Rott's approach from experimental transfer matrices of a thermoacoustic core. 2020.
  49. Penelet G, Lotton P, Bruneau M, Blanc-Benon P, Gusev V. Machines thermoacoustiques.
  50. Blok KD. Low operating temperature integral thermo acoustic devices for solar cooling and waste heat recovery. J Acoust Soc Am. 2008;123(5):3541.
  51. Olivier C, Penelet G, Poignand G, Lotton P. Active control of thermoacoustic amplification in a thermo-acousto-electric engine. J Appl Phys. 2014 May 7;115:174905–174905.

52. Bou Nader W, Chamoun J, Dumand C. Thermoacoustic engine as waste heat recovery system on extended range hybrid electric vehicles. *Energy Convers Manag.* 2020 Jul 1;215:112912.
53. Janssen LJJ. Hydrogen fuel cells for cars and buses. *J Appl Electrochem.* 2007 Oct 15;37(11):1383–7.
54. Peugeot 207 Epure [Internet]. Hydrogen Cars Now. [cited 2022 Aug 18].
55. Toyota FCHV [Internet]. Hydrogen Cars Now. [cited 2022 Aug 19].
56. Jangalwa A, Singh AK, Jain A, Barua A. SCUDERI SPLIT CYCLE ENGINE: A REVIEW. 2013 Oct;2(4).
57. Singh R, Maity A, Nataraj PSV. Dynamic modeling and robust nonlinear control of a laboratory gas turbine engine. *Aerosp Sci Technol.* 2022 Jul 1;126:107586.
58. Ranieri S, Prado GAO, MacDonald BD. Efficiency Reduction in Stirling Engines Resulting from Sinusoidal Motion. *Energies.* 2018 Nov;11(11):2887.
59. Bonnet S, Alaphilippe M, Stouffs P. Energy, exergy and cost analysis of a micro-cogeneration system based on an Ericsson engine. *Int J Therm Sci.* 2005 Dec 1;44(12):1161–8.
60. Kreuer KD. Fuel Cells, Introduction. In: Kreuer KD, editor. *Fuel Cells: Selected Entries from the Encyclopedia of Sustainability Science and Technology.* New York, NY: Springer; 2013. p. 1–7.
61. Christodoulou F, Giannakakis P, Kalfas AI. Performance Benefits of a Portable Hybrid Micro-Gas Turbine Power System for Automotive Applications. *J Eng Gas Turbines Power.* 2011 Feb 1;133(2).
62. Ji F, Zhang X, Du F, Ding S, Zhao Y, Xu Z, et al. Experimental and Numerical Investigation on Micro Gas Turbine as a Range Extender for Electric Vehicle. *Appl Therm Eng.* 2020 Mar 23;115236.
63. Karvountzis-Kontakiotis A, Andwari AM, Pesyridis A, Russo S, Tuccillo R, Esfahanian V. Application of Micro Gas Turbine in Range-Extended Electric Vehicles. *Energy.* 2018 Mar 15;147:351–61.
64. 2014 BMW i3 Electric Car: Why California Set Range Requirements, Engine Limits [Internet]. Green Car Reports. [cited 2022 Aug 19].
65. Sim K, Koo B, Kim CH, Kim TH. Development and performance measurement of micro-power pack using micro-gas turbine driven automotive alternators. *Appl Energy.* 2013 Feb 1;102:309–19.
66. Jaguar Introduces C-X75 Gas Micro-turbine Extended Range Electric Vehicle Concept [Internet]. Green Car Congress. [cited 2022 Aug 17].
67. GM EV1, la voiture électrique qui a marqué l'histoire... [Internet]. Automobile Propre. 2015 [cited 2022 May 13].
68. Volvo ECC – Un concept de durabilité captivant de 1992 | VPP Blog [Internet]. 2019 [cited 2022 May 11].
69. ETV Motors- Electric Technology for Vehicles [Internet]. 2011 [cited 2022 May 16].
70. Salton J. Capstone CMT-380 electric hybrid supercar with microturbines [Internet]. New Atlas. 2009 [cited 2020 Feb 26].
71. JaguarC-X75 [Internet]. Green Car Congress. 2010 [cited 2020 Feb 26].
72. Techrules [Internet]. Green Car Congress. 2016 [cited 2020 Apr 17].
73. Kane M. Wrightspeed Unveils Improved Turbine Range Extender [Internet]. InsideEVs. 2015 [cited 2020 Mar 5].
74. Walmart Range Extender Turbine [Internet]. Green Car Congress. 2014 [cited 2020 Feb 26].
75. Tan FX, Chiong MS, Rajoo S, Romagnoli A, Palenschat T, Martinez-Botas RF. Analytical and Experimental Study of Micro Gas Turbine as Range Extender for Electric Vehicles in Asian Cities. *Energy Procedia.* 2017 Dec 1;143:53–60.
76. Mackay R. Development of a 24 kW Gas Turbine-Driven Generator Set for Hybrid Vehicles. Warrendale, PA: SAE International; 1994 Mar. Report No.: 940510.
77. Zhao J, Ma Y, Zhang Z, Wang S, Wang S. Optimization and matching for range-extenders of electric vehicles with artificial neural network and genetic algorithm. *Energy Conversion and Management.* 2019 Mar 15;709–25.

78. Bassett M, Fraser N, Brooks T, Taylor G, Hall J, Thatcher I. A Study of Fuel Converter Requirements for an Extended-Range Electric Vehicle. *SAE Int J Engines*. 2010 Apr 12;3(1):631–54.
79. Borghi M, Mattarelli E, Muscoloni J, Rinaldini CA, Savioli T, Zardin B. Design and experimental development of a compact and efficient range extender engine. *Appl Energy*. 2017 Sep 15;202:507–26.
80. Breeze P. Gas-Turbine Power Generation - 1st Edition [Internet]. UK; 2016 [cited 2019 Oct 2].
81. Moran JM, Shapiro HN. Fundamentals of Engineering Thermodynamics. 5 th. 2006.
82. Sherwin K. Introduction to Thermodynamics. Springer Science & Business Media; 2012. 319 p.
83. Cadorin M, Pinelli M, Vaccari A, Calabria R, Chiariello F, Massoli P, et al. Analysis of a Micro Gas Turbine Fed by Natural Gas and Synthesis Gas: MGT Test Bench and Combustor CFD Analysis. *J Eng Gas Turbines Power*. 2012 Jul 1;134(7):071401.
84. Giampaolo T. Gas Turbine Handbook: Principles and Practice. The Fairmont Press, Inc.; 2009. 462 p.
85. Saravanamuttoo HIH, Rogers GFC, Cohen H. Gas Turbine Theory. Pearson Education; 2009. 616 p.
86. Bou Nader WS, Mansour CJ, Nemer MG. Optimization of a Brayton external combustion gas-turbine system for extended range electric vehicles. *Energy*. 2018 May 1;150:745–58.
87. Barakat AA, Diab JH, Badawi NS, Bou Nader WS, Mansour CJ. Combined cycle gas turbine system optimization for extended range electric vehicles. *Energy Convers Manag*. 2020 Dec 15;226:113538.
88. Boyce MP. Gas turbine engineering handbook. 2nd ed. Boston, MA: Gulf Professional Pub; 2002. 799 p.
89. Bathie WW. Fundamentals of Gas Turbines. Second Edition. 1996.
90. Dettmers PS. Gas Turbine range-extender for automotive applications. 2016.
91. Salpingidou C, Tsakmakidou D, Vlahostergios Z, Misirlis D, Flouros M, Yakinthos K. Analysis of turbine blade cooling effect on recuperative gas turbines cycles performance. *Energy*. 2018 Dec 1;164:1271–85.
92. Xiao G, Yang T, Liu H, Ni D, Ferrari ML, Li M, et al. Recuperators for micro gas turbines: A review. *Appl Energy*. 2017 Jul 1;197:83–99.
93. Kesseli J, Wolf T, Nash J, Freedman S. (1) Micro, Industrial, and Advanced Gas Turbines Employing Recuperators 2003.
94. Utriainen E, Sundén B. A Comparison of Some Heat Transfer Surfaces for Small Gas Turbine Recuperators. In American Society of Mechanical Engineers Digital Collection; 2014.
95. Tsai BJ, Wang YL. A novel Swiss-Roll recuperator for the microturbine engine. *Appl Therm Eng*. 2009 Feb 1;29(2):216–23.
96. Wang QW, Liang HX, Luo LQ, Wang JW, Huang ZP, Feng ZP, et al. Experimental Investigation on Heat Transfer and Pressure Drop in a Microturbine Recuperator With Cross-Wavy Primary Surface Channels. In: Volume 3: Turbo Expo 2005, Parts A and B. Reno, Nevada, USA: ASMEDC; 2005. p. 293–8.
97. Qiuwang W, Hongxia L, Gongnan X, Min Z, Laiqin L, ZhenPing F. Genetic Algorithm Optimization for Primary Surfaces Recuperator of Microturbine. *J Eng Gas Turbines Power*. 2007 Apr 1;129(2):436–42.
98. Robey E, Ramesh S, Sabau AS, Abdoli A, Black J, Straub D, et al. Design optimization of an additively manufactured prototype recuperator for supercritical CO<sub>2</sub> power cycles. *Energy*. 2022 Jul 15;251:123961.
99. Wakim S. Parametric optimization of heat exchangers, Validation by 3D printing. Mines Paristech, PSL Université, France; 2021.
100. Turbo Machinery Hieta. HiETA. 2019 [cited 2020 Feb 26].
101. Carman BG, Kapat JS, Chow LC, An L. Impact of a Ceramic Microchannel Heat Exchanger on a Micro Turbine. In American Society of Mechanical Engineers Digital Collection; 2009. p. 1053–60.
102. Halbig M, Jaskowiak M, Kiser J, Zhu D. Evaluation of Ceramic Matrix Composite Technology for Aircraft Turbine Engine Applications. In: 51st AIAA Aerospace Sciences Meeting including

- the New Horizons Forum and Aerospace Exposition, Texas: American Institute of Aeronautics and Astronautics; 2013 [cited 2022 Aug 22].
- 103. Razak AMY. Industrial gas turbines. Woodhead Publishing; 2007. 137–173 p. (Performance and Operability; vol. Chapter 6).
  - 104. Xing F, Kumar A, Huang Y, Chan S, Ruan C, Gu S, et al. Flameless combustion with liquid fuel: A review focusing on fundamentals and gas turbine application. *Appl Energy*. 2017 May 1; 193:28–51.
  - 105. Cavigiolo A, Galbiati MA, Effuggi A, Gelosa D, Rota R. Mild combustion in a laboratory-scale apparatus. *Combust Sci Technol*. 2003 Aug; 175 (8):1347–67.
  - 106. de Joannon M, Cavaliere A, Faravelli T, Ranzi E, Sabia P, Tregrossi A. Analysis of process parameters for steady operations in methane mild combustion technology. *Proc Combust Inst*. 2005 Jan 1; 30(2):2605–12.
  - 107. Khosravy M. Review of the New Combustion Technologies in Modern Gas Turbines. In: Benini E, editor. *Progress in Gas Turbine Performance*. InTech; 2013.
  - 108. Flamme M. New combustion systems for gas turbines (NGT). *Appl Therm Eng*. 2004 Aug 1; 24(11):1551–9.
  - 109. Wang YD, Huang Y, McIlveen-Wright D, McMullan J, Hewitt N, Eames P, et al. A techno-economic analysis of the application of continuous staged-combustion and flameless oxidation to the combustor design in gas turbines. *Fuel Process Technol*. 2006 Aug 1; 87 (8):727–36.
  - 110. Bazooyar B, Darabkhani HG. Design and numerical analysis of a 3 kWe flameless microturbine combustor for hydrogen fuel. *Int J Hydrg Energy*. 2019 Apr 23; 44(21):11134–44.
  - 111. Alshammari F. Radial Turbine ExpanderDesign, Modelling and Testing for Automotive Organic Rankine Cycle Waste Heat Recovery. Brunel University London; 2018.
  - 112. Korpela SA. Principles of turbomachinery. Hoboken, N.J: Wiley; 2020. 457 p.
  - 113. McDonald CF, Rodgers C. Small recuperated ceramic microturbine demonstrator concept. *Appl Therm Eng*. 2008 Jan 1; 28(1):60–74.
  - 114. Soares C. Chapter 2 - Design and components of microturbines. In: Soares C, editor. *Microturbines*. Burlington: Butterworth-Heinemann; 2007. p. 9–19. A
  - 115. Shan XC, Zhang Q, Sun YF, Maeda R. A MICRO TURBINE DEVICE WITH ENHANCED MICRO AIR-BEARINGS. In: DTIP 2006. Stresa, Lago Maggiore, Italy: TIMA Editions; 2006. p. 6 p.
  - 116. Muruganandam M, Nadarajan S. Design of Air Bearing for High Speed Micro Gas Turbine. : 10.
  - 117. Permanent Magnet Generators & Products | Low RPM | Mecc Alte [Internet]. [Cited 2022 Aug 24].
  - 118. Fosheim J, Gagne A, Johnson P, Thomas B. Enhancing the Undergraduate Educational Experience: Development of a Micro-Gas Turbine Laboratory. *Int J Mech Eng Educ*. 2014 Jul 1; 42:267–78.
  - 119. do Nascimento MAR, de L, dos Santos EC, Batista Gomes EE, Goulart FL, Gutirrez Velsques EI, et al. Micro Gas Turbine Engine: A Review. In: Benini E, editor. *Progress in Gas Turbine Performance*. InTech; 2013.
  - 120. Micro gas turbine – ETgroup [Internet]. 2019 [cited 2020 Apr 22].
  - 121. Gasturbineworld. Capstone Microturbine C30 Specification [Internet]. 2009 [cited 2019 Nov 19].
  - 122. Pickering C. Delta Motorsport launches gas turbine range extender [Internet]. The Engineer. 2016 [cited 2019 Nov 18].
  - 123. BraytonEnergy. 60 kW Microturbine [Internet]. Brayton Energy - Research and Development in Alternative Energies. 2019 [cited 2019 Nov 20].
  - 124. Micro Turbine Genset [Internet]. Bladon. 2019 [cited 2020 Apr 22].
  - 125. Mom AJA. Introduction to gas turbines. In: *Modern Gas Turbine Systems*. Elsevier; 2013 p. 3–20.
  - 126. Andriani R, Gamma F, Ghezzi U. Main Effects of Intercooling and Regeneration on Aeronautical Gas Turbine Engines. In: 46th AIAA/ASME/SAE/ASEE Joint Propulsion Conference & Exhibit. Nashville, TN: American Institute of Aeronautics and Astronautics; 2010.
  - 127. Rao AD. 2 - Gas-fired combined-cycle power plant design and technology. In: Roddy D, editor. *Advanced Power Plant Materials, Design and Technology*. Woodhead Publishing; 2010. p. 32–53. (Woodhead Publishing Series in Energy).

128. Nada T. Performance characterization of different configurations of gas turbine engines. *Propuls Power Res.* 2014 Sep 1; 3(3):121–32.
129. Ooms T, Vantyghem G, Van Coile R, De Corte W. A parametric modelling strategy for the numerical simulation of 3D concrete printing with complex geometries. *Addit Manuf.* 2021 Feb 1; 38:101743.
130. Soumikh R, Kumar R, Anurag, Panda A, Das RK. A Brief Review on Machining of Inconel 718. *Mater Today Proc.* 2018 Jan 1; 5(9, Part 3):18664–73.
131. Unger D, Herzog H. Comparative Study on Energy R&D Performance: Gas Turbine Case Study. 2016; 65.
132. Zhang Y, Duda T, Scobie JA, Sangan CM, Copeland CD, Redwood A. Design of an Air-Cooled Radial Turbine: Part 1 — Computational Modelling. In American Society of Mechanical Engineers Digital Collection; 2018.
133. Zhang Y, Duda T, Scobie J, Sangan C, Redwood A, Copeland C. Design of an Air-Cooled Radial Turbine Part 2: Experimental Measurements of Heat Transfer. 2018.
134. Okazaki Y, Matsudaira N, Matsuda M. Ceramic Turbine Wheel Developments for Mitsubishi Turbocharger. *SAE Trans.* 1985; 94:849–57.
135. Katayama K, Watanabe T, Matoba K. Development of Nissan High Response Ceramic Turbocharger Rotor. *SAE Trans.* 1986; 95:654–63.
136. Baker CC, Kobayashi RJ, Baker DE. Garrett Experience in Ceramic Turbocharger Turbine Wheels. *SAE Trans.* 1989; 98:368–76.
137. Lundberg R, Ferrato M. Ceramic Component Development for Agata. In American Society of Mechanical Engineers Digital Collection; 2014.
138. Takehara I, Inobe I, Tatsumi T, Ichikawa Y, Kobayashi H. Research and development of ceramic gas turbine (CGT302). *J Eng Gas Turbines Power.* 1998 Jan 1 120(1).
139. Tredway B, Shi J, Holowczak J, Vedula V, Bird C, Ochs S, et al. Design of Ceramic Components for an Advanced Micro-Turbine Engine. In 2004.
140. Matsunuma T, Yoshida H, Iki N, Ebara T, Sodeoka S, Inoue T, et al. MICRO GAS TURBINE WITH CERAMIC NOZZLE AND ROTOR. In Nevada, USA; 2005.
141. Hosseini E, Popovich VA. A review of mechanical properties of additively manufactured Inconel 718. *Addit Manuf.* 2019 Dec 1;30:100877.
142. Facchini B, Innocenti L. Refroidissement des turbines à gaz - Techniques et efficacité. In: Techniques de l'ingénieur. 2005. (Mécanique | Machines hydrauliques, aérodynamiques et thermiques).
143. Han JC, Park JS. Developing heat transfer in rectangular channels with rib turbulators. *Int J Heat Mass Transf.* 1988 Jan 1; 31(1):183–95.
144. Zuckerman N, Lior N. Jet Impingement Heat Transfer: Physics, Correlations, and Numerical Modeling. In: Advances in Heat Transfer. Elsevier; 2006. p. 565–631.
145. Bunker R. Gas Turbine Cooling: Moving From Macro to Micro Cooling. Vol. 3, Proceedings of the ASME Turbo Expo. 2013.
146. Wright L, Han JC. Heat Transfer Enhancement for Turbine Blade Internal Cooling. Vol. 21, Journal of Enhanced Heat Transfer. 2013.
147. Jordal K. Gas Turbine Cooling Modeling - Thermodynamic Analysis and Cycle Simulations. 1999.
148. Liang C, Rao Y, Luo J, Luo X. Experimental and Numerical Study of Turbulent Flow and Heat Transfer in a Wedge-shaped Channel with Guiding Pin Fins for Turbine Blade Trailing Edge Cooling. *Int J Heat Mass Transf.* 2021 Oct 1; 178:121590.
149. Chyu MK, Hsing YC, Shih TIP, Natarajan V. Heat Transfer Contributions of Pins and Endwall in Pin-Fin Arrays: Effects of Thermal Boundary Condition Modeling. *J Turbomach.* 1999 Apr 1; 121(2):257–63.
150. Effendy M, Yao Y, Yao J, Marchant DR. Pin-fin shape and orientation effects on wall heat transfer predictions of gas turbine blade. In Surakarta, Indonesia; 2019. p. 020008.
151. Chyu MK, Yen CH, Siw S. Comparison of heat transfer from staggered pin fin arrays with circular, cubic and diamond shaped elements. 2007 ;(GT2007-28306).
152. Jeng TM, Tzeng SC. Pressure drop and heat transfer of square pin-fin arrays in in-line and staggered arrangements. *Int J Heat Mass Transf.* 2007 Jun 1; 50(11):2364–75.

153. Kirsch KL, Ostanek JK, Thole KA. Comparison of pin surface heat transfer in arrays of oblong and cylindrical pin fins. *J Turbomach*. 2013; 136(4).
154. Axtmann M, Poser R, von Wolfersdorf J, Bouchez M. Endwall heat transfer and pressure loss measurements in staggered arrays of adiabatic pin fins. *Appl Therm Eng*. 2016 Jun 25; 103:1048–56.
155. Lyall ME, Thrift AA, Thole KA, Kohli A. Heat transfer from low aspect ratio pin fins. *J Turbomach*. 2011; 133(1).
156. Chyu M, Yu Y, Ding H, Downs J, Soechting F. Concavity enhanced heat transfer in an internal cooling passage. *ASME*. 1997; Paper 97-GT-437.
157. Ligrani PM, Harrison JL, Mahmmud GI, Hill ML. Flow structure due to dimple depressions on a channel surface. *Phys Fluids*. 2001; 13(11):3442–51.
158. Vorayos N, Katkhaw N, Kiatsiriroat T, Nuntaphan A. Heat transfer behavior of flat plate having spherical dimpled surfaces. *Case Stud Therm Eng*. 2016 Sep 1; 8:370–7.
159. Du W, Luo L, Wang S, Liu J, Sundén B. Heat transfer and flow structure in a detached latticework duct. *Appl Therm Eng*. 2019 Jun 5; 155:24–39.
160. Bunker R. Thermal Engineering in Power Systems. Vol. Vol 42, Chap 7. GE, global research center, USA; 2008.
161. Pudake P, Elgandelwar AM, M.Lele M. Gas Turbine Blade Cooling Technology—A Case Study. In 2017.
162. Guo Z, Song Z, Fan J, Yan X, Huang D. Experimental and analytical investigation on service life of film cooling structure for single crystal turbine blade. *Int J Fatigue*. 2021 Sep 1; 150:106318.
163. Liu R, Li H, Lin J, You R, Tao Z. An experimental and numerical investigation of film cooling effectiveness on a gas turbine blade tip region. *Int J Therm Sci*. 2022 Jul 1; 177:107544.
164. Zhang B lun, Yao CY, Zhu H ren, Liu C liang, Sundén B. Experimental study on film cooling performance of a turbine blade tip with a trapezoidal slot cooling scheme in transonic flow using PSP technique. *Exp Therm Fluid Sci*. 2022 Jan 1; 130:110513.
165. Liu C, Zhang F, Zhang S, Shi Q, Song H. Experimental investigation of the full coverage film cooling effectiveness of a turbine blade with shaped holes. *Chin J Aeronaut*. 2022 Mar 1; 35(3):297–308.
166. Yalcin E, Sögüt Z, Durmus S, Karakoc T. Thermodynamics assessment of transpiration cooling effects in gas turbine blades based on turbine inlet temperature. In Istanbul, Turkey; 2015.
167. XU L, BO S, Hondge Y, Lei W. Evolution of Rolls-royce Air-cooled Turbine Blades and Feature Analysis | Elsevier Enhanced Reader. 2015.
168. Roelke RJ. Radial Turbine Cooling. NASA Lewis Research Center; 1992.
169. Lane JM. Cooled Radial In-Flow Turbines for Advanced Gas Turbine Engines. 1981;
170. Calvert GS, Beck SC, Okapuu U. Design and Experimental Evaluation of a HighTemperature Radial Turbine. 1971 May. (USAAMRDL Technical Report 71-20).
171. Ewing BA, Monson DS, Lane JM. U .S. Army/ Detroit Diesel Allison High-Temperature Radial Turbine Demonstration. In California; 1980. p. 80–0301.
172. Vershure Jr. RW, Large GD, Meyer LJ, Lane JM. Cooled Laminated Radial Turbine Demonstration Program. *Journal of Aircraft*. 1981; 731–8.
173. Hamed A, Baskharone E, Tabakoff W. Temperature Distribution Study in a Cooled Radial Inflow Turbine Rotor. *JAircraft*. Vol.14, No.2. 1977 Feb.
174. Kumar GN, DeAnna RG. Development of a Thermal and Structural Analysis Procedure for Cooled Radial Turbines - PDF Free Download. NASA Technical Report 88-C-037, Presented at the 33rd International Gas Turbine and Aeroengine Congress and Exhibition, Amsterdam; 1988.
175. SHIH T, ROELKE R. Computations of the three-dimensional flow and heat transfer within a coolant passage of a radial turbine blade. In: 27th Joint Propulsion Conference. American Institute of Aeronautics and Astronautics.
176. Johnson BV, Wagner JH. Heat transfer experiments in the internal cooling passages of a cooled radial turbine rotor. 1996. (NASA Contractor Report 198472).
177. Schwerdt C. Modelling NO<sub>x</sub>-Formation in Combustion Processes [Internet]. ISSN 0280-5316 ISRN LUTFD2/TFRT--5769--SE; 2006 [cited 2021 May 3].

178. Richards JR. Control of Nitrogen Oxides Emissions. Robert M. Schell. ICES Ltd.; 2000. (Air Control Techniques, P.C.; vol. EPA Contract No. 68D99022).
179. Pavri R, Moore GD. Gas Turbine Emissions and Control. Atlanta, GA; Report No.: GER-4211.
180. Schorr MM, Chalfin J. Gas Turbine Nox Emissions Approaching Zero – Is it worth the price ? Schenectady, New York; (General Electric Power Systems). Report No.: GER 4172.
181. Forzatti P, Lietti L. The reduction of NOx stored on LNT and combined LNT-SCR systems. 2010 Oct; 155(1–2):131–9.
182. Bosch H, Janssen F. Catalytic reduction of nitrogen oxides. 1988; 2:369–532.
183. Nam CM, Gibbs BM. Selective non-catalytic reduction of NOx under diesel engine conditions. Proc Combust Inst. 2000 Jan; 28(1):1203–9.
184. Long RQ, Yang RT. Selective catalytic reduction of NO with ammonia over V2O5 doped TiO2 pillared clay catalysts. Appl Catal B Environ. 2000 Jan; 24(1):13–21.
185. Miller JA, Bowman CT. Mechanism and modeling of nitrogen chemistry in combustion. Prog Energy Combust Sci. 1989 Jan; 15(4):287–338.
186. Alne KS. Reduction of NOx Emissions from the Gas Turbines for Skarv Idun. Norway: Norwegian University of Science and Technology Department of Energy and Process Engineering;
187. Fousová M, Vojt D. 3D printing as an alternative to casting, forging and machining technologies? 2015; 8.
188. Melchels FPW, Feijen J, Grijpma DW. A review on stereolithography and its applications in biomedical engineering. Biomaterials. 2010 Aug 1; 31(24):6121–30.
189. Ngo TD, Kashani A, Imbalzano G, Nguyen KTQ, Hui D. Additive manufacturing (3D printing): A review of materials, methods, applications and challenges. Compos Part B Eng. 2018 Jun 15; 143:172–96.
190. Stansbury JW, Idacavage MJ. 3D printing with polymers: Challenges among expanding options and opportunities. Dent Mater. 2016 Jan 1; 32(1):54–64.
191. Wu P, Wang J, Wang X. A critical review of the use of 3-D printing in the construction industry. Autom Constr. 2016 Aug 1; 68:21–31.
192. Nichols MR. How does the automotive industry benefit from 3D metal printing? Met Powder Rep. 2019 Sep 1; 74(5):257–8.
193. Joshi SC, Sheikh AA. 3D printing in aerospace and its long-term sustainability. Virtual Phys Prototyp. 2015 Oct 2; 10(4):175–85.
194. Wang X, Jiang M, Zhou Z, Gou J, Hui D. 3D printing of polymer matrix composites: A review and prospective. Compos Part B Eng. 2016 Nov 1; 110.
195. Frazier WE. Metal Additive Manufacturing: A Review. J Mater Eng Perform. 2014 Jun; 23(6):1917–28.
196. Hajare DM, Gajbhiye TS. Additive manufacturing (3D printing): Recent progress on advancement of materials and challenges. Mater Today Proc. 2022 Jan 1; 58:736–43.
197. Mohamed OA, Masood SH, Bhowmik JL. Optimization of fused deposition modeling process parameters: a review of current research and future prospects. Adv Manuf. 2015 Mar 1; 3(1):42–53.
198. Chohan J, Singh R, Boparai KS, Penna R, Fraternali F. Dimensional accuracy analysis of coupled fused deposition modeling and vapour smoothing operations for biomedical applications. 2017;
199. Sachs EM, Haggerty JS, Cima MJ, Williams PA. Three-dimensional printing techniques. 1993.
200. Gibson I, Rosen D, Stucker B. Directed Energy Deposition Processes. In: Additive Manufacturing Technologies. New York, NY: Springer New York; 2015. p. 245–68.
201. Gibson I, Rosen D, Stucker B. Sheet Lamination Processes. In: Additive Manufacturing Technologies. New York, NY: Springer New York; 2015. p. 219–44.
202. Arifin M, Wahono B, Junianto E, Pasek AD. Process manufacture rotor radial turbo-expander for small scale organic Rankine cycles using selective laser melting machine. In: Energy Procedia. 2nd International Conference on Sustainable Energy Engineering and Application, ICSEEA 2014; 2015. p. 305–10.
203. Rahbar K, Mahmoud S, Al-Dadah RK, Moazami N, Mirhadizadeh SA. Development and experimental study of a small-scale compressed air radial inflow turbine for distributed power generation. Appl Therm Eng. 2017 Apr 1; 116:549–83.

204. Hernandez-Carrillo I, Wood CJ, Liu H. Advanced materials for the impeller in an ORC radial microturbine. *Energy Procedia*. 2017 Sep;129:1047–54.
205. Weiß AP, Novotný V, Popp T, Streit P, Špale J, Zinn G, et al. Customized ORC micro turbo-expanders - From 1D design to modular construction kit and prospects of additive manufacturing. *Energy*. 2020 Oct 15; 209:118407.
206. Razak AMY. 3 - Complex gas turbine cycle. In: Razak AMY, editor. *Industrial Gas Turbines*. Woodhead Publishing; 2007. p. 60–97.
207. Janes J. A Fully Enhanced Gas Turbine for Surface Ships. In American Society of Mechanical Engineers Digital Collection; 2015.
208. Oyedepo S, Fagbenle R, Adefila S s. Exergoeconomic analysis and performance assessment of selected gas turbine power plants. *World J Eng*. 2015 Aug 1; 12:283–300.
209. Datta A, Som SK. Energy and exergy balance in a gas turbine combustor. *Proc Inst Mech Eng Part J Power Energy*. 1999 Feb 1; 213(1):23–32.
210. HiETA Technologies [Internet]. HiETA. [Cited 2022 Jun 16].
211. Louis JF, Hiraoka K, El Masri MA. A Comparative Study of the Influence of Different Means of Turbine Cooling on Gas Turbine Performance. In ASME; 2015.
212. Ba W, Gu C, Ren X, Li X. Convective cooling model for aero-thermal coupled through-flow method. *Proc Inst Mech Eng Part J Power Energy*. 2017 Mar; 231(2):133–44.
213. Jordal K, Torbidoni L, Massardo AF. Convective Blade Cooling Modelling for the Analysis of Innovative Gas Turbine Cycles. In: Volume 2. New Orleans, Louisiana, USA: American Society of Mechanical Engineers; 2001. p. V002T04A024.
214. Sanjay, Singh O, Prasad BN. Influence of different means of turbine blade cooling on the thermodynamic performance of combined cycle. *Appl Therm Eng*. 2008 Dec 1; 28(17):2315–26.
215. Bala Prasad K, Tara Chand V, Niranjan Kumar IN, Ravindra K, Naga Bhushana Rao V. Thermodynamic Analysis of Air Cooled Gas Turbine used in Marine Applications. In 2016. (*International Journal of Thermal Technologies*).
216. Hartsel JE. Prediction of effects of mass-transfer cooling on the blade-row efficiency of turbine airfoils | Aerospace Sciences Meetings. IAAA. 1972.
217. Young JB, Horlock JH. Defining the Efficiency of a Cooled Turbine. *J Turbomach*. 2006 Oct 1; 128(4):658–67.
218. Ba W, Wang X chen, Li X song, Ren X dong, Gu C wei. Definition of cycle based comprehensive efficiency of a cooled turbine. *Energy*. 2019 Feb 1; 168:601–8.
219. Uysal SC. Analytical modelling of the effects of different gas turbine cooling techniques on engine performance. Benjamin Statler College of Engineering, Morgantown West Virginia University; 2017.
220. El-Masri MA. An interactive code for thermal analysis of gas turbine systems. 1988 ;( 110):201–9.
221. ASME. BPVC Section II-Materials-Part D- Properties. ASME; 2013. (ASME Boiler and Pressure Vessel Code).
222. Kranz J, Herzog D, Emmelmann C. Design guidelines for laser additive manufacturing of lightweight structures in TiAl6V4. *J Laser Appl*. 2015 Feb; 27(S1):S14001.
223. Design Guidelines for Stainless Steel | Metal 3D Printing at Materialise [Internet]. [Cited 2022 Sep 7].
224. Tsopanos S, Sutcliffe C, Owen I. The Manufacture of Micro Cross-Flow Heat Exchangers by Selective Laser Melting. 2005 Jan 1.
225. Design Rules & Best Practices for FFF 3D Printing [Internet]. Hydra Research. [Cited 2022 Sep 7].
226. Hubs. How to design parts for metal 3D printing [Internet]. [Cited 2022 Jul 8].
227. Reine A, Bou Nader W. Fuel consumption potential of different external combustion gas-turbine thermodynamic configurations for extended range electric vehicles. *Energy*. 2019 May 15; 175:900–13.
228. McDonald CF. Recuperator considerations for future higher efficiency microturbines. *Appl Therm Eng*. 2003 Aug; 23(12):1463–87.
229. Kays WM, London AL. Compact heat exchangers. 1984 Jan 1 [cited 2022 Sep 2].

230. Duan F, Song K, Li H, Chang L, Zhang Y, Wang L. Numerical study of laminar flow and heat transfer characteristics in the fin side of the intermittent wavy finned flat tube heat exchanger. *Appl Therm Eng.* 2016 Jun 25; 103:112–27.
231. Aliabadi MK, Samani MG, Hormozi F, Asl AH. 3D-CFD simulation and neural network model for the  $j$  and  $f$  factors of the wavy fin-and-flat tube heat exchangers. *Braz J Chem Eng.* 2011; 28(3):505–20.
232. Ismail LS, Velraj R. Studies on Fanning Friction ( $f$ ) and Colburn ( $j$ ) Factors of Offset and Wavy Fins Compact Plate Fin Heat Exchanger—A CFD Approach. *Numer Heat Transf Part Appl.* 2009 Dec 24; 56(12):987–1005.
233. Junqi D, Jiangping C, Zhijiu C, Yimin Z, Wenfeng Z. Heat transfer and pressure drop correlations for the wavy fin and flat tube heat exchangers. *Appl Therm Eng.* 2007 Aug 1; 27(11):2066–73.
234. Qasem NAA, Zubair SM. Generalized air-side friction and heat transfer correlations for wavy-fin compact heat exchangers. *Int J Refrig.* 2019 Jan 1; 97:21–30.
235. Chang YJ, Wang CC. A generalized heat transfer correlation for Louver fin geometry. *Int J Heat Mass Transf.* 1997 Feb 1; 40(3):533–44.
236. Kedam N, Dmitry A U, Evgeniy V B, Alexey A G. Heat transfer factor  $j$  and friction factor  $f$  correlations for offset strip fin and wavy fin of compact plate-fin heat-exchangers. *Case Stud Therm Eng.* 2021 Dec 1; 28:101552.
237. Bhowmik H, Lee KS. DESIGN ANALYSIS OF OFFSET STRIP FIN HEAT EXCHANGER. In 2008.
238. Webb RL. Plate Fin Surface Geometries. *Heat Exch Des Handb Multimed Ed.* 2018 Oct 25.
239. Alberto T, Massardo A. Optimal design of compact recuperators for microturbine application. *Appl Therm Eng.* 2005 Oct 1; 25:2054–71.
240. Wen J, Yang H, Tong X, Li K, Wang S, Li Y. Optimization investigation on configuration parameters of serrated fin in plate-fin heat exchanger using genetic algorithm. *Int J Therm Sci.* 2016 Mar; 101:116–25.
241. Sanaye S, Hajabdollahi H. Thermal-economic multi-objective optimization of plate fin heat exchanger using genetic algorithm. *Appl Energy.* 2010 Jun; 87(6):1893–902.
242. Shah RK, Sekulic DP. *Fundamentals of Heat Exchanger Design.* John Wiley & Sons, Ltd; 2003.
243. Austrin L, Torabzadeh-Tari M, Engdahl G. A new high power density generation system. *ICAS.* 2006;
244. Lallemand A. Energie, exergie, économie, thermo-économie. 2007 [cited 2022 Jun 17].
245. Costall AW, Gonzalez Hernandez a, Newton PJ, Martinez-Botas RF. Design methodology for radial turbo expanders in mobile organic Rankine cycle applications. *Appl Energy.* 2015 Nov 1; 157:729–43.
246. Vilim RB. Development and validation of a radial inflow turbine model for simulation of the SNL S-CO<sub>2</sub> split-flow loop. Argonne National Lab. (ANL), Argonne, IL (United States); 2012 Jul. Report No.: ANL-ARC-195.
247. Han Z, Jia X, Li P. Preliminary design of radial inflow turbine and working fluid selection based on particle swarm optimization. *Energy Convers Manag.* 2019 Nov 1; 199:111933.
248. Deligant M, Huebel M, Djianne TN, Ravelet F, Specklin M, Kebedani M. Design and off-design system simulation of concentrated solar super-critical CO<sub>2</sub> cycle integrating a radial turbine meanline model. *Energy Rep.* 2022 Nov 1; 8:1381–93.
249. Zhou K, Wang J, Xia J, Guo Y, Zhao P, Dai Y. Design and performance analysis of a supercritical CO<sub>2</sub> radial inflow turbine. *Appl Therm Eng.* 2020 Feb 25; 167:114757.
250. Wei Z. *Meanline Analysis of Radial Inflow Turbines at Design and Off-Design Conditions,* Carleton University; Canada; 2014; 178.
251. Al Jubori AM, Al-Mousawi NF, Rahbar K, AL-Dadah R. Design and manufacturing a small-scale radial-inflow turbine for clean organic Rankine power system | Elsevier Enhanced Reader. 2020.
252. da Silva ER, Kyprianidis KG, Camacho RGR, Säterskog M, Angulo TMA. Preliminary design, optimization and CFD analysis of an organic rankine cycle radial turbine rotor. *Appl Therm Eng.* 2021 Aug 1; 195:117103.
253. Aungier R. *Turbine Aerodynamics, Axial-flow and radial-inflow turbine design and analysis.* 2005.

254. Dixon SL, Hall C. Fluid Mechanics and Thermodynamics of Turbomachinery. Butterworth-Heinemann; 2010. 319–360 p.
255. Balje OE. Turbomachines : A Guide to Design, Selection, and Theory. Wiley; 1981.
256. Chain H, Baines NC. Performance parameters and assessment. U.K.: V.K.I.; (Lecture series).
257. Fiaschi D, Manfrida G, Maraschillo F. Design and performance prediction of radial ORC turboexpanders. *Appl Energy*. 2015 Jan 15; 138:517–32.
258. Whitfield A, Baines NC. Design of Radial Turbomachines. 1990th ed. 1990. (Longman Scientific and Technical).
259. Rohlik HE. Analytical Determination of Radial Inflow Turbine Design Geometry for Maximum Efficiency. TN D-4384. 1968;
260. Watanabe I, Ariga I, Mashimo T. Effect of Dimensional Parameters of Impellers on Performance Characteristics of a Radial Inflow Turbine. *Transactions ASME Journal Engineering for Power*. : 81–102.
261. Moustapha H, Zelesky MF, Baines NC, Japikse D. Axial and Radial Turbines Part 3: Radial Turbine Design. Concepts NREC. Vol. Chap 7, 8,9. White River Junction; 2003. pp. 197-326.
262. Glassman AJ. Enhanced Analysis and User's Manual for Radial Inflow Turbine Conceptual Design Code RTD. Vol. NASA-CR-195454, E-9538, NAS 1.26:195454; NASA. Washington, DC, USA, 1995.
263. Quoilin S, Broek MVD, Declaye S, Dewallef P, Lemort V. Techno-economic survey of Organic Rankine Cycle (ORC) systems. *Renew Sustain Energy Rev*. 2013 Jun 1; 22:168–86.
264. Espinosa Sarmiento AL, Ramirez Camacho RG, de Oliveira W. Performance analysis of radial-inflow turbine of ORC: New combined approach of preliminary design and 3D CFD study. *J Mech Sci Technol*. 2020 Jun; 34(6):2403–22.
265. Verma R, Sam AA, Ghosh P. CFD Analysis of Turbo Expander for Cryogenic Refrigeration and Liquefaction Cycles. *Phys Procedia*. 2015 Jan 1; 67:373–8.
266. Chen Y, Liu Y, Liu W, Ge Y, Xue Y, Zhang L. Optimal design of radial inflow turbine for ocean thermal energy conversion based on the installation angle of nozzle blade. *Renew Energy*. 2022 Jan 1; 184:857–70.
267. Odabae M, Sauret E, Hooman K. Computational Fluid Dynamics Simulation And Turbomachinery Code Validation Of A High Pressure Ratio Radial-Inflow Turbine. In 2014.
268. Schultz M, Finlay J, Callow M, Callow J. Three Models to Relate Detachment of Low Form Fouling at Laboratory and Ship Scale. *Biofouling*. 2003 May 1; 19 Suppl: 17–26.
269. Sauret E. Open Design of High Pressure Ratio Radial-Inflow Turbine for Academic Validation. Vol. 7, ASME International Mechanical Engineering Congress and Exposition, Proceedings (IMECE). 2012.
270. Pereiras B, Castro F, El Marjani A, Rodríguez M. Tip Clearance Effect on the Flow Pattern of a Radial Impulse Turbine for Wave Energy Conversion. *J Turbomach*. 2011 Oct 1; 133.
271. Al-Kayiem HH, Al-taie AK, Tiat Dong W. Analysis on Gas Turbine Blade Cooling by Compressed Air Channels using CFD Simulation. Malaysia. 2013; 467–77.
272. Do KDC, Chung DH, Tran DQ, Dinh CT, Nguyen QH, Kim KY. Numerical Investigation of Heat Transfer Characteristics of Pin-Fins with Roughed Endwalls in Gas Turbine Blade Internal Cooling Channels. *Int J Heat Mass Transf*. 2022 Oct 1; 195:123125.
273. Irfan Ahmed S, Kumar Balguri P, Govardhan D, Habeeb S. Numerical study and heat transfer analysis of nickel-chromium and titanium carbide gas turbine blades cooling. *Mater Today Proc*. 2022 Jan 1; 62:2709–13.
274. Zhang Y, Cao Y, Feng Y, Li D, Qin J. Numerical simulation of convective heat transfer for an internally cooled gas turbine using liquid metal. *Int J Therm Sci*. 2022 Jan 1; 171:107230.
275. Menter FR. Two-equation eddy-viscosity turbulence models for engineering applications. *AIAA J*. 1994 Aug; 32(8):1598–605.

## RÉSUMÉ

---

Le développement de solutions permettant d'électrifier les voitures est un enjeu majeur sur le plan environnemental. D'importants efforts de recherche ont été réalisés dans l'industrie automobile sur les nouveaux carburants et les nouvelles chaînes de traction hybride électrique afin de réduire les émissions de carbone des véhicules. Les systèmes de turbines à gaz ont été identifiés comme l'un des meilleurs convertisseurs d'énergie potentielle pour les chaînes de traction hybride série (SHEV). Le cycle qui nous intéresse dans cette thèse est celui d'une turbine à gaz (avec compression refroidie, régénérateur et réchauffement durant la détente (IRReGT)) car il offre un rendement et une densité de puissance élevés ainsi qu'une consommation de carburant réduite. La présente thèse propose une nouvelle configuration d'un cycle comportant une turbine refroidie dans le but d'augmenter la température à l'entrée de la turbine et le rendement du cycle. Cette thèse s'intéresse particulièrement à la conception de cette turbine radiale refroidie, réalisée à l'aide de l'impression 3D. Il s'agit d'une turbine d'une puissance de l'ordre de 20 kW qui fonctionne à une pression de 9 bars et une température de l'ordre de 1450°C avec des vitesses de rotation allant jusqu'à 120 000 tours par minute. La turbine refroidie conçue a atteint un rendement de 74 %, avec une amélioration de 3 points par rapport au cycle de référence.

## MOTS CLÉS

---

Voiture hybride, turbine radiale, aubes refroidies, Haute Pression, Haute Température, Impression 3D, refroidissement par convection.

## ABSTRACT

---

The development of solutions to electrify cars is a major environmental issue. Major research efforts have been invested in the automotive industry on new fuels and new hybrid electric powertrains to reduce vehicle carbon emissions. Gas turbine systems have been identified as one of the best potential energy converters for series hybrid powertrains (SHEV). The cycle of interest in this thesis is a gas turbine (with cooled compression, regenerator, and reheat during expansion (IRReGT)) because it offers high efficiency and power density as well as reduced fuel consumption. This thesis is interested in proposing a new configuration of the cycle including a cooled turbine to increase the temperature at the turbine inlet and the efficiency of the cycle. This thesis is particularly interested in the design of this cooled radial turbine, manufactured by 3D printing. The turbine has a power of about 20 kW and operates at a pressure of 9 bar and a temperature of about 1450°C with rotational speeds up to 120 000 rpm. The designed cooled turbine achieved an efficiency of 74 %, with an increase of the overall cycle efficiency by 3 points compared to the baseline cycle.

## KEYWORDS

---

SHEV, radial turbine, cooled blade, High-pressure, High-Temperature, 3D printing, convection cooling.